Multilevel Algebraic Reconstruction Techniques for X-Ray Computed Tomography

by

HUAIQUN GUAN

A Thesis
Submitted to the Faculty of Graduate Studies
in Partial Fulfillment of the Requirements
for the Degree of

DOCTOR OF PHILOSOPHY

Department of Physics
University of Manitoba
Winnipeg, Manitoba

National Library
of Canada

Acquisitions and
Bibliographic Services Branch

395 Wellington Street
Ottawa, Ontario
K1A 0N4

Bibliothèque nationale
du Canada

Direction des acquisitions et
des services bibliographiques

395, rue Wellington
Ottawa (Ontario)
K1A 0N4

Your file Votre référence

Our file Notre référence

ISBN 0-612-13158-0

Canada

Name _____

Dissertation Abstracts International is arranged by broad, general subject categories. Please select the one subject which most nearly describes the content of your dissertation. Enter the corresponding four-digit code in the spaces provided.

PHYSICS / RADIATION — SUBJECT TERM

0756 — SUBJECT CODE

U·M·I

Subject Categories

THE HUMANITIES AND SOCIAL SCIENCES

COMMUNICATIONS AND THE ARTS
Architecture 0729
Art History 0377
Cinema 0900
Dance 0378
Fine Arts 0357
Information Science 0723
Journalism 0391
Library Science 0399
Mass Communications 0708
Music 0413
Speech Communication 0459
Theater 0465

EDUCATION
General 0515
Administration 0514
Adult and Continuing 0516
Agricultural 0517
Art 0273
Bilingual and Multicultural 0282
Business 0688
Community College 0275
Curriculum and Instruction 0727
Early Childhood 0518
Elementary 0524
Finance 0277
Guidance and Counseling 0519
Health 0680
Higher 0745
History of 0520
Home Economics 0278
Industrial 0521
Language and Literature 0279
Mathematics 0280
Music 0522
Philosophy of 0998
Physical 0523
Psychology 0525
Reading 0535
Religious 0527
Sciences 0714
Secondary 0533
Social Sciences 0534
Sociology of 0340
Special 0529
Teacher Training 0530
Technology 0710
Tests and Measurements 0288
Vocational 0747

LANGUAGE, LITERATURE AND LINGUISTICS
Language
- General 0679
- Ancient 0289
- Linguistics 0290
- Modern 0291

Literature
- General 0401
- Classical 0294
- Comparative 0295
- Medieval 0297
- Modern 0298
- African 0316
- American 0591
- Asian 0305
- Canadian (English) 0352
- Canadian (French) 0355
- English 0593
- Germanic 0311
- Latin American 0312
- Middle Eastern 0315
- Romance 0313
- Slavic and East European 0314

PHILOSOPHY, RELIGION AND THEOLOGY
Philosophy 0422
Religion
- General 0318
- Biblical Studies 0321
- Clergy 0319
- History of 0320
- Philosophy of 0322

Theology 0469

SOCIAL SCIENCES
American Studies 0323
Anthropology
- Archaeology 0324
- Cultural 0326
- Physical 0327

Business Administration
- General 0310
- Accounting 0272
- Banking 0770
- Management 0454
- Marketing 0338

Canadian Studies 0385
Economics
- General 0501
- Agricultural 0503
- Commerce-Business 0505
- Finance 0508
- History 0509
- Labor 0510
- Theory 0511

Folklore 0358
Geography 0366
Gerontology 0351
History
- General 0578
- Ancient 0579
- Medieval 0581
- Modern 0582
- Black 0328
- African 0331
- Asia, Australia and Oceania 0332
- Canadian 0334
- European 0335
- Latin American 0336
- Middle Eastern 0333
- United States 0337

History of Science 0585
Law 0398
Political Science
- General 0615
- International Law and Relations 0616
- Public Administration 0617

Recreation 0814
Social Work 0452
Sociology
- General 0626
- Criminology and Penology 0627
- Demography 0938
- Ethnic and Racial Studies 0631
- Individual and Family Studies 0628
- Industrial and Labor Relations 0629
- Public and Social Welfare 0630
- Social Structure and Development 0700
- Theory and Methods 0344

Transportation 0709
Urban and Regional Planning 0999
Women's Studies 0453

THE SCIENCES AND ENGINEERING

BIOLOGICAL SCIENCES
Agriculture
- General 0473
- Agronomy 0285
- Animal Culture and Nutrition 0475
- Animal Pathology 0476
- Food Science and Technology 0359
- Forestry and Wildlife 0478
- Plant Culture 0479
- Plant Pathology 0480
- Plant Physiology 0817
- Range Management 0777
- Wood Technology 0746

Biology
- General 0306
- Anatomy 0287
- Biostatistics 0308
- Botany 0309
- Cell 0379
- Ecology 0329
- Entomology 0353
- Genetics 0369
- Limnology 0793
- Microbiology 0410
- Molecular 0307
- Neuroscience 0317
- Oceanography 0416
- Physiology 0433
- Radiation 0821
- Veterinary Science 0778
- Zoology 0472

Biophysics
- General 0786
- Medical 0760

EARTH SCIENCES
Biogeochemistry 0425
Geochemistry 0996
Geodesy 0370
Geology 0372
Geophysics 0373
Hydrology 0388
Mineralogy 0411
Paleobotany 0345
Paleoecology 0426
Paleontology 0418
Paleozoology 0985
Palynology 0427
Physical Geography 0368
Physical Oceanography 0415

HEALTH AND ENVIRONMENTAL SCIENCES
Environmental Sciences 0768
Health Sciences
- General 0566
- Audiology 0300
- Chemotherapy 0992
- Dentistry 0567
- Education 0350
- Hospital Management 0769
- Human Development 0758
- Immunology 0982
- Medicine and Surgery 0564
- Mental Health 0347
- Nursing 0569
- Nutrition 0570
- Obstetrics and Gynecology 0380
- Occupational Health and Therapy 0354
- Ophthalmology 0381
- Pathology 0571
- Pharmacology 0419
- Pharmacy 0572
- Physical Therapy 0382
- Public Health 0573
- Radiology 0574
- Recreation 0575
- Speech Pathology 0460
- Toxicology 0383

Home Economics 0386

PHYSICAL SCIENCES
Pure Sciences
Chemistry
- General 0485
- Agricultural 0749
- Analytical 0486
- Biochemistry 0487
- Inorganic 0488
- Nuclear 0738
- Organic 0490
- Pharmaceutical 0491
- Physical 0494
- Polymer 0495
- Radiation 0754

Mathematics 0405
Physics
- General 0605
- Acoustics 0986
- Astronomy and Astrophysics 0606
- Atmospheric Science 0608
- Atomic 0748
- Electronics and Electricity 0607
- Elementary Particles and High Energy 0798
- Fluid and Plasma 0759
- Molecular 0609
- Nuclear 0610
- Optics 0752
- Radiation 0756
- Solid State 0611

Statistics 0463

Applied Sciences
Applied Mechanics 0346
Computer Science 0984
Engineering
- General 0537
- Aerospace 0538
- Agricultural 0539
- Automotive 0540
- Biomedical 0541
- Chemical 0542
- Civil 0543
- Electronics and Electrical 0544
- Heat and Thermodynamics 0348
- Hydraulic 0545
- Industrial 0546
- Marine 0547
- Materials Science 0794
- Mechanical 0548
- Metallurgy 0743
- Mining 0551
- Nuclear 0552
- Packaging 0549
- Petroleum 0765
- Sanitary and Municipal 0554
- System Science 0790

Geotechnology 0428
Operations Research 0796
Plastics Technology 0795
Textile Technology 0994

PSYCHOLOGY
General 0621
Behavioral 0384
Clinical 0622
Developmental 0620
Experimental 0623
Industrial 0624
Personality 0625
Physiological 0989
Psychobiology 0349
Psychometrics 0632
Social 0451

Nom _____

Dissertation Abstracts International est organisé en catégories de sujets. Veuillez s.v.p. choisir le sujet qui décrit le mieux votre thèse et inscrivez le code numérique approprié dans l'espace réservé ci-dessous.

_____ ☐☐☐ U·M·I

SUJET — CODE DE SUJET

Catégories par sujets

HUMANITÉS ET SCIENCES SOCIALES

COMMUNICATIONS ET LES ARTS
Architecture 0729
Beaux-arts 0357
Bibliothéconomie 0399
Cinéma 0900
Communication verbale 0459
Communications 0708
Danse 0378
Histoire de l'art 0377
Journalisme 0391
Musique 0413
Sciences de l'information 0723
Théâtre 0465

ÉDUCATION
Généralités 515
Administration 0514
Art 0273
Collèges communautaires 0275
Commerce 0688
Économie domestique 0278
Éducation permanente 0516
Éducation préscolaire 0518
Éducation sanitaire 0680
Enseignement agricole 0517
Enseignement bilingue et multiculturel 0282
Enseignement industriel 0521
Enseignement primaire. 0524
Enseignement professionnel 0747
Enseignement religieux 0527
Enseignement secondaire 0533
Enseignement spécial 0529
Enseignement supérieur 0745
Évaluation 0288
Finances 0277
Formation des enseignants 0530
Histoire de l'éducation 0520
Langues et littérature 0279
Lecture 0535
Mathématiques 0280
Musique 0522
Orientation et consultation 0519
Philosophie de l'éducation 0998
Physique 0523
Programmes d'études et enseignement 0727
Psychologie 0525
Sciences 0714
Sciences sociales 0534
Sociologie de l'éducation 0340
Technologie 0710

LANGUE, LITTÉRATURE ET LINGUISTIQUE
Langues
- Généralités 0679
- Anciennes 0289
- Linguistique 0290
- Modernes 0291

Littérature
- Généralités 0401
- Anciennes 0294
- Comparée 0295
- Médiévale 0297
- Moderne 0298
- Africaine 0316
- Américaine 0591
- Anglaise 0593
- Asiatique 0305
- Canadienne (Anglaise) 0352
- Canadienne (Française) 0355
- Germanique 0311
- Latino-américaine 0312
- Moyen-orientale 0315
- Romane 0313
- Slave et est-européenne 0314

PHILOSOPHIE, RELIGION ET THÉOLOGIE
Philosophie 0422
Religion
- Généralités 0318
- Clergé 0319
- Études bibliques 0321
- Histoire des religions 0320
- Philosophie de la religion 0322

Théologie 0469

SCIENCES SOCIALES
Anthropologie
- Archéologie 0324
- Culturelle 0326
- Physique 0327

Droit 0398
Économie
- Généralités 0501
- Commerce-Affaires 0505
- Économie agricole 0503
- Économie du travail 0510
- Finances 0508
- Histoire 0509
- Théorie 0511

Études américaines 0323
Études canadiennes 0385
Études féministes 0453
Folklore 0358
Géographie 0366
Gérontologie 0351
Gestion des affaires
- Généralités 0310
- Administration 0454
- Banques 0770
- Comptabilité 0272
- Marketing 0338

Histoire
- Histoire générale 0578
- Ancienne 0579
- Médiévale 0581
- Moderne 0582
- Histoire des noirs 0328
- Africaine 0331
- Canadienne 0334
- États-Unis 0337
- Européenne 0335
- Moyen-orientale 0333
- Latino-américaine 0336
- Asie, Australie et Océanie 0332

Histoire des sciences 0585
Loisirs 0814
Planification urbaine et régionale 0999
Science politique
- Généralités 0615
- Administration publique 0617
- Droit et relations internationales 0616

Sociologie
- Généralités 0626
- Aide et bien-être social 0630
- Criminologie et établissements pénitentiaires 0627
- Démographie 0938
- Études de l' individu et de la famille 0628
- Études des relations interethniques et des relations raciales 0631
- Structure et développement social 0700
- Théorie et méthodes. 0344
- Travail et relations industrielles 0629

Transports 0709
Travail social 0452

SCIENCES ET INGÉNIERIE

SCIENCES BIOLOGIQUES
Agriculture
- Généralités 0473
- Agronomie. 0285
- Alimentation et technologie alimentaire 0359
- Culture 0479
- Élevage et alimentation 0475
- Exploitation des pâturages 0777
- Pathologie animale 0476
- Pathologie végétale 0480
- Physiologie végétale 0817
- Sylviculture et faune 0478
- Technologie du bois 0746

Biologie
- Généralités 0306
- Anatomie 0287
- Biologie (Statistiques) 0308
- Biologie moléculaire 0307
- Botanique 0309
- Cellule 0379
- Écologie 0329
- Entomologie 0353
- Génétique 0369
- Limnologie 0793
- Microbiologie 0410
- Neurologie 0317
- Océanographie 0416
- Physiologie 0433
- Radiation 0821
- Science vétérinaire 0778
- Zoologie 0472

Biophysique
- Généralités 0786
- Medicale 0760

SCIENCES DE LA TERRE
Biogéochimie 0425
Géochimie 0996
Géodésie 0370
Géographie physique 0368
Géologie 0372
Géophysique 0373
Hydrologie 0388
Minéralogie 0411
Océanographie physique 0415
Paléobotanique 0345
Paléoécologie 0426
Paléontologie 0418
Paléozoologie 0985
Palynologie 0427

SCIENCES DE LA SANTÉ ET DE L'ENVIRONNEMENT
Économie domestique 0386
Sciences de l'environnement 0768
Sciences de la santé
- Généralités 0566
- Administration des hôpitaux 0769
- Alimentation et nutrition 0570
- Audiologie 0300
- Chimiothérapie 0992
- Dentisterie 0567
- Développement humain 0758
- Enseignement 0350
- Immunologie 0982
- Loisirs 0575
- Médecine du travail et thérapie 0354
- Médecine et chirurgie 0564
- Obstétrique et gynécologie 0380
- Ophtalmologie 0381
- Orthophonie 0460
- Pathologie 0571
- Pharmacie 0572
- Pharmacologie 0419
- Physiothérapie 0382
- Radiologie 0574
- Santé mentale 0347
- Santé publique 0573
- Soins infirmiers 0569
- Toxicologie 0383

SCIENCES PHYSIQUES
Sciences Pures
Chimie
- Généralités 0485
- Biochimie 487
- Chimie agricole 0749
- Chimie analytique 0486
- Chimie minérale 0488
- Chimie nucléaire 0738
- Chimie organique 0490
- Chimie pharmaceutique 0491
- Physique 0494
- PolymÈres 0495
- Radiation 0754

Mathématiques 0405
Physique
- Généralités 0605
- Acoustique 0986
- Astronomie et astrophysique 0606
- Électronique et électricité 0607
- Fluides et plasma 0759
- Météorologie 0608
- Optique 0752
- Particules (Physique nucléaire) 0798
- Physique atomique 0748
- Physique de l'état solide 0611
- Physique moléculaire 0609
- Physique nucléaire 0610
- Radiation 0756

Statistiques 0463

Sciences Appliqués Et Technologie
Informatique 0984
Ingénierie
- Généralités 0537
- Agricole 0539
- Automobile 0540
- Biomédicale 0541
- Chaleur et thermodynamique 0348
- Conditionnement (Emballage) 0549
- Génie aérospatial 0538
- Génie chimique 0542
- Génie civil 0543
- Génie électronique et électrique 0544
- Génie industriel 0546
- Génie mécanique 0548
- Génie nucléaire 0552
- Ingénierie des systèmes 0790
- Mécanique navale 0547
- Métallurgie 0743
- Science des matériaux 0794
- Technique du pétrole 0765
- Technique minière 0551
- Techniques sanitaires et municipales 0554
- Technologie hydraulique 0545

Mécanique appliquée 0346
Géotechnologie 0428
Matières plastiques (Technologie) 0795
Recherche opérationnelle 0796
Textiles et tissus (Technologie) 0794

PSYCHOLOGIE
Généralités 0621
Personnalité 0625
Psychobiologie 0349
Psychologie clinique 0622
Psychologie du comportement 0384
Psychologie du développement 0620
Psychologie expérimentale 0623
Psychologie industrielle 0624
Psychologie physiologique 0989
Psychologie sociale 0451
Psychométrie 0632

THE UNIVERSITY OF MANITOBA

FACUTY OF GRADUATE STUDIES

COPYRIGHT PERMISSION

MULTILEVEL ALGEBRAIC RECONSTRUCTION TECHNIQUES FOR X-RAY COMPUTED TOMOGRAPHY

BY

HUAIQUN GUAN

A Thesis/Practicum submitted to the Faculty of Graduate Studies of the University of Manitoba in partial fulfillment of the requirements for the degree of

DOCTOR OF PHILOSOPHY

ABSTRACT

Image reconstruction is one of the key stages in computed tomography (CT). With limited dose, the reconstruction accuracy can only be improved by the development of more efficient detectors and the optimization of reconstruction algorithms to make more efficient use of the available dose. The work in this thesis addresses largely the latter issue considering the detectors' efficiency to have already reached their limit.

In CT, two image reconstruction techniques have been formulated: the Convolution Backprojection (CBP) method and the Algebraic Reconstruction Techniques (ART). In this thesis, we first analyze the factors affecting the performance of ART. We then present a novel projection access order, the multilevel scheme (MLS), for ART. MLS is exactly the sequence for 1D Fast Fourier Transform (FFT) if the number of projections is a power of 2. Experimental testing using real CT data demonstrates that the new technique outperforms CBP, by producing better spatial resolution when the number of projections is sufficient to satisfy the sampling criterion, or reduced noise when the number of projections is relatively small. A simulation study which matches real CT dosage and noise conditions, and a further comparison which employs reprojected CT scans of phantoms, demonstrate that MLS produces a larger modulation transfer function (MTF) when the number of projections is taken above half of that required by the sampling criterion, and a larger signal to noise ratio (SNR) when the number of projections is taken less than half. MLS also improves the performance of ART itself, in both the computational speed (by more than 10 times) and the physical image quality (both the high and low contrast detectabilities). This work provides a thorough physical comparison among CT reconstruction techniques and it confirms that MLS will find wide applications in reconstructions of different CT models.

ACKNOWLEDGMENTS

Firstly, I would like to deeply acknowledge my advisor Dr. Richard Gordon, along with my advisory committee Dr. Norm Davison, Dr. Roger Palser, Dr. Martin Reed and Dr. Byron Southern for their many invaluable guidances and advises on making this project to be compactly done. The critical comments and constructive suggestions from the External Examiner, Dr. Michael W. Vannier, have dramatically improved this thesis in both contents and presentation.

I would also like to thank B. Wowk in the Institute of Biodiagnostics (IBD) of NRC and Dr. S. Rathee in the Medical Physics of Manitoba Cancer Treatment and Research Foundation (MCTRF) who provided me their real CT data for reconstruction test, and Dr. W. Van der Putten who allowed me using his CT phantom. Thanks also extend to the CT staff of Radiology who helped me taking the CT scans and Dr. H. Shukla who helped to transfer the scans. I wish also to express my gratitude to Mr. S. Nagarajan from Picker International who did real scans of phantoms from a clinical CT and Mr. W. Dabrowski and Dr. A. Fenster in the U. Western Ontario who also showed their interest in providing me raw data scanned from a quantitative CT.

This work is supported by a University of Manitoba Graduate Study Fellowship. I regret that I terminate the relationship with Dr. W. Falk after my M.Sc. study and owe a deep gratitude to him. Special thanks also extend to Dr. R. C. Barber and Department of Physics for the financial support through TA works. Thanks again for Dr. M. Reed for his similar financial support.

Last, but not least, I would like to sincerely thank my wife, Congju, for her continuous encouragement, support and patience during my graduate study.

List of Abbreviations

ART	Algebraic Reconstruction Techniques
CBP (FBP)	Convoluted (Filtered) Backprojection
CD	Contrast Detail
CT	Computed Tomography
DQE	Detective Quantum Efficiency
FFT	Fast Fourier Transform
HU	Hounsfield Unit
IBD	Institute of Biodiagnostics
MLS	Multilevel Scheme
MCTRF	Manitoba Cancer Treatment and Research Foundation
MTF	Modulation Transfer Function
NEQ	Noise Equivalent Quanta
NPS	Noise Power Spectrum
OTF	Optical Transfer Function
QC	Quality Control
RPS	Random Permutation Scheme
SAS	Sequential Access Scheme
SD	Standard Deviation
SNR	Signal to Noise Ratio

Contents

Chapter 1
Introduction

The aim of computed tomography is to estimate a physical characteristic at each point within an object from external measurements. X-ray Computed tomography (CT) is an indispensable diagnostic imaging tool in medicine, and is widely used in radiotherapy treatment planning. It offers high spatial and contrast resolution. Quantitative CT allows measurements that are both accurate and precise [McClean, Holdsworth, Goodsitt, Robertson]. There are many laboratory CT scanners specifically designed to provide high resolution images for research purposes [Holdsworth, Hangartner, Drangova].

To obtain high quality tomograms, image reconstruction is essential. A reconstruction algorithm determines, along with the measured data, how accurately the linear attenuation coefficient can be calculated in medical x-ray CT. In clinical scanning, since the patient's dose must be limited and the efficiency of the detectors are constrained both by the techniques and costs (the quantum detection efficiency is very high in x-ray CT currently [Krestel, Morgan]), the most convenient way to improve the accuracy is to optimize the reconstruction algorithm. High performance algorithms are sought to achieve reconstructions yielding more diagnostic information [Waggener, Keselbrener, Cline, Crawford, Chase].

Several key factors characterize the performance of a CT reconstruction algorithm. The first and most important one is accuracy: how faithfully the precious diagnostic information can be reconstructed and presented in the tomogram. The image quality can be evaluated by different criteria, each characterizing a specific kind of information. (Subjective image quality is also critical since most images are interpreted visually. Freedom from artifacts is

crucial to avoid misleading human interpretations) Another important factor is the computational speed. Fast reconstruction is always expected to reduce the diagnostic time. Other factors include how flexible the algorithm is, how easy it is to be implemented, etc.

Improving the image quality when there is a limited amount of projection data is also important in x-ray CT. Research indicates that there are potential hazards that can result from the use of diagnostic x-rays, as discussed in detail in [Hall, Mazur]. Some human organs such as the female breasts are known to be particularly susceptible to radiation induced cancer [ICRP, NIH]. For the patient's sake, the amount of dose delivered during a single examination should be as low as possible. This contradicts the requirement for a high quality image which requires high dose. Developing dose-efficient reconstruction methods is the only direct way to improve the tomogram quality when scanning with limited dosage. Further, low dose CT is just one of many tomographic situations (see Chapter 8) where the data are either sparse or noisy. These include different CT models for basic science research and industrial applications. An efficient reconstruction algorithm benefits all kinds of tomographic imaging with limited data.

Major progress in developing CT reconstruction algorithms took place in late 60's and early 70's, in pace with the extensive research and development work for clinical x-ray CT scanners. In the past several years, a major thrust has been to improve algorithms for spiral/helical CT [Vannier, Wang] and cone beam CT [Wang 1993, Smith, Defrise]. Basically, two kinds of image reconstruction techniques were formulated. The first kind is the Convolution Backprojection (CBP) method and the second is the Algebraic Reconstruction Technique (ART). In CBP, the reconstruction doesn't depend on the projection access order in which the projection data is used (I will restrict this

thesis to parallel projections, so that the projection access order can be specified by the angles of the projections), since it is a backprojection back-summation method, and these operations are linear and commutative. However, in ART, that dependence is heavy for in ART each projection modifies the reconstruction by previous projections. Many people realized the importance of projection access order and tried various ways to optimize the order [Hounsfield, Shepp, Kuhl, Herman, van Dijke], but the optimal order remained unknown. If such an ordering were found, then a technique upgrading the current performance of ART and outperforming the CBP in some aspects may be developed.

The organization of this thesis is as follows. The principle of computed tomography (CT) and the concept of image reconstruction in CT are briefly reviewed in Chapter 2, along with the description of two major categories of reconstruction methods: CBP and ART, their advantages and limitations. In Chapter 2, we also discuss commonly used image quality criteria. In Chapter 3, we first analyze the factors affecting the performance of classical ART. Then we present a novel projection access order, called the multilevel scheme (MLS), which appears to yield the most efficient algebraic image reconstruction. Chapters 4-7 cover thorough experimental tests to demonstrate the advantages of the new algorithm over the conventional ones by using those image quality criteria outlined in Section 2.4. In Chapter 4, the comparison between CBP and MLS is made using the real data taken from two laboratory CT scanners. Chapter 5 extends the comparison study of Chapter 4 with a detailed computer simulation of CT as well as CT reconstructions. In Chapter 6, we further extend the comparison of MLS and CBP by using data reprojected from CT scans. Such scans were experimentally taken from CT phantoms by a clinical scanner. Chapter 7

covers a performance comparison between MLS and the classical ART algorithm. Chapter 8 discusses the applications of the new algorithm in medicine, both for diagnostic and therapeutic CT. In Chapter 8, we also outlined the recent progress in CT, CT applications in both medical and non-medical areas, CT models using different kinds of radiation, covering different energy ranges, imaging different types of interaction parameters, using different kinds of detectors, etc. We also discuss the role that the new algorithm may play in these new CT models. Concluding remarks and future work are included in the last chapter: how to employ more complicated image quality criteria for additional comparison studies, what are the further CT reconstruction research topics based on the MLS technique, how to implement MLS in divergent beam CT. (Nowadays most conventional CT scanners use high intensity fan beam x-ray sources to acquire data for fast scanning). The application of MLS ART in nuclear medicine tomographic reconstruction and its comparison to the conventional algorithms in the field is also an important research topic, and is outlined.

References

Chase R. C. and J. A. Stein, An improved algorithm for CT reconstructions, *Med. Phys.* 5 497-9, 1978.

Cline H. E., W. E. Lorensen, S. Ludke, C. R. Crawford and B. C. Teeter, Two algorithms for the three-dimensional reconstruction of tomograms, *Med. Phys.* 15, 320-327, 1988.

Crawford C. R., G. T. Gullberg and B. M. W. Tsui, Reconstruction for fan beam with an angular dependent displaced center of rotation, *Med. Phys.* 15, 67-71, 1988.

Defrise M. and R. Clack, A cone beam reconstruction algorithm using shift-variant filtering and cone beam backprojection, *IEEE Trans. Med. Imag. 13* , 186-195, 1994.

Drangova M. and A. Fenster, A laboratory CT scanner for dynamic imaging, *Med. Phys.* 21, 731-740, 1994.

Goodsitt M. M. and R. H. Johnson, Precision in quantitative CT - impact of x-ray dose and matrix size, *Med. Phys.* 19, 1025-1036, 1992.

Hall E. J., *Radiobiology for the radiologist*, Philadelphia, PE: Harper and Row Publishers Inc., 1978.

Hangartner T. N., A variable resolution rotate-only computed tomography scanner, *Med. Phys.* 21, 1557-1563, 1994.

Herman G. T. and L. B. Meyer, Algebraic reconstruction techniques can be made computationally efficient *IEEE Trans. Med. Imaging* 12, 600-609, 1993.

Holdsworth D. W., M. Drangova and A. Fenster, A high-resolution XRII-based quantitative volume CT scanner, *Med. Phys.* 20, 449-462, 1993.

Hounsfield G. N., *A method of and apparatus for examination of a body by radiation such as x or gamma radiation.* The Patent Office, London, Patent Specification 1283915, 1972.

ICRP publication No. 26, *Recommendations of the International commission on radiological protection (ICRP),* Pergamon Press, 1977.

Keselbrener L., Y. Shimoni and S. Akselrod, Nonlinear filters applied to computerized axial tomography: theory and phantom images, *Med. Phys.* 19, 1057-1064, 1992.

Krestel E., *Imaging systems for medical diagnostics*, Siemens Medical Division, 1991.

Kuhl D. E., R. Q. Edwards, A. R. Ricci and M. Reivich, Quantitative section scanning using orthogonal tangent correction *J. Nucl. Med.* 14, 196-200, 1973.

Mazur E. J., *Numerical simulations in low dose computed tomography*, Ph. D. thesis, University of Manitoba.

McClean B. A., T. R. Overton, T. N. Hangartner and S. Rathee, A special purpose x-ray fan-beam CT scanner for trabecular bone density measurement in the appendicular skeleton, *Phys. Med. Biol.* 35, 11-19, 1990.

Morgan C. L., *Basic principles of computed tomography*, University Park Press, Baltimore, 1983.

NIH publication no. 85-2748, Report of the National Institutes of Health ad hoc working group to develop radioepidemiological tables, 1985.

Robertson D. D. and H. K. Huang, Quantitative bone measurements using x-ray computed tomography with 2nd order correction, *Med. Phys.* 13, 474-479, 1986.

Shepp L. A. and B. F. Logan, The Fourier reconstruction of a head section, *IEEE Trans. Nucl. Sci.* 21, 21-43, 1974.

Smith B. D., Cone beam tomography: recent advances and a tutorial review, *Opt. Eng.* 29, 524-534, 1990.

van Dijke M. C. A., *Iterative methods in image reconstruction*, Ph.D. dissertation, Rijksuniversiteit Utrecht, Utrecht, The Netherlands, 1992.

Vannier M. W and G. Wang, Spiral CT refines temporal bone imaging, *Diagnostic Imaging* 15, 116-121, 1993.

Vannier M. W and G. Wang, M. W. Skinner and G. H. Esselman, Imaging the temporal bone by spiral CT, *MEDIZIN IM BILD* 1, 23-29, 1995.

Waggener R., M. Lee, D. Mickish, J. Lange and J. Feldmeier, Hybrid reconstruction algorithm for x-ray computed tomography, *Med. Phys.* 16, 197-201, 1989.

Wang G. and M. W. Vannier, Longitudinal resolution in volumetric x-ray computerized tomography - Analytical comparison between conventional and helical computerized tomography, *Med. Phys.* 21, 429-33, 1994.

Wang G., J. A. Brink and M. W. Vannier, Theoretical FWTM values in helical CT, *Med. Phys.* 21, 753-4, 1994.

Wang G. and M. W. Vannier, Spatial variation of section sensitivity profile in spiral computed tomography, *Med. Phys.* 21, 1491-7, 1994.

Wang G. and M. W. Vannier, Preliminary study on helical CT algorithms for patient motion estimation and compensation, *IEEE Trans. Med. Imag. 14*, 205-211, 1995.

Wang G., T. Lin, P. Cheng and D. M. Shinozaki, A general cone beam reconstruction algorithm, *IEEE Trans. Med. Imag.* 12 , 486-496, 1993.

Chapter 2
Physical Principles of Computed Tomography (CT), CT Reconstruction and CT Image Quality Evaluation

In this chapter, we first give a brief introduction to the physical principles of computed tomography (CT) as well as the concept of image reconstruction in CT. (A detailed discussion of these topics can be found in many books [Krestel, Hendee, Morgan, Herman 1980, Natterer, Kak 1987].) We then discuss two major categories of reconstruction methods, their principles, advantages and limitations. Descriptions of various physical criteria for the evaluation of medical images follow afterwards.

2.1 Physical principles of CT

The fundamental concept underlying the technique of CT is the capability of reconstructing a cross-section of the internal structure of an object from multiple projections of a collimated beam of radiation passing through the object. The mathematical basis dates back to the work of J. Radon in [1917], who proved that a 2D or 3D object could be reproduced from an infinite set of all projections. The physical application of the concept was first utilized by Bracewell [1956] to reconstruct a map of solar microwave emissions. Oldendorf [1961] and Cormack [1963] later each built a laboratory model using isotope γ-ray sources (also see [Kalos]). Kuhl and Edwards [1963] introduced transverse body section imaging by isotope scanning, subsequently further developing and refining the technique referred to now as emission computed tomography. The first CT for clinical application, the EMI head scanner, was developed by Hounsfield in [1972, 1973]. It was the

first time that the attenuation differences between various soft tissues, which are less than a few percent, were observed. The minimum attenuation difference detectable in CT is ~0.5% while the conventional x-ray radiograph cannot show an attenuation difference less than 10% due to the tissue overlap [Krestel].

To discuss the principle of CT, we first cite Cormack [1980] and Hounsfield's [1980] early concept of "tomogram". Cormack originated his idea of a tomogram from radiation therapy. It occurred to him that "in order to improve the radiation treatment planning, one had to know the distribution of the attenuation coefficient of tissues in the body, and that this distribution had to be found by measurements made external to the body." "If a fine beam of gamma rays of intensity I_0 is incident on the body and the emerging intensity is I, then the measurable quantity $g=\ln(I_0/I)=\int_L f ds$. Hence if f is a function in two dimensions, and g is known for all lines intersecting the body, the question is: can f be determined if g is known?". Hounsfield, on the other hand, "first investigated the possibility that a computer might be able to reconstruct a picture from sets of very accurate x-ray measurements taken through the body at a multitude of different angles. Many hundreds of thousands of measurements would have to be taken, and reconstructing a picture from them seemed to be a mammoth task, as it appeared at the time that it would require hundreds of thousands of simultaneous equations to be solved". When he "investigated the advantages over conventional x-ray techniques, however, it become apparent that the conventional methods were not making full use of all the information the x-rays could give. On the other hand, calculations showed that the new system uses the data very efficiently and would be two magnitudes more sensitive than conventional x-rays".

Although today different generations of CT scanners including the modern spiral/helical CT vary in design, the procedure of acquiring a CT image basically consists of 3 steps:

1. A thin slice of 1-10mm is examined from multiple angles. In each angle (see Fig. 2.1), finely collimated x-ray beams are measured across a slice before and after the transmission. Collimation is employed to greatly reduce the photons scattered into the detector system.

2. The transmitted photons are counted or accumulated by high signal-to-noise detectors which allow a minimum 0.5% difference of the x-ray attenuation to be detected and recorded. In accordance with Beer's law:

$$N = N_0 e^{-\int_l \mu(x,y)dl} \tag{2.1}$$

The attenuation integral $\int_l \mu(x,y)dl$ of a single measurement is

$$\int_l \mu(x,y)\ dl = \ln \frac{N_0}{N}$$

where N_0 and N is the number of incident and transmitted x-ray photons in the measurement, respectively.

3. The attenuation integrals of all measurements in all directions are read into a computer and reconstructed as a tomographic image using reconstruction algorithm. The tomogram represents a map of the linear attenuation coefficients $\mu(x,y)$ of the cross section.

Fig. 2.1 shows schematically a CT in its simplest design form to illustrate the formation of a tomogram [Krestel].

The $\mu(x,y)$ is a function of the x-ray photon energy E, the atomic number Z, and the electron density of the substance. It consists of two parts: the absorption by the Photoelectric Effect (P.E.) and the absorption and scattering by the Compton Effect, or

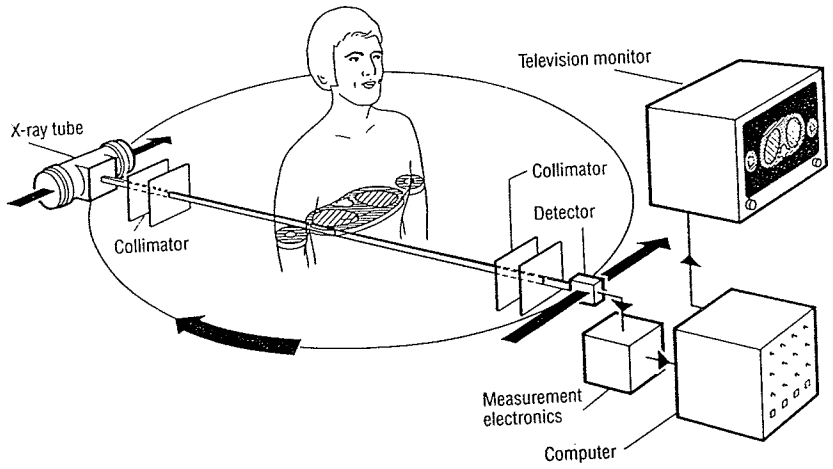

Fig. 2.1 Basic representation of a computer tomograph in the simplest design form (the early EMI scanner). The measurement system, consisting of x-ray tube and radiation detector, is first moved linearly in the slice plane over the entire object cross section. The measurement system is then rotated ~1° and then a new linear scanning movement performed, etc., until an angle of at least 180° has been traversed. Throughout the entire scanning process, the measurement signal is transferred to a computer. This computes a two-dimensional distribution of attenuation values corresponding to the object layer from the measurement values, which is displayed as a tomogram on a TV monitor after conversion to video signals. (Courtesy of the Siemens Aktiengesellschaft [Krestel]).

$$\mu(x,y)=\mu_p(x,y)+\mu_c(x,y)$$

The subscripts p and c referring to the photoelectric and Compton effects, respectively. $\mu_p(x,y)$ is strongly dependent on both the atomic number ($\sim Z^3$) and the beam energy ($\sim 1/E^3$), and $\mu_c(x,y)$ depends on electron density but not atomic number. The energy dependence of $\mu_c(x,y)$ is also much less [Krestel, Morgan, Hendee].

The difference in attenuation among different tissues for the P.E., depending upon their atomic numbers, results in a marked difference in absorption and leads to great contrast between the different tissues, a

desirable property in producing an image. The lack of any dependence of the Compton effect upon the atomic number provides little contrast enhancement between different tissues.

The effective energy of the x-ray source is 60 KeV (100-140KV tube voltage) [Herman 1980, Krestel] with a beam width of ~25 KeV. For a beam energy lower than 60 KeV, due to restrictions on the patient dosage, few photons have to be used. Although the attenuation differences are larger, the image noise also considerably increases. For higher energy beams, the attenuation differences are smaller and hence the image contrast is reduced. (The attenuation increment due to Compton scattering cannot balance the increment due to scattering.) Brooks and Di Chiro [1976] also calculated that beam energies around 60KeV yield the minimum noise standard deviation for a fixed amount of dosage since for higher energy photons, despite more photon transmission, quantum noise per photon appears larger. In practice, the x-ray beam is polychromatic. Since the softer x-rays are absorbed preferentially compared to higher energy photons, the remaining relative penetrating capability of the beam increases and it is said to become "harder". This is a non-linear effect which is largely attributed to the photoelectric effect. The problem of beam hardening and its correction have been discussed in detail in [Barrett] and also in [Krestel].

There are two kinds of x-ray detectors generally used: scintillation crystal and ionization chamber. The overall detection efficiencies for both are about the same (~50%). Both technologies have reached their detection limits [Krestel, Morgan].

2.2 Image reconstruction in CT

As discussed above, image reconstruction is one of the key stages in computed tomography. Cormack [1980] in his Nobel lecture addressed CT largely as a reconstruction problem. Herman [1980] also took image reconstruction as the fundamentals of CT.

In principle, the accuracy to determine the linear attenuation coefficients, both absolutely and relatively, is only limited by the patient's exposure, the detector's properties (efficiency, sizes, etc.), and the reconstruction technique. With limited dose, it can only be improved by the development of more efficient detectors and the optimization of the reconstruction algorithm to make more efficient use of the dose. The work in this thesis addresses largely the latter issue considering that the detectors' efficiency is technically difficult to improve and beyond the scope of this dissertation.

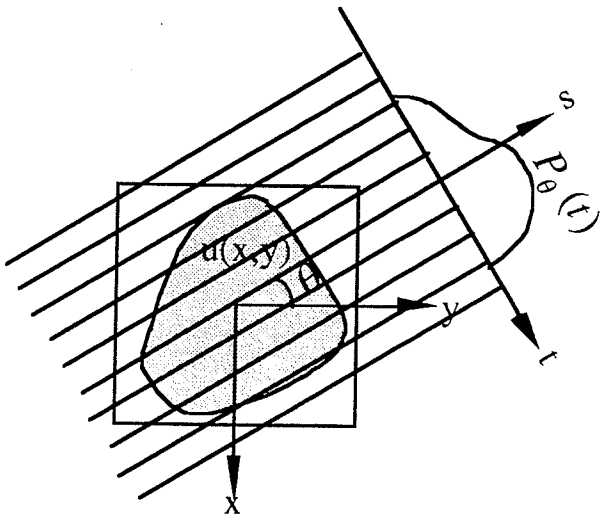

Fig. 2.2 Geometry of a projection $P_\theta(t)$ in computed tomography

In general, image reconstruction refers to the problem of estimating a function $f(x,y)$ from a finite number of integrals or projections. In x-ray CT, this function is the linear attenuation coefficient $\mu(x,y)$.

The measurement of one projection from parallel beams is shown in Fig. 2.2. A projection is denoted as $P_\theta(t)$, where θ is the measurement angle and t is the distance of the detector from the origin, with $t = x\cos\theta + y\sin\theta$ for any point (x,y). For $\mu(x,y)$,

$$P_\theta(t) = \int_{-\infty}^{\infty}\int_{-\infty}^{\infty} \mu(x,y)\delta(x\cos\theta + y\sin\theta - t)dxdy \qquad (2.2)$$

which represents the attenuation integral of $\mu(x,y)$ along the line $x\cos\theta + y\sin\theta = t$, and δ is the Dirac delta function.

Projections using fan beams are taken in the modern clinical CT scanners for fast data acquisition. A schematic diagram is shown in Fig. 2.3. Ray integrals are also measured in the same manner but the image reconstruction is more complicated than that for parallel beam. The fan beam reconstruction algorithm, however, can be derived from the parallel one by coordinates transformation [Krestel]. Further, the set of projection data originally measured by the fan-beam are usually rearranged to parallel projections before the actual reconstruction starts [Krestel]. Therefore in this thesis, our concern is only with reconstructions from parallel projection data, which will allow us to focus on the essential details. The principles of direct fan-beam reconstruction can be found in many other sources [Kak, Edelheit, Ledley, Crawford 1988].

2.3 Reconstruction methods

There are two major categories of image reconstruction methods used in CT. The first kind is a direct analytical method based on the Fourier transform and is called the Filtered or Convolution Backprojection (FBP or CBP) technique. It is first proposed by Ramachandran and Lakshminarayanan [1971]. The second kind takes the image reconstruction as

a problem of solving a system of simultaneous linear equations using iterative methods. These are called the Algebraic Reconstruction Techniques (ART). Historically, ART was first used in the early EMI scanner [Hounsfield] and in electron microscopy [Gordon 1970]. In the following two subsections, we give a brief introduction to each of the two techniques.

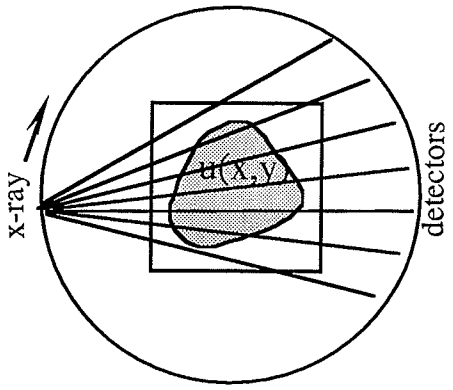

Fig. 2.3 Geometry of fan-beam data acquisition in computed tomography

2.3.1 Filtered or convolution backprojection (FBP or CBP)

FBP (CBP) is based on the central slice theorem that relates the 1D Fourier transform of a projection of $\mu(x,y)$ to its 2D Fourier transform. Let $F(u,v)$ be the Fourier transform of $\mu(x,y)$, i.e.,

$$F(u,v)=\int_{-\infty}^{\infty}\int_{-\infty}^{\infty}\mu(x,y)e^{-j2\pi(ux+vy)}dxdy \tag{2.3}$$

Also let $S_\theta(\omega)$be the Fourier transform of the projection $P_\theta(t)$, that is

$$S_\theta(\omega)=\int_{-\infty}^{\infty}P_\theta(t)e^{-j2\pi\omega t}dt \tag{2.4}$$

Then by considering $F(u,v)$ along the line $v=0$, Eq. (2.3) gives

$$\begin{aligned}F(u,0)&=\int_{-\infty}^{\infty}[\int_{-\infty}^{\infty}\mu(x,y)dy]e^{-j2\pi ux}dx\\&=\int_{-\infty}^{\infty}P_0(t)e^{-j2\pi\omega t}dt=S_0(\omega)\end{aligned} \tag{2.5}$$

where $P_0(t) = \int \mu(x,y)dy$ is the projection along $\theta = 0$. Note that for this special orientation, $x = t$. Eq.(2.5) indicates that the Fourier transform of a projection along $\theta = 0$ (1D) represents the line $v = 0$ in $F(u,v)$ plane (2D), as illustrated in Fig. 2.4. This result can be generalized to show that if $F(\omega,\theta)$ denotes the values of $F(u,v)$ along a line at an angle θ passing through the center, as shown in Fig. 2.3, and if $S_\theta(\omega)$ is the Fourier transform of the projection $P_\theta(t)$, then

$$S_\theta(\omega) = F(\omega,\theta) \tag{2.6}$$

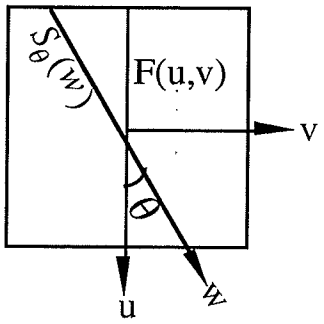

Fig. 2.4 An illustration of the Fourier central slice theorem

Eq. (2.6) is known as the *Fourier central slice theorem* [Ramachandran]. Note that this theorem is only applicable for parallel beams. There is no counterpart for fan-beam projections. The reason reconstruction is not directly performed in frequency domain by filling $S_\theta(\omega)$ to $F(\omega,\theta)$ is that in a digital case, the 1D function $S_\theta(\omega)$ has to be interpolated to fill the 2D $F(u,v)$ since $u = \omega\cos\theta$ and $v = \omega\sin\theta$ may not be integers. Such a interpolation in frequency domain may cause large errors in the spatial domain. Although there are some studies on minimizing such interpolation errors [Stark, Matej], the method still lacks wide application.

The Fourier Backprojection (FBP) method is inversely formulated as follows:

$$\begin{aligned}
\mu(x,y) &= \int_{-\infty}^{\infty}\int_{-\infty}^{\infty} F(u,v)e^{j2\pi(xu+yv)}dudv && \text{(i)} \\
&= \int_{0}^{\infty}\int_{0}^{2\pi} F(\omega,\theta)e^{j2\pi(x\omega\cos\theta+y\omega\sin\theta)}\omega d\omega d\theta && \text{(ii)} \\
&= \int_{0}^{\infty}\int_{0}^{2\pi} F(\omega,\theta)e^{j2\pi\omega t}\omega d\omega d\theta && \text{(iii)} \\
&= \int_{0}^{\pi}[\int_{-\infty}^{\infty}|\omega|S_\theta(\omega)e^{j2\pi\omega t}d\omega]d\theta && \text{(iv)}
\end{aligned} \qquad (2.7)$$

where (i) is just the 2-D inverse FT, (ii) we use $u=\omega\cos\theta$, $v=\omega\sin\theta$ where ω is the frequency axis u rotated by an angle θ, (iii) we use $x\cos\theta+y\sin\theta=t$ and (iv) we use the Fourier slice theorem $S_\theta(\omega)=F(\omega,\theta)$ plus some mathematical manipulation. Step (iv) indicates that the procedure for the reconstruction is:

1. take the Fourier transform of a projection $P_\theta(t)$ to obtain its FT $S_\theta(\omega)$,

2. multiply $S_\theta(\omega)$ by $|\omega|$, then do the inverse FT to obtain the filtered projection $P_\theta'(t)=\int_0^{\infty}|\omega|S_\theta(\omega)e^{j2\pi\omega t}d\omega$,

3. do backprojection to obtain the estimated function $\mu(x,y)$:

$$\mu(x,y)=\int_0^{\pi}P_\theta'(t)d\theta=\int_0^{\pi}P_\theta'(x\cos\theta+y\sin\theta)d\theta \qquad (2.8)$$

Theoretically, filter $|\omega|$ is for high frequency enhancement. In practice, noise is always introduced into the projection data and propagated into the reconstruction. If noise is not negligible, using $|\omega|$ tends to amplify it as well. To achieve a compromise, Shepp and Logan [1974] designed a modified filter $|\omega\cdot\mathrm{sinc}(\omega)|$ to reduce the high frequency amplification, while for the low frequencies it converges to $|\omega\cdot\sin c(\omega)|\approx|\omega|$.

The filtered projection $P_\theta'(t)$ can be equivalently calculated in the spatial domain by convoluting the projection data $P_\theta(t)$ with $h(t)$, the inverse Fourier transform of filter $|\omega|$ (or $|\omega\cdot\mathrm{sinc}(\omega)|$) by

$$P'_\theta(t) = \int_{-\infty}^{\infty} P_\theta(t) \cdot h(t-\alpha) d\alpha \tag{2.9}$$

where

$$h(t) = \int_{-W}^{W} |\omega| \exp(j2\pi\omega t) d\omega = \frac{W \sin(2\pi W t)}{\pi t} - \frac{\sin^2(\pi W t)}{(\pi t)^2} \tag{2.10}$$

In reality, the above operations have to be performed in digital form. Suppose the projection data is sampled at an interval of τ, then it implies that a bandwidth of $W = 1/(2\tau)$ has to be used in order that no aliasing error occur [Kak 1984] (CT sampling will be discussed in detail in sections 5.4 and 5.5). Replace $t = n\tau$ and $\tau = 1$, (2.10) becomes

$$h(n) = \begin{cases} 1/4 & n = 0 \\ 0 & n = even \\ -1/(n\pi)^2 & n = odd \end{cases} \tag{2.11}$$

For the modified filter $|\omega \cdot \mathrm{sinc}(\omega)|$, the corresponding representation is

$$h_s(n) = \begin{cases} 2/\pi^2 & n = 0 \\ -2/(\pi^2(4n^2-1)) & n \neq 0 \end{cases} \tag{2.12}$$

Some research on the design and application of different filters [Keselbrener, Chase] and their impact on the utility of CT has been reported.

2.3.2 Algebraic reconstruction technique (ART)

In contrast to CBP which is analytically formulated, ART directly does reconstructions in discrete form. Fig. 2.5 shows a region overlaid with a grid of pixels to be reconstructed from its equal-spaced parallel projections. We use μ_i - the discretized $\mu(x,y)$ above, to denote the attenuation value of each pixel (voxel), where $i = (1, 2, \cdots, N)$ and $N = n^2$ is the total number of pixels. Hence $\boldsymbol{\mu} = (\mu_1, \mu_2, \cdots, \mu_N)$ is a vector in an N-dimensional space. A ray is defined to be a projection line with the width equal to the detector

width (which generally equals the pixel size). All rays along one direction form a projection. The integral of the pixel values along one ray is denoted as p_j, the discretized $P_\theta(t)$. If there is a total of P projections and in each projection there are R rays, then $j=(1,2,\cdots,M)$ where $M=P\times R$. The relationship between μ and p can be expressed as

$$\sum_{i=1}^{N} w_{ji}\mu_i = p_j, \qquad j=(1,2,\cdots,M)$$

$$\begin{aligned} &or \\ &w_{11}\mu_1 + w_{12}\mu_2 + \cdots + w_{1N}\mu_N = p_1 \\ &w_{21}\mu_1 + w_{22}\mu_2 + \cdots + w_{2N}\mu_N = p_2 \\ &\vdots \qquad \vdots \qquad \vdots \qquad \vdots \\ &w_{M1}\mu_1 + w_{M2}\mu_2 + \cdots + w_{MN}\mu_N = p_M \end{aligned} \qquad (2.13)$$

where w_{ji} represents the contribution of the *ith* pixel to the *jth* ray integral. Assuming the total attenuation by a pixel is proportional to its volume and the scanning slice is constant in thickness, the attenuation is proportional to area. w_{ji} can therefore be taken as the fractional area of the *ith* pixel in the *jth* ray. Note in each equation in (2.13) only those pixels intercepted by the *jth* ray ($w_{ji}>0$) contribute to the integral p_j and most of the w_{ji} are zero. Thus the w_{ji} matrix is sparse. (In a simple vector form, (2.13) can also be written as $\mathbf{W}\mu=\mathbf{P}$, where $\mathbf{W}$ is the weight matrix, μ and $\mathbf{P}$ are the unknown and the projection vectors, respectively.)

A direct matrix inversion of (2.13) is practically impossible [Kak, Barrett]. The ART algorithm, first proposed for CT by Gordon *et al* [1970, 1974], provides an efficient iterative method to solve the problem. It is a variation of the early Kaczmarz's [1937] projection method for solving a system of linear equations. The process can be described by the sequence of functions

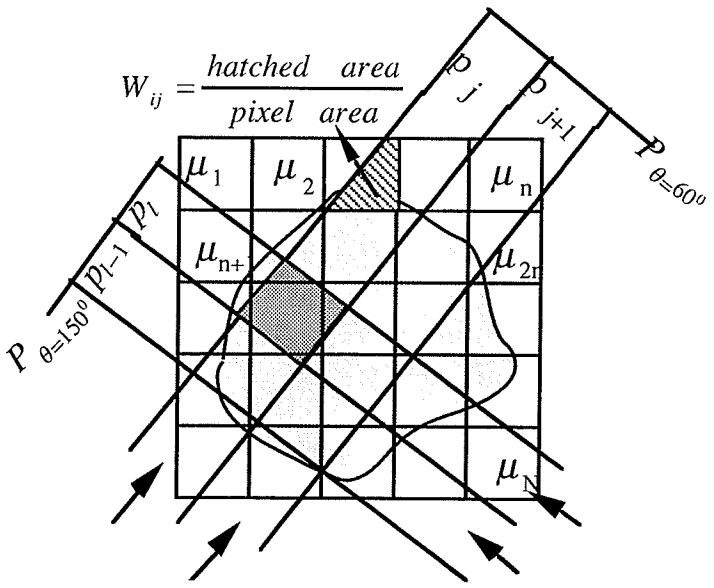

Fig. 2.5 A schematic diagram of a region overlaid with a grid of pixels ($N = n^2$) to be reconstructed from its equally-spaced parallel projections, where P_j and P_{j+1} are two adjacent rays in one projection and P_l is a ray in a perpendicular projection. The ray width equal to pixel size. P_j and P_l has an intersection (shadowed) whose area equal to that of a pixel.

$$\mu^{(j,m)} = \mu^{(j-1,m)} - \lambda \frac{\mu^{(j-1,m)} \cdot \mathbf{w}_j - p_j}{\mathbf{w}_j \cdot \mathbf{w}_j} \mathbf{w}_j \qquad (2.14)$$

where j is the subiteration index over rays 1 to M, $\mathbf{w}_j = (w_{j1}, w_{j2}, \cdots, w_{jN})$, m is the iteration index and $\lambda = 1$. In N-dimensional space, each equation in (2.13) represents a hyperplane and an image is a point represented by $\mu = (\mu_1, \mu_2, \cdots, \mu_N)$. When a unique solution to these equations exists, the intersection of all these hyperplanes is that single point. The first iteration starts with an initial guess $\mu^{(0,1)}$. It is projected on the hyperplane 1 represented by the first equation in (2.13). The resulting point $\mu^{(1,1)}$ is then projected on hyperplane 2 represented by the second equation to yield $\mu^{(2,1)}$, and so on. When $j = M$, the first iteration is finished (over all rays in all projections). In the second iteration, $\mu^{(M,1)}$ works as $\mu^{(0,2)}$ and the above

process repeats. This procedure will eventually converge to the intersection point. The convergence may also be slowed by using a value of $\lambda < 1$ (λ is called the relaxation factor [Herman 1980]) to improve the noise performance.

The procedure can be illustrated intuitively in a case in which just two variables are involved and constrained by

$$\begin{aligned} w_{11}\mu_1 + w_{12}\mu_2 &= p_1 \\ w_{21}\mu_1 + w_{22}\mu_2 &= p_2 \end{aligned} \qquad (2.15)$$

The process for locating the solution of (2.15) using (2.14), as shown in Fig. 2.6, is to start with an initial guess A ($\boldsymbol{\mu}^{(0,1)}$) and then have it projected onto the first line to get $R_1(\boldsymbol{\mu}^{(1,1)})$. Projection of R_1 on the second line generates $S_1(\boldsymbol{\mu}^{(2,1)})$ and projection of S_1 back onto the first line generates R_2. Repeat of the projections between the two lines back and forth will eventually arrive at the solution Q.

Tanabe [1971] once showed that if a unique solution of Eqs.(2.13) exists, Eq. (2.14) will converge to the solution. Herman [1973] also investigated the theoretical foundation of ART for image reconstruction and proved that it converges in the case of consistent projection data. In practice, whether the data is consistent or not totally depends on the amount of noise introduced. If noise is negligible such that the projections accurately represent the attenuation integral, the system can be thought of as essentially consistent. The success of ART with a pseudo random projection access order applied in the early EMI scanner [Housfield 1972] suggests that if the noise is less than 1% (the number of photons > 10^4 per measurement), the system can be thought consistent. The switch from ART to CBP later in the EMI scanner is largely due to the slow speed of ART.

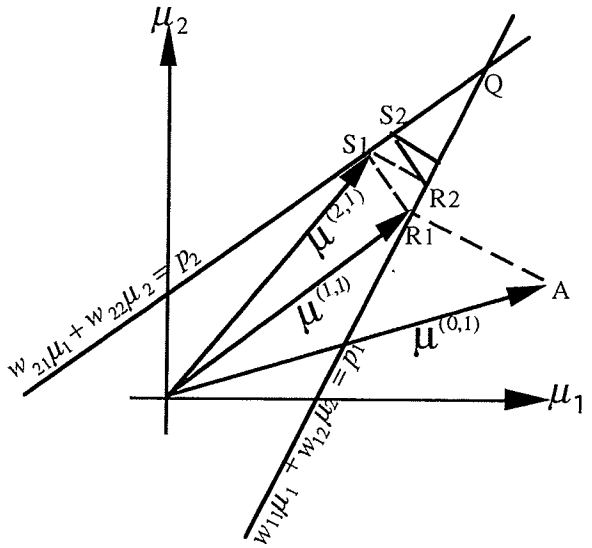

Fig. 2.6 The process for locating the solution of Eqs. (2.15) with two variables using ART (Eq. 2.14): start with an initial guess A and then have it projected onto the first line to get R_1. Projection of R_1 on the second line generates S_1 and projection of S_1 back onto the first line generates R_2. Repeat of such projections between the two lines back and forth will eventually arrive at the solution Q.

Eq. (2.14) is called the additive ART. There are also variations of it such as the multiplicative ART (MART), the simultaneous ART (SART) [Anderson 1984] and others [Gordon, Herman, Natterer] etc. Recent work with ART can also be found in [Kouris, Censor, Lewitt, Natterer, Anderson 1989]. There are also variant iterative techniques such as the simultaneous iterative reconstruction technique (SIRT [Gilbert], which differs from ART in that each pixel in the image is addressed one at a time. Rays from all projections passing through the pixel are calculated and summed. It is slow and requires large number of iterations for convergence), the iterative least squares technique (ILST) [Goitein] and the maximum likelihood methods (MLE) [Lange].

In the next chapter, we first analyze the factors affecting the performance of ART. Based on the analyses, we then introduce a novel MLS ART technique.

2.3.3 Comparisons of CBP and ART

A comparison of classical ART and CBP is outlined below. Later we will demonstrate that our new multilevel ART can significantly eliminate the major limitations of classical ART making ART superior to CBP in many circumstances.

ART and CBP are not equivalent. ART is more accurately constrained by the projection data. CBP, even in the cases where it performs better than ART, yields large errors and produces images having inconsistent ray integrals with the given projection data [Herman 1976, Cho].

ART is slow, generally needing 3-10 iterations [Herman 1976]. CBP is much faster and the reconstruction can even be performed during the data acquisition (using the pipeline method [Krestel]). But in those scanners such as the fourth generation systems with a stationary detector array, it is no longer possible for CBP to process the data during the data acquisition [Krestel], since all measurements have to be collected first and then rearranged to obtain proper projection data. In these systems, the fan beam projections are usually remapped to parallel ones. When noisy data needs to be smoothed using a low pass filter such as *sinc*, CBP needs no extra time due to its analytical formulation. However, smoothing is an extra computation for ART. In most applications, one iteration of ART costs about the same computation time as CBP required [Herman 1976, Morgan, Brooks 1976b].

The accuracy of ART is limited by the number of iterations one is willing to compute and its possible lack of convergence with noisy data. One has to adopt a criterion to end the iteration scheme, which may affect the accuracy as well. A principal limitation to the accuracy of CBP is the bandlimiting or spatial frequency cutoff [Morgan, Brooks 1976b]. Not only has the projection data to be filtered with a limited bandwidth (Eq. 2. 10), but practically the convolution involves only a few kernel points [Crawford 1991]. These factors reduce the spatial resolution in reconstructions. In contrast, in ART, the modifications are only made to the pixels along a ray path itself and therefore the spatial resolution is better. This is experimentally demonstrated later.

In the case where one can take a large number of projections, ART will produce a poorer reconstruction than CBP [Herman 1976]. On the other hand, in the case of a limited number of projections ($P \leq 1/3n$, n is the number of rays per projection), ART was found to be more accurate than CBP. ART also works much better in cases where the data is incomplete (limited range of projection angle, missed detector rays or projections, etc.) while CBP is generally much more adversely affected by such kinds of data. ART can easily incorporate prior information and constraints while CBP cannot do this at all. Nonlinear constraints like: 1) no attenuation value can be less than 0 or exceed a specific maximum; 2) pixels within rays whose ray sum is 0 are assigned attenuation value of 0; are commonly incorporated in ART to speed up the convergence and improve the accuracy. They are not available for CBP, except by post processing.

In Table 2.1, we summarize the comparisons discussed above. It is interesting to note that there is also an investigation studying the connection between ART and CBP. Under the formulation of least square matrices,

Older [1993] thought that the dichotomy between the two different approaches reduces to the choice of metric.

Table 2.1 The important reconstruction features of ART and CBP

	ART	CBP
Speed	Considerably slower (3-10 iterations)	Significantly faster (can proceed during scanning in some scanners)
Accuracy	Limited by finite iterations and possible lack of convergence with noisy data (more consistent with projection data)	Problem with band limiting and interpolation (less consistent with projection data)
Constraints	Allows additional constraints	not allowed
Limited data	performs relatively better	performs relatively less well

2.4 Physical evaluation of reconstruction techniques

Since image reconstruction is one of a series of cascaded processes in CT imaging, we can employ the commonly used physical image quality criteria for the evaluation of reconstruction techniques. In the past 10-15 years, there has been significant progress in the area of image evaluation. For example, unified noise theory by Wagner [1977] demonstrates that noise is the major factor affecting low contrast object detection [Evans]. To date, the modulation transfer function (MTF) is a standard way to characterize the spatial resolution. The signal to noise ratio (SNR) or simply, the noise standard deviation (SD), is a common measure for low contrast detectibility. The noise power spectrum (NPS), on the other hand, depicts noise energy distribution versus spatial frequency. The contrast detail (CD) evaluation provides an additional assessment for combined low and high contrast threshold detection.

There are some more complicated measures such as the detective quantum efficiency (DQE), the noise equivalent quanta (NEQ) etc., which describe the

noise in a frequency dependent form. These quantities, when coupled with the MTF of a cascaded imaging system, which may include human vision, provides additional image quality characterizations [Wagner, Munro, Cunningham]. Further, there are also sophisticated SNR measures representing different models of detection process [Loo]. Details of them will be discussed in chapter 9.

In the present work, we employ MTF, SNR, CD, NPS for comparing the performance of CT reconstruction techniques. Below we give a short introduction to each of them.

2.4.1 Image noise description

Image noise can be described by either the local statistics or the spatial correlation between different locations. Typically the local noise distribution is Gaussian and can be characterized by a single parameter - the standard deviation (SD) of the local image intensity. Although in CT noise is spatially correlated, Gaussian is still a good approximation at least for a local region such that the standard deviation is still commonly used to quantify the noise level, both in research [Brooks, Goodenough] and in CT quality assurance work [Bassano, Payne]. The spatial pattern of the noise is generally characterized by the autocorrelation function (*ACF*) and the noise power spectrum (*NPS*).

The autocorrelation function $ACF(x,y)$ of an image $I(x,y)$ is defined as [Barrett, Leszczynski]:

$$ACF(x,y)=\left\langle \frac{1}{A}\int\int_{A} n(x',y')\cdot n(x+x',y+y')dx'\,dy' \right\rangle \qquad (2.16)$$

where $n(x,y)$ is the local noise intensity at the location (x,y), i.e., $n(x,y)=I(x,y)-\bar{I}(x,y)$. $\bar{I}(x,y)$ is the expectation value of $I(x,y)$ for an

ensemble of images. The $\langle\ \rangle$ symbol represents the process of taking an ensemble average of the quantity inside and A represents the image area. The NPS is then defined as the Fourier transform of the ACF:

$$NPS(u,v) = \iint_A ACF(x,y)e^{-j2\pi(ux+vy)}dxdy \qquad (2.17)$$

Equivalently, the NPS can be defined as the squared magnitude of the Fourier transform of the noise image $n(x,y)$:

$$NPS(u,v) = \left\langle \frac{1}{A}\left| \iint_A n(x,y)e^{-j2\pi(ux+vy)}dxdy \right| \right\rangle \qquad (2.18)$$

In Chapter 5, we will adopt Eq. (2.18) to calculate the NPS.

2.4.2 The signal to noise ratio (SNR)

The low contrast detectibility measures the threshold contrast for detecting a tumor against its background. It is characterized by the SNR. Although there are many complicated definitions of SNR [Munro, Loo], a straightforward one defined as [Rajapakshe, Goodenough]

$$SNR = \frac{|CT\#1 - CT\#2|}{\sqrt{\sigma_1^2 + \sigma_2^2}} \qquad (2.19)$$

is used most commonly to evaluate CT (and other radiological imaging system) detectibility, where CT#1 and CT#2 are the average CT#'s inside the tumor and its background, respectively. σ_1 and σ_2 are the corresponding noise standard deviations inside the two regions.

2.4.3 The contrast detail (CD) evaluation

The contrast detail evaluation is a quantity combining both the high and low contrast resolution measures for the minimum detectable contrast of an

object versus its size. At high contrast the minimum detectable object size depends largely on the spatial resolution, whereas a low contrast object's detection is relatively independent of the spatial resolution but rather depends on image noise or patient dose [McDavid]. In general, the threshold contrast is plotted against the object size, termed the contrast detail diagram. It was first applied by Cohen [1979] for evaluating CT image quality. Faulkner [1986] later did further work on this topic.

Rose [1948, 1973], in his pioneering work, recognized that the threshold contrast of a human observer ultimately depends on the number of photons incident on the scene and the ability of the imaging system to utilize these photons. For an object having an area of A imaged by a photon flux of N, the object contrast is $C = \Delta N / N$ where ΔN is the amount of photon flux attenuated by the object. Rose suggested that for threshold detection with a given detection uncertainty, this contrast must be a few times larger than the noise level, which is represented by $1/\sqrt{NA}$, that is,

$$\frac{\Delta N / N}{(NA)^{-1/2}} = k \quad or \ for \ threshold \ detection, \ C_T = \frac{k}{(NA)^{1/2}} \qquad (2.20)$$

Eq. (2.20) is termed as the Rose model. This simple model predicts that the required threshold contrast is larger for smaller size of objects and smaller for larger size of objects, in agreement with our intuition. Schnizler [1973] has analyzed the data of Blackwell [1963] and found k to be approximately 2.5 ± 0.35 over a scene brightness range of six orders of magnitude for a detection probability of 50%. Comparisons of the Rose model to experimental data and the further modifications of it can be found in [Evans].

In section 4.3 we will employ the Rose model to estimate the number of photons per measurement in CT from the known CT contrast detectibility. In

section 5.8, we will design a contrast detail phantom for an experimental study of the detectibility in CT reconstructions.

2.4.4 The modulation transfer function (MTF)

The modulation transfer function (MTF) characterizes the spatial resolution of an imaging system. It is generally measured with a high dosage to reduce the noise effect (that is why the spatial resolution is also called high dose high contrast resolution). The MTF can be measured in two ways: 1. 1D Fourier transform of the line spread function (LSF) (or 2D Fourier transform of the point spread function (PSF)), 2. measurement of the standard deviation inside a set of bar patterns. The first is a direct method following the definition of MTF, whereas the second one is a derived technique by Droege *et al* [1982]. In real measurement, the first method requires extreme care in aligning the test object (thin wire) while the second method is more practical to perform. Details of experimental MTF measurement can be found in [Rao, Linstrom].

The Fourier transform of the PSF of an imaging system is referred to as the Optical Transfer Function (OTF) [Krestel, Leszczynski]:

$$OTF(u,v) = \int_{-\infty}^{\infty} PSF(x,y) e^{-j2\pi(ux+vy)} dxdy \qquad (2.21)$$

The MTF is the amplitude (modulus) of the OTF.

In the derived method [Droege], the MTF is calculated from images of cyclic bar patterns according to the formula:

$$MTF(f) = \frac{\pi}{4A_0}[A(f) + \frac{A(3f)}{3} - \frac{A(5f)}{5} + \frac{A(7f)}{7} \cdots] \qquad (2.22)$$

where A_0 is the amplitude of a square wave input, $A(f)$ is the amplitude of a sinusoidal component of frequency f and so on. Eq. (2.22) is based on the

theorem that a square wave of frequency f can be considered to be a sum of sinusoidal components of frequency f, $3f$ etc. If the MTF is 0 beyond a cutoff frequency f_c which is less than $3f$, then

$$MTF(f) = \frac{\pi A(f)}{4A_0} \qquad f \le f_c / 3 \qquad (2.23)$$

In the presence of CT noise, the signal amplitude A is difficult to determine. However, the standard deviation M is easily measured. One can then utilize the relationship between A and M (for a square wave input, $M_0^2 = A_0^2$, for the sinusoidal output, $M^2 = 1/2A^2$) to get

$$MTF(f) = \frac{\pi\sqrt{2}}{4A_0}\frac{M(f)}{M_0} \qquad (2.24)$$

This method also has the advantage of easy noise effect correction. In the presence of noise, $M(f)$ is corrected to be $\sqrt{M(f)^2 - N^2}$, where N is the standard deviation within a uniform region.

In chapters 5-7, we frequently use Eq. (2.24) (occasionally use Eq. 2.21) for the MTF calculation.

References

Andersen A. H., Algebraic reconstruction in CT from limited views, *IEEE Trans. Med. Imag.* 8, 50-55, 1989.

Andersen A. H. and Kak A. C., Simultaneous algebraic reconstruction technique (ART): a superior implementation of the ART algorithm, *Ultrason. Imag.* 6, 81-94, 1984.

Barrett H. H. and W. Swindell, *Radiological imaging, the theory of image formation, detection and processing* (Academic Press), Vol. 2, 1981.

Bassano D. A., Specification and quality assurance for CT scanners, in *Medical Physics of CT and Ultrasound (AAPM monograph No. 6)*, Eds. G. D. Fullerton and J. A. Zagzebski, 1980.

Blackwell H. R., Neural theories of simple visual discriminations, *Journal of the Optical Society of American* 53, 129-60, 1963.

Bracewell R. N., Strip integration in radio astronomy, *Australian Journal of Physics* 9, 198-217, 1956.

Brooks R. A. and G. Di Chiro, Statistical limitations in x-ray reconstructive tomography, *Med. Phys.* 3, 237-240, 1976.

Brooks R. A. and G. Di Chiro, Principles of computer assisted tomography, *Phys. Med. Biol.* 21, 689-732, 1976b.

Censor Y., On variable block algebraic reconstruction techniques, *Mathematical Methods in Tomography*, 1497, eds. G. T. Herman, A. K. Louis and F. Natterer (Springer-Verlag), 133-140, 1990.

Chase R. C. and J. A. Stein, An improved algorithm for CT reconstructions, *Med. Phys.* 5, 497-499, 1978.

Cho Z. H., J. K. Chan, E. L. Hall, R. P. Kruger and D. G. McCaughey, A comparative study of 3D image reconstruction algorithms with reference to number of projections and noise filtering, *IEEE Trans. Nucl. Sci.* NS-XXII, 344-358, 1975.

Cohen G. and F. A. DiBianca, The use of contrast-detail-dose evaluation of image quality in a computed tomographic scanner, *Journal of Computer Assisted Tomography* 3, 189-195, 1979.

Cormack A. M., Representation of a function by its line integrals with some radiological applications, *Journal of Applied Physics* 34, 2722-2727, 1963.

Cormack A. M., Early two-dimensional reconstruction and recent topics stemming from it (Nobel lecture), *Science*, 1482-1486, 1980.

Crawford C. R., G. T. Gullberg and B. M. W. Tsui, Reconstruction for fan beam with an angular dependent displaced center of rotation, *Med. Phys.* 15, 67-71, 1988.

Crawford C. R., CT filtration aliasing artifacts, *IEEE Trans. Med. Imag.* 10, 99-102, 1991.

Cunningham I. A. and B. K. Reid, Signal and noise in modulation transfer function determinations using the slit, wire and edge techniques, *Med. Phys.* 19, 1037-44, 1992.

Droege R. T. and R. L. Morin, A practical method to measure the MTF of CT scanners, *Med. Phys.* 9, 758-760, 1982.

Edelheit L. S., G. T. Herman and A. V. Lakshminarayanan, Reconstruction of objects from divergent x-rays, *Med. Phys.* 4, 226-31, 1977.

Evans A. L., *The evaluation of medical images*, Medical Physics Handbooks 10, Adam Hilger Ltd., Bristol, 1981.

Faulkner K. and B. M. Moores, Contrast detail assessment of computed tomography scanners, *Phys. Med. Bio.* 31, 993-1003, 1986.

Gilbert P., Iterative methods for the reconstruction of three dimensional objects from their projections, *J. Theor. Biol.* 36, 105-117, 1972.

Goitein M., Three-dimensional density reconstruction from a series of two-dimensional projections, *Nucl. Instrum. Methods* 101, 509-518, 1972.

Goodenough D. J. and K. E. Weaver, Introduction to computed tomography, in *Computed tomography in radiation therapy* , Eds. C. C. Ling, C. C. Rogers and R. J. Morton, 121-127, Raven Press, 1983.

Gordon R., A tutorial on ART (Algebraic Reconstruction Techniques), *IEEE Nucl. Sci. NS* 21, 78-93, 1974.

Gordon R., R. Bender and G. T. Herman, Algebraic reconstruction techniques (ART) for three-dimensional electron microscopy and x-ray photography, *J. Theor. Biol.* 29, 471-481, 1970.

Hendee W. R., *The physical principles of computed tomography*, 1st ed., Little Brown, Boston, 1983.

Herman G. T., *Image reconstructions from projections: the fundamentals of computerized tomography*, Academic Press, New York, 1980.

Herman G. T. and A. Lent, Iterative Reconstruction Algorithms, *Computers in Medicine and Biology* 6, 273-294, 1976.

Herman G. T., A. Lent and S. W. Rowland, ART: Mathematics and applications. A report on the mathematical foundations and on the applicability to real data of the Algebraic Reconstruction Techniques. *J. Theor. Biol.* 42, 1-32, 1973.

Hounsfield G. N., A method of and apparatus for examination of a body by radiation such as x or gamma radiation. The Patent Office, London, Patent Specification 1283915, 1972.

Hounsfield G. N., Computerized transverse axial scanning (tomography): Part I. Description of the system, *British Journal of Radiology* 46, 1016-1022, 1973.

Hounsfield G. N., Computed Medical Imaging (Nobel lecture), *Science*, 22-28, 1980.

Kaczmarz S., Angenaeherte Aufloesung von Systemen linearer Gleichungen, Bulletin International des Sciences et des Lettres, Classe des Sciences Mathematiques et naturelles, Serie A: Sciences Mathematiques, 355-357, 1937.

Kak A. C., Image reconstruction from projections, in *Digital imaging processing techniques* 111-170 Ed. M. P. Ekstrom, Academic Press Inc., 1984.

Kak A. C. and M. Slaney, *Principles of Computerized Tomographic Imaging*, IEEE Press, New York, 1987.

Kalos M. H., S. A. Davis, P. S. Mittelman and P. Mastras, *Conceptual Design of a vapor fraction instrument.* White Plains, NY: Nuclear Development Corp. of America. pp. 31, 1961.

Keselbrener L., Y. Shimoni and S. Akselrod, Nonlinear filters applied to computerized axial tomography: theory and phantom images, *Med. Phys.* 19, 1057-1064, 1992.

Kouris K., H. Tuy, A. Lent, G. T. Herman and R. M. Lewitt, Reconstruction from sparsely sampled data by ART with interpolated rays, *IEEE Trans. Med. Imag.* 1, 161-167, 1982.

Krestel E., *Imaging systems for medical diagnostics*, Siemens Medical Division, 1991.

Kuhl D. E. and R. Q. Edwards, Image separation radioisotope scanning, *Radiology* 80, 653-661, 1963.

Lange K., M. Bahn and R. Little, A theoretical study of some maximum likelihood algorithm for emission and transmission tomography, *IEEE Trans. Med. Imaging* 6, 107-114, 1987.

Ledley R. S., Introduction to computerized tomography, *Computers in Medicine and Biology* 6, 239-246, 1976.

Lewitt R. M., Alternatives to voxels for image representation in iterative reconstruction algorithms, *Phys. Med. Biol.* 37, 705-715, 1992.

Leszczynski K. W., *Digital imaging techniques for radiotherapy treatment verification*, Ph.D. thesis, University of Manitoba, 1991.

Lindstrom W. W. and H. K. Tuy, Directional-dependent calculation of CT image MTF and noise power spectrum, *Med. Phys.* 13, 594-594, 1986.

Loo L. D., K. Doi and C. E. Metz, A comparison of physical image quality indices and observer performance in the radiographic detection of nylon beads, *Phys. Med. Biol.* 29, 837-856, 1984.

Matej S. and I. Bajla, A high speed reconstruction from projections using direct Fourier method with optimized parameters - An experimental analysis, *IEEE Trans. Med. Imaging* 9, 412-427, 1991.

McDavid W. D., R. G. Waggener and M. J. Dennis, Physics principles of computed tomography, in *CRC Handbook of Medical Physics,* Vol. II, Eds. R. G. Waggener, 37-80, 1983.

Morgan C. S., *Basic principles of computed tomography*, University Park Press, Baltimore, 1983.

Munro P. F., J. A. Rawlinson and A. Fenster, Therapy imaging: A signal-to-noise analysis of metal plate/film detectors, *Med. Phys.* 14, 975-984, 1987.

Natterer F., *The mathematics of computed tomography,* Addison-Wiley, 1986.

Older J. K and P. C. Johns, Matrix formulation of computed tomogram reconstruction, *Phys. Med. Biol.* 38, 1051-64, 1993.

Oldendorf W. H., Isolated flying spot detection of radiodensity discontinuities-Displaying the internal structure pattern of a complex object. *IEEE Tran. Bio-Medical Electronics BMW* 8, 68-72, 1961.

Payne J. T. and E. C. McCullough, Quality assurance and radiation exposure levels in computed tomography, in *CRC Handbook of Medical Physics,* Eds. R. G. Waggener, Vol. II, 311-333, 1983.

Radon J., On the determination of functions from their integrals along certain manifolds, *Mathematisch-Physiche Klasse* 69, 262-277, 1917.

Rajapakshe R., *Optimization of a real-time portal imaging system for quantitative imaging,* Ph.D. thesis, University of Manitoba, 1995.

Ramachandran G. N. and A. V. Lakshminarayanan, Three-dimensional reconstruction from radiographs and electron micrographs: application of convolutions instead of Fourier transforms, *Proc. Natl. Acad. Sci. U. S.* (68) 2236-40, 1971.

Rao G. U., Measurement of modulation transfer functions, in *CRC Handbook of Medical Physics,* Eds. R. G. Waggener, Vol. II, 159-179, 1983.

Rose A., The sensitivity performance of the human eye on an absolute scale, *Journal of the Optical Society of American* 38, 196-208, 1948.

Rose A., *Vision: Human and Electronics,* New York NY, Plenum Press, 1973.

Schnitzler A. D., Image detector model and parameters of the human visual system, *Journal of the Optical Society of American* 63, 1357-68, 1973.

Shepp L. A. and B. F. Logan, The Fourier reconstruction of a head section, *IEEE Trans. Nucl. Sci.* 21, 21-43, 1974.

Stark H. and I. Paul, An investigation of computerized tomography by direct Fourier inversion and optimum interpolation, *IEEE Trans. Biomed. Eng. BME* 28, 496-505, 1981.

Tanabe K., Projection method for solving a singular system, *Numer. Math.* 17, 1971, 203-214.

Wagner R. F., Toward a unified view of radiological imaging system. Part II: Noisy images, *Med. Phys.* 4, 275-295, 1977.

Chapter 3
A Multilevel Projection Access Scheme for Multiresolution Image Reconstruction using ART

3.1 Introduction

Algebraic reconstruction techniques (ART) and its variants are important image reconstruction techniques for computed tomography. It is often used in CT for 2D and 3D reconstructions when the projections are sparse, noisy or non-uniformly distributed. The principal disadvantages of ART are its excessive computing time and its possible lack of convergence under noisy situations.

The key point to improve the computational efficiency of ART is to speed up the convergence rate of the high frequency components of the image. Considering that in an iterative process, the low frequency components are recovered first and the high frequency components are recovered late and slowly (we will show this later experimentally for ART), Ranganath *et al.* [1988] introduced an iterative expectation maximization (EM) algorithm in a multigrid multiresolution fashion for positron emission tomography (PET) reconstruction. Their approach allows the low frequency components to be efficiently approximated and recovered on coarse grids while the high frequency components are recovered on the fine grids, resulting in a speed-up factor of 10 for EM.

A multigrid ART which gradually recovers frequencies from low to high might still lack efficiency. A scheme which can recover high frequencies from its initiation is desirable. Since high correlation between projections makes ART very slow in recovering high frequency information (in fact, the more the projections, the higher the correlation and hence the slower the convergence of ART), we adjusted the projection orders such that

projections at angles far apart are updated consecutively. Two projections that are 90° apart are minimally correlated (but not to zero due to the finite digitization). Note that the reconstruction object itself may also influence the convergence speed as we discuss later, but we leave that for future work.

In principle, the efficiency of ART can be maximized if the total number of M constrained equations each with N variables are orthogonalized, where M is the total number of measurements (rays) in all the projections and N is the total number of pixels in the image. However, in practice, the full orthogonalization is computationally not feasible. Ramakrishnam *et al.* [1979] suggested a pairwise orthogonalization scheme with less computational complexity.

Early experimental work on algebraic reconstruction using orthogonal pairs of projections was due to Kuhl *et al* [1973]. They presented an orthogonal tangent correction technique to do nuclear medicine section reconstruction. A recent study was reported by Herman and Meyer [1993] where a permutation operation for divergent beams was introduced which performs the same ordering for projections and the rays in each projection. They applied the technique to PET reconstruction and concluded that ART can be made to match the performance of EM but is more than 10 times computationally more efficient. Unfortunately, their permutation cannot apply when either the number of projections or the number of rays in each projection is a prime number. Van Dijke [1992] attempted to permute among the projections and concluded that random permutation sequence was best.

In this chapter, we report our investigation for a projection access order that maximizes the orthogonality among projections at each iterative step for parallel beams (published in [Guan and Gordon 1994]). We first analyze the factors affecting the performance of ART. In section 3.3 we discuss the access scheme itself. In section 3.4 we experiment with reconstructions using

this scheme and compare our results with conventional ordering. Further discussion and conclusion are included in the last section.

3.2 The performance of ART

We begin analyses of the performance of ART using a simple two-variable system (see Eq. 2.15) as shown in Fig 3.1, in which each plot is similar to Fig. 2.6 but simplified. As Figs. 3.1a and 3.1b demonstrate, the larger the acute angle between the two lines, the less the number of iterations needed for convergence. Only two steps are needed to reach the solution when the two lines are perpendicular to each other (Fig. 3.1c). In this case, the orthogonal condition $\cos\alpha=0$ $(\mathbf{w}_1 \cdot \mathbf{w}_2 = 0)$ is satisfied, where $\mathbf{w}_1 = (w_{11}, w_{12})$ and $\mathbf{w}_2 = (w_{21}, w_{22})$ are vectors in 2-D space. Similarly, for a large system defined by Eq. (2.13) in the N-dimensional space, the hyper-angle formed by two hyperplanes j and k is

$$\cos\alpha_{j,k} = \frac{\mathbf{w}_j \cdot \mathbf{w}_k}{|\mathbf{w}_j||\mathbf{w}_k|} \qquad (3.1)$$

where $|\mathbf{w}_j| = \sqrt{\sum_{i=1}^{N} w_{ji}^2}$ is the "length" of ray p_j. If all the M-hyperplanes defined by Eqs. (2.13) are mutually orthogonal, i.e., $\cos\alpha_{j,k}=0$ for any $j \neq k$, then M iteration steps guarantee the convergence.

Among the equations in (2.13), if w_{ji}'s are simply replaced by 1's or 0's in the 1st order approximation, those corresponding to rays within the same projection are orthogonal to each other. If the fractional area is used for w_{ji}, then consecutive equations for adjacent rays are correlated. (Occasionally a correlation may exist between rays p_{j-1} and p_{j+1} as shown in Fig. 3.2(a), but it is negligible.) The worst case is shown in Fig. 3.2(b), where half of a pixel is in ray j and the other half is in ray $j+1$. Correlation is due to pixels whose centers lie on the interface of the two rays. Since the hyperangle formed by ray j and ray $j+1$ is about

$\cos\alpha_{j,j+1} \approx 1/4$ ($\alpha_{j,j+1} \approx 80^0$), the two are still orthogonal, to a good approximation. This suggests that reordering the rays in each projection would have little effect on the convergence performance. This conclusion is also applicable to the divergent beam case and hence permutation of rays as done in Herman and Meyer [1993] may not be necessary.

For any two rays not in the same projection, as shown in Fig. 2.5 of chapter 2, those pixels that fall partly under the intersections of the ray paths will have their values contributed to by each equation (by different weights) and make them correlated. Any two rays each from one of the two projections will have the same intersection area. But the smaller the difference of the projection angles θ, the large the rhomboidal intersection area $1/\sin\theta$ and hence the more the correlation (the curve of $1/\sin\theta$ versus θ is plotted in Fig. 3.3) The correlation is highest when both the rays have short "lengths" $|\mathbf{w}_j|$ and $|\mathbf{w}_k|$ (i.e., the rays cross the corner of the image). In this situation, the hyperangle calculated from Eq. (3.1) could be quite small. Thus if iterations are performed projection by projection, sequentially, the update step will be very small, as in the 2-D case shown in Fig. 3.1a. On the other hand, for two projections that are 90^0 apart, the correlation will be a minimum since any two rays each from one projection have the smallest intersection area 1. Another important feature is that, when the "length" of one ray is short, the other is correspondingly long considering that their intersection area should fall inside the reconstruction region (see Fig. 2.3). This ensures a reasonably large hyperangle α such that the convergence can be taken in a large step. We intuitively illustrate the point in Fig. 3.4 by showing 4 symbolic "hyperplanes" - lines, with the angle formed in between any two being the hyperangles (i.e., α_{12} is the hyperangle between hyperplanes 1 and 2, etc.). A is the initial guess and Q is the solution. Clearly, in 1-iteration, the sequential access A to E (solid line, access order 1234) is much slower in convergence than that by route A to F

(dash line, access order 1342) toward Q, i.e., EQ is much longer in distance than FQ. The MLS scheme we describe below is based on these analyses.

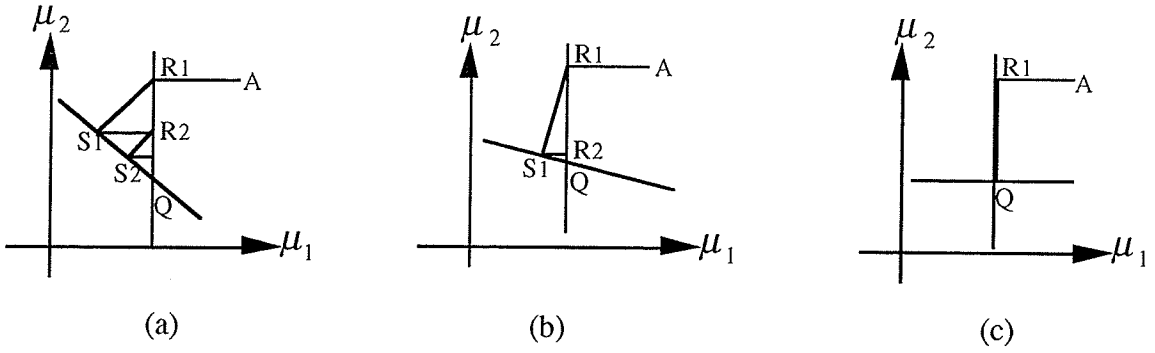

Fig. 3.1 In a two-variable system (see Eq. (2.15)) for the three different angles between the two lines shown in (a), (b) and (c), the number of steps by ART taken to approach the intersection point Q to a given accuracy decreases. Each of (a), (b) and (c) is similar to Fig. 2.6 but simplified.

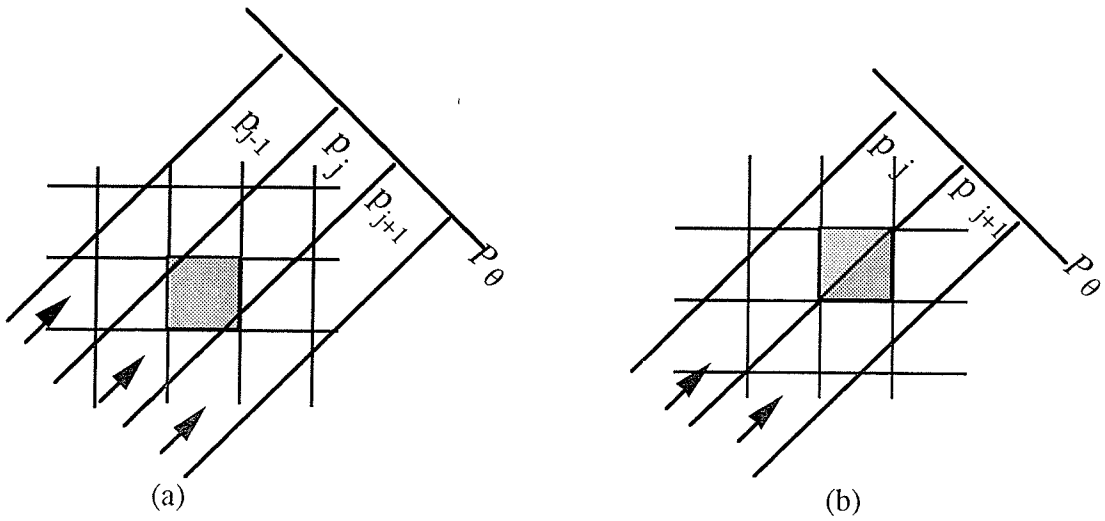

Fig. 3.2 (a) Example of the negligible correlation existing between rays P_{j-1} and P_{j+1}. (b) Worst situation of correlation between adjacent rays in one projection. Correlation is due to pixels whose centers lie on the interface of the two rays.

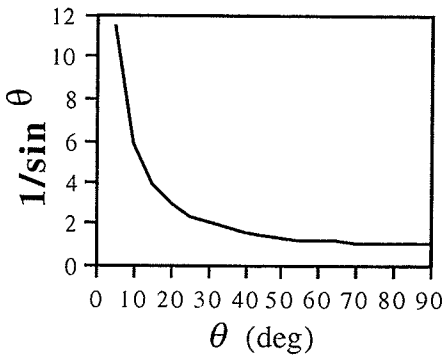

Fig. 3.3 The curve of $1/\sin\theta$ versus θ, giving the overlap between two rays of width 1 intersecting at angle θ.

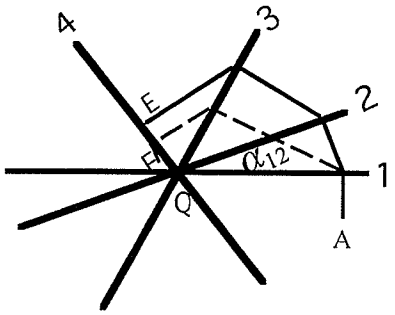

Fig. 3.4 Reordering four symbolic "hyperplanes" - thick lines (α_{12} is the hyperangle between hyperplanes 1 and 2, etc.). A is the initial guess and Q is the solution. In 1-iteration, the sequential access A to E (solid line, access order 1234) is much slower in convergence than that by route A to F (dash line, access order 1342) toward Q, i.e., EQ is much longer in distance than FQ.

3.3 A multilevel projection access ordering

Before proceeding to discuss how to order the projections, we show that for two rays intersecting at an angle θ_o (Fig. 3.5a), a 3rd ray could orient at the direction either halving θ_o or halving its complementary angle $180^0 - \theta_o$ such that its total intersection area to the two rays would be a minimum (Fig. 3.5b). This is straightforward since for the ray in the θ_o region (Fig. 3.5a), the total intersection area is

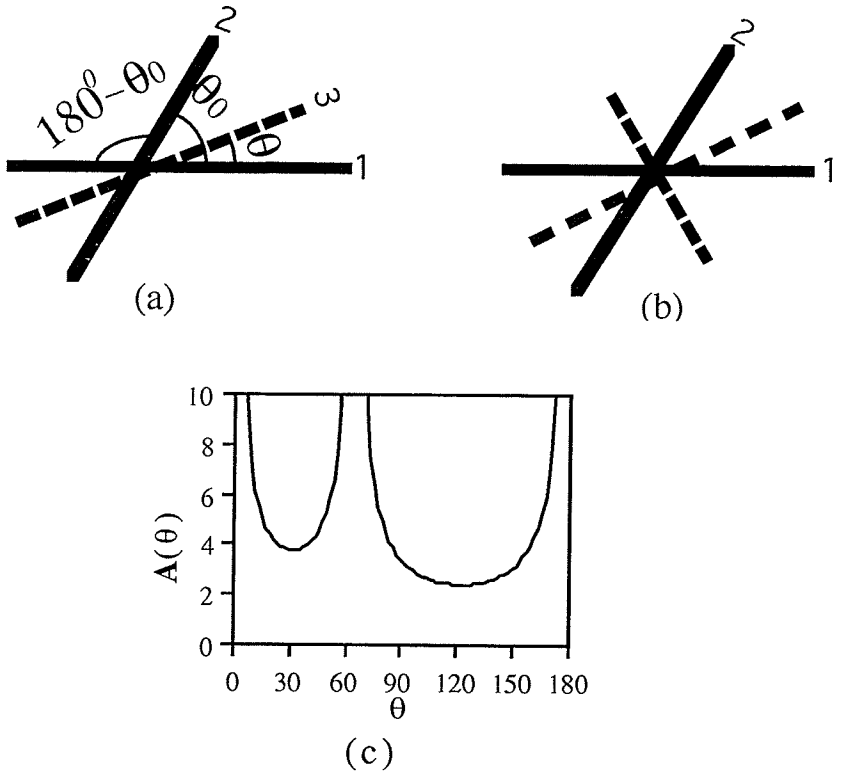

Fig. 3.5 (a) Two rays 1 and 2 intersecting at a fixed angle θ_o, with ray 3 at an angle θ varied to ray 1. (b) Ray 3, set either halving θ_o or halving the complementary angle $180^0 - \theta_o$, will make its total intersection area with ray 1 and ray 2, $A(\theta)$, a minimum. (c) The plot of $A(\theta)$ against θ over the whole 180^0 region for $\theta_o = 65^0$. $A(\theta)$ goes to infinity when ray 3 coincides with either ray 1 or ray 2.

$$A(\theta) = \frac{1}{\sin\theta} + \frac{1}{\sin(\theta_o - \theta)} \qquad (3.2)$$

By taking the first order derivative of $A(\theta)$ and setting it to 0, we obtain $\theta = \theta_o / 2$. A similar derivation can be made for the ray in the complementary region and $\theta = (180^0 - \theta_o)/2$. Fig. 3.5c shows how $A(\theta)$ changes with θ over the whole 180^0 region for $\theta_o = 65^0$. $A(\theta)$ goes to infinity when the 3rd ray coincides with either of the first two rays. The two minima values are

$$A(\theta_o / 2) = \frac{2}{\sin\theta_o / 2} \quad \textit{and} \quad A(\tfrac{180^0 - \theta_o}{2}) = \frac{2}{\cos\theta_o / 2}$$

If $\theta_o \le 90^o$, then $A(\theta_o / 2) \ge A(\frac{180^0 - \theta_o}{2})$ or vice versa. Hence we should set the 3rd ray to the angle halving θ_o or $180^0 - \theta_o$, whichever $\ge 90^0$. In this way, the overall correlation among the three rays, or the three projections each ray belongs to (see analyses in the last section), is at a minimum. When $\theta_o = 90^o$, the two minima are equal and the 3rd ray could be set along either of the two directions.

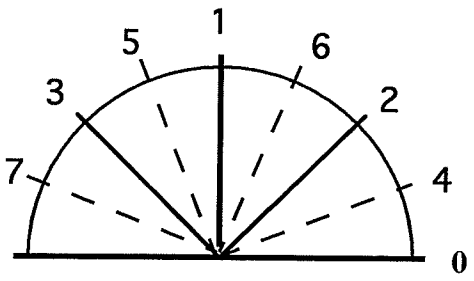

Fig. 3.6 The access orders for 8 projections in the multilevel scheme.

The above derivation, together with that two projections of 90^0 apart are minimally correlated, will in fact decide what is the ideal number of equally spaced projections to take, and hence leads us to a multilevel scheme (MLS). Clearly, the number of projections P should ideally be a power of 2, say $P = 2^L$. Suppose they are indexed as 0,1,.. P-1 sequentially. Then projection 0 (0^0) and projection $P/2$ (90^0) with a maximum orthogonality are accessed first. The 3rd one could be either projection $P/4$ (45^0) or projection $3P/4$ (135^0) both halving the first two. We decide that if two projections have the same access privilege, then the one with a smaller projection angle is preferred: in this case, projection $P/4$ (45^0) and then projection $3P/4$ (135^0). Following the rules, the next one is projection $P/8$ (22.5^0) and then $5P/8$ (112.5^0), $3P/8$ (67.5^o) and $7P/8$ (135^o) projections etc. Each time we select a projection to keep the overall correlation minimal (minimal to the last one, and also to the others already accessed). One sees that in such a scheme, projections can be nominally arranged in a total of L levels for

accessing. In level l=1: 0 and $P/2$, level l=2: $P/4$ and $3P/4$ and level l=3: $P/8$, $5P/8$, $3P/8$ and $7P/8$ and so on. Views in one level halve the projections in all previous levels and hence double the total number. Fig. 3.6 shows the situation for P=8 by labeling the projection index on the corresponding projection angles. Table 3.1 summarizes the result for a few levels. It is interesting to note that the 2^L projections are arranged in the same order as that in doing a 1D FFT with 2^L data.

This scheme will allow speedy convergence since the update is initially very large and then gradually reduces to approach the solution. The implementation of the ordering is also easy if P is a power of 2. One method is to do the bit reversal to the sequential projection number as that in doing 1D FFT. The other is that starting at level l=2 (see Table 3.1), the number of projections in each level is equal to sum of all preceding levels (from 1 to l-1). By adding a value of $P/2^l$ to each of the projection index number in all preceding levels will yield the access orders for level l.

In practical situations, for a given number of projections that is not a power of 2, the MLS scheme can still apply. In level l=1, any two projections that are 90^0(or close) apart are updated and in l=2, the two that halve (or nearly) the angles between the first two are updated, and so on. Projection access can still follow the sequence listed in Table 3.1, with a total of $L=[\log_2^P]+1$ levels ([ ] = truncate to integer). The implementation of the ordering is exactly the same as the second method used for P a power of 2 case but just with the values rounded to integers. Note that in level L only the first $P-2^{L-1}$ projections are taken. From level l=1 to $l=L-1$, no reuse occurs since the minimum difference is $P/2^{L-1}>1$. A flag is set for each of the values used. In level L, additional work needs to be done since occasionally the calculated value may have been already accessed. If so, we search both sides of the value until the closest unused value is found and then put it into the sequence and set a flag. In general it is just the neighbor or

next neighbor. Our tests suggest that only for the last one or two values, a large difference may occur.

Shown in Fig. 3.7 is the flow chart for image reconstruction using MLS ART .

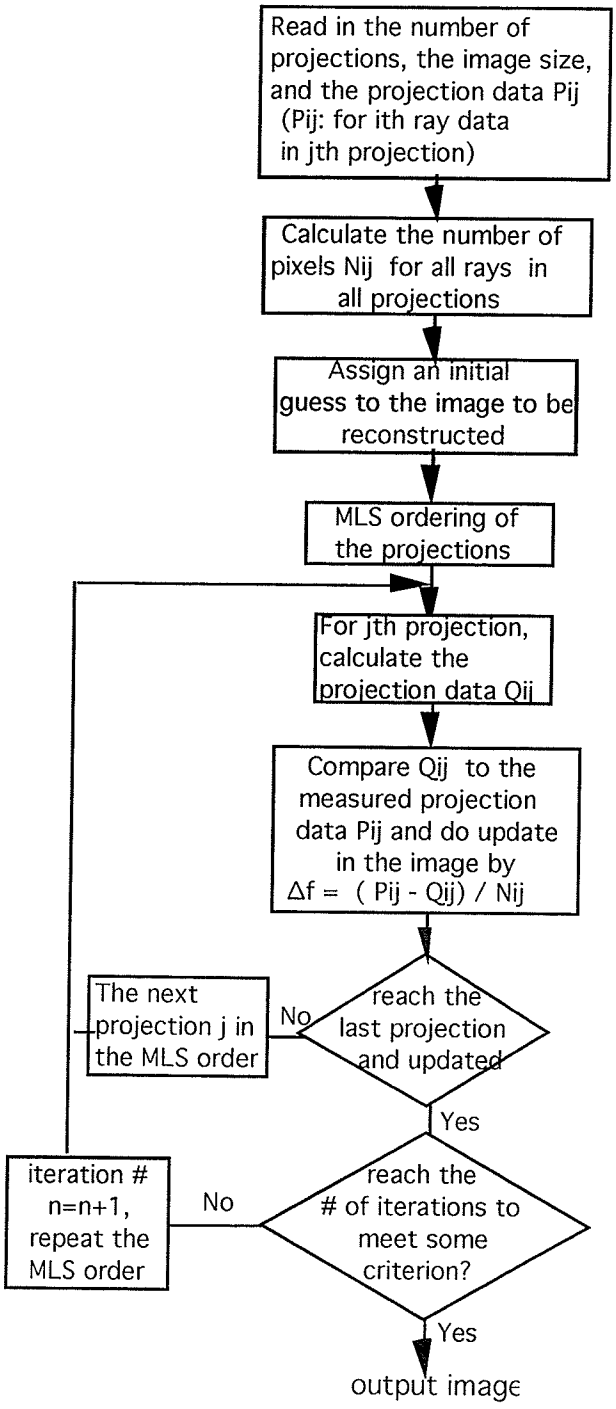

Fig. 3.7 The flow chart of image reconstruction using MLS ART.

Table 3.1 Access orders for P total projections in the multilevel scheme (MLS).

1.($\times P/2$)	0	1														
2.($\times P/4$)	1	3														
3.($\times P/8$)	1	5	3	7												
4.($\times P/16$)	1	9	5	13	3	11	7	15								
5.($\times P/32$)	1	17	9	25	5	21	13	29	3	19	11	27	7	23	15	31
6.($\times P/64$)	1	33	17	....												

3.4 Experiments and results

Additive ART, Eq. (2.14), is used for the experiments presented here. We measure the ray integrals using the same method as that in Mazur and Gordon [1994]. The Shepp-Logan (1974) phantom shown in Fig. 3.8 is the first object we tested.

To compare the multilevel scheme (MLS), the sequential accessing scheme (SAS) and the random permutation scheme (RPS), we show for each scheme, with 30 projections, 5 images each representing an intermediate reconstruction from the first 2, 4, 8, 16 and 30 projections in Fig. 3.9, respectively. SAS recovers most of the high frequency information in the latter half of the iteration while the other two recover it right from the beginning. Comparing MLS and RPS, we see that multilevel accessing produces better images at each intermediate reconstruction. MLS yields

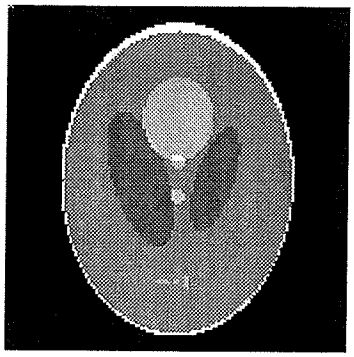

Fig. 3.8 The Shepp-Logan phantom used for the experimental test.

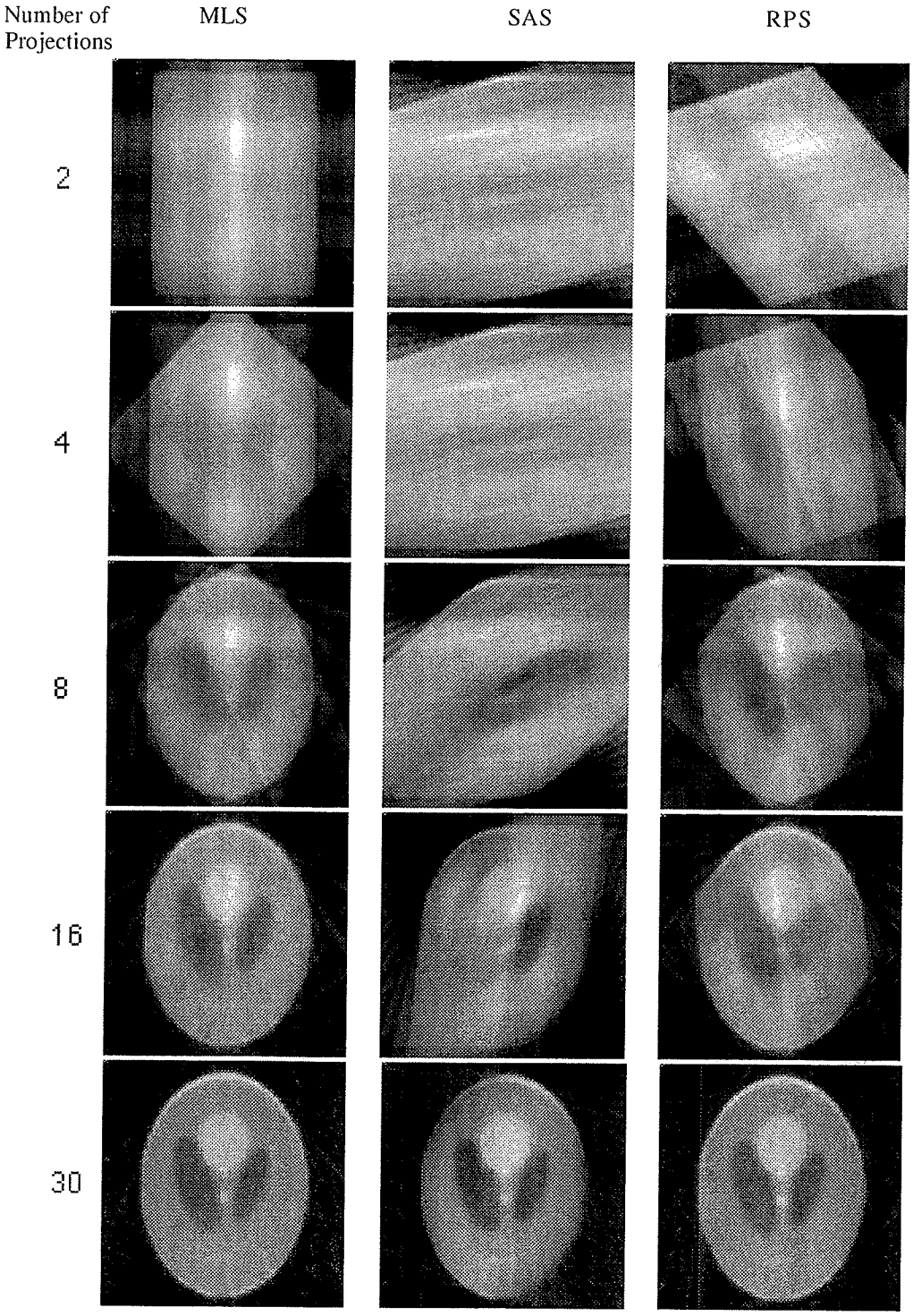

Fig. 3. 9 Intermediate reconstructions of the Shepp-Logan phantom from the first 2, 4, 8, 15, 30 projections within 1 iteration, under total of 30 projections. The first column is from the multilevel scheme (MLS), the second column is from the sequential accessing scheme (SAS) and the last column is from the random permutation scheme (RPS). The reconstruction accuracy (defined in Eq. (3.3) below) is measured and the results are plotted in Fig. 3.11(a).

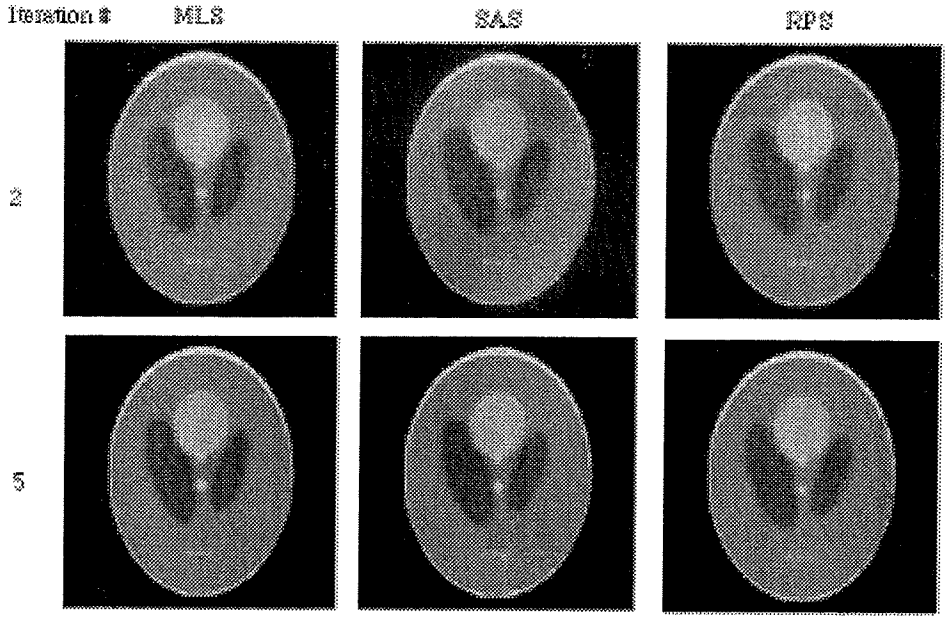

Fig. 3.10 Reconstructions of the Shepp-Logan phantom from 2 and 5 iterations, under a total of 30 projections. The first column is from MLS, the second column is from SAS and the last column is from RPS. The reconstruction accuracy (defined in Eq. (3.3) below) is measured for upto 10 iterations and the results are plotted in Fig. 3.11(b).

reasonable reconstructions even after only 8 projections are accessed. Fig. 3.10 shows for each scheme, two reconstructions from 2 and 5 iterations. There are no perceivable difference among the three 5-iteration images on the 2nd row.

For a preliminary evaluation of the reconstructed images, the following correlation coefficient measure is used:

$$\varepsilon_1 = \frac{\sum_{i=1}^{N}(\mu_i - \bar{\mu})(\mu_i^* - \bar{\mu}_i^*)}{\left[\sum_{i=1}^{N}(\mu_i - \bar{\mu})^2 \cdot \sum_{i=1}^{N}(\mu_i^* - \bar{\mu}_i^*)^2\right]^{1/2}} \qquad (3.3)$$

where $\mu_i(\bar{\mu})$ and $\mu_i^*(\bar{\mu}_i^*)$ each represent the pixel value in the original and the reconstructed images, respectively. ε_1 measures the extent to which two images are similar to each other and it takes the highest value of 1 if the two are exactly the same. The ε_1 versus the accessed number of projections within the first iteration for each of the three schemes are measured and

plotted in Fig. 3.11(a). Clearly, MLS recovers the image features early and fast. The ε_1 is also measured for a few iterations and the results are plotted in Fig. 3.11(b). The three different schemes reach the same ε_1 value after 5 iterations, in agreement with the visual appearance of reconstructions (see Fig. 3. 10. Note that for RPS, we used different orders from iteration to iteration). A detailed physical evaluation of the effect of these schemes on ART reconstructions will be conducted in Chapter 7 and we will see that the performance of RPS varies in between those of MLS and SAS.

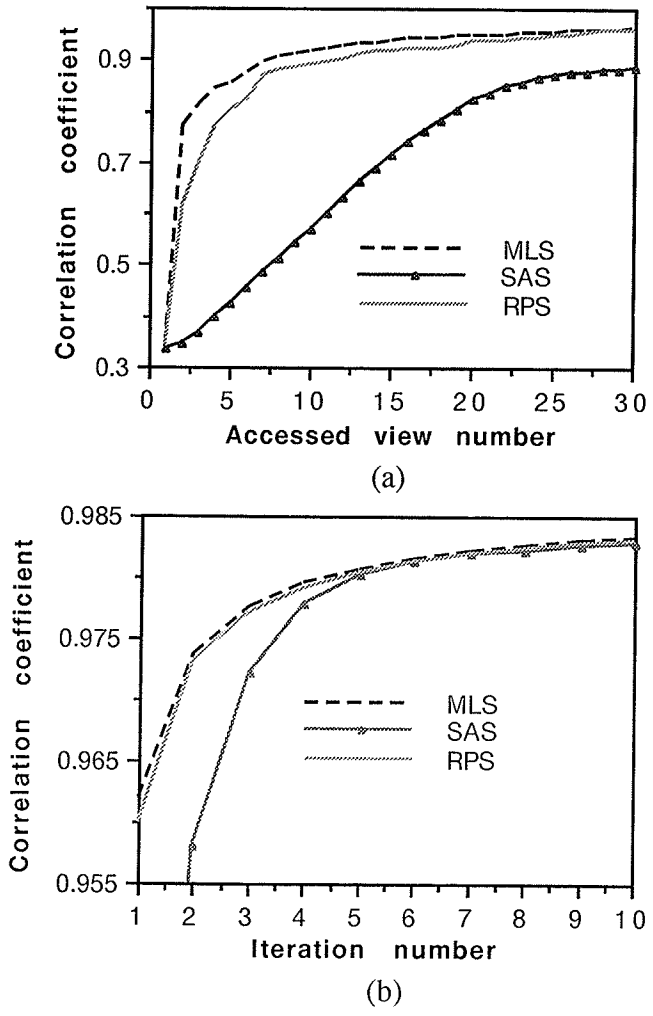

Fig. 3.11 Plots of the correlation coefficients ε_1 (a) versus the accessed projection number within the first iteration and (b) versus the iteration numbers, for the reconstructions of the Shepp-Logan phantom using the multilevel scheme (MLS), the sequential accessing scheme (SAS), and the random permutation scheme (RPS). Note that the access orders for RPS change from iteration to iteration in (b).

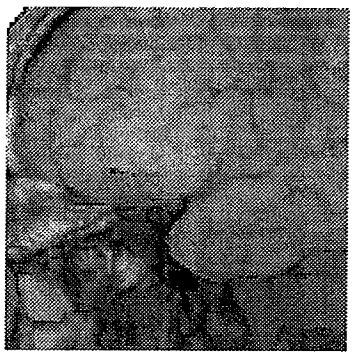

Fig. 3.12 Part of a brain magnetic resonance image (BMRI) in a volumetric human sagittal scan. It is just used as a test image (size 128x128).

We have carried out similar tests on a few other medical images. The MLS scheme outperforms the other two on all of the images. As an example, for the one shown in Fig. 3.12, which is part of a brain magnetic resonance image (BMRI), we show its intermediate reconstructions in Fig. 3.13. Similar effects as seen in Fig. 3.9 can be observed.

In doing the tests above, we used an initial image of 0. We also tried using different initial images and found that compared to SAS, MLS has little dependence on initial image. The result will appear in [Guan 1996]. We also checked that 1-iteration MLS takes ~ (1/3-1) more in computation time than CBP does. This is consistent with Herman's conclusion that 1-iteration ART takes ~(1-3) times of computations by CBP. It is hard to be more precise than this, since even the same programs will require different times relative to each other depending on the number of projections and the image size [Herman 1976]. In [Brooks 1976], a detailed analysis indicated that 1-iteration ART requires a number of $4n^2$ multiplications for reconstructing a single projection, while that number for FBP (CBP) is $(n^2+4n\log_2^n)$. The numbers of additions are about the same for each method.

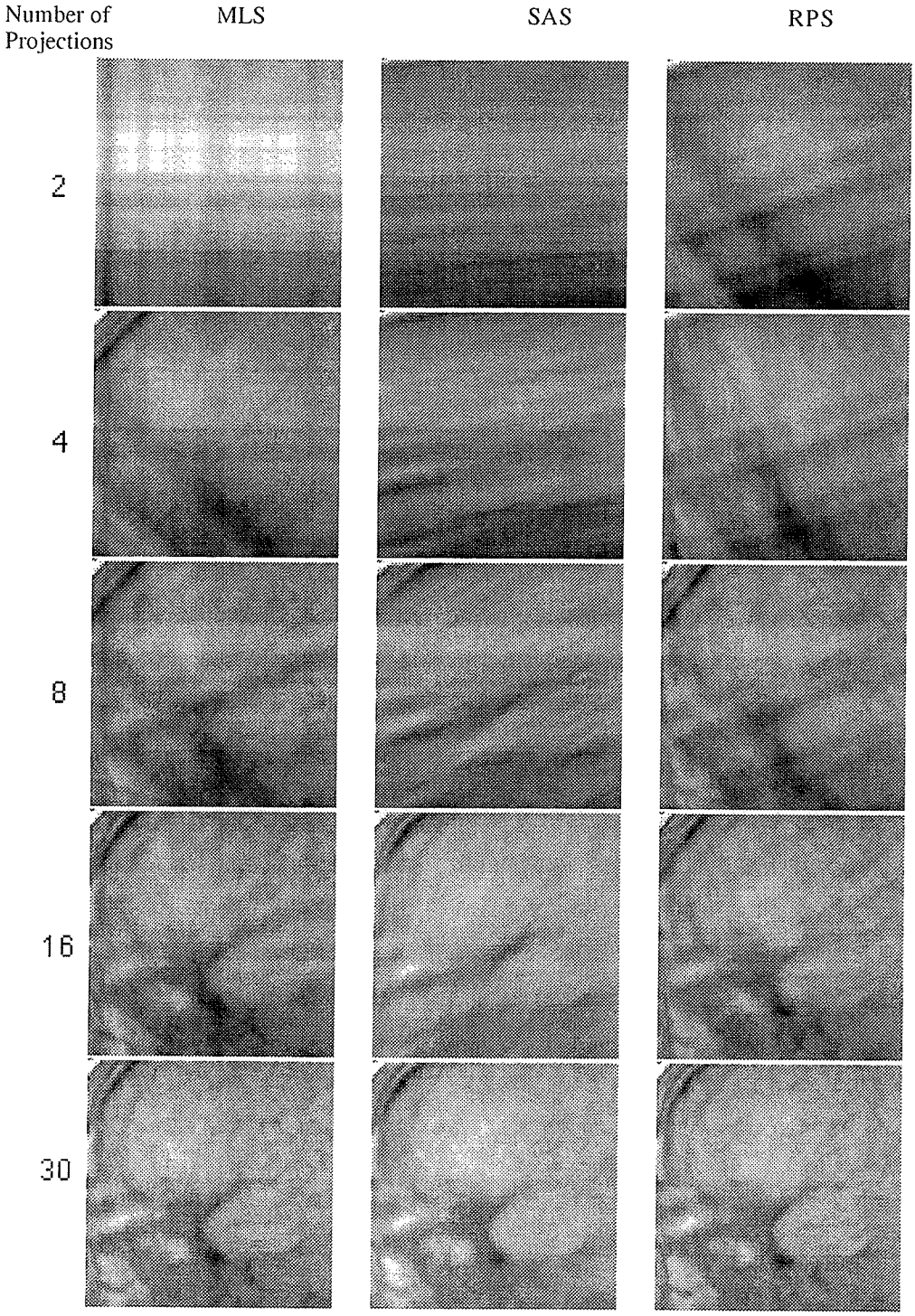

Fig. 3. 13 Intermediate reconstructions of the BMRI image from the first 2, 4, 8, 15, 30 projections within 1-iteration, under total 30 projections. The first column is from the multilevel scheme (MLS), the second column is from the sequential accessing scheme (SAS) and the last column is from the random permutation scheme (RPS).

3.5 A look at the reconstructions in Fourier space

We also demonstrate that MLS represents an efficient and fast implementation of the Fourier central slice theorem in the frequency domain.

Fig. 3.14 shows the Fourier transform of the intermediate reconstructions of the S-L phantom from the first 2, 4, 8, 16, 32 and 64 projections for a total of 64 projections, by MLS (1st row), RPS (2nd row) and SAS (3rd row), respectively. Also shown at the bottom-right is the Fourier transform of the phantom itself. One sees that each projection updated by MLS fills the Fourier domain by a line passing through the origin, in good agreement with the central slice theorem. The frequency domain is uniformly and symmetrically filled to each level. On the other hand, in the corresponding versions of RPS or SAS, besides the central lines, spurious lines also appear (especially the first three). These spurious lines represent the 2-D spatial correlation of the updated projections. In the last one of each row, the MLS and RPS versions (minor difference between them) looks very close to the original, but not the SAS version, in which only the latter half of the projections efficiently fill the Fourier domain.

3.6 Discussion and conclusion

The multilevel scheme described here is in some sense also a multiresolution reconstruction. Frequency components corresponding to different scales are reconstructed gradually, with edges of large objects being reconstructed first and small objects late, as can be seen from Fig. 3.9. Each level makes the best use of the image information reconstructed in the preceding levels and hence the information recovered from consecutive projections is less redundant compared to sequential updating.

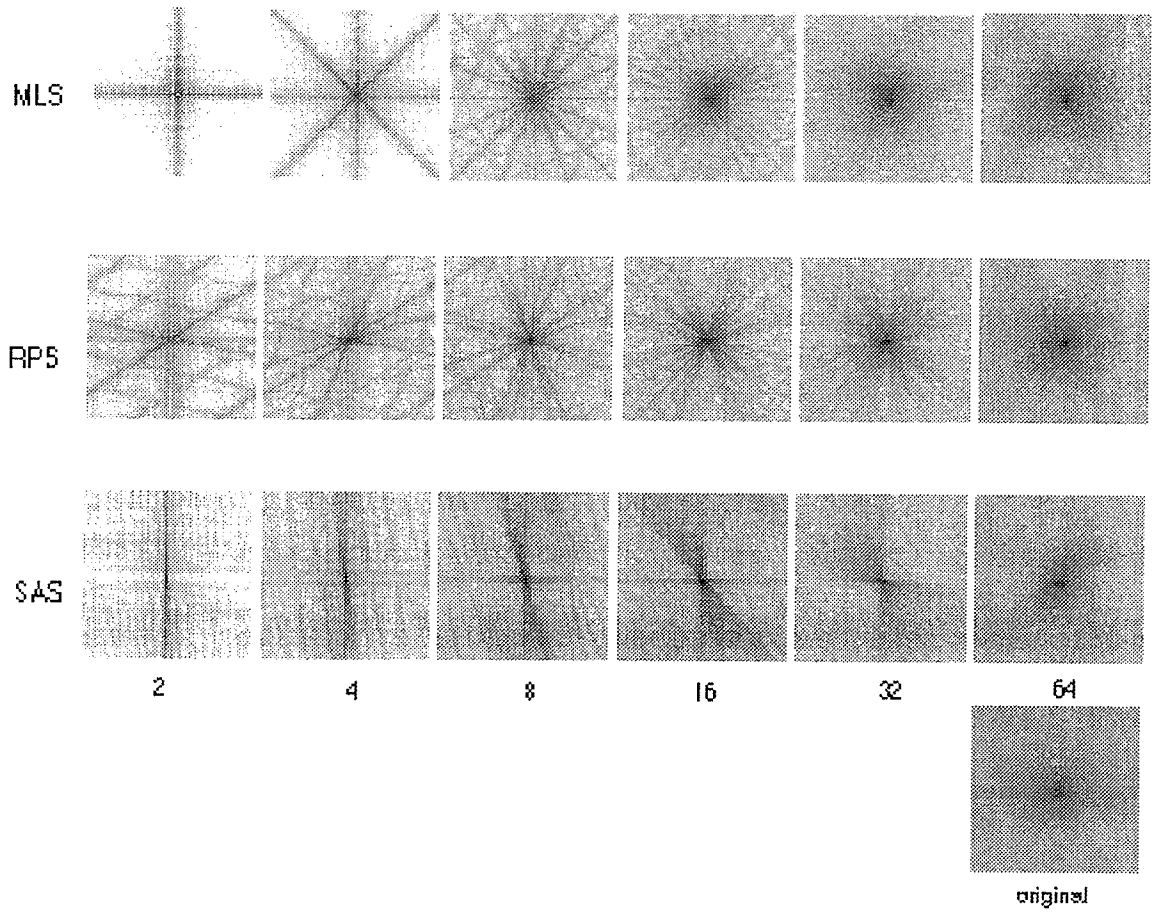

Fig. 3.14 The Fourier transform of the intermediate reconstructions of the Shepp-Logan phantom from the first 2, 4, 8, 16, 32 and 64 projections for a total of 64 projections within 1 iteration, by MLS (1st row), RPS (2nd row) and SAS (3rd row), respectively. Also shown at the bottom-right is the Fourier transform of the phantom itself.

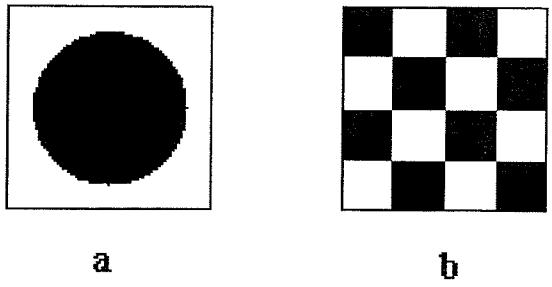

Fig. 3.15 Two objects, (a) a disk and (b) a checkerboard, to illustrate how the spatial distribution but not the symmetry of the object affects the reconstruction speed. Each object's 0^0 projection and 90^0 projection are identical.

A potential practical application of the MLS scheme is to control the patient dose in CT imaging. Projections could be taken directly in the MLS orders and hence images could be reconstructed at each level (this is also applicable to CBP or FBP). If, from a certain level, specific diagnostic information is available, then no more projections need be taken.

The spatial distribution of the object also influences the convergence speed. A larger imaging region than the object's section may be used such that the section's contour can be reconstructed very fast, as Fig. 3.9 but not Fig. 3.13 demonstrated. The spatial distribution, not the symmetry, determines how much high frequency information (variations of the intensity normalized by the ray "length") is contained in each projection. For extreme cases, consider two objects shown in Fig. 3.15, (a) a disk and (b) a chessboard. Each object has its own identical 0^0 projection and 90^0 projection. After these two projections are accessed, the disk can be reconstructed to a large extent but not the checkerboard. This is because each projection of the disk contains high frequency components to modify the initial guess, which is blank, while the chessboard's two projections themselves are flat and hence do nothing to the initial guess. For the checkerboard, the 45^0 projection is a better choice to start the reconstruction than the 0^0 projection.

In conclusion, MLS is the best choice for the algebraic reconstruction technique: it yields speedy convergence without orthogonalization. It is the optimal ordering for that at any time during the reconstruction, it produces both the maximum space uniformity and projection orthogonality. This scheme, easily implemented, performs a multi-level reconstruction using parallel projection data. Its extension to fan beam CT reconstruction is easy (see Chapter 9). It parallel implementation is also feasible since Fitchett [1993] already implemented a version for the sequential ART (also see

[Lattard]). Experimental tests using various sources of data and employing different physical criteria will be made in following chapters.

References

Barrett H. H. and W. Swindell, *Radiological imaging, the theory of image formation, detection and processing* (Academic Press), 1981.

Brooks R. A. and G. Di Chiro, Principles of computer assisted tomography, *Phys. Med. Biol.* 21, 689-732, 1976.

Fitchett J. W., *A locally synchronous globally asynchronous vertex-8 processing element for image reconstruction on a mesh, M. Sc. thesis,* University of Manitoba, Winnipeg, Canada, 1993.

Gordon R., R. Bender and G. T. Herman, Algebraic Reconstruction Techniques (ART) for three-dimensional electron microscopy and x-ray photography, *J. Theoret. Biol.* 29, 471-482, 1970.

Guan H. and R. Gordon, A projection access order for speedy convergence of ART: A multilevel scheme for computed tomography, *Phys. in Med. and Bio.* 39, 2005-2022, 1994.

Guan H. and R. Gordon, Computed tomography using ART with different projection access schemes: A comparison study under practical situations, *Phys. in Med. and Bio.*, accepted for publication, 1996.

Herman G. T., *Image reconstructions from projections: the fundamentals of computerized tomography* (New York: Academic Press), 1980.

Herman G. T. and L. B. Meyer, Algebraic reconstruction techniques can be made computationally efficient, *IEEE Trans. Med. Imaging* 12, 600-609, 1993.

Kuhl D. E., R. Q. Edwards, A. R. Ricci and M. Reivich, Quantitative section scanning using orthogonal tangent correction, *J. Nucl. Med.* 14, 196-200, 1973.

Lattard D. and G. Mazare, A VLSI implementation of parallel image reconstruction, *CVGIP: Graphical Models and Image Processig* 53, 581-591, 1991.

Mazur E. J. and R. Gordon, Interpolative ART without beam partitioning (IART) for computed tomography *Med. Biol. Eng. Comp.* 33, 82-86, 1995.

Ramakrishnam R. S., S. K. Mullick, R. K. Rathore and R. Subramanian, Orthogonalization, Bernstein polynomials, and image restoration, *Appl. Opt.* 18, 464-468, 1979.

Ranganath M. V., A. P. Dhawan and N. Mullani, A multigrid expectation maximization reconstruction algorithm for Positron Emission Tomography, *IEEE Trans. Med. Imaging* 7, 273-278, 1988.

Shepp L. A. and B. F. Logan, The Fourier reconstruction of a head section, *IEEE Trans. Nucl. Sci.* 21, 21-43, 1974.

van Dijke M. C. A., *Iterative methods in image reconstruction,* Ph.D. dissertation, Rijksuniversiteit Utrecht, Utrecht, The Netherlands, 1992.

Chapter 4
A Comparison between CBP and MLS Using Real Data from CT Scans

4.1 Introduction

In chapter 3, we presented a novel MLS scheme for the most efficient algebraic image reconstruction. One iteration of this multilevel ART yields high quality images in a preliminary evaluation, nearly eliminating the iterative nature of ART. In this chapter, we will investigate the physical performance of the scheme using real CT projections. The reconstructions are compared to those from CBP.

Shepp and Logan [1974] once made a comparison study between CBP and ART by computer simulation. They concluded that 12-iteration ART is not much different from CBP and both are about equally sensitive to noise. In fact, they found that with noisy projections, reconstructions by ART exhibit more SNR than CBP. They further incorporated a *sinc* filter in CBP and then claimed that this modified version, or *sinc* CBP for short, shows 50% less noise amplification than the 12th iteration of ART. From then, considering both the image quality and the computation time, almost all commercial x-ray CT machines use CBP.

Since we have dramatically enhanced the computation efficiency and image quality of ART, a new comparison between it and CBP on both the spatial and noise characteristics is worth carrying out here, by employing real data. In Section 4.2 we first test with raw projection data taken from a prototype γ-ray CT. Section 4.3 covers further experiments using the data

scanned from a special purpose x-ray CT. Discussion and conclusion are included in the last section.

4.2 Test with the real data of a prototype γ-ray CT

Brian Wowk [1992] built a prototype laboratory CT scanner doing computed γ-ray tomography. He used a ^{57}Co source of approximately 1 mCi. The detector was a sodium iodide scintillator and photo-multiplier tube. The system schematic was shown in Fig. 4.2.1(a). Objects to be scanned were placed on the rotating/translating turnable table (the source/detector system remains fixed). The translation and rotation were each driven by a motor. The collimators produced a γ ray beam 3.05 mm wide and 2 cm height. The scanning used the 122 KeV line of ^{57}Co whose attenuation in water is about $0.145/cm$. There are 64 translation steps (samples) in each projection and there are 100 rotation steps (projections). The translation and rotation sampling satisfy the sampling criterion (see Eq. 5.16). Each sampling took 5 sec to acquire ~10000 counts such that the statistical uncertainty is about 1%, which is close to that of clinical CT. Using the system, Wowk scanned a number of objects such as the COMPLEX shown in Fig. 4.2.1(b), the biological specimen like the honey dew (DEW) shown in Fig. 4.2.1(c). He kindly provided me his experimental data for a real test of the new algorithm. (No more data is available since this scanner has been disassembled.)

For the objects COMPLEX and DEW, we show three reconstructions in Fig. 4.2.2 and Fig. 4.2.3 respectively, by (a) 1-iteration MLS, (b) CBP and (c) *sinc* CBP. Clearly, for COMPLEX, the MLS version shows better spatial resolution than the CBP versions, with the small objects having been more compactly reconstructed and the edges more sharply exhibited. For the

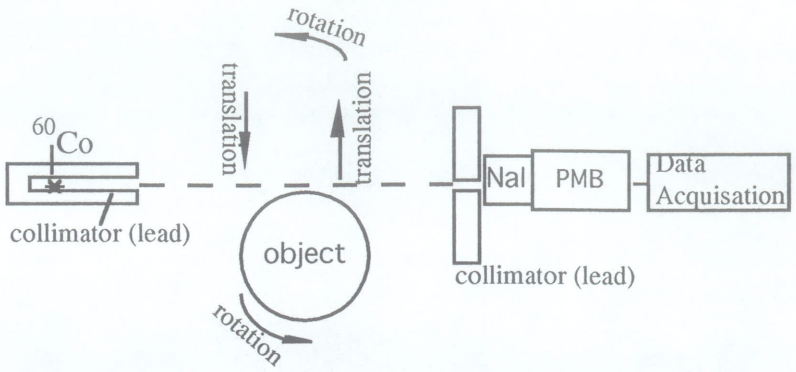

(a)

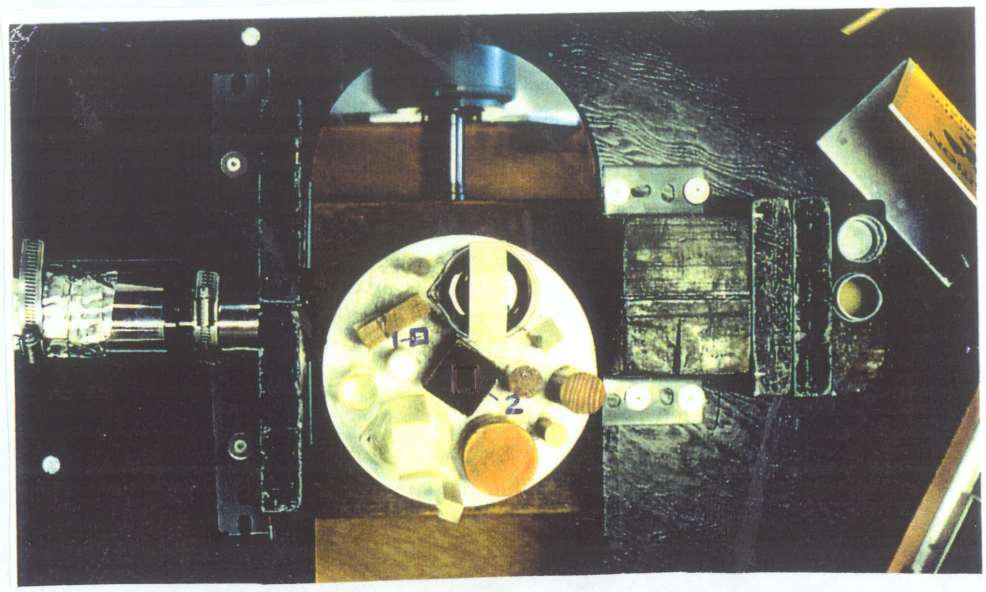

(b)

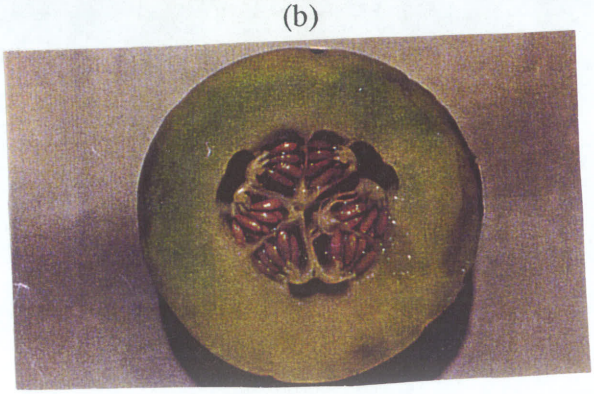

(c)

Fig. 4.2.1 (a) The system schematic of a γ-ray CT (1st generation geometry, pencil beam) and (b) an object COMPLEX under scanning (standard deviations will be measured inside the two marked squares in the reconstructions). (c) Another object, a honey dew melon (DEW) for scanning. A total of 100 projections were taken and the reconstruction size is 64×64.

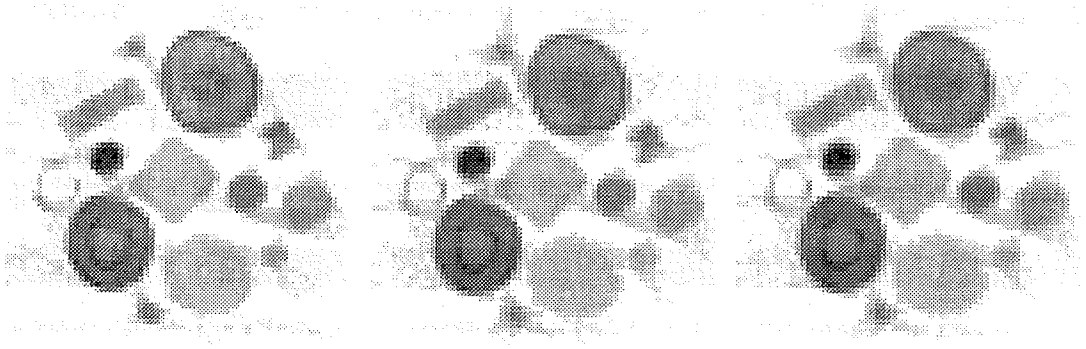

(a) MLS 1 (b) CBP (c) *sinc* CBP

Fig. 4.2.2 Reconstructions of COMPLEX by (a) 1-iteration MLS-ART, (b) CBP and (c) *sinc* CBP, from a total of 100 projections. The image size is 64×64.

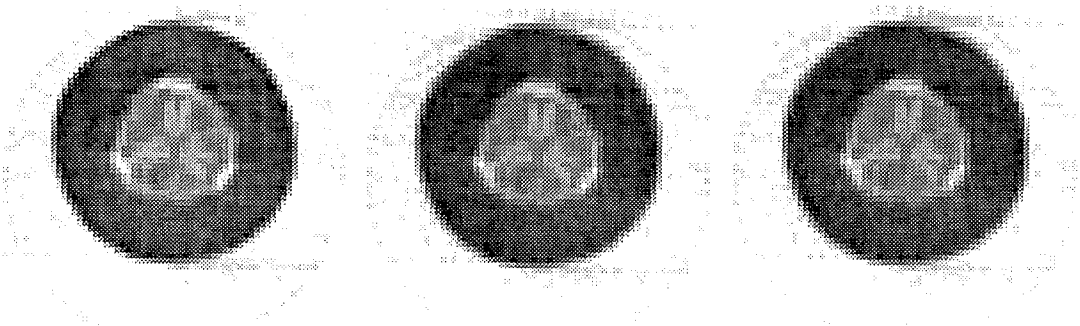

(a) MLS 1 (b) CBP (c) *sinc* CBP

Fig. 4.2.3 Reconstructions of DEW by (a) 1-iteration MLS-ART, (b) CBP and (c) *sinc* CBP, from a total of 100 projections. The image size is 64×64.

object DEW, although the difference is less visually apparent, the MLS reconstruction still shows a marginally higher contrast than those of CBP.

We also tested these algorithms using a subset of equal-spaced projections. In Fig. 4.2.4(a) and (b), we show the 1 and 2-iteration results of MLS for COMPLEX from 25 projections. The reconstruction from CBP and *sinc* CBP are shown in 4.2.4(c) and (d), respectively. Strong streak artifacts

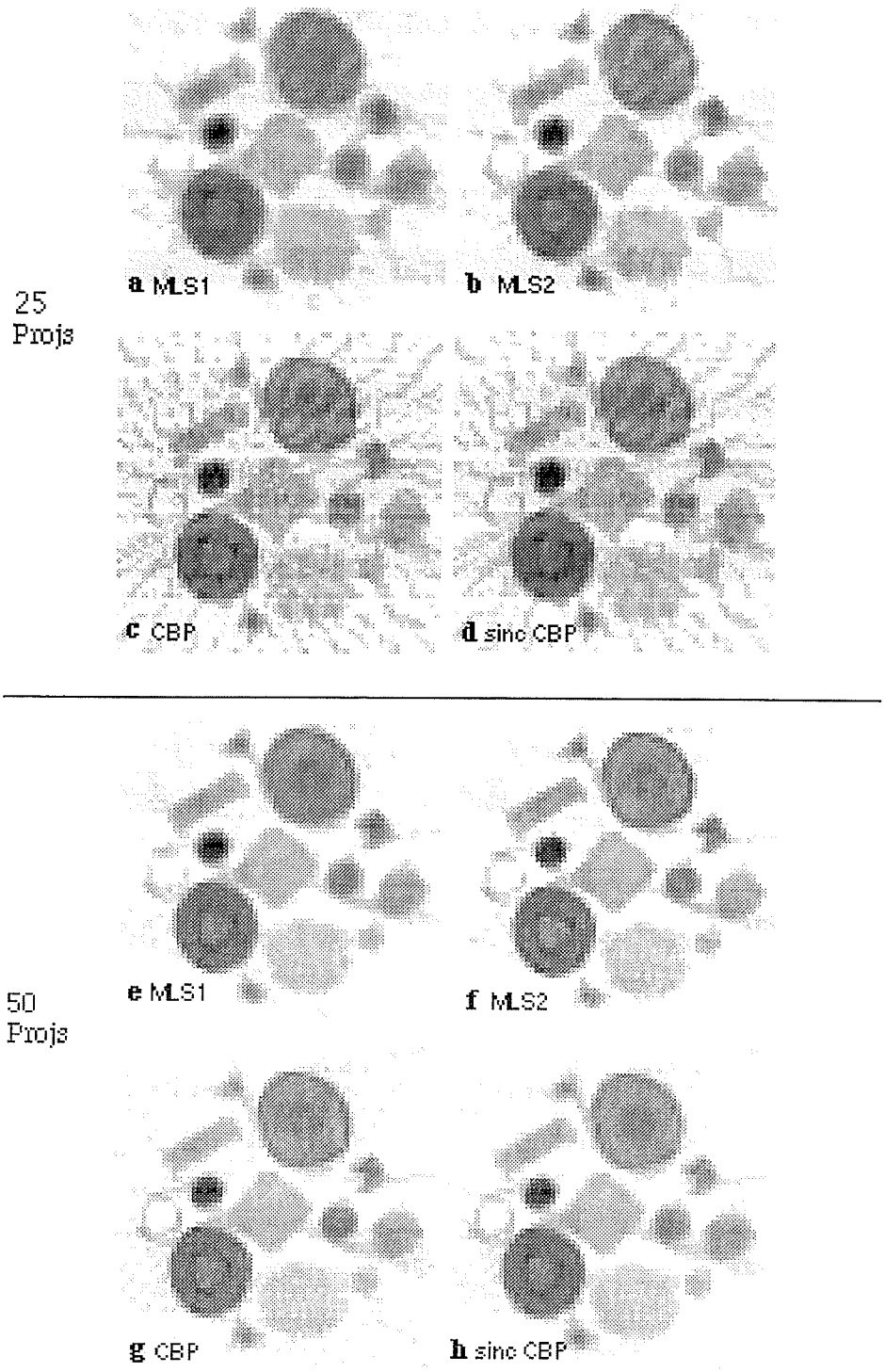

Fig. 4.2.4 The reconstructions of COMPLEX by (a) 1-iteration MLS, (b) 2-iteration MLS, (c) CBP and (d) *sinc* CBP, from 25 projections. The corresponding four reconstructions from 50 projections are shown in (e), (f), (g) and (h), in parallel to (a), (b), (c) and (d) respectively. The individual image size is 64×64.

appeared in both (c) and (d), although the latter is less severely affected due to the filtering. It is hard to distinguish small objects from artifacts. The corresponding four reconstructions from 50 projections are shown in Fig. 4.2.4 (e), (f), (g) and (h), in parallel to (a), (b), (c) and (d) respectively. The streak artifacts are still seen in the CBP versions (g) and (h). In chapter 5 we will demonstrate that when the number of projections is less than that required by the sampling criterion (see Eq. 5.16), 2 or more iterations can improve the spatial resolution. This effect is exhibited in Fig. 4.2.4 if one compares (a) and (b), or (e) and (f).

By comparing Fig. 4.2.2 (b) and Fig. 4.2.4 (f), one sees that 2-iteration MLS with 50 projections produces even sharper and more compact reconstruction than CBP with 100 projections. It suggests that at least for this object having many small and sharp details, dose can be cut by a factor of 2 using MLS.

Fig. 4.2.5 shows 4 another images of DEW, by (a) 1-iteration MLS and (b) *sinc* CBP from 25 projections, and (c) 1-iteration MLS and (d) CBP from 50 projections. Similar effect as Fig. 4.2.4 can be perceived.

One may also notice that not only do the objects in Fig. 4.2.2(b) look more blurred than those in (a), but the image also appears more noisy. The reason is that with many details of high contrast close to each other, CBP spreads the edges of each one such that the background is "messy". MLS however, reconstructs the objects more compactly and hence the background is cleaner. This is also seen in the DEW images in Fig. 4.2.3(a) and (b). We measured the noise standard deviation (SD) inside two small regions as drawn in Fig. 4.2.1(b), one in air (region 1, noise only) and the other in the central block wood (region 2, inside an object). Fig. 4.2.6 (a) and (b) show the plots of the measured SD versus the number of projections for region 1

and region 2, respectively. In region 1, both CBP and *sinc* CBP produce more noise than both 1 and 2-iteration MLS. The 2-iteration MLS shows the lowest noise level, whereas in region 2, the CBPs generate much more noise than the MLSs when the number of projections is less than 50. The 2-iteration MLS produces greater noise than its 1-iteration's, in contrast to the result of region 1.

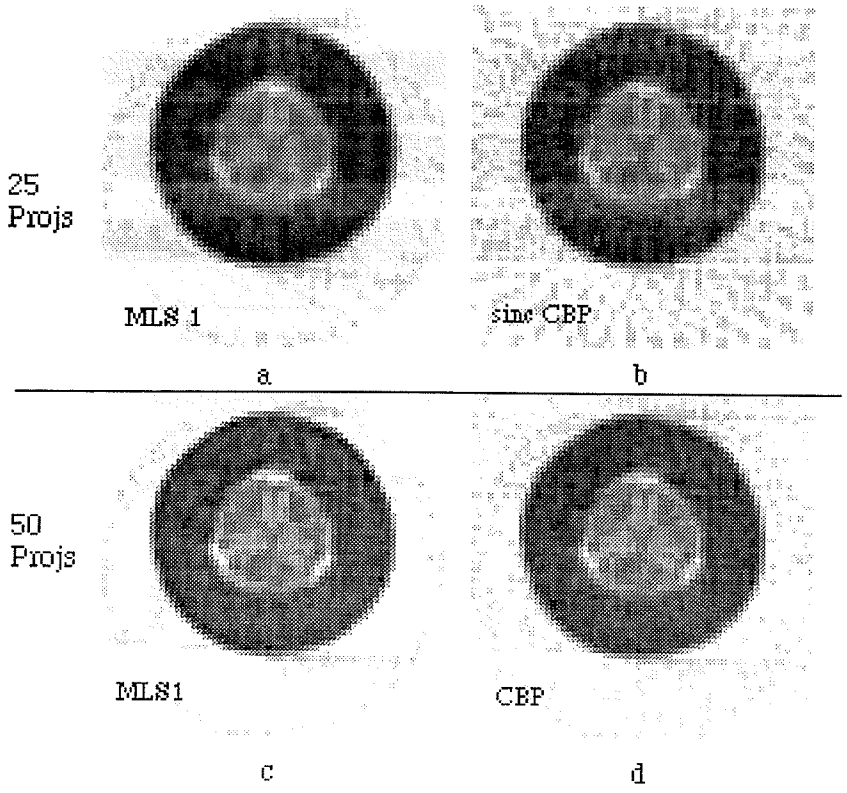

Fig. 4.2.5 Reconstructions of DEW by (a) 1-iteration MLS and (b) *sinc* CBP from 25 projections, and (c) 1-iteration MLS and (d) CBP from 50 projections. The image size is 64×64.

4.3 Test with the real data scanned from a research x-ray CT

Another set of real projection data, taken from a special purpose x-ray CT dedicated to trabecular bone density measurement for the slice of the

distal end of a cadaver femur [McClean, Rathee], was kindly provided by Dr. S. Rathee (Department of Medical Physics, Manitoba Cancer Treatment and

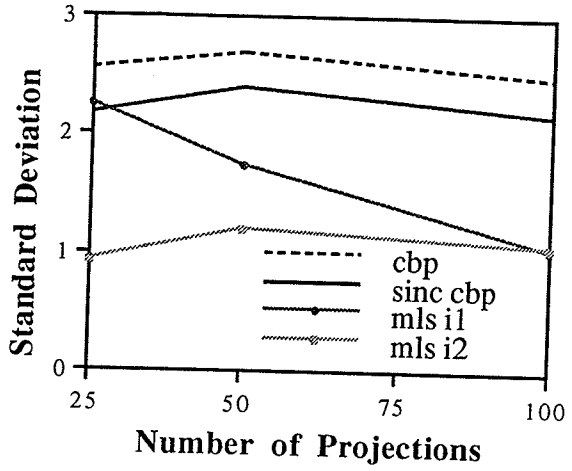

(a) region 1

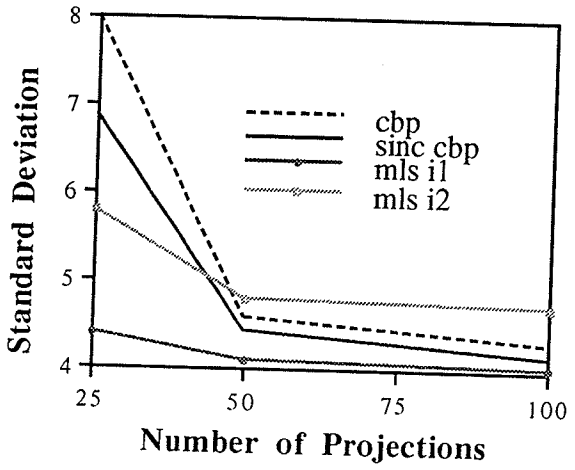

(b) region 2

Fig. 4.2.6 Plots of the standard deviation measured in (a) region 1 and (b) region 2 in the reconstructions of COMPLEX object (see Fig. 4.2.1b) versus the number of projections by 1 and 2-iteration MLS, CBP and *sinc* CBP.

Research Foundation) for our reconstruction tests. This is a rotate only, third-generation geometry fan beam CT scanner using an equivalent beam energy of $40KeV$. A system schematic of this scanner is shown in Fig. 4.3.1

[McClean]. Unlike similarly designed scanners, it allows user-defined, variable spatial resolution for a fixed object size. The photon detection system is an array of 26 photomultiplier tube/NaI detectors uniformly spaced at 2^{o} intervals in the beam. The initially collected fan beam data is remapped to parallel data. The remapping process is relatively trivial and one can refer to [Kak] for details. The number of samplings per projection is 256 (image size is 256x256) and the total number of projections is 270, evenly spaced over 180^{0}. Notice that the number of projections is much less than 400 - that required by the sampling criterion Eq. (5. 16).

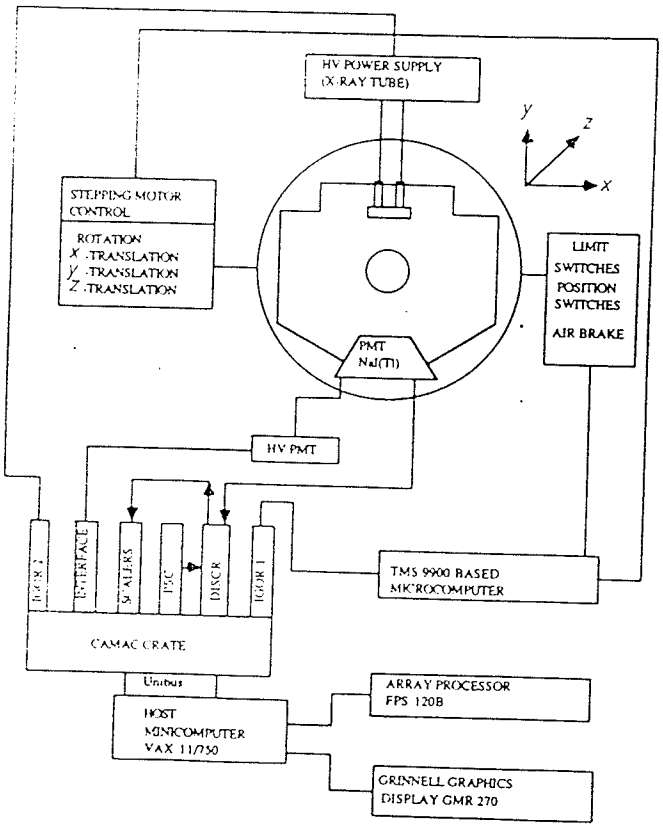

Fig. 4.3.1 A system schematic of the x-ray CT scanner dedicated for bone research [McClean].

Fig. 4.3.2 shows four images reconstructed from this data set, with (a), (b) and (c) by 1, 2 and 4-iteration MLS, respectively, and (d) by CBP. While the visual quality of (a) is about the same as (d), (b) and (c) show more readibility of small bone details. Because the number of projections is less than that required by the sampling criterion, 1-iteration MLS doesn't show superiority over CBP. Fig. 4.3.3 shows another three reconstructions by half of the data, or 135 projections, with (a) and (b) by 2 and 5-iteration MLS, respectively, and (c) by CBP. Although there appears little difference in the printed images of Fig. 4.3.2 and 4.3.3, the differences are more apparent on the computer screen. It is the opinion of the author that both (a) and (b), especially (b), reveal more small details than (c) does.

Whether the MLS truly reconstructs more small details but not lead to more amplification of noise artifacts (since noise always exists in real data) than CBP needed further verification. To test this, we measured the standard deviation (SD) inside 4 regions of interest (ROI) as shown in Fig. 4.3.4, where just the noise exists, versus the number of projections. Fig. 4.3.5 shows the plots of the SD measured in (a) region 1 and (b) region 4, for the 1, 2 and 5-iteration MLS as well as in the CBP reconstructions. Clearly, MLS produces less noise with a small number of projections and more with a large number of projections, than CBP. Also the more the MLS iterations, the bigger the SD. These results agree with those seen in Fig. 4.2.5(b) but not in 4.2.5(a). For 270 projections, the noise level of CBP is about the same as those of 1 or 2-iteration MLS. For 135 projections, the noise of CBP is about the same as that of 5-iteration MLS. This confirms that 2 or more MLS iterations truly produces more detectibility than CBP does.

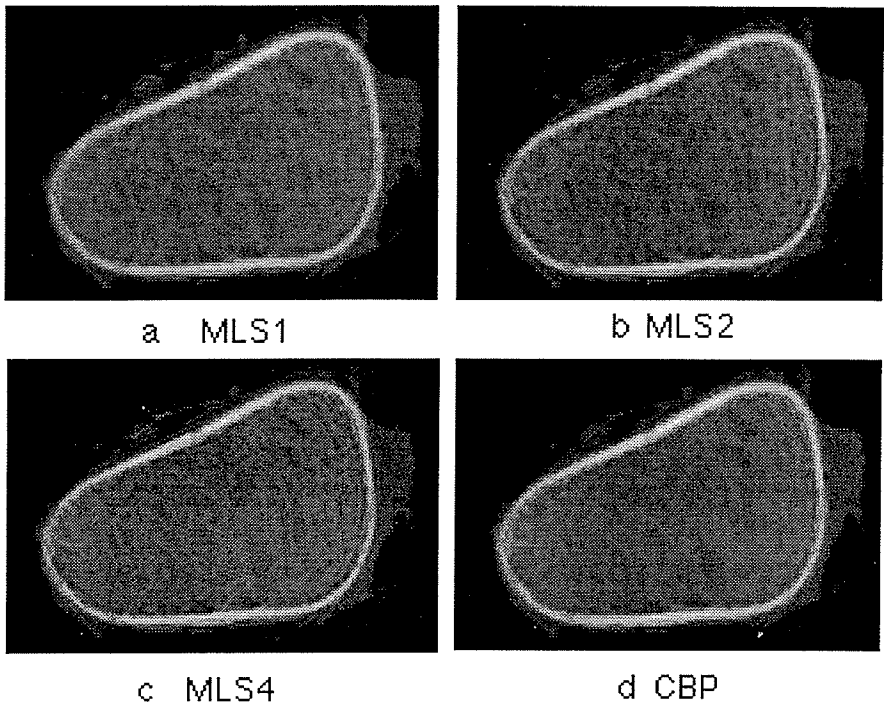

Fig. 4.3.2 Four reconstructions of the distal end of a cadaver femur, by (a) 1, (b) 2 and (c) 4-iteration MLS, respectively, and (d) CBP, from a total of 270 projections.

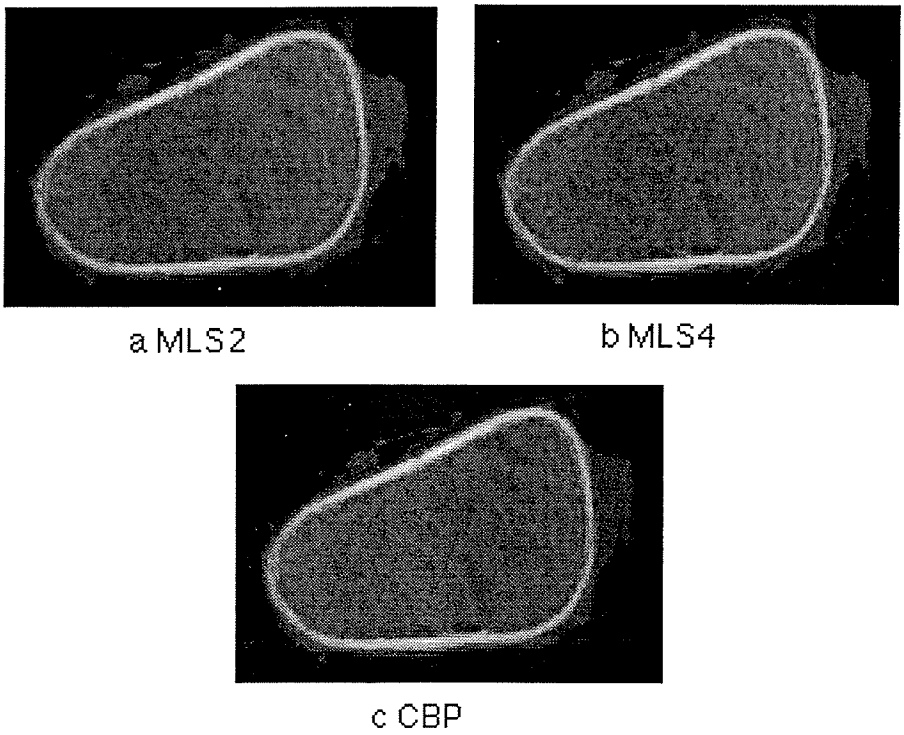

Fig. 4.3.3 Three reconstructions of the distal end of a cadaver femur, by (a) 1-iteration MLS, (b) 2 -iteration MLS and (c) CBP, from 135 projections.

To check the noise structure, we also measured the noise intensity distribution (histogram) inside the 4 regions. Fig. 4.3.6(a) shows such histograms for 1-iteration MLS and CBP in region 1, and (b) shows them for 2-iteration MLS and CBP in region 4. The number of projections is 270.

4.4 Discussion and conclusion

Since the data we used are not scanned from CT phantoms, those physical quantities such as MTF and SNR which characterize the high and low contrast detectibilities of CT can not be directly measured. This is left for the future work using the data scanned from a number of CT quality assurance phantoms by the clinical scanners provided by the Picker International Corporation [1995].

A *sinc* filter used in CBP reduces noise in the reconstruction, at the cost of reduced spatial resolution. Again although the paper print images do not adequately reflect the computer screen image, the *sinc* CBP image shown in

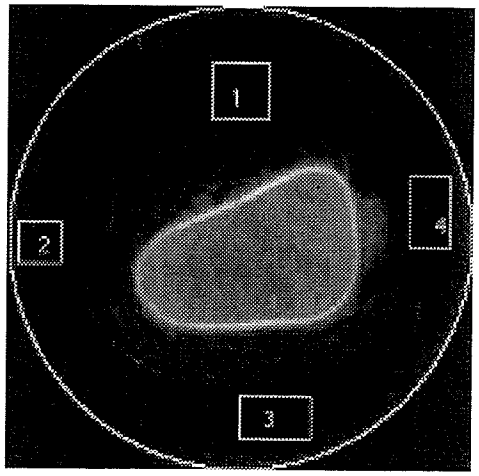

Fig. 4.3.4 Four noise only region of interest inside the reconstruction circle for noise standard deviation measurement.

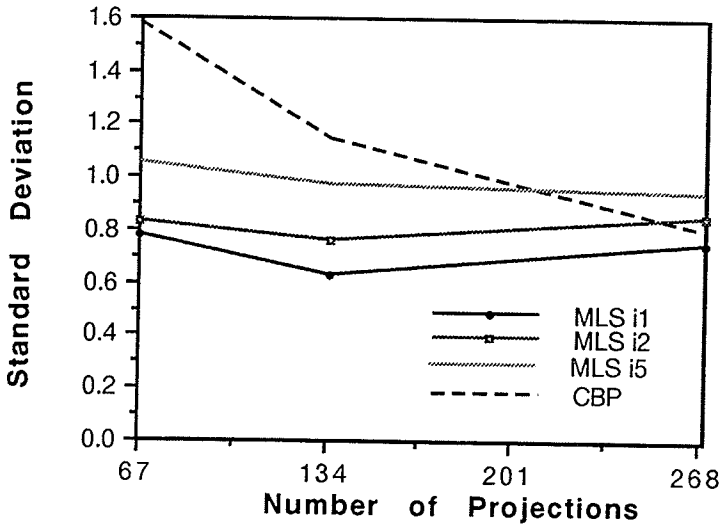

(a) region 1

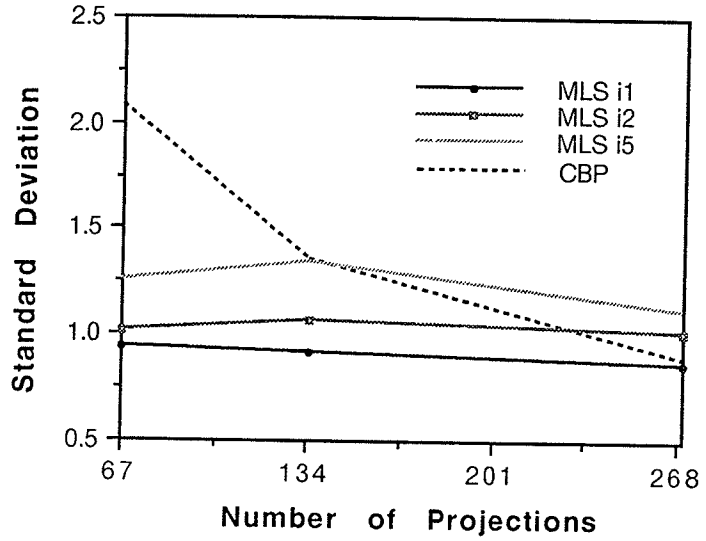

(b) region 4

Fig. 4.3.5 Plots of the standard deviation measured in (a) region 1 and (b) region 4, from 1, 2 and 5-iteration MLS as well as from CBP reconstructions, versus the number of projections (3 different number of projections: 270, 135 and 67 are tested).

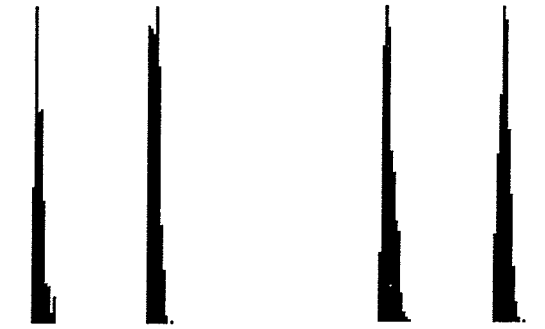

(a) region1 (b) region 4

Fig. 4.3.6 Noise histograms. (a) 1-iteration MLS (mean 1.02) and CBP (mean 1.08) in region 1, and (b) 2-iteration MLS (mean 1.54) and CBP (mean 1.57) in region 4. The number of projections is 270.

Fig. 4.2.2(c) is smoother than the CBP version in Fig. 4.2.2(b), with the edges of objects more blurred. The *sinc* filtering commonly improves the readability of relatively large objects [McDavid]. Objects of small sizes need larger threshold contrast to be detected (i.e., need better spatial resolution, see the contrast detail analysis in section 5.7) and the filtering won't improve effectively. We have performed a *sinc* CBP reconstruction for the bone image and found no improvement with bone detail reading.

From the test results of COMPLEX (Fig. 4.2.1b), we conclude that MLS can do better job than CBP for reconstructions of high contrast objects, at least in cases where the number of projections is above half of that required by the sampling criterion, producing sharper edges and smaller background noise even with half of the CBP dosage. The noise standard deviation measurements also demonstrate that MLS has more dose efficiency than CBP for low contrast object detection when the number of projections is less than half of that required by the sampling criterion. Such a conclusion is in

excellent agreement with that obtained by computer simulation in the next chapter.

References

Kak A. C., Image reconstruction from projections, in *Digital imaging processing techniques* 111-170, Ed. M. P. Ekstrom, Academic Press Inc., 1984.

McClean B. A., T. R. Overton, T. N. Hangartner and S. Rathee, A special purpose x-ray fan-beam CT scanner for trabecular bone density measurement in the appendicular skeleton, *Phys. Med. Biol.* 35, 11-19, 1990.

McDavid W. D., R. G. Waggener and M. J. Dennis, Physics principles of computed tomography, in *CRC Handbook of Medical Physics,* Vol. II, Eds. R. G. Waggener, 37-80, 1983.

Picker International, *Software documentation for CT data acquisition* (proprietary information), 1995.

Rathee S., Z. J. Koles and T. R. Overton, Image restoration in computed tomography: restoration of experimental CT images, *IEEE Trans. Med. Imaging* 11, 546-553, 1992.

Shepp L. A. and B. F. Logan, The Fourier Reconstruction of a Head section, *IEEE Trans. Nucl. Sci.* NS-21, 21-43, 1974.

Wowk B., *Computed Gamma Ray Tomography*, Reserach report, Department of Physics, University of Manitoba, Winnipeg, Canada, 1992.

Chapter 5
Simulation of CT and CT Reconstructions using MLS ART and CBP

5.1 Introduction

In this chapter, we perform a computer simulation on CT and CT reconstructions using MLS ART and CBP. The tomogram qualities are measured using four physical criteria: signal to noise ratio (SNR), modulation transfer function (MTF), contrast detail (CD) evaluation and noise power spectrum (NPS). Details of these have been discussed in section 2.4. The simulation study has advantages in:

1. Allowing one to understand the influence purely of the reconstruction algorithm (or any other particular process in the cascaded CT imaging process) on the tomogram quality. This cannot be directly measured from a real scan because of the interconnections among individual processes;

2.Low cost, flexibility of adjusting various parameters and test of extreme cases.

This work provides a thorough physical comparison among CT reconstruction techniques. Sections 5.2 to 5.5 discuss in detail the physical arrangements of the simulation study, whereas sections 5.6 to 5.10 cover the results generated from the study. In each section of 5.6 to 5.9, we design a phantom to test one physical quality. All the phantoms are $25cm$ in diameter, 512x512 pixels in size (i.e., 512 samples/projection, or 20 samples in $1cm$) and cover a CT# range of 0 - 255. For each phantom, ray integrals of the phantom along a series of angles are calculated to obtain a set of

projection data. Section 5.2 below discuss how to introduce Poission noise into the projections to simulate the real CT data.

This simulation study was implemented in Sun Pascal and performed on the Sun Unix system. The program was simply *procedure* based and no user interface used. All parameters such as the number of projections, the image size and the number of photons per measurement etc. are defined as constants. All variables are implemented in single precision (word length 16 bits). The computer source codes are included in Appendix I.

5.2 Projection noise simulation

In computed tomography, there are five different noise sources [Morgan]: statistical noise, electronic noise, roundoff errors, artifactual noise and reconstruction algorithm noise. Among these, statistical or Poisson noise, which is due to the quantum nature of x-ray photons, inherently plays the major and crucial role (also in other radiographic imaging systems), primarily because of the large energy of x-ray photons (compare to the visible range photons in photography). Most importantly, Poisson noise from different detectors is uncorrelated or "white". Electronics in CT are sufficiently well designed such that the electronic noise contribution is only a small fraction of that of the statistical noise [Cohen]. Also, sufficiently accurate digitizers with many bits today make the roundoff error negligible. Artifactual noise due to beam hardening, defective detectors and patient motion, etc., is assumed absent in this simulation study (except for that introduced by the reconstruction technique which, of course, is not primary noise involved in projection data).

By assuming Poisson noise is the major noise source, Kijewski and Judy [1987] calculated the noise power spectrum (NPS) of CT by computer simulation. Their calculation agrees very well with the experimentally measured NPS of a real scanner. Many simulation studies on CT also consider Poisson noise the only primary source [Riederer, Wagner, Goodsitt, Mazur].

In the acquisition of projection data, the number of photons reaching each detector follows the Poisson distribution:

$$P(K) = \exp(-\overline{K})\overline{K}^{K} / K! \tag{5.1}$$

The Poisson distribution will approach a Gaussian for a large mean $\overline{K}$ (empirically for $\overline{K} \geq 10$):

$$P(K) = \frac{1}{\sqrt{2\pi\overline{K}}}\exp[-(K-\overline{K})^2 / (2\overline{K})] \tag{5.2}$$

In the simulation, we introduce quantum noise directly into the detector reading by assuming that the number of photons reaching a single detector is the mean in the distribution of that detector. The simulation procedure for generating a single measurement is as follows:

1. For a well collimated beam with N_0 monochromatic photons emitted from the x-ray tube toward the $i-th$ detector, the average number reaching the detector will become

$$N = N_0 e^{-\int \mu dl} = N_0 e^{-P_i} = N_0 e^{-k\int g dl} \tag{5.3}$$

due to the attenuation, where P_i is the attenuation integral along a line l, and g is the CT number in the simulated object. g is scaled by a constant k such that it can match the linear attenuation coefficient μ of tissues to x-rays as discussed in section 5.6.

2. For a mean number of N photons reaching the $i-th$ detector, the actually detected number, say N', can be selected from the Poisson statistics (5.1), where $\overline{K} = N$, using a Monte Carlo method. The noisy attenuation integral can then be calculated inversely by

$$P_i' = -\ln \frac{N'}{N_o} \qquad (5.4)$$

Since the Poisson noise in separate detectors is uncorrelated, one can then repeat the procedure for each detector to generate one noisy projection. Rotating the source/detector combination generates multiple projections.

5.3 Incident photon number per measurement

Different numbers of incident photons ranging from $N_o = 10^5$ to 10^8 per measurement were used: 2×10^5, 1.6×10^6, 1.28×10^7 and 1.02×10^8. We assume that the incident number is the same for each single measurement.

The last two numbers are of the order used in clinical CT scanners, which we estimated to be 10^7-10^8 (not seen in publications) in two ways: 1. a reverse calculation from the typical surface dosage and 2. an estimate based on the contrast detectibility of a CT scanner. Theoretically, calculation of the bremsstrahlung x-ray production based on the x-ray tube voltage (KV), the tube current×exposure time (mAs) and the target material atomic number (Z) can be made (see p. 69-70 in [Krestel]). But it is difficult to calculate the x-ray attenuation within the target, by the tube window and by the added filters to shape the spectrum (all are machine dependent). Estimation based on the case independent quantities is more approachable.

5.3.1 Calculation from the surface dosage

The calculation procedure is: 1. convert the tissue surface dose D_t to the equivalent air dose D_a; 2. calculate the exposure X from the air dose D_a; 3. calculate the photon fluence from the exposure X.

Under the same photon fluence, the absorbed dose in two different media, say tissue (D_t) and air (D_a), is related by

$$\frac{D_a}{D_t} = \frac{(\frac{\mu_{ab}}{\rho})_a}{(\frac{\mu_{ab}}{\rho})_t} \qquad (5.5)$$

where $\frac{\mu_{ab}}{\rho}$ is the mass energy absorption coefficient. For an average energy of 60 KeV in x-ray CT, $(\frac{\mu_{ab}}{\rho})_a$ = 0.0289 cm^2/g and $(\frac{\mu_{ab}}{\rho})_t$ = $0.0312 cm^2/g$ [Jones]. Hence Eq. (5.5) reduces to $D_a = 0.926 D_t$.

The exposure X relates to the air dose D_a by

$$D_a(rad) = 0.873 X(R) \qquad (5.6)$$

and the exposure X itself can be directly calculated from

$$X = 1.833 \times 10^{-11} \Phi E (\frac{\mu_{en}}{\rho})_a \frac{g \cdot R}{KeV} \qquad (5.7)$$

where Φ is the photon fluence ($1/cm^2$), $(\frac{\mu_{en}}{\rho})_a$ is the mass energy transfer coefficient in air and E is the photon energy. For $60 KeV$ x-rays, $(\frac{\mu_{en}}{\rho})_a = (\frac{\mu_{ab}}{\rho})_a$. Combining (5.5), (5.6) and (5.7), we get

$$\Phi = 3.3 \times 10^{10} D_t / cm^2 \qquad (5.8)$$

The typical value of tissue surface dose D_t is 2-5 Rad. Taking D_t=$3 Rad$, then $\Phi \sim 10^{11} / cm^2$.

In a simple picture for head scanning as shown in Fig. 5.2.1 (assume L =25 cm), consider a small volume v close to the surface being cylindrical (isotropic) and its diameter equal to the detector width w (assumed $1.5 mm$) and its height equal to the scanning slice thickness (assumed $10 mm$), then the total number of photons across the volume (cross section $0.15 cm^2$) is

1.5×10^{10}. This number of photons is contributed from all of the projections each having one measurement passing through the small volume. The contribution from each depends on the attenuation length.

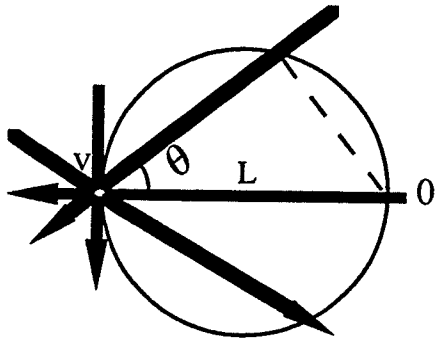

Fig. 5.2.1 A simplified view of head scanning in CT, where v is a small cylindrical volume close to skin surface.

Beams from the right hand side ($|\theta|\leq 90^0$) will be attenuated by a length $L\cos\theta$ while beams from the left hand ($|\theta|\geq 90^0$) are free of attenuation. For a total of P projections and a number of photons per measurement N_0, the number of photons from all the left beams is simply $n_l = N_0 P/2$.

The number of photons from all the right beams is approximately

$$n_r = 2\int_0^{P/4} N_0 e^{-\mu L\cos\frac{2\pi p}{P}} dp$$
$$= 2N_0 P\int_0^{1/4} e^{-\mu L\cos 2\pi y} dy \qquad (5.9)$$

For 60 *KeV* x-ray, $\mu\sim 0.20/cm$, $\mu L = 5$. A numerical calculation of the integration in (5.9) gives 0.0335 and hence n_r=0.067N_0P. The total number of photons reaching the small volume is hence $n_l + n_r$ =0.567N_0P. Commonly, a total of $P\approx 1000$ projections is used in clinical CT. Therefore the number of photons per measurement is $N_0\sim 2.65\times10^7$.

5.3.2 Calculation from the contrast detection threshold of CT

CT scanners allow measuring the attenuation coefficient of tissues with an accuracy of ±0.5% [Morgan, Hendee]. This means that for 60 *KeV* x-rays, μ can be measured to an accuracy of $\Delta\mu = 0.001/cm$ for $\mu \sim 0.20/cm$. Suppose, as shown in Fig. 5.2.2, we want to analyze a circular object with a constant μ except for a small square object along a diameter, whose size equals the detector width w and whose attenuation coefficient is μ-$\Delta\mu$. With an incident number of photons n_0, the detected photon number is greater than that detected without the small object by an amount

$$\Delta n = n_0 e^{-\mu L}(e^{\Delta\mu \cdot w} - 1) = n_0 \cdot e^{-\mu L}\Delta\mu \cdot w = n\Delta\mu \cdot w \qquad (5.10)$$

The number n of photons arriving at the detector will follow the Poisson distribution with a standard deviation equal to $\sqrt{n}$. To be able to detect the difference of the small square from the background, Δn must be greater than $\sqrt{n}$:

$$n\Delta\mu \cdot w > \sqrt{n} \qquad (5.11)$$

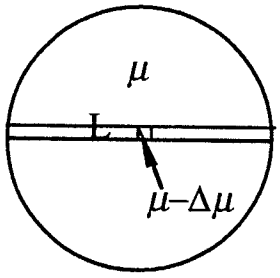

Fig. 5.2.2 A circular object with a constant attenuation coefficient of μ, except for a small square object along a diameter whose attenuation is μ-.

Further, in accordance with Rose model [Rose, Hasagawa] (see section 2.4.3), if the difference $\Delta\mu$ is to be reliably detected, Δn should be k times greater than $\sqrt{n}$, or $n\Delta\mu \cdot w = k\sqrt{n}$. Then the detected photon number must be

$$n = \frac{k^2}{w^2(\Delta\mu)^2} \tag{5.12}$$

For k=2.5 [Schnitzler], $w = 1.5mm$, $n = 2.8\times10^8$ or the number of incident photons $n_0 = ne^{\mu L} = ne^{5.0} = 4.1\times10^{10}$. It was shown [Brooks] that these n_0 counts can be divided independently among the total number of P projections. For P=1000, the number of the incident photons for a single measurement is

$$N_0 = n_0 / P = 4.10\times10^7$$

From the two different estimation methods, we conclude that the number of incident photons per measurement in the real CT scanner is $(2-5)\times10^7$.

5.4 The number of samples in one projection

Suppose a sampling interval of d is used, then the number of samples in a projection is

$$n_s = L / d \tag{5.13}$$

Note that, in principle, d is not equal to the width of the detector w_d. A detailed analysis based on sampling theory [Barrett] gives that

$$d \le w_d / 2 \tag{5.14}$$

That is, the detector-source line of sight should be stepped in increments of half the detector width or less. We assume the detector width w_d=1 mm and the data sampling increment d=0.5mm. Therefore for head scanning of L=25 cm, we need 512 samples per projection. The reconstructed matrix is hence 512×512.

CT artifacts due to digital sampling (particularly, undersampling in both radial and azimuthal directions), such as the aliasing streaks and Moire pattern etc. have been discussed in detail and demonstrated in [Kak 1984].

Many important points were also in section 6 of [Brooks 1976b] and Hendee [1983]. Some of the artifacts, either from the limited number of projections or from the limited number of measured data per projection, are also shown in [Krestel] from real x-ray CT scans.

5.5 The number of projections

We discuss the azimuthal sampling (the number of projections) by considering from: 1. sampling theory and 2. determinacy of the reconstruction problem.

In order to completely sample the Fourier space of an object having a width of L, the spacing between samples in azimuthal direction must be at least $\Delta f = 1/L$. Considering the highest spatial frequency is $f_{\max} = 1/(2d)$, the angle $\Delta\phi$ between two adjacent projections should be

$$\Delta\phi = \frac{\Delta f}{f_{\max}} = \frac{2d}{L} \qquad (5.15)$$

Hence the number of azimuthal sampling (projections) n_ϕ^s, which relates the number of sampling per projection n_s, is

$$n_\phi^s = \pi / \Delta\phi = \pi L / (2d) = \pi n_s / 2 \qquad (5.16)$$

From a different point of view, reconstruction is also a problem of solving a large linear system with a total of $\pi n_s^2 / 4$ unknown pixel values inside the circle containing the object. For n_s measurements made in each projection, $\pi n_s / 4$ projections should be taken if the equations are to be determined. With more scans the system is overdetermined; with fewer it is underdetermined. This number is just half of the n_ϕ^s in (5.16). The reason is that the azimuthal sampling is non-uniform. Meeting the Nyquist criterion requires the periphery of the circle being adequately sampled. The interior is

unavoidably oversampled [Barrett]. In x-ray CT, the projection number is even more than n_ϕ^s. For example, in the Siemens Somotom Plus-S CT model [1991], the projection number is as high as 1254. Brooks [1976] thought that the extra projections do not yield independent information but rather help to improve the statistics. In this simulation work, we decided that three different number of projections, $\pi n_s/2$, $\pi n_s/4$, and $\pi n_s/8$, would be tested. For n_s=512, they are 800, 400 and 200, respectively. The underdetermined situation happens in cases where the data is either inherently limited or when the dose must be minimized [Gordon 1976].

5.6 Low contrast detectibility (SNR)

We designed a simulated phantom as shown in Fig. 5.6.1(a) to simulate the low contrast detection of CT. The out-most circle is bone (CT# 255) and the inside region is tissue (CT# ~128). The air has a CT# of ~0.

The phantom is digitized into 20 pixels/cm, with a total attenuation of ~2560/cm in CT#. Therefore for tissue attenuation μ~0.2/cm, the scaling factor k in Eq.(5.3) is 1/12800. This value also applies for phantoms in the next few sections. Fig. 5.6.1(b) displays the central part of the phantom windowed at a CT# of 124 with a width of 12. There are 5 low contrast disks: each has a difference in CT# against its background (CT# 127) equal to its index number, i.e., 1 to 5 units. The diameter of these disks is 2.3 cm. Disk 1 has a contrast value of 1/255 = 0.4%, close to the detection limit 0.5% of x-ray CT.

We measured the SNR of Disk 1 versus the number of photons per measurement from the raw reconstructed image and plotted the results in

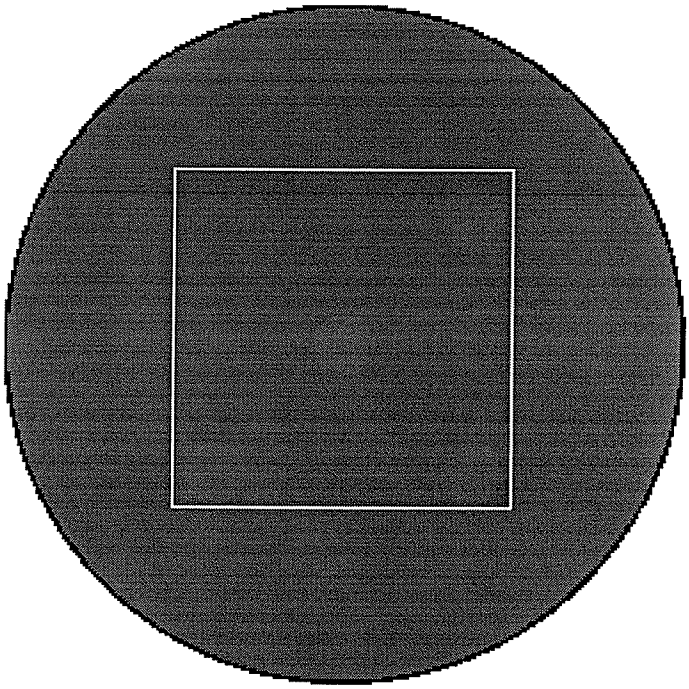

(a)

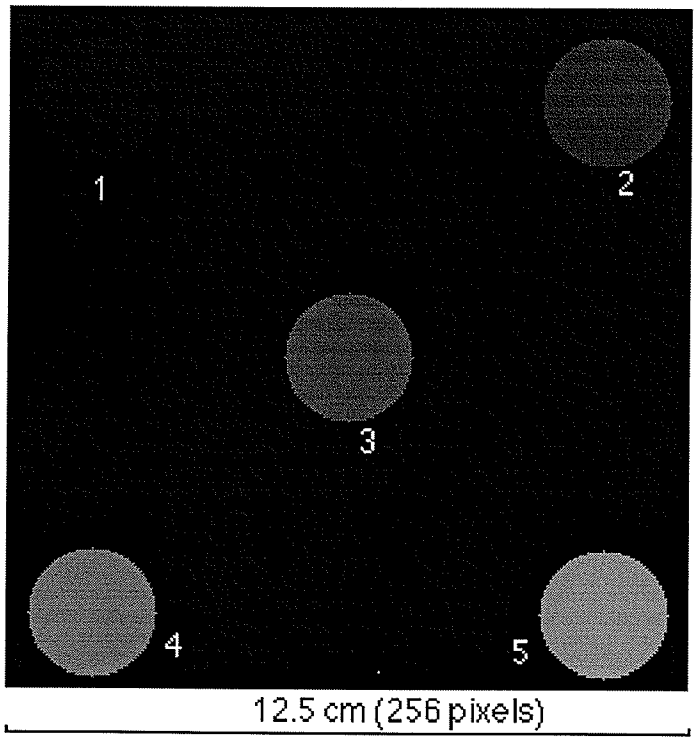

(b)

Fig. 5.6.1 (a) A low contrast CT phantom containing 5 low contrast disks (25 cm in diameter, image size 512x512). Since the disks have contrast ≤ 2% against the background, they are difficult to perceive. The central part containing the disks is windowed to a small range of gray level in (b) (center: 124, width: 12) to show an enhanced visual contrast.

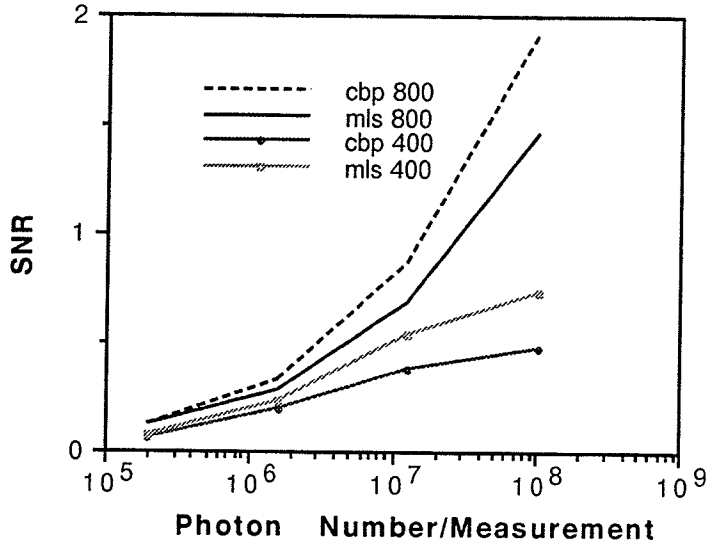

Fig. 5.6.2 Plots of the SNR of Disk 1 versus the number of photons per ray for both the 1-iteration MLS and CBP, each with 2 different number of projections: 800 and 400.

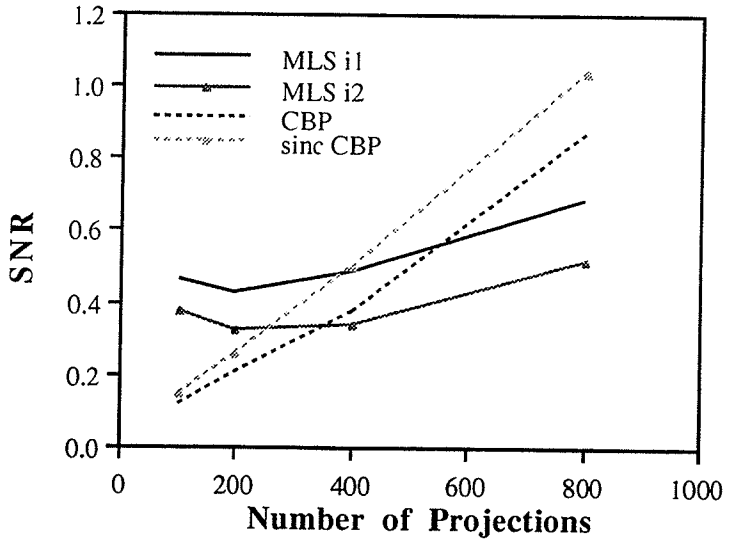

Fig. 5.6.3 Plots of the SNR of Disk 1 versus the number of projections for 1 and 2-iteration MLS as well as for CBP and *sinc* CBP, with photons per measurement equal to 1.28×10^7.

Fig. 5.6.2, for both 1-iteration MLS and CBP. The reconstructions are from two different numbers of projections: 800 and 400. With 800 projections, CBP produces a higher SNR value than MLS, but with 400 projections, the result is the opposite. We observed that the SNR reduces as the projection number decreases. It was known that the typical standard deviation of the early EMI scanner is 3.8 HU [Brooks]. Considering a 0.4% detection limit, or 4HU for the early -500 to +500 range (now is -1000 - to 1000), the SNR of the EMI scanner is around 1.0. In the next chapter, we will see that the SNR of a Siemens Somotom-Plus CT is also about 1.0 for the 0.4% detection limit. These threshold SNR values fall in the range of our calculation here, indicating that this simulation study matches the real CT dosage and noise conditions. Conversely, from the CBP's curve for 800 projections in Fig. 5.6.2, a SNR of 1.0 will require a number of photons per measurement being about (2-3)x10^7. This number is also close to those we estimated in section 5.2 above. The other four disks also show consistent SNR values versus the disk contrast (see Fig. 7.2.2, the MLS curves).

Fig. 5.6.3 shows how the SNR of Disk 1 varies with the number of projections for 1 and 2-iteration MLS as well as for CBP and *sinc* CBP, with the photons per measurement at 1.28x10^7. The 2-iteration MLS generates more noise. The *sinc* filter provides larger SNR for CBP, especially at larger number of projections. The trends of these curves are consistent with those seen in Fig. 4.2.5(b) and 4.3.4 from real data, since the larger the standard deviation, the smaller the SNR.

Fig. 5.6.4 shows the central part of the phantom reconstructed by (a) 1-iteration MLS, (b) CBP and (c) *sinc* CBP, from 800 projections and windowed the same as Fig. 5.6.1(b) did (photons per measurement: 1.28x10^7). Fig. 5.6.5 shows another three images with just 200 projections.

Apparently, the MLS version in Fig. 5.6.4 is more noisy than both the CBP and *sinc* CBP images, but in Fig. 5.6.5, the situation is just opposite (*sinc* CBP didn't show improved smoothness over CBP). The visual appearance agrees with the SNR measures.

We also measured the noise histograms inside Disk 1 for both the 1-iteration MLS and CBP, each from two different number of projections: 800 and 200. The results are shown in Fig. 5.6.6 and the distributions are visually close to Gaussian. We also tested the dependence of 1-iteration MLS on the initial starting projection. For a sample of 8 reconstructions, the mean SNR from 800 projections is 0.705 ± 0.017 and the mean SNR from 200 projections is 0.530 ± 0.037.

We calculated the mean SNR of Disk 1 and its standard deviation from a sample of 10 reconstructions for both 1-iteration MLS and CBP. In Fig. 5.6.7 we plot the ratio of MLS's mean SNR over that of CBP versus the number of projections (photons per measurement: 1.28×10^7). The fractional error of the ratio (summing the standard deviation over mean for both the MLS and CBP) is ~10%.

5.7 The contrast detail (CD) evaluation

A contrast-detail (CD) phantom of $25cm$ in diameter was designed and is shown in Fig. 5.7.1(a) for a contrast-detail evaluation of CT reconstruction algorithms. The phantom consists of 6 sets of disks. Each set has 6 disks of the same size but with different contrast. The smallest contrast is 0.4% and the largest is 2.4%. The smallest disk size is $0.2cm$ and the largest is $2cm$. The central part, windowed the same as Fig. 5.6.1(b), is shown in Fig. 5.7.1(b).

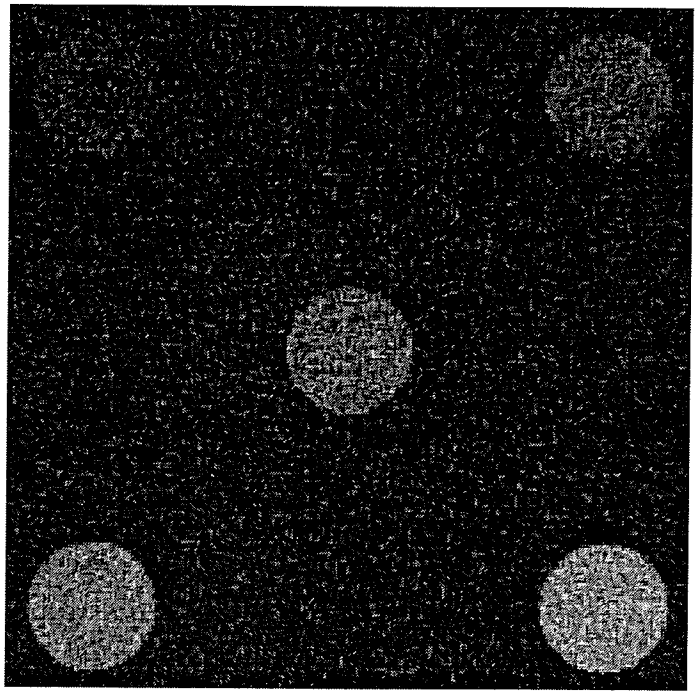

(a) 1-iteration MLS

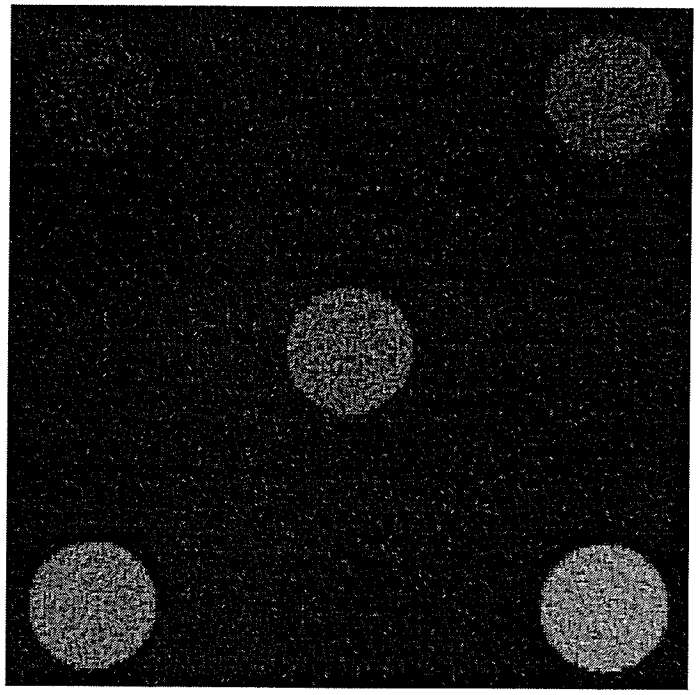

(b) CBP

Fig. 5.6.4 The central part of the low contrast phantom reconstructed by (a) 1-iteration MLS, (b) CBP and (continue on the next page)

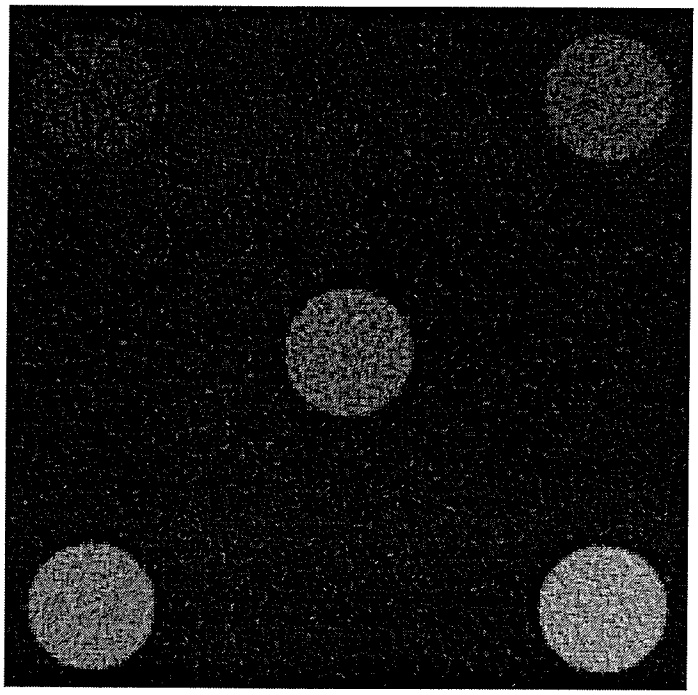

(c) *sinc* CBP

Fig. 5.6.4 (continued from the last page) (c) *sinc* CBP, from 800 projections and windowed the same as Fig. 5.6.1(b) did (photons per measurement 1.28×10^7). Note that although Disk 1's contrast (0.4%) is less than the detection limit (0.5%), it is still readable in (b) and (c) for its relatively large size. (In a real CT scan as shown in Fig. 6.3.1c, a "tumor" of 0.4% contrast is also visible.) Disks of sizes less than 0.4cm are difficult to perceive (see the bottom left two disks in Fig. 5.7.3b in the contrast detail phantom). The threshold detection contrast for a 2cm disk is ~0.2% (see the contrast detail diagram in [McDavid]).

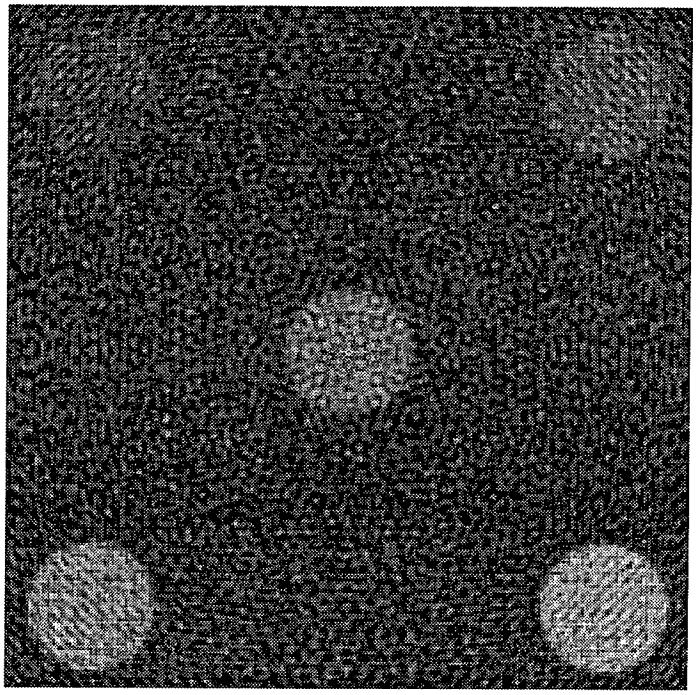

(a) 1-iteration MLS

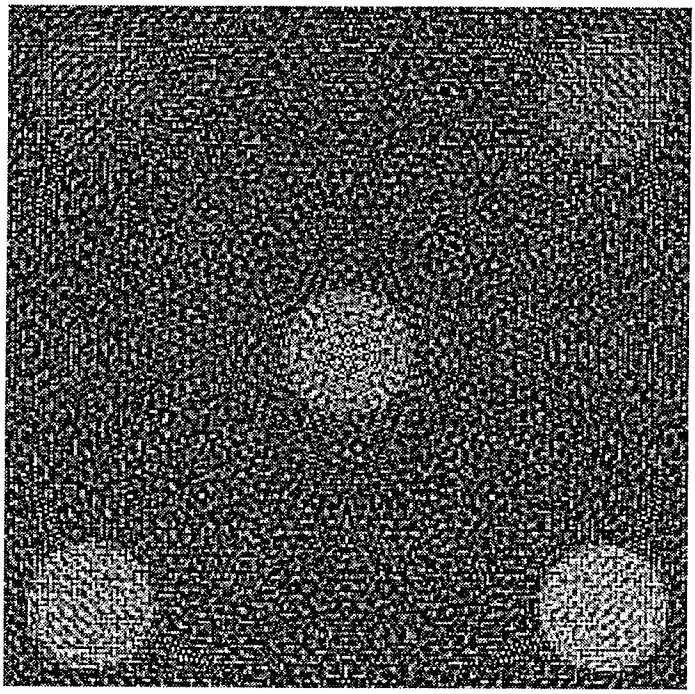

(b) CBP

Fig. 5.6.5 The central part of the low contrast phantom in the reconstructions by (a) 1-iteration MLS, (b) CBP and (continue on the next page)

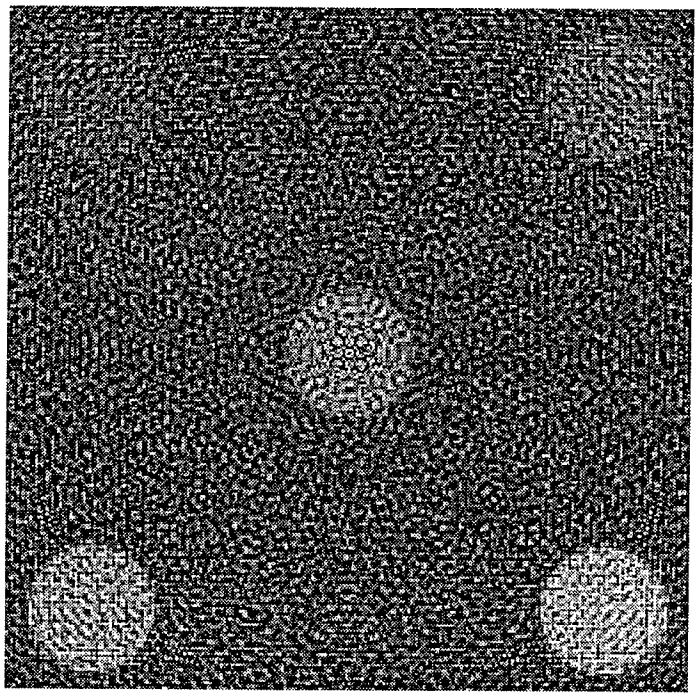

(c) *sinc* CBP

Fig. 5.6.5 (continued from the last page) (c) *sinc* CBP, from 200 projections and windowed the same as Fig. 5.6.1(b) did (photons per measurement 1.28×10^7).

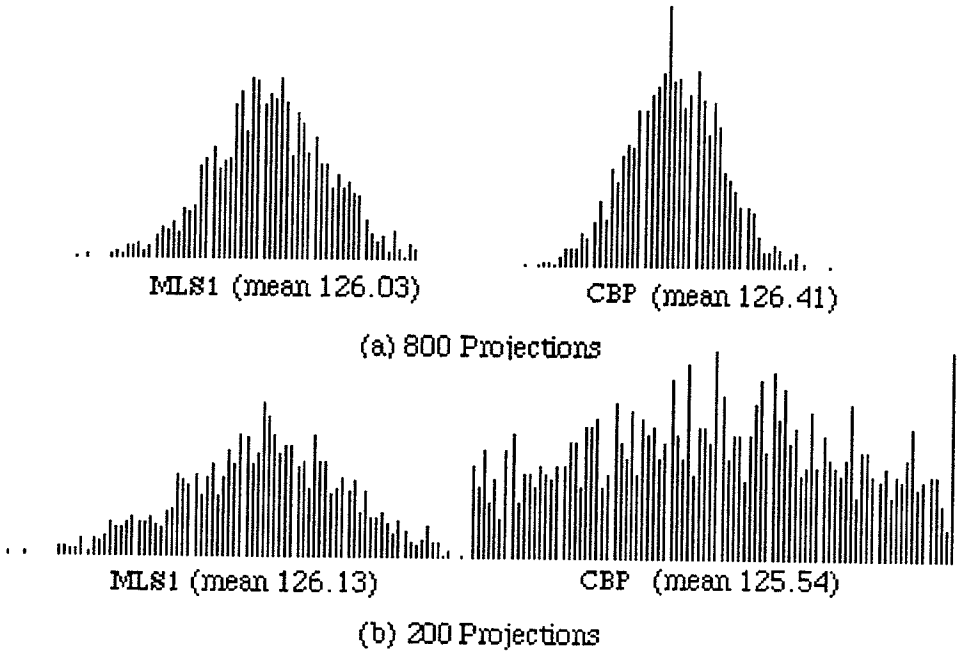

Fig. 5.6.6 Noise histograms in Disk 1 in both the 1-iteration MLS and CBP reconstructions, from (a) 800 and (b) 200 projections.

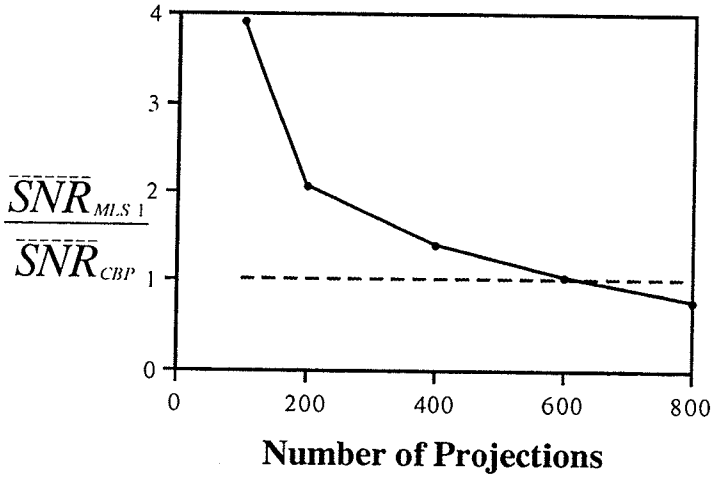

Fig. 5.6.7 Plot of the ratio of 1-iteration MLS's mean SNR over that of CBP for Disk 1, from a sample of 10 reconstructions of the low contrast phantom, versus the number of projections (photons per measurement: 1.28×10^7). The fractional error of the ratio of SNR (summing the ratio of standard deviation over mean) is ~10%.

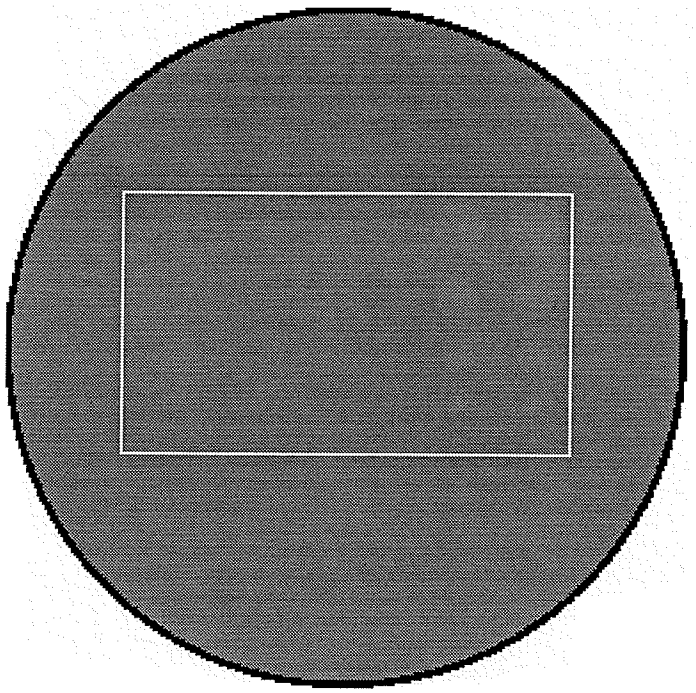

(a)

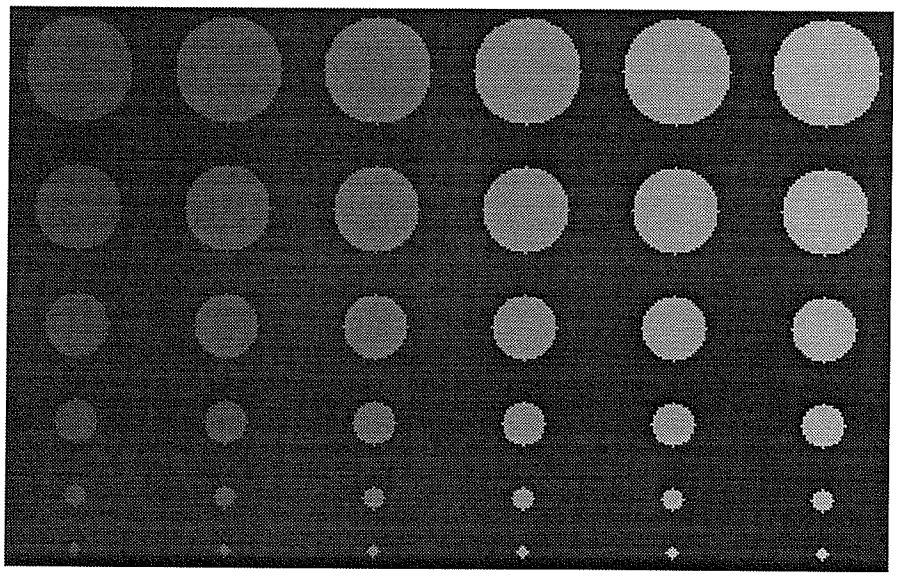

(b)

Fig. 5.7.1 (a) A contrast detail CT phantom containing 6 sets of low contrast disks (25 cm in diameter, image size 512x512). Since the disks have contrast $\leq$ 2.4% against the background, they are hard to perceive. The central part containing the disks is windowed to a small range of gray level in (b) (center: 124, width: 12) to show enhanced visual contrast.

Fig. 5.7.2 shows four images of the central part from 100 projections, with the photon number per measurement being 1.28×10^7. Images in (a) and (b) are from 1 and 2-iteration MLS, respectively. (c) is from CBP and (d) is from *sinc* CBP. Clearly, 1-iteration MLS produces much more readability on the lower contrast disks as well as the small size ones than CBP and *sinc* CBP do. The 2-iteration MLS, however, doesn't show much difference from its 1-iteration counterpart for the lower contrast disks in the left two columns, especially the smaller ones. For the higher contrast disks, it appears that 2-iteration MLS even produces a little better readability, at least for smaller disks. This is because 2-iteration MLS yields larger high contrast resolution. The *sinc* CBP image in Fig. 5.7.2(d) doesn't show noticeable improved smoothness over its CBP counterpart (c).

Fig. 5.7.3 shows three reconstructions from 800 projections, by (a) 1-iteration MLS, (b) CBP and (c) *sinc* CBP. In this case, (a) appears more noisy than (b) and (c), similar to Fig. 5.6.4. The disks in the left most column of (a) are more difficult to perceive than their corresponding ones in (b) and (c). The *sinc* filter also produce noticable smoothness over CBP such that the left most disks appear more readable. (Due to the fact that disks (signals) themselves are not properly reconstructed, using filters with even larger high frequency suppression won't yield better results than *sinc* .)

5.8 The high contrast high resolution detectibility (MTF)

Fig. 5.8.1 shows a high contrast phantom in which 5 sets of bar patterns which are consecutively doubled in size, are laid. The standard deviation inside a small square centered at each set of bar pattern, as the one drawn in the bottom-right for the largest bars, were measured in the reconstructions.

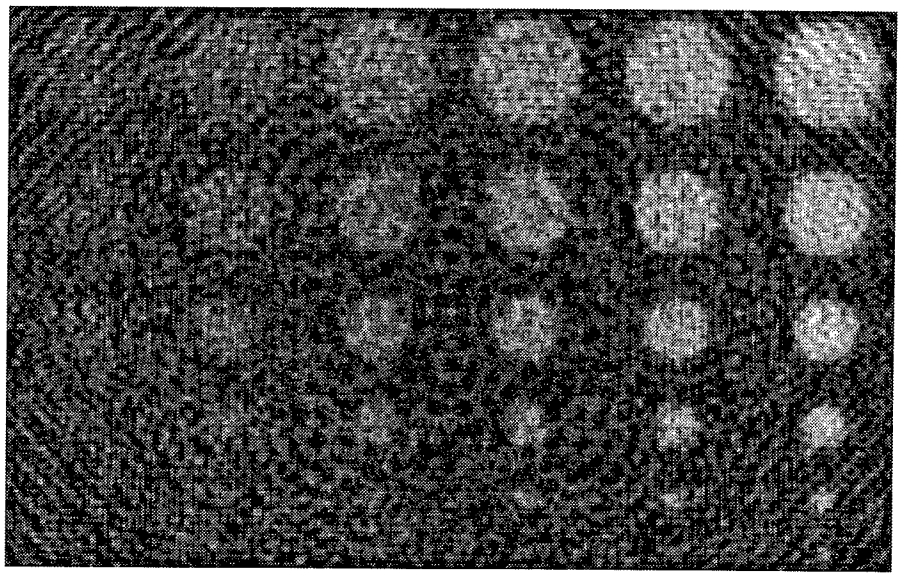

(a) 1-iteration MLS

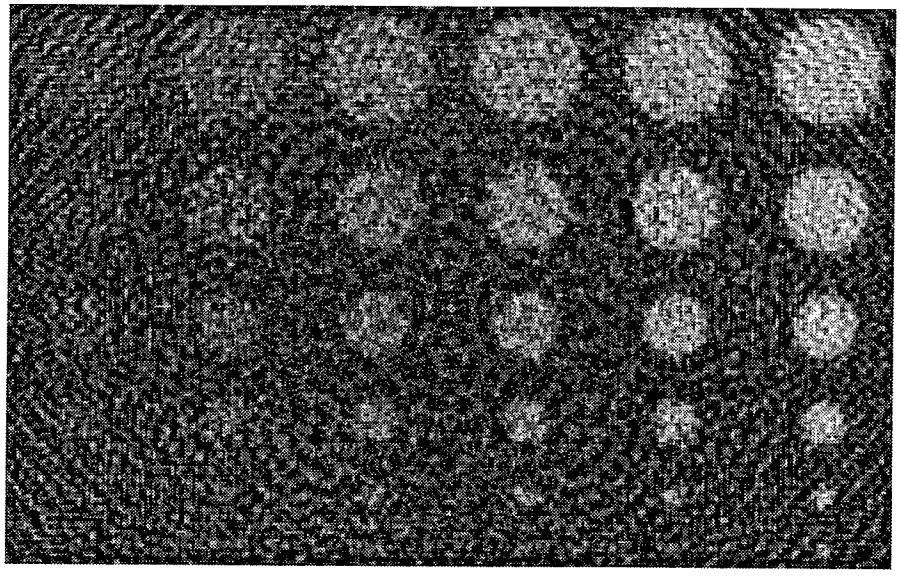

(b) 2-iteration MLS

Fig. 5.7.2 The central part of the reconstructions (windowed) from 100 projections, with the photon number per ray being 1.28×10^7, by (a) 1-iteration MLS, (b) 2-iteration MLS, (continued on next page)

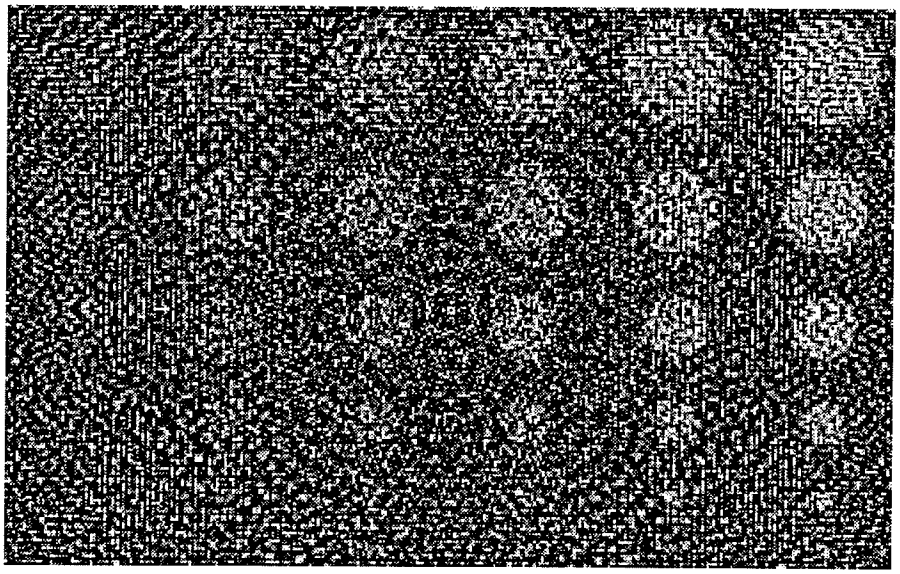

(c) CBP

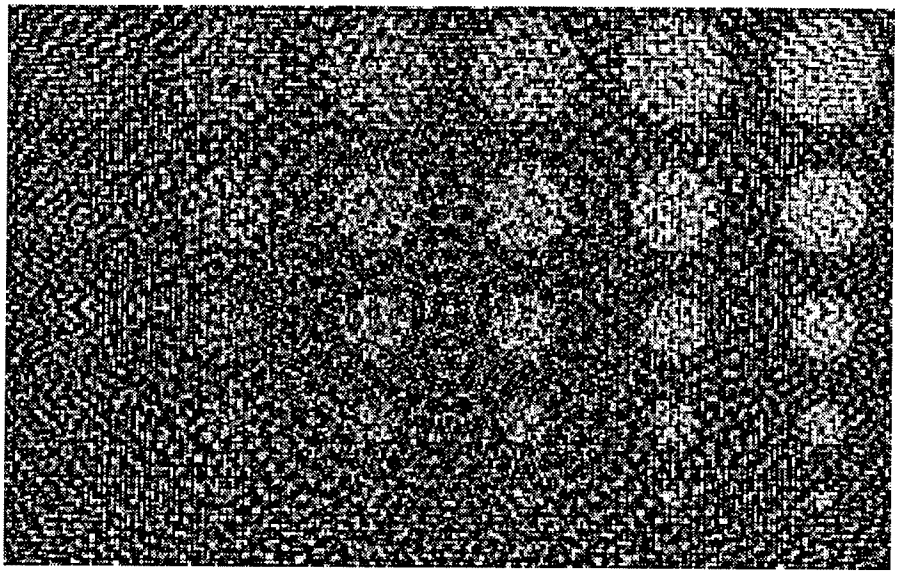

(d) *sinc* CBP

Fig. 5.7.2 (continued from the last page) (c) CBP and (d) *sinc* CBP.

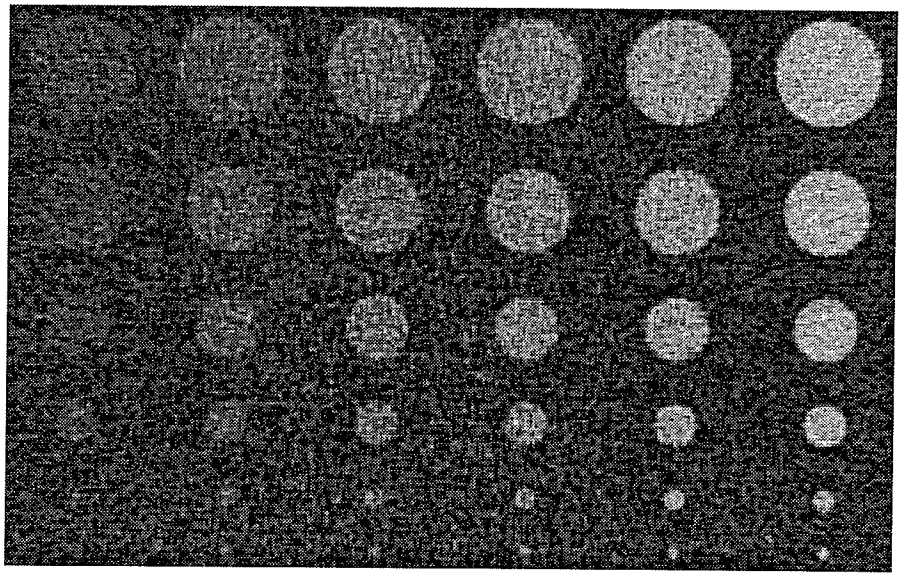

(a) 1-iteration MLS

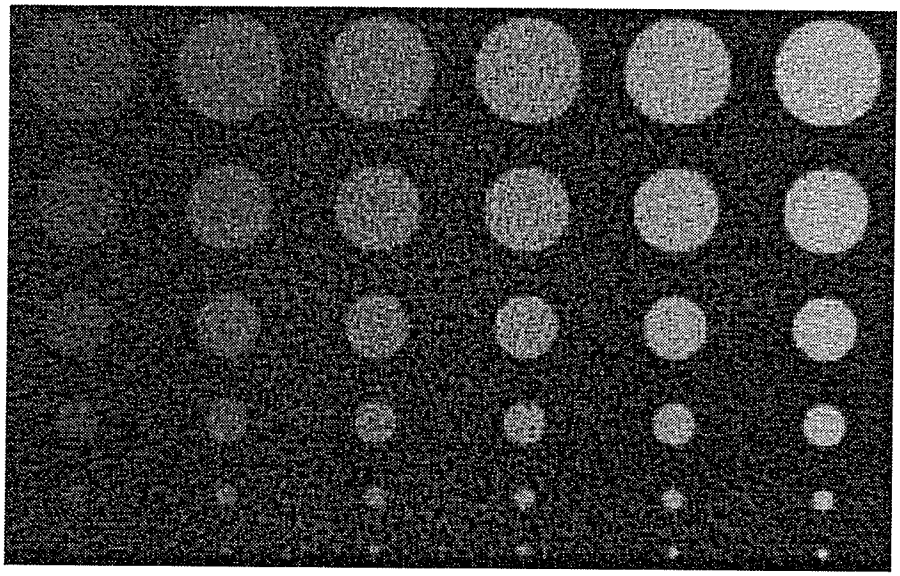

(b) CBP

Fig. 5.7.3 The central part of the reconstructions (windowed) from 800 projections, with the photon number per ray being 1.28×10^7, by (a) 1-iteration MLS, (b) CBP and

(continue on the next page)

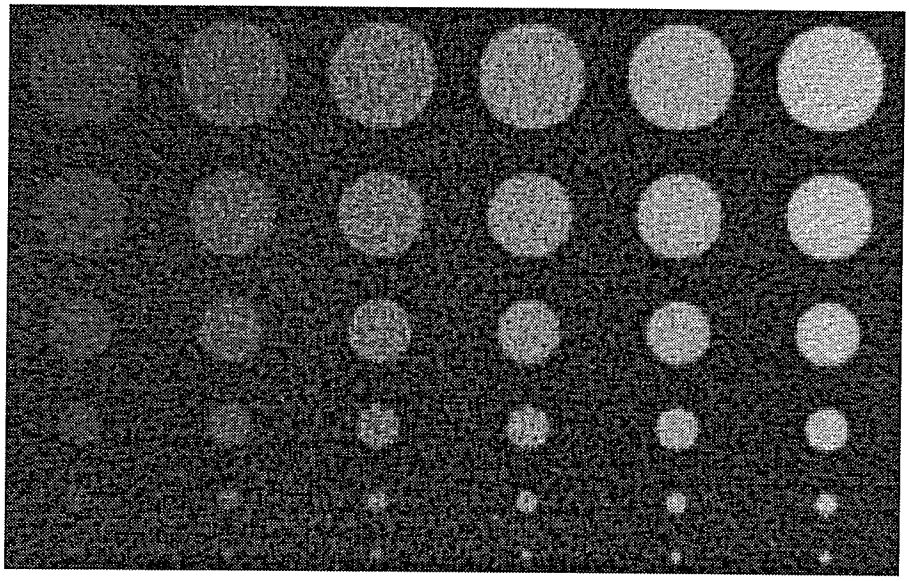

(c) *sinc* CBP

Fig. 5.7.3 (continued from the last page) (c) *sinc* CBP.

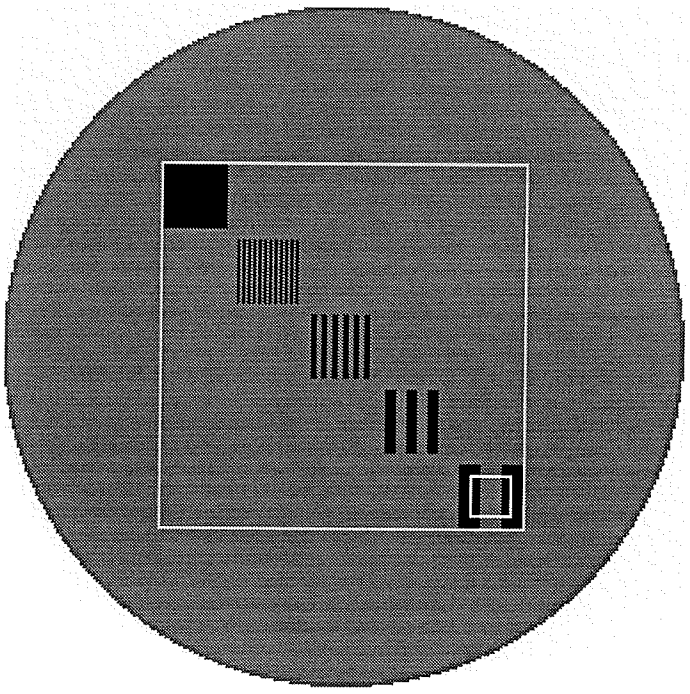

Fig. 5.8.1 A high contrast phantom of 25 cm in diameter, 512x512 pixels, in which 5 sets of bar patterns that are consecutively doubled in size (1, 2, 4, 8 and 16 pixels/bar), are laid. The standard deviation inside a small square centered at each set of bar pattern, as the one shown in the bottom-right for the largest set, will be measured in the reconstructions. The central part of the phantom containing all the bars (inside the large square) will be shown in Fig. 5.8.2 after reconstructions.

Fig. 5.8.2 shows four reconstructions from 800 projections, by (a) 1-iteration MLS, (b) CBP, (c) 2-iteration MLS and (d) *sinc* CBP. The number of photons per measurement is 1.28×10^7. Apparently the bars in the CBP versions (b) and (d) appear to have more blurring in edges than those in the MLS versions (a) and (c). The measured standard deviation of each set is then plugged into Eq. (2.24) to calculate the MTF. In Fig. 5.8.3, we plot these calculated MTF values. That MLS produces better spatial resolution is quantitatively exhibited. The largest improvement is at half of the Nyquist limit (the second set of bars from the top-left). Note that at very high frequencies near the Nyquist limit (the top-left set of smallest sizes), 1-iteration MLS is not better than CBP but 2-iteration outperforms. This can be seen from both the images in Fig. 5.8.2 and the MTF plots in Fig. 5.8.3.

In Fig. 5.8.4, we show the MTF plots for 400 projections. In this case, the 1-iteration MLS is just a little better than CBP for frequencies below half of the Nyquist limit but not above. 2-iteration MLS yields larger MTF than that of CBP at frequencies above 8 lp/cm and matches that of 1-iteration MLS for 800 projections in Fig. 5.8.3. Fig. 5.8.5 shows the images of the three smaller sets of bars (bar size 1, 2 and 4 pixels) from 400 projections, by (a) 1-iteration MLS, (b) CBP and (c) 2-iteration MLS. The visual appearance agrees with the MTF measures.

We also tested the dependence of MTF on different locations and orientations of bars. We found that the standard deviation / mean MTF is not more than 1% for all 5 sets, for both 1-iteration MLS and CBP. The results are based on a sample of 8 reconstructions (4 with changed positions and 4 with changed orientations) from 800 projections.

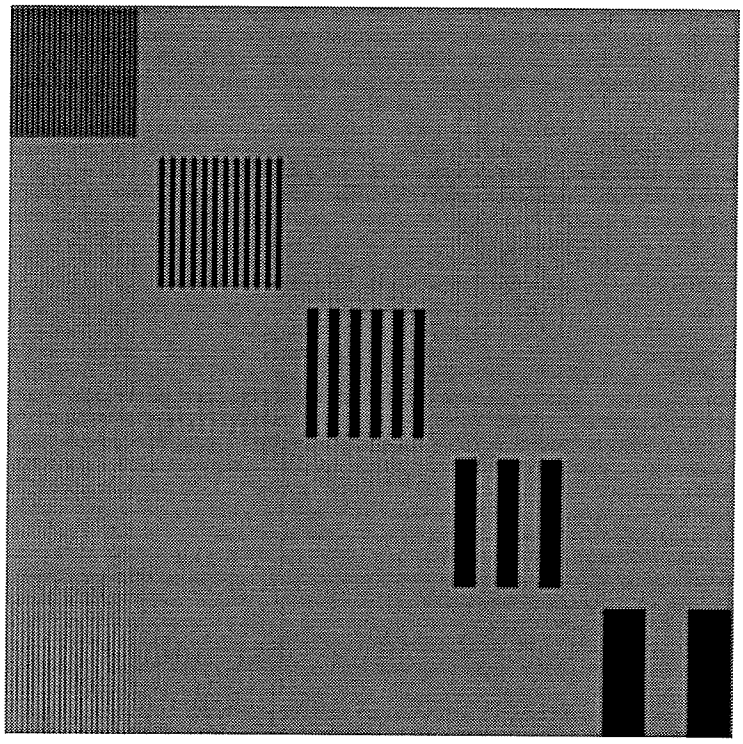

(a) 1-iteration MLS

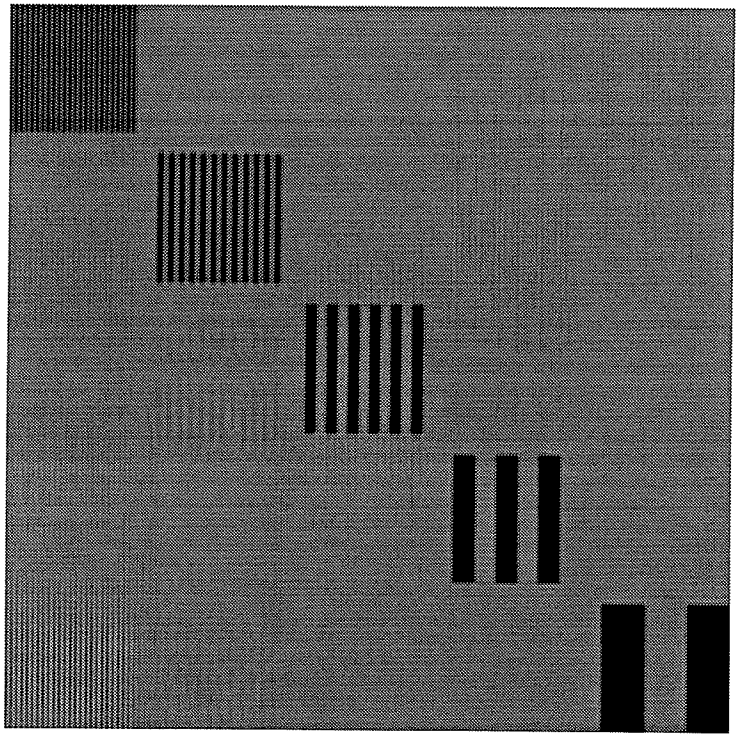

(b) CBP

Fig. 5.8.2 Reconstructions of the bar patterns from 800 projections, by (a) 1-iteration MLS, (b) CBP, (continue on the next page)

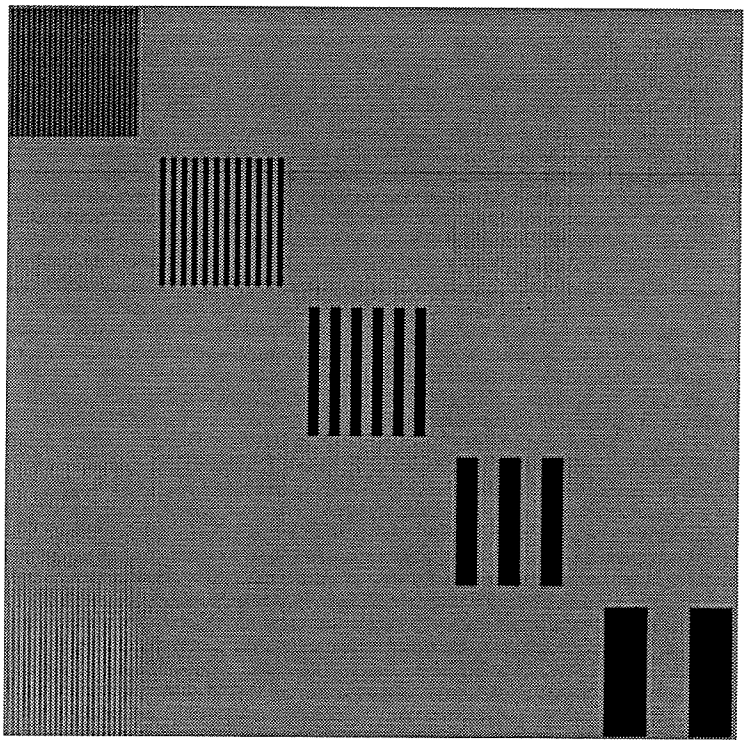

(c) 2-iteration MLS

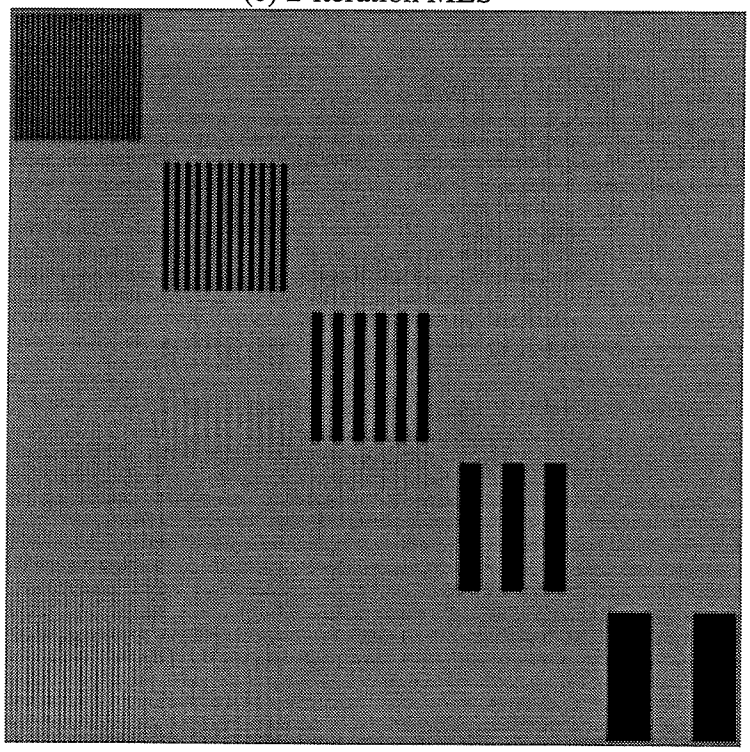

(d) *sinc* CBP

Fig. 5.8.2 (continued from the last page) (c) 2-iteration MLS and (d) *sinc* CBP. The number of photons per measurement is 1.28×10^7.

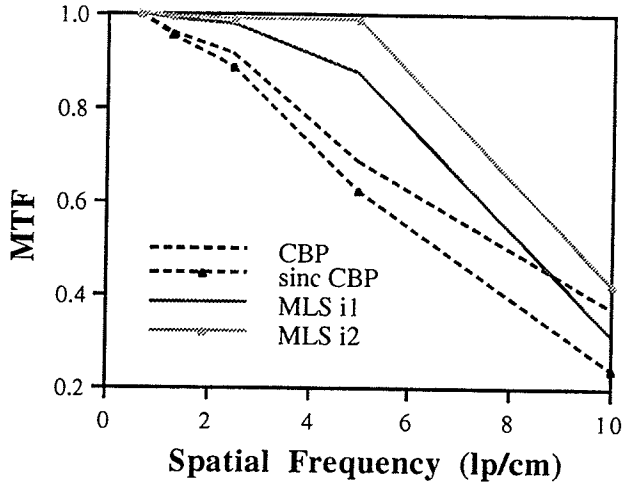

Fig. 5.8.3 Plots of the MTF (calculated from the standard deviations inside the bar patterns reconstructed from 800 projections), for 1 and 2-iteration MLS, as well as for CBP and *sinc* CBP.

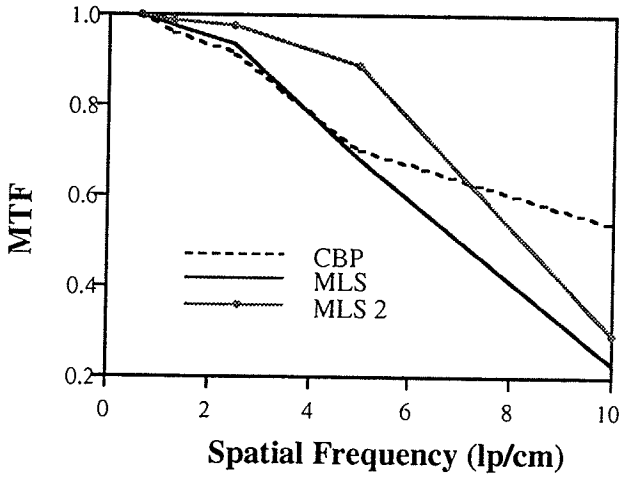

Fig. 5.8.4 Plots of the MTF (calculated from the standard deviations inside the bar patterns reconstructed from 400 projections), for 1 and 2-iteration MLS as well as CBP.

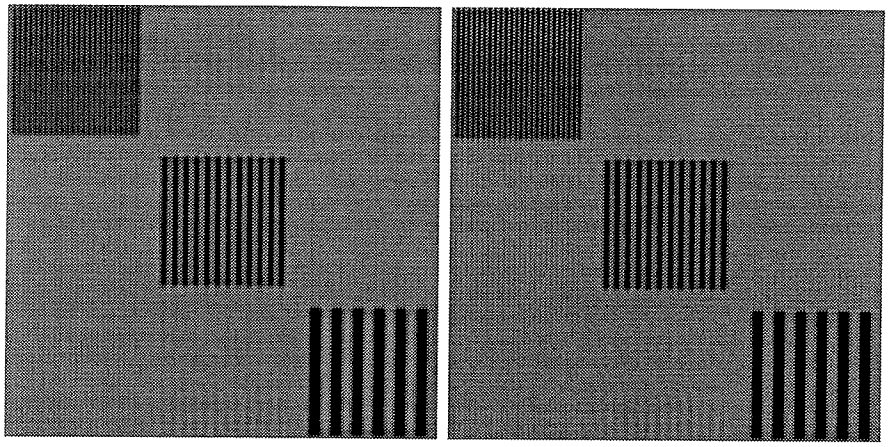

(a) 1-iteration MLS (b) CBP

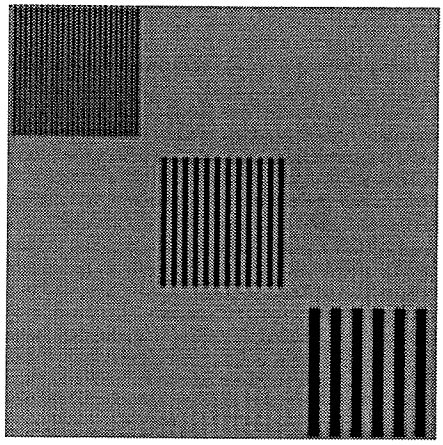

(c) 2-iteration MLS

Fig. 5.8.5 Images of the three smaller sets of bars reconstructed from 400 projections by (a) 1-iteration MLS, (b) CBP and (c) 2-iteration MLS.

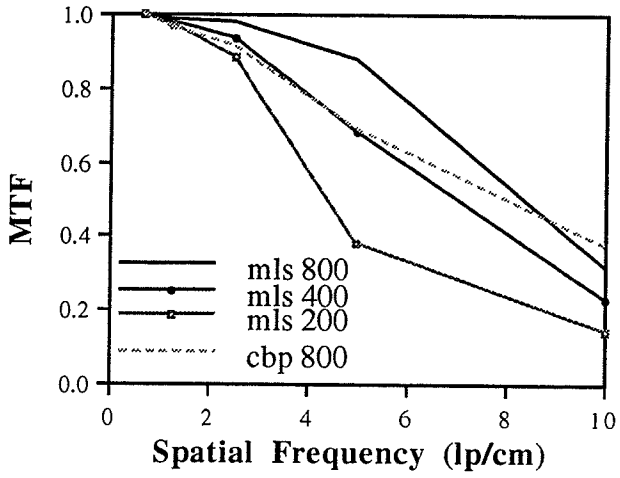

(a)

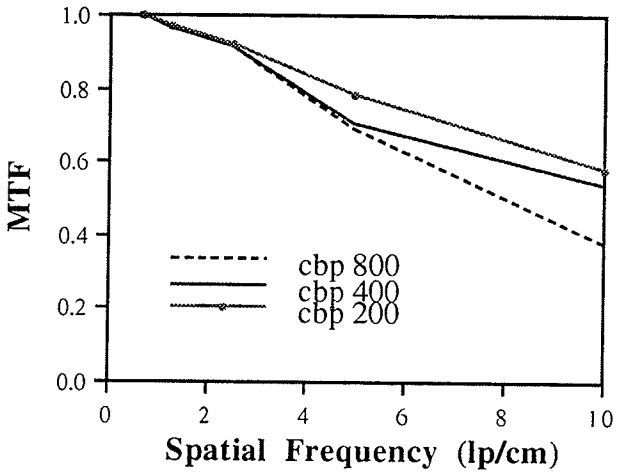

(b)

Fig. 5.8.6 Plots of MTF for three different number of projections 800, 400 and 200, in (a) for 1-iteration MLS and in (b) for CBP. The MTF of CBP from 800 projections is also plotted in (a) for comparison.

In Fig. 5.8.6, we plot the MTF for 3 different number of projections, 800, 400 and 200 together, in (a) for 1-iteration MLS and in (b) for CBP. The MTF of CBP from 800 projections is also plotted in (a) for comparison. One sees that while the MLS's MTF drop as the number of projections reduce, the CBP's do not change much (the improvement with smaller number of projections is not obvious and it is not in other measures of image qualities). This might be attributed to CBP satisfying the "Fourier central slice theorem" and to its linearity. MLS is a somewhat nonlinear algorithm.

5.9 The noise power spectrum (NPS)

We calculated the noise power spectrum following Eq. (2.18). A noise only image is obtained by subtracting the CT reconstruction of a water only phantom from its original, a method similar to that used by Kijewski [1987] and Rathee [1992] in investigating the NPS of CT scanners (they subtracted consecutive pairs of CT scans and hence the noise amplitude is doubled). A water only phantom of $25cm$ diameter is used. After doing a reconstruction (on 512x512 pixels), the subtraction of it from its original is made. Then the central 256x256 subimage in the difference image was extracted to make sure it was contained in the water region. In order to reduce the truncation errors (reducing the effects of a square window superimposed on the data such that a discrete Fourier transform is used to approximate an analytic Fourier transform [Press]), we multiplied the sub-image with a 2D "Parzen" window (similar to the one used in [Kijewski])

$$W(i,j) = 1 - \frac{[i-\frac{n}{2}]^2 + [j-\frac{n}{2}]^2}{n^2/2}$$

and then computed the 2D FFT of this subimage. The squared amplitude of the FFT was then averaged over a total of 25 images and the result was the NPS of the reconstruction.

Fig. 5.9.1 shows the NPS of (a) CBP and (b) 1-iteration MLS. (c) and (d) are (a) and (b) displayed in 3D, respectively. A total of 800 projections is used and the number of photons per measurement is 1.28×10^7. The CBP version looks the same as those in [Kijewski, Rathee], in both 2D and 3D forms, indicating that the calculation is correct. No NPS has previously been computed for CT reconstructions using the algebraic method and hence no comparison can be made.

The NPS of CBP and MLS looks quite different. The MLS's has quite large low frequency components, whereas the CBP version has few low frequency amplitudes. There is a common feature in both: NPS is affected by the digital sampling (both within the projection and angular), such that the distributions are not circularly symmetrical as predicted by the continuous theory [Wagner, Hanson]. The digital sampling causes 2-D aliasing such that the noise power amplitude is larger along 0^o and 90^o polar angles and smaller along 45^o and 135^o, as seen more clearly from the 3D versions in Fig. 5.9.1 (c) and (d). This is also the reason for a non-zero NPS at zero-frequency for CBP, as should be in the continuous model. This phenomenon was first noted by Kijewski and Judy [1987]. They derived an analytical NPS expression for CBP and then did a computer simulation of it assuming Poission statistics for the projection noise, both agree with the experimentally measured NPS from a CT scanner.

Fig. 5.9.2 shows, the same as Fig. 5.9.1(a) and (b) did, the NPS from 100 projections instead of 800. It appears that the noise energy of MLS version is more concentrated in lower frequencies whereas that of CBP is more in high

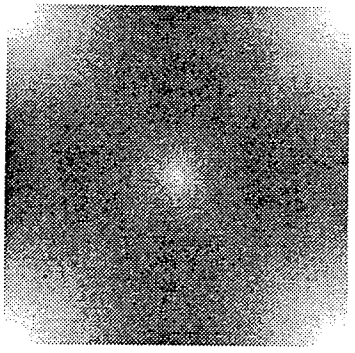

(a) CBP

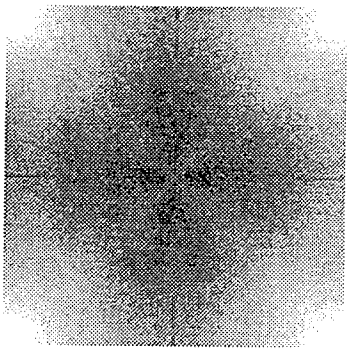

(b) 1-iteration MLS

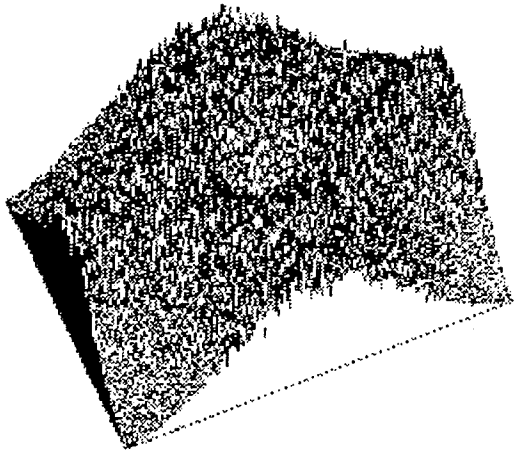

(c) CBP

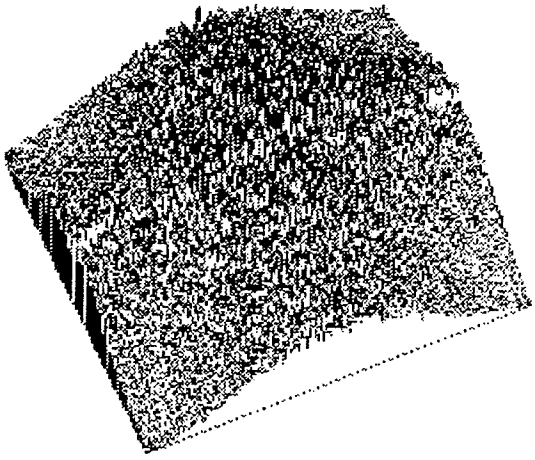

(d) 1-iteration MLS

Fig. 5.9.1 The noise power spectrum (NPS) of CT reconstructions by (a) CBP and (b)1-iteration MLS. (c) and (d) are the NPS displayed in 3D. A total of 800 projections is used and the number of photons per ray is 1.28×10^7.

frequencies. This could be part of the reason for MLS producing larger SNR than CBP when the number of projections is small.

5.10 The reconstruction accuracy measures

First we demonstrate that MLS is more accurate than CBP by showing the subtractions of reconstructions (the number of projections is 800) from original test phantoms. Fig. 5.10.1 exhibits two such subtractions for the bar pattern phantom, for (a) CBP and (b) 1-iteration MLS. Clearly, the errors of the four larger size bars in (a) appear larger in intensity than those in (b), especially the 2nd smallest set from the top-left. For the smallest set, the differences are visually about the same. These agree with the MTF measures in Fig. 5.8.3.

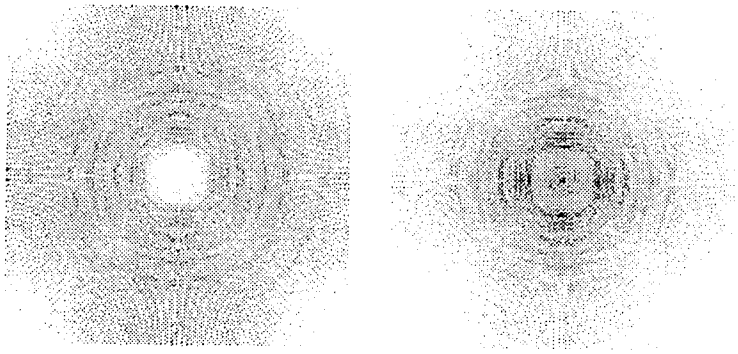

(a) CBP (b) 1-iteration MLS

Fig. 5.9.2 The noise power spectrum (NPS) of CT reconstructions by (a) CBP and (b) 1-iteration MLS, from a total of 100 projections. The number of photons per ray is 1.28×10^7.

We also measured the correlation coefficient (cc) following Eq. (3.3) and the root mean square (rms) error to quantify the reconstruction accuracy. For the low contrast phantom (see Fig. 5.6.1), Fig. 5.10.2 shows the plots of (a) cc and (b) rms error versus the number of photons per measurement from 800 projections. These criteria demonstrate that 1-iteration MLS produces more accurate reconstructions than CBP (errors occur mostly around edges), even with less than 1/10 of photon numbers per measurement. However, these global measures give us a false sense of local image quality in terms of SNR since we saw in Fig. 5.6.2 that CBP produces larger SNR than 1-iteration MLS does in the case of 800 projections. The *sinc* filter produces more accurate reconstructions for CBP only when the number of photons per measurement is less than 10^6 (otherwise it smoothes the reconstructions too much such that the accuracy is reduced.)

The cc and rms error versus the number of projections have also been quantified for 1 and 2-iteration MLS as well as for CBP, at a fixed number of photons per measurement 1.28×10^7. The results are plotted in Fig. 5.10.3 for the low contrast phantom. The 1 and 2-iteration MLS don't show much differences when the number of projections is large, and both result in better accuracy than CBP. As the number reduces to below 200 where 1-iteration MLS is less accurate than CBP, 2 iteration MLS improves dramatically. That cc and rms are somewhat opposite measures to SNR (but rather proportional to MTF) is demonstrated again.

5.11 Discussion and conclusion

In doing the simulation study, we made some implicit approximations besides those in section 5.2-5.5 such as: (1) the attenuation coefficient of

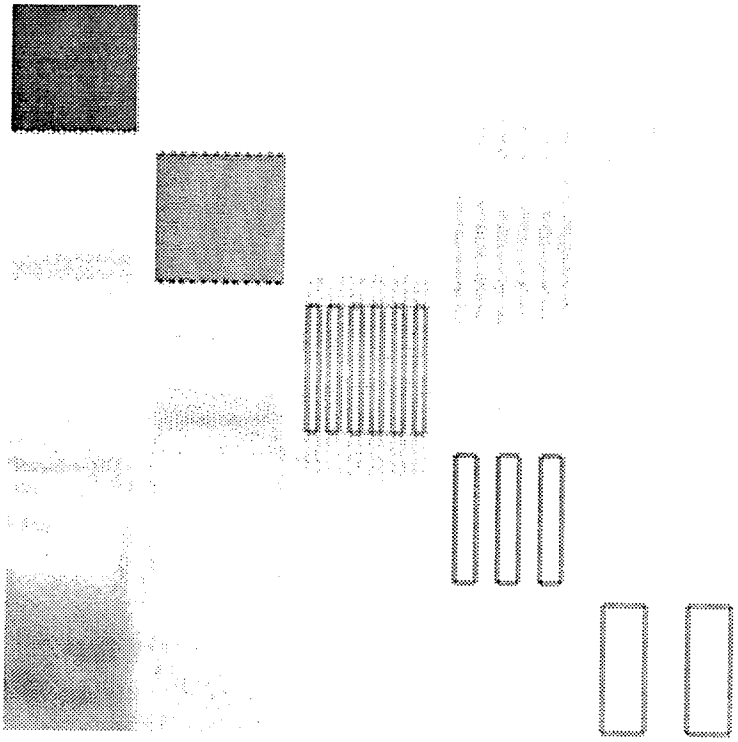

(a) CBP

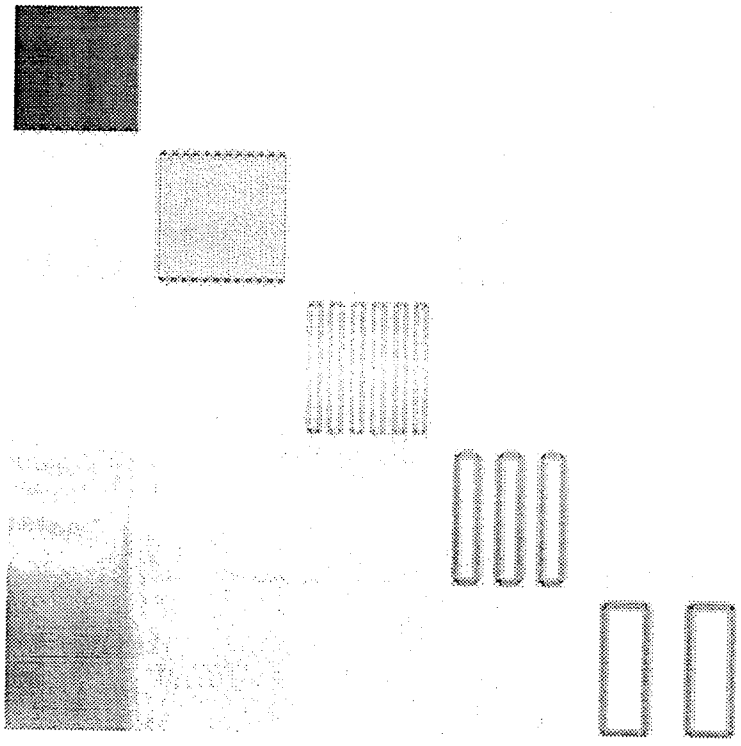

(b) 1-iteration MLS

Fig. 5.10.1 The subtractions of the reconstructions (the number of projections is 800) from the original for the bar pattern phantom for (a) CBP and (b) 1-iteration MLS.

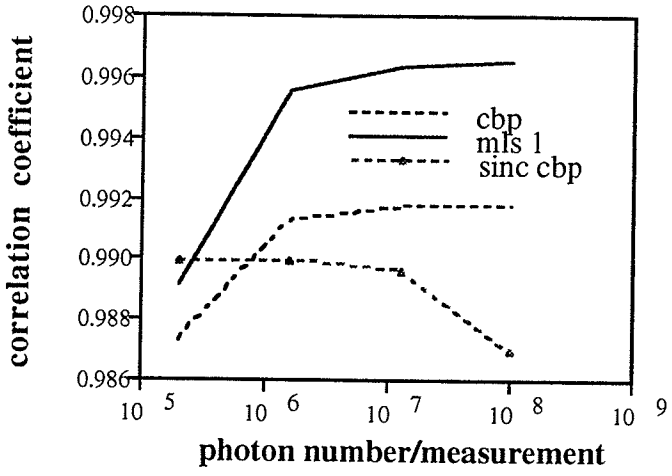

(a)

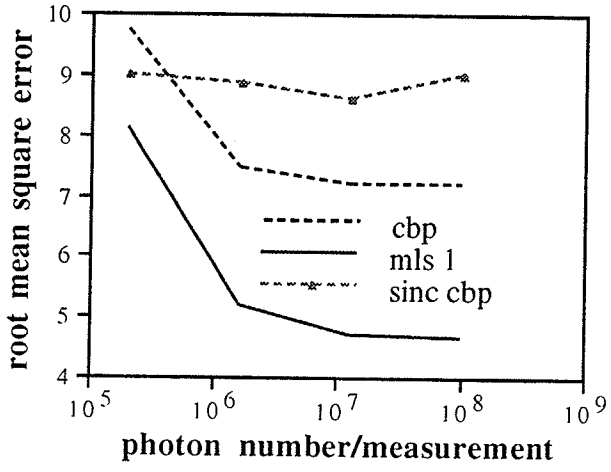

(b)

Fig. 5.10.2 Plots of the (a) correlation coefficient and (b) root mean square error versus the number of photons per measurement for the reconstructions of the low contrast phantom from 800 projections, by the 1-iteration MLS, CBP and *sinc* CBP.

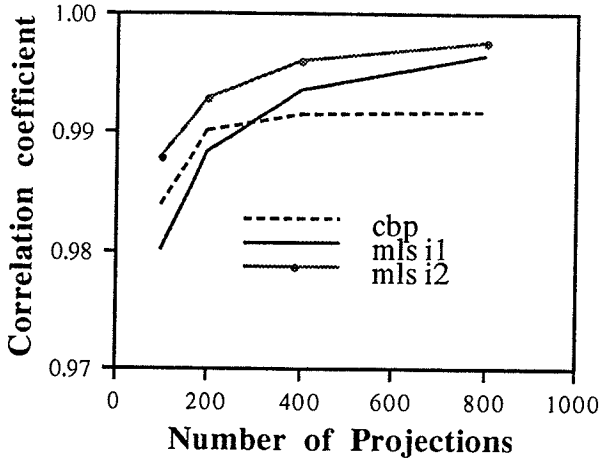

(a)

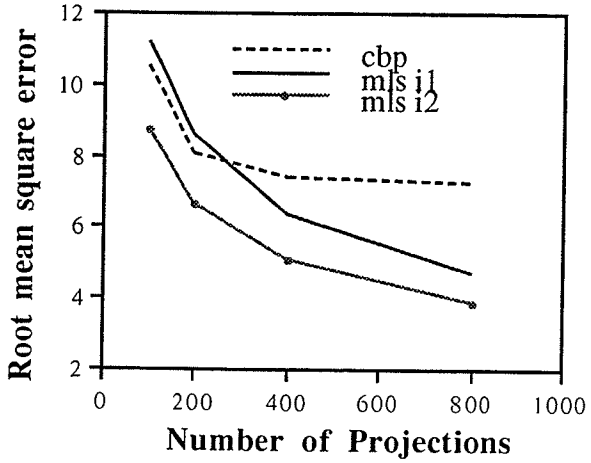

(b)

Fig. 5.10.3 Plots of the (a) correlation coefficient and (b) root mean square error versus the number of projections for the reconstructions of the low contrast phantom, by 1 and 2-iteration MLS as well as CBP.

water is used instead of that of tissue, (2) the reference detector noise is neglected, (3) beam scattering is completely eliminated. However, at least based on our calculated SNR, which is consistent with the values of real CT scanning, these approximations are acceptable.

In conclusion, MLS produces larger high contrast resolution in cases when the number of projections is taken above half of that required by the sampling criterion. In the low contrast detection, CBP produces larger SNR when the number of projections is taken to satisfy the sampling criterion (the number is 800 for a 512x512 image). But even in this case, the SNR of MLS may be improved by applying a low pass filter such as *sinc* to smooth the projection data prior to reconstruction, and further, due to the nonlinearity of MLS, better spatial resolution may still be achievable. When the number of projections is less than 400, 1-iteration MLS produces a larger SNR than both CBP and *sinc* CBP. Note that the SNR is only calculated from a uniform "tumor" against its uniform background - an ideal situation. If there are small, sharp details in the background, as we have seen in Fig. 4.2.2(b) and (c), then CBP will be affected more by the influence of edge spreading or cluttering.

From the test results of this chapter, we conclude that dose reduction in CT can be made in two cases by using MLS ART instead of CBP. 1. When the spatial resolution is of primary concern, reduce the number of projections from 800 down to 400 (see Fig. 5.8.4). The 2 or 3-iteration MLS ART will produce spatial resolutions as better as that from CBP using 800 projections. 2. In cases where limited number of projections can be taken, 1-iteration MLS ART will provide a few times more dose efficiency than CBP for low contrast object detection. For example, in the pair of SNR curves in Fig. 5.6.2 for 400 projections, 1-iteration MLS need ~1/10 CBP dosage (i.e.,

1/10 photon number per measurement: from 10^8 down to 10^7) to produce a same SNR value.

References

Barrett H. H. and W. Swindell, *Radiological imaging, the theory of image formation, detection and processing* (Academic Press), Vol. 2, 1981.

Brooks R. A. and G. Di Chiro, Statistical limitations in x-ray reconstructive tomography, *Med. Phys.* 3, 237-240, 1976.

Brooks R. A. and G. Di Chiro, Principles of computer assisted tomography, *Phys. Med. Biol.* 21, 689-732, 1976b.

Cohen G. and F. A. DiBianca, The use of contrast-detail-dose evaluation of image quality in a computed tomographic scanner, *Journal of Computer Assisted Tomography* 3, 189-195, 1979.

Goodsitt M. M., Beam hardening errors in post-processing dual energy quantitative computed tomography, *Med. Phys.* 22, 1039-1048, 1995.

Gordon R., Dose reduction in computed tomography. Guest Editorial, *Investigative Radiology* 11, 508-517, 1976.

Hanson K. M., Detectibility in computed tomographic images, *Med. Phys.* 6, 441, 1979.

Hasegawa B., *The physics of medical x-ray imaging*, 2nd Ed., Medical Physics Publishing, 1991.

Hendee W. R., *The physical principles of computed tomography,* 1st ed., Little Brown, Boston, 1983.

Hobbie R. K., *Intermediate Physics for Medicine and Biology,* 2nd Ed., John Wiley & Sons, 1988.

Johns H. E., *The physics of radiology,* 4th Ed., Springfield, Ill., U.S.A.: Charles C. Thomas, 1983.

Kak A. C., Image reconstruction from projections *Digital imaging processing techniques* 111-170, Ed Ekstrom M. P., Academic Press Inc., 1984.

Kijewski M. F. and P. F. Judy, The noise power spectrum of CT images, *Phys. Med. Biol.* 32, 565-576, 1987.

Krestel E., *Imaging systems for medical diagnostics*, Siemens Medical Division, 1991.

Mazur E., *Numerical simulation of low dose CT scanning*, Ph.D. thesis, University of Manitoba, 1993

Morgan C. S., *Basic principles of computed tomography*, University Park Press, Baltimore, 1983.

Press W. H., *Numerical recipes: the art of scientific computing (FORTRAN version)*, Cambridge, New York , Cambridge University Press, 1989.

Rathee S., Z. J. Koles and T. R. Overton, Image restoration in computed tomography: restoration of experimental CT images, *IEEE Trans. Med. Imaging* 11, 546-553, 1992.

Riederer S. J., The noise power spectrum in computed x-ray tomography, *Phys. Med. Biol.* 23, 446-454, 1978.

Schnitzler A. D., Image detector model and parameters of the human visual system, *Journal of the Optical Society of American* 63, 1357-68, 1973.

Siemens, *Somatom PLUS-S operator's manual (with SOMARIS/2)*, Version 11.91, Siemens Medical Systems Inc., Erlangen, Germany, 1991.

Wagner R. F., D. G. Brown and M. S. Pastel, Application of information theory to the assessment of computed tomography, *Med. Phys.* 6, 83, 1979.

Chapter 6
A Comparison of CBP and MLS Using the Reprojected Data from CT Scans

6.1 Introduction

In this chapter, we provide further comparisons between MLS and CBP using the data reprojected from a number of CT quality assurance (QA) scans taken from a clinical scanner. Two physical quantities MTF and SNR will be measured from the corresponding high and low contrast inserts respectively.

Scans of two phantoms have been taken from a Siemens Somotom PLUS-S [1991] CT machine. All the images are 512x512 pixels in size. The first phantom is the one in the Department of Medical Physics, Manitoba Cancer Treatment and Research Foundation (MCTRF), which is designed [Nuclear Associates, AAPM 1976] for the acceptance test and routine QA of CT scanners. It has a number of inserts each designed to test one physical parameter, such as the high and low contrast resolutions, the linearity of attenuation coefficient, etc. The other one is a Siemens phantom which has a bar pattern insert and a thin wire insert not available in the first one. The scans were taken at $500mAs$ and $120KV$ (mean energy $60KeV$) and 1 cm slice thickness - the settings for general QA and following the AAPM [1976, 1993] guidelines for CT QA testing. For each of the scans, we reproject the image to obtain a set of projection data to approximately simulate the real data with noise.

6. 2 Spatial resolution

The MTF has been measured by using both the Fourier and the standard deviation methods as described in section 2.4.4.

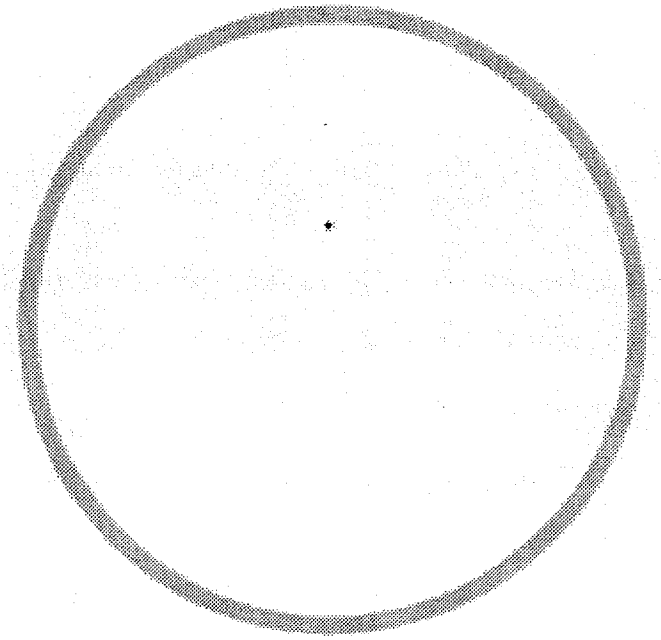

Fig. 6.2.1 The dark point is the cross section of a thin wire (d=0.01mm) inserted in the Siemens phantom to test the MTF of CT scanners. (the out-circle d=22cm is made of plexiglass.) The image size is 512x512.

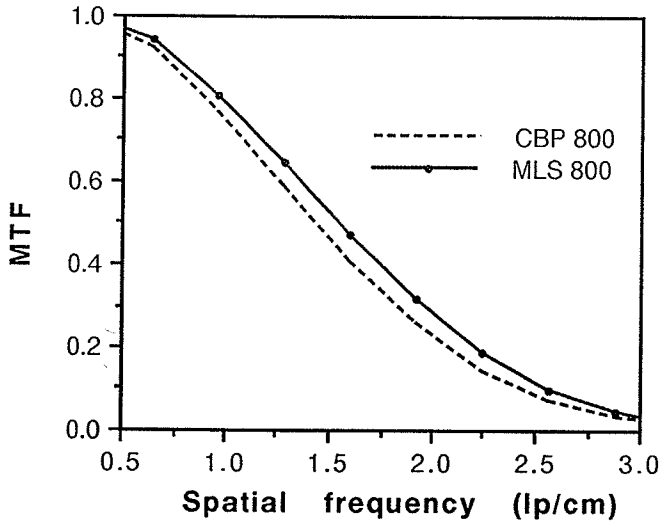

Fig. 6.2.2 Plots of the MTF measured from the Fourier transform of the thin wire in the CBP and 1-iteration MLS reconstructions from a total of 800 projections.

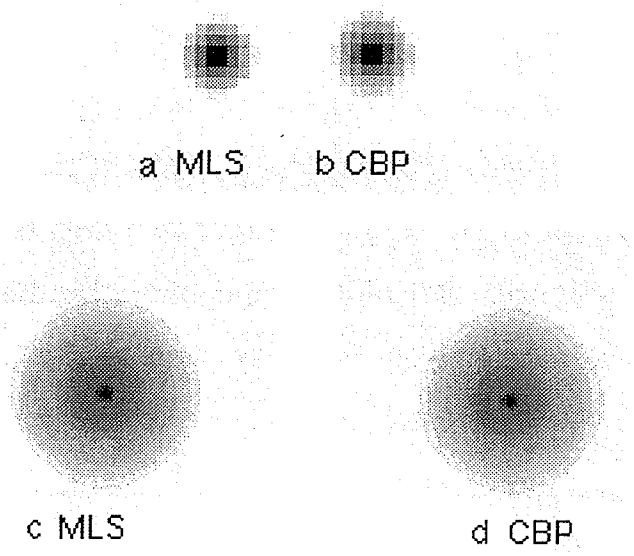

Fig. 6.2.3 The enlarged thin wire cross section after reconstruction by (a) 1-iteration MLS and (b) CBP. (c) and (d) are their corresponding Fourier transforms.

Test with a thin wire insert The dark point shown in Fig. 6.2.1 is the cross section of a thin wire (d=0.01*mm*) inserted in the Siemens phantom. After reprojecting the scan for a total of 800 projections and doing the reconstructions using both the 1-iteration MLS and CBP, we performed the FFT of a 32x32 sub-image centered at the wire, a method similar to that used by Droege [1982]. The MTF is then calculated by averaging the FFT amplitude along the 0^0 and 90^0 axes. In Fig. 6.2.2, we plotted these MTF values versus the spatial frequency. Apparently, MLS enhances the MTF more at medium to high frequencies than does CBP. For a straightforward demonstration, we show the point image itself (enlarged) and its Fourier transform in Fig. 6.2.3 after reconstructions. Clearly, the MLS point (a) spreads less than its CBP counterpart (b), while the result in Fourier space is just opposite, as should be expected.

Fig. 6.2.4 shows the plots of MTF for a number of different projections for (a) 1-iteration MLS and (b) CBP. We see that while the MLS curves drop as the projection number reduce, the CBP curves coincide. We do not see the little differences among curves at high frequencies as we did in Fig. 5.8.6. The reason is explained in section 6.5 below. In Fig. 6.2.4(a), the CBP's MTF for 800 projections is also plotted and one sees that as long as a projection number is 400 or greater, the 1-iteration MLS's MTF is higher than that of CBP.

Test with bar patterns Shown in Fig. 6.2.5 is an insert for testing the spatial resolution as well, which consists of bar patterns of 5 different sizes. The standard deviations (SD) in a marked region in each set were measured from the reconstructions and are directly proportional to MTF (see Eq. 2.24). In Fig. 6.2.6, we plot these SD measures for the case of 800 projections. That MLS allows higher modulation transfer functions is again demonstrated. The two images are shown in Fig. 6.2.7 (a) and (b), where the bars (a) in the MLS version exhibit more high contrast and sharper edges than their counterparts (b) in the CBP version.

The test proceeds using a series of projection numbers. Fig. 6.2.8 shows together these SD plots, similar to Fig. 6.2.4, for (a)1-iteration MLS and (b) CBP. The same as noted above, MLS curves drop as the number of projections decreases but the CBPs don't change (the difference between Figs. 6.2.8 and 5.8. 6 is also noted in section 6.5). Also, the 1-iteration MLS has higher values than CBP when the number of projections is larger than 400, and, lower otherwise. In Fig. 6.2.9 we plot the SD measures from 400 projections, for both 1 and 2-iteration MLS as well as CBP. One sees that 2-

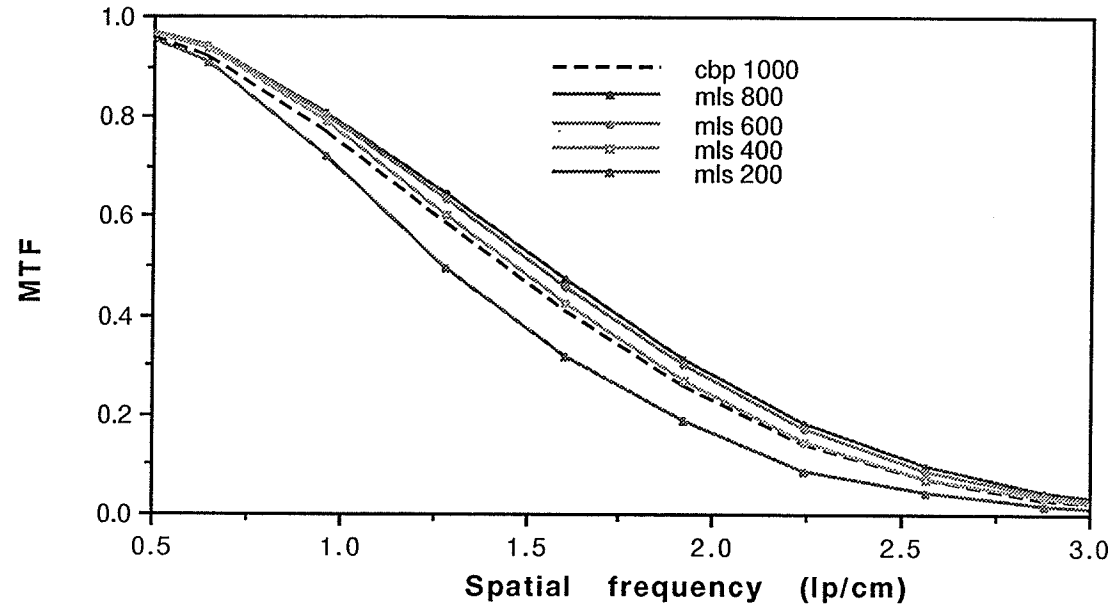

(a)

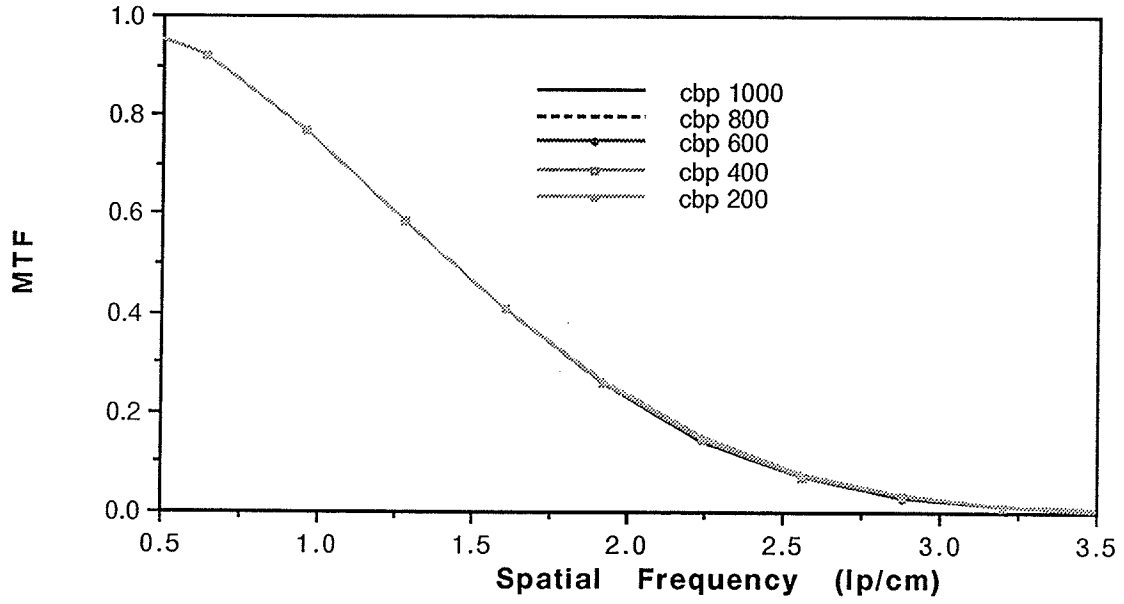

(b)

Fig. 6.2.4 Plots of MTF by measuring the Fourier transform of the thin wire in the reconstructions from a number of different projections for (a) the 1-iteration MLS and (b) CBP.

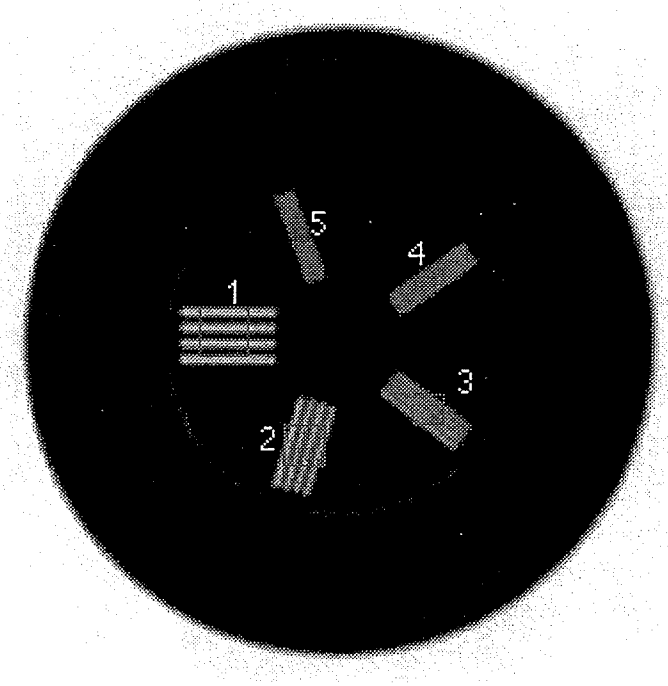

Fig. 6.2.5 A bar-pattern insert in a CT phantom for testing the spatial resolution. The standard deviations (SD) inside the marked square region in each set will be measured from the reconstructions. Note that in applying this method, each marked square should cover a same number of black/white pixels and it does not necessarily align with the bars. The phantom diameter is 22cm and the image size is 512x512.

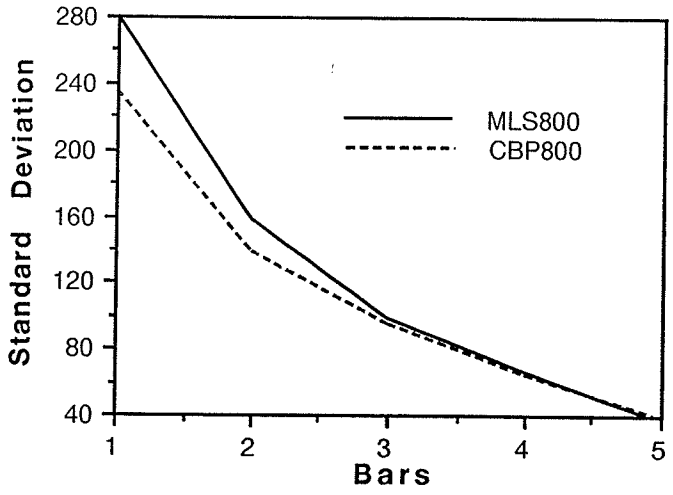

Fig. 6.2.6 Plots of the standard deviation measured inside the marked regions from the reconstructions of 800 projections, by CBP and 1-iteration MLS.

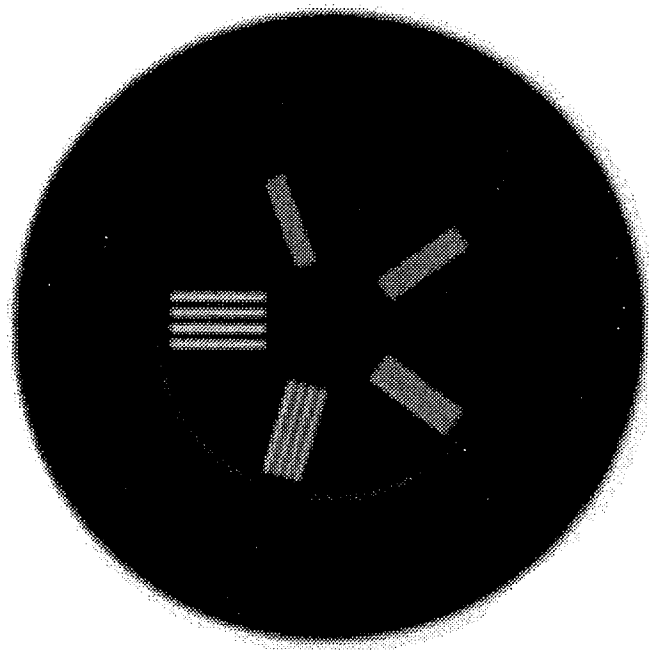

(a)

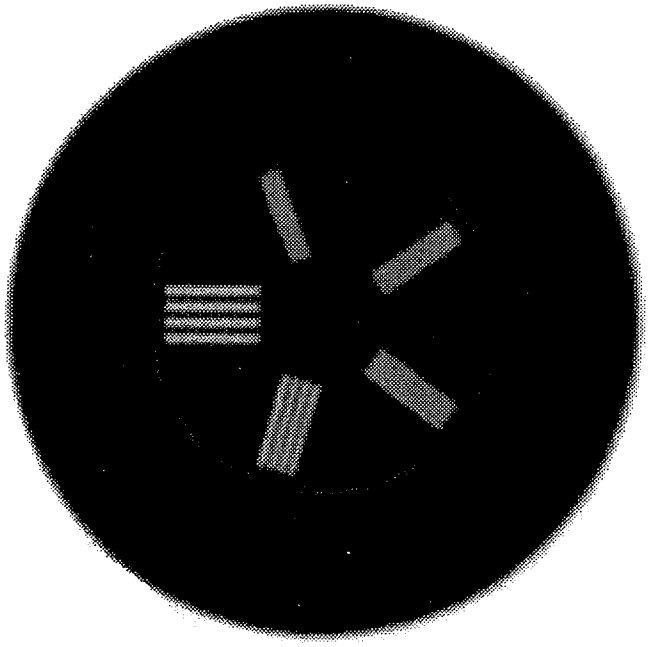

(b)

Fig. 6.2.7 Reconstructions of the bar pattern phantom by (a) 1-iteration MLS and (b) CBP from a total of 800 projections.

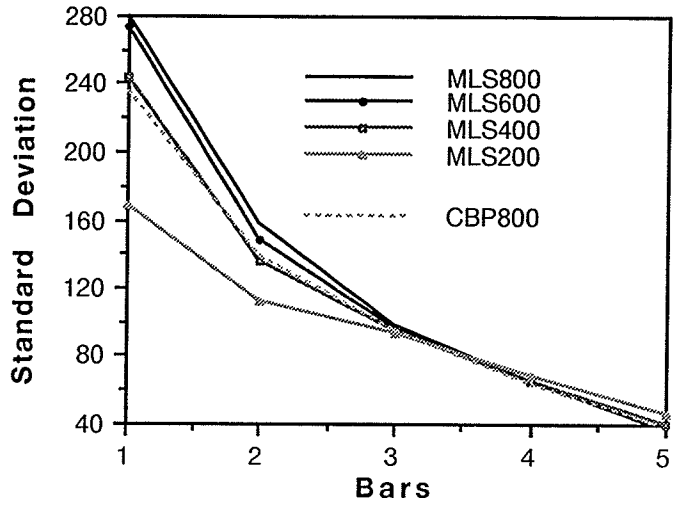

(a)

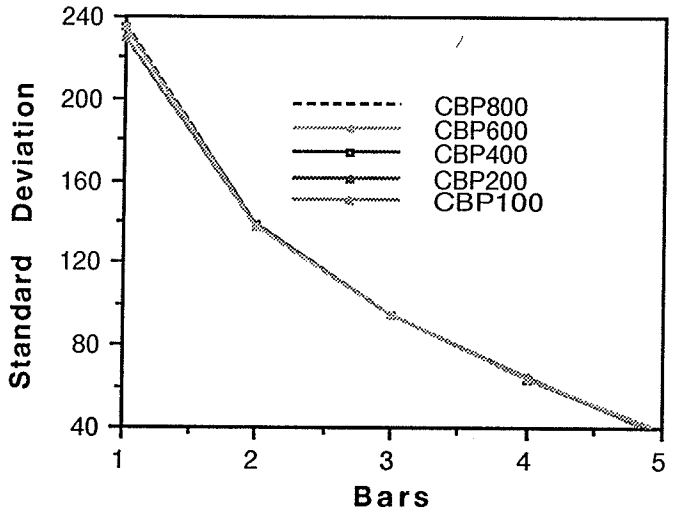

(b)

Fig. 6.2.8 Plots of the standard deviation measured inside the marked regions of the bar patterns in the reconstructions from a number of different projections by (a) the 1-iteration MLS and (b) CBP.

iteration MLS improves its 1-iteration's performance dramatically and its curve overlaps with that of 800 projections.

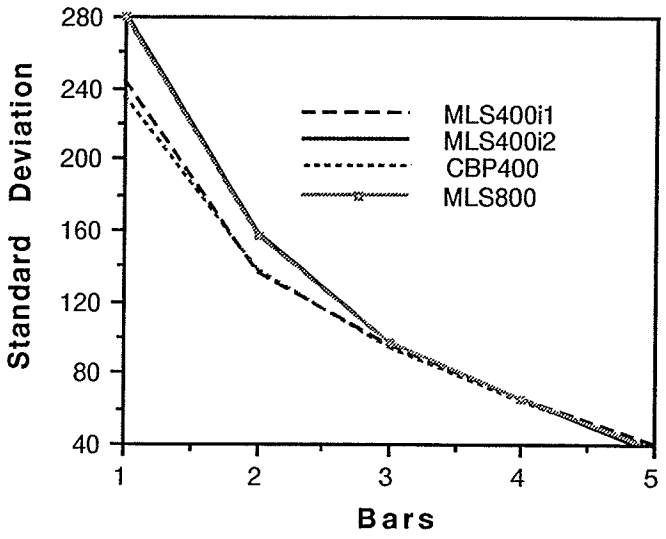

Fig. 6.2.9 Plots of the standard deviation measured inside the marked regions of bar patterns in the reconstructions by 1 and 2-iteration MLS from 400 projections, 1-iteration MLS from 800 projections and CBP from 400 projections.

Fig. 6.2.10 shows two reconstructions of an adult chest from 800 projections by (a) 1-iteration MLS and (b) CBP. As indicated by arrows, the small details and blood vessels in (a) appear sharper and more clearly delineated than their counterparts in (b).

6. 3 Low contrast resolution

Fig. 6.3.1(a) is the scan of a low contrast insert. Fig. 6.3.1(b) is its windowed version centered at a CT # of 1080, spanning 1080 ± 126 for better visibility inside. The regions indicated by circle 1 are located in water (CT # 1024) and circle 2 is located in a material whose average CT # is 1030. The dark central region (circle 3) is plexiglass (CT# 1117) inside which, a small

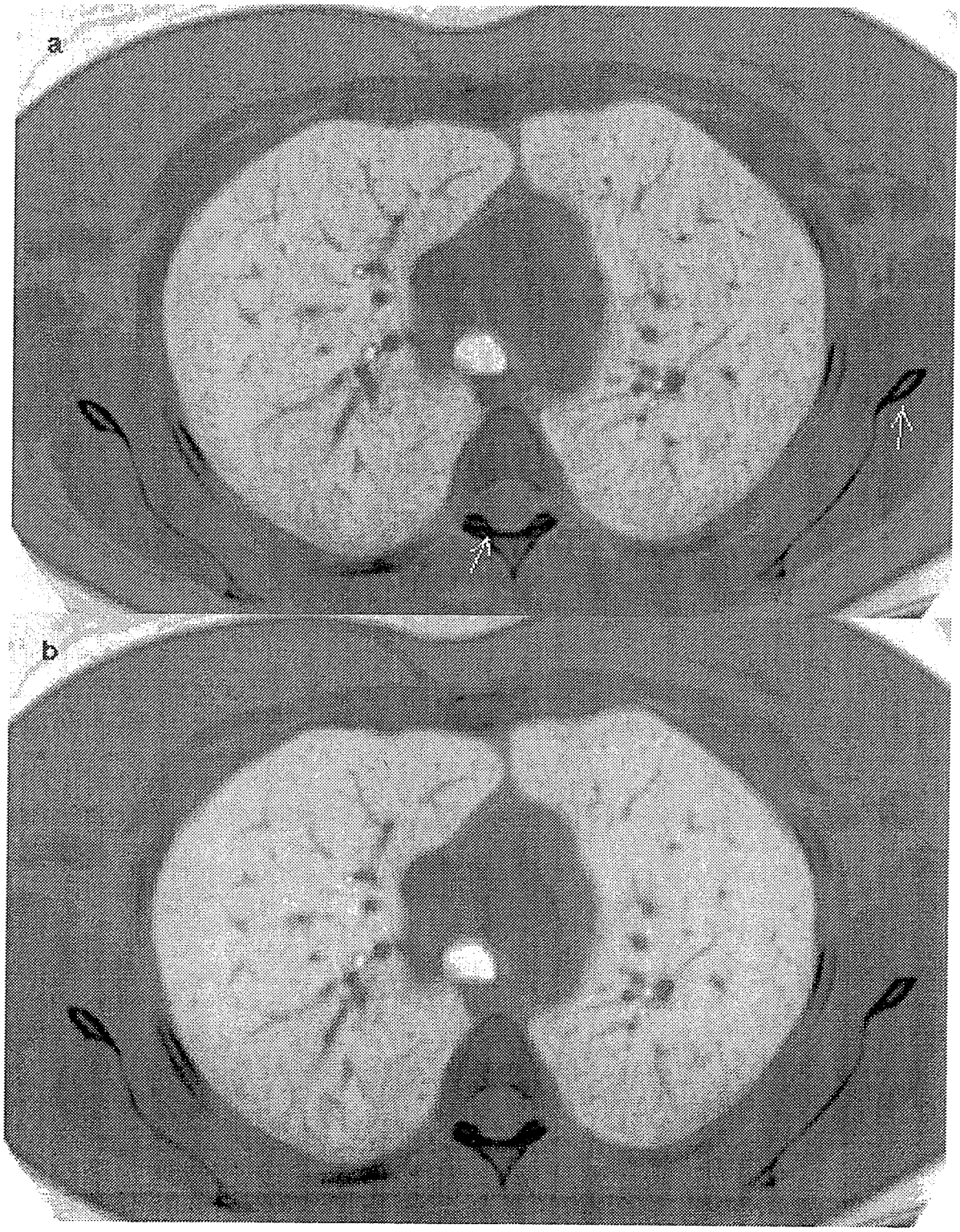

Fig. 6.2.10 The reconstructions of an adult thorax from 800 projections by (a) 1-iteration MLS and (b) CBP. The arrows in (a) indicate some small details which look sharper and clearer than their corresponding ones in (b). The two images have been scaled and windowed to the same ranges in CT number.

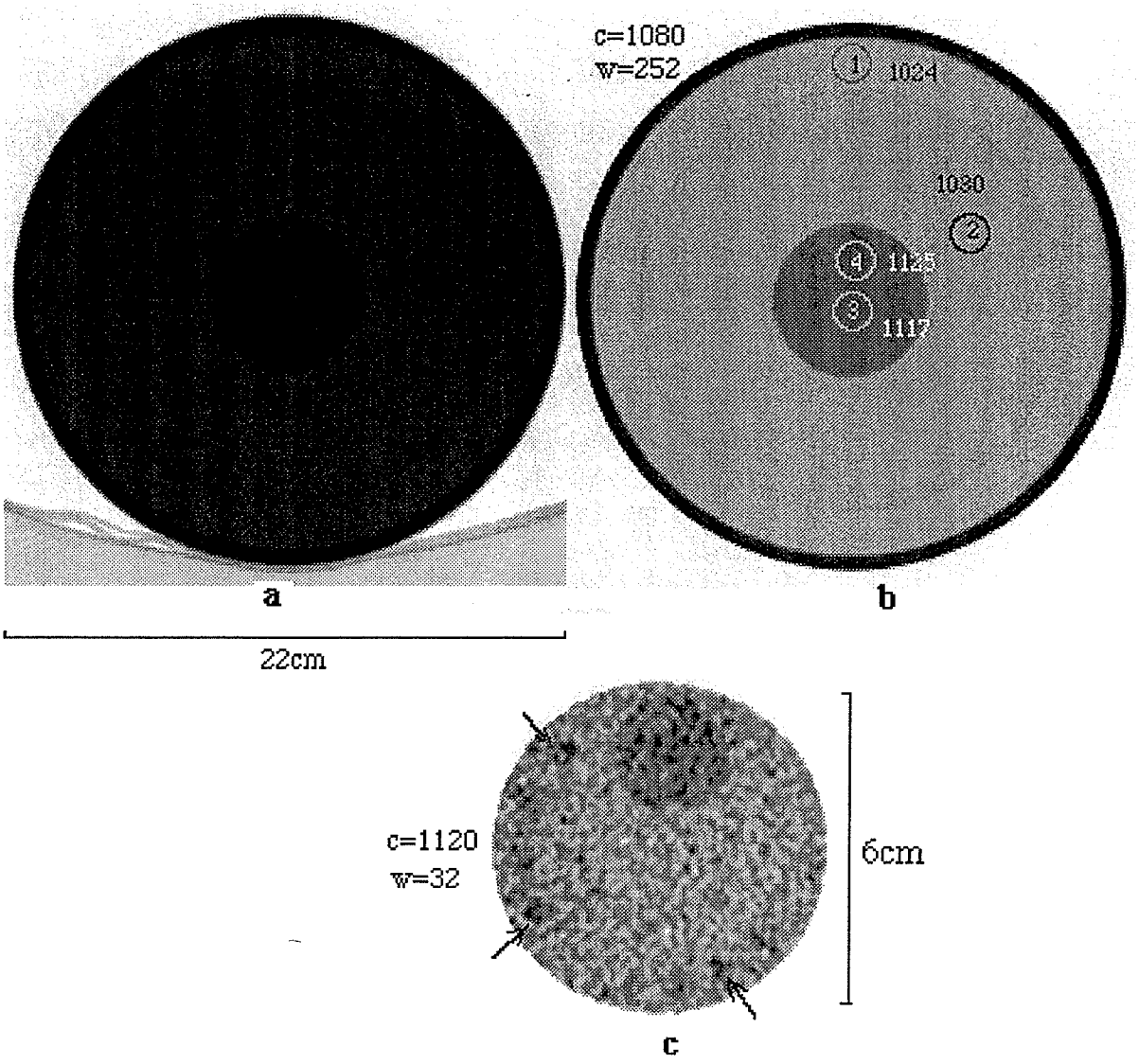

Fig. 6.3.1 (a) A low contrast CT scan (the phantom is 25cm in diameter, 512x512 pixels, CT #: 0-4095) and (b) its windowed version centered at a CT # of 1080, spanning 1080 ± 126. (c) The central darker region windowed at a CT # of 1120 with a width of 32. The arrows indicate a number of small details in the phantom.

area (circle 4) was further replaced by a different kind of glass whose average CT # is 1125 for simulating a tumor. The central region is further windowed at CT # 1120 with a width of 32 in Fig. 6.3.1(c). The "tumor" has a contrast of about 0.4% against its background representing the detectibility limit of CT scanners. There are also a number of small details having about the same contrast as the tumor, as indicated by arrows.

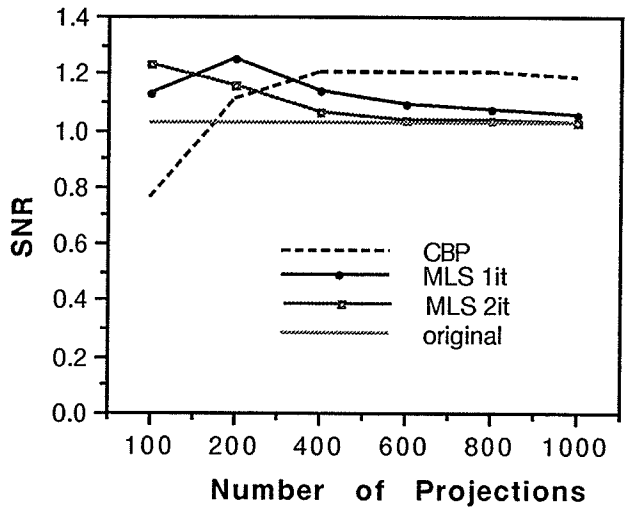

Fig. 6.3.2 Plots of the SNR of the "tumor" (region 4) against its background (region 3) versus the number of projections in the 1 and 2-iteration MLS, as well as in the CBP reconstructions. The SNR in the original CT scan is also plotted as a horizontal line.

We measured the SNR of the "tumor" (region 4) versus the number of projections in the 1 and 2-iteration MLS, as well as in the CBP reconstructions. The SNR definition Eq. (2.19) is used. In Fig. 6.3.2, we plotted these SNR values, along with the value in the original CT scan as a horizontal line. It is seen that with more than 400 projections, CBP will produce a little larger SNR than MLS. With less than 400, the MLS's SNR becomes larger. The 2-iteration MLS further degrades the SNR. It seems that

the better SNR of CBP can be attributed, at least partly, to its band limitation property, since, as we found, the same amplitude of signals ($|CT\#1 - CT\#2|$) has been generated by both the methods, but just in the CBP version, the standard deviation is smaller. Band limitation restricts the reconstruction of high frequency components and hence it smoothes the noise. Note that MLS is more accurate since its SNR curves are closer to the SNR of the original. Here we infer that those physical arrangements and approximations made in the last chapter are correct, since the SNR of the original scan is about 1.0 for a detection contrast of 0.4%, the same as that from the calculation (see Figs. 5.6.2 and 5.6.3).

Fig. 6.3.3 shows the noise histograms inside the "tumor" in (a) the original CT scan; (b) 1-iteration MLS and CBP reconstructions from 800 projections; (c) 1-iteration MLS and CBP reconstructions from 200 projections. Clearly, the 1-iteration MLS's histogram is broader than that of CBP from 800 projections. But in the case of 200 projections, CBP's histogram is broader.

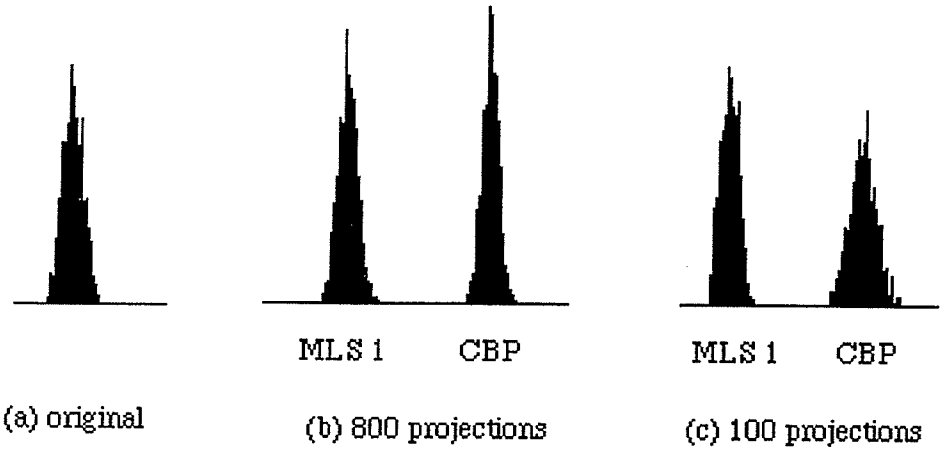

Fig. 6.3.3 The noise histograms inside the "tumor" in (a) original CT scan; (b) 1-iteration MLS and CBP reconstructions from 800 projections; (c) 1-iteration MLS and CBP reconstructions from 100 projections.

Fig. 6.3.4 displays the central region of the reconstructions, windowed the same as Fig. 6.3.1(c), for four different numbers of projections, each for one row as labeled. The 1st column contains the CBP images. The 2nd and 3rd columns exhibit the corresponding 1-and 2-iteration MLS reconstructions. We find that as the number of projections decrease, the CBP versions become more noisy, in contrast to the MLS ones which are increasingly smooth. The CBP image from 100 projections (the bottom left one) is so noisy that those small details as indicated in Fig. 6.3.1(c) are hard to perceive. In short, the visual appearance agrees with the SNR measures for all images.

6.4 Reconstruction error measures

The reconstruction error is also intuitively exhibited by subtracting images from the original scan. Fig. 6.4.1 shows, for the low contrast insert in Fig. 6.3.1(a), two such error images for (a) 1-iteration MLS and (b) CBP. We measured the mean of three small squares in both the images and found that the CBP generates much larger errors around edges and wherever abrupt changes occur. In smooth regions, there is not much difference.

The reconstruction accuracy is also quantified by measuring the correlation coefficient (cc) and the root mean square (rms) error for the low contrast insert versus the number of projections. The results are plotted in Fig. 6.4.2 for 1 and 2-iteration MLS as well as CBP. The two plots look almost the same as those in Fig. 5.10.3. The cc and rms are not applicable for quantifying the SNR.

6.5 Discussion and conclusion

The experimental results agree, at least qualitatively, with those seen in the previous 2 chapters. The results further qualitatively verify that MLS can

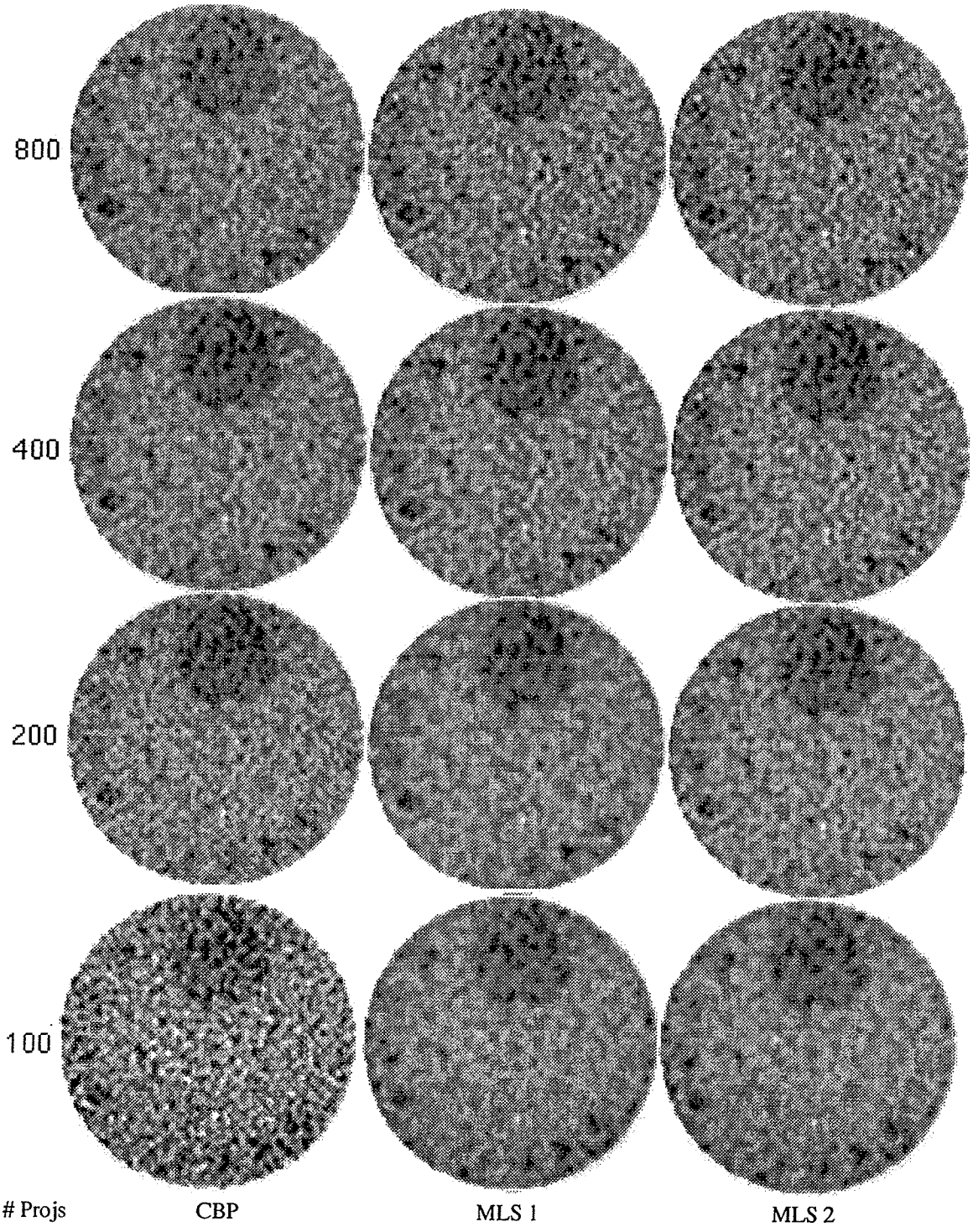

Fig. 6.3.4 The central region after reconstructions, windowed the same as Fig. 6.3.1(c), for four different numbers of projections from the 1st to 4th rows. The 1st column contains the CBP images. The 2nd and 3rd columns exhibit the corresponding 1-and 2-iteration MLS images.

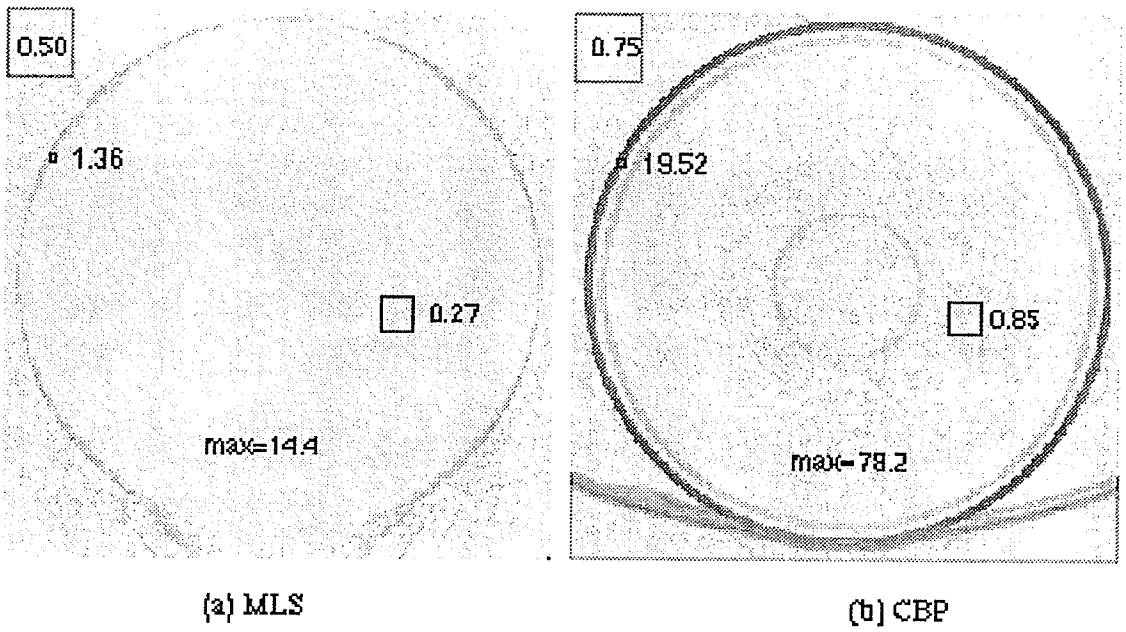

Fig. 6.4.1 The subtraction of the reconstruction of the low contrast insert from the original CT image, for (a) 1-iteration MLS and (b) CBP.

reduce the dosage by half while still preserve the spatial resolution. MLS also provides higher dose efficiency in low contrast detectibility when the number of projections is small (see Fig. 6.3.3).

It is worth noting that in Fig. 6.3.2, as the projection number decreases, the SNR of MLS shows a slow increase, in contrast to a slow decrease in Fig. 5.6.3 and also, the CBP curve drops less steeply, in spite of the agreement of relative trends. This suggests that using reprojected data from CT scans only partially or qualitatively simulated the real situation. The reason is: in CT scans noises are already correlated (see the NPS in Figs. 5.9.1 and 5.9.2). Reprojection can not fully duplicate the original projection in which the noise is totally Gaussian (white). This may also explain why in Fig. 6.3.3, the 1-iteration MLS images from 100 or 200 projections appears too smooth.

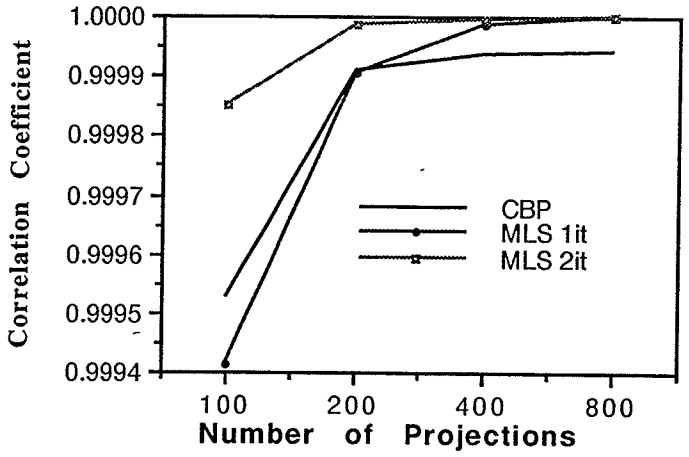

(a)

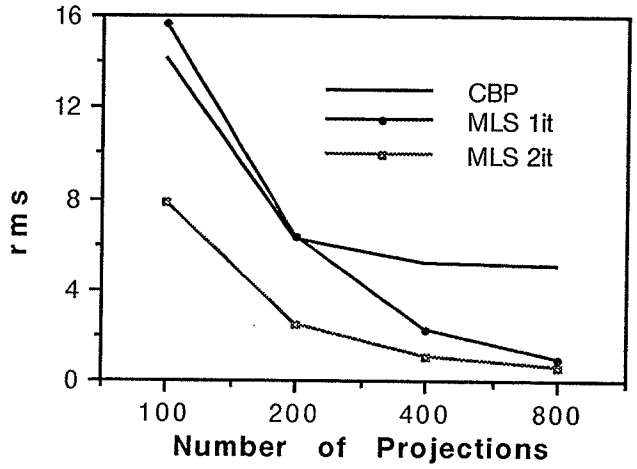

(b)

Fig. 6.4.2 Measures of the (a) correlation coefficient and (b) root mean square error for the low contrast insert reconstructions versus the number of projections for 1 and 2-iteration MLS as well as CBP.

In testing the MTF of reconstructions, we used a "thin" wire of a few pixels in diameter and a set of bar patterns (especially the small size ones) which are already blurred by edges (so that it is very difficult to assign exactly the same number of black/white pixels in each marked square in Fig. 6.2.5). Therefore the MTF, especially at high frequencies, can not be accurately determined for both the MLS and CBP, such that the little differences among curves of

different projections in Fig. 5.8.6 are not seen in Figs. 6.2.4 and 6.2.8. For example, in the bar pattern image (Fig. 6.2.5), the 5th set would be rather a single large bar than a set of smallest bars. The further reason to address the difference may be the one we discussed above: reprojection of CT scans cannot fully duplicate the characteristics of the original projection. Even further, the effect of interconnections among cascaded CT processes may have been distorted in the reprojection data. One actually has to resort to real projection data scanned from a thin wire or a set of bar patterns for accurate MTF determination, which we left for future work.

References

AAPM Report No. 1, *Phantoms for performance evaluation and quality assurance of CT scanners*, 1976.

AAPM Report No. 39, *Specification and acceptance testing of computed tomography scanners*, 1993.

Droege R. T. and R. L. Morin, A practical method to measure the MTF of CT scanners, *Med. Phys.* 9, 758-760, 1982.

Nuclear Associates, *Instruction manual*, Computed tomography performance phantom, Models 76-410 and 76-411, 1980.

Siemens, *Somatom PLUS-S operator's manual (with SOMARIS/2)*, Version 11.91, Siemens Medical Systems Inc., Erlangen, Germany, 1991.

Chapter 7
The Improvement of MLS over the Conventional Schemes of ART

7.1 Introduction

In section 3.1 we saw that MLS outperforms the two conventionally used projection access orderings of ART, the random permutation scheme (RPS) and the sequential access scheme (SAS). In this chapter, we provide further experiments to verify that MLS truly and dramatically improves the performance of ART itself, not only in computational speed, but also in the physical image quality produced. The tests employ simulated projection data, reprojected data of CT scans and real data, which have been extensively used in the last three chapters.

Historically, ART was first used in the early EMI scanner. Hounsfield [1972] realized the problem of correlations among projections and suggested a pseudo-random ordering of them. (He took projections of 40° apart.) Shepp and Logan [1974] followed the point by taking 37° between consecutive projections. The EMI scanner later switched from ART to CBP, basically because of the possible lack of convergence with noisy data and the longer reconstruction time of ART. The orthogonal pair ordering, which inherently differs from the random one, was first used by Kuhl et al [1973]. But they arranged just 4 projections and stopped going any further to get a scheme applicable for any number of projections. It was not until very recently that van Dijke [1992] and Herman [1993] picked up this topic again, but unfortunately they were still trying random or intuitive ordering. In this chapter, we demonstrate for the first time that classical ART using orders such as SAS and RPS truly lead to poor (and even very poor) low contrast

detection, let alone needing many iterations for convergence (note that the reconstruction times for 1-iteration MLS, RPS and SAS are exactly the same). With the advent of the MLS scheme, 1-iteration yields the largest SNR such that the fundamental limitations of classical ART are nearly eliminated.

Sections 7.2 and 7.3 cover tests using simulated projection data and reprojected CT data, respectively. Comparisons using real data are described in Section 7.4. Discussion and conclusion are included in the last section.

The simulations and reconstructions were performed on a Sun Sparc 4 workstation. Typical reconstruction times were about 30 minutes per iteration for a 512x512 matrix and 800 projections, with the program and all data stored in memory.

7.2 Tests with the simulated data

Shown in Fig. 7.2.1 are 5 images of the central part of the low contrast phantom (see Fig. 5.6.1b) reconstructed by (a) 1, (b) 6, (c) 12 and (d) 20-iteration SAS, and (e) 1-iteration MLS. The number of projections is 100 and the number of photons per measurement is 1.28×10^7. Visually, in (a), (b) and even (c), a large part of the object is poorly reconstructed and disks having relatively higher contrast cannot even be perceived. Although the full features are adequately reconstructed in (d) by 20 iterations, the image, however, appears more noisy than the 1-iteration MLS version (e).

Fig. 7.2.2 shows the plots of the SNR measured from the disks versus their contrast, for 1 and 16-iteration MLS as well as for 1, 6 and 20-iteration SAS. The MLS's SNR monotonically and linearly increases with the disk contrast (the 1st iteration has the largest SNR). But in the SAS reconstructions, larger contrast disks have lower SNR and lower contrast

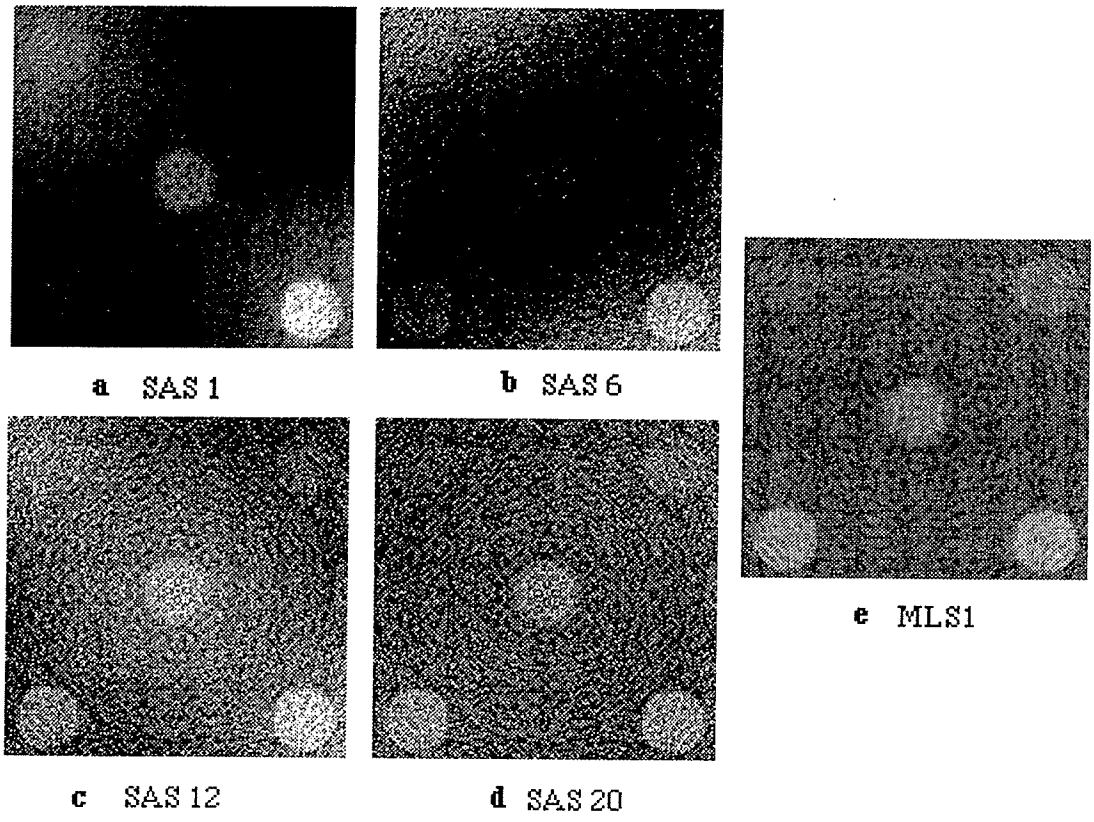

Fig. 7.2.1 The central part of the low contrast phantom (Fig. 5.6.1) in the reconstructions by (a) 1, (b) 6, (c) 12 and (d) 20 iterations of SAS, and (e) 1-iteration MLS, from 100 projections with a photon number per measurement of 1.28×10^7.

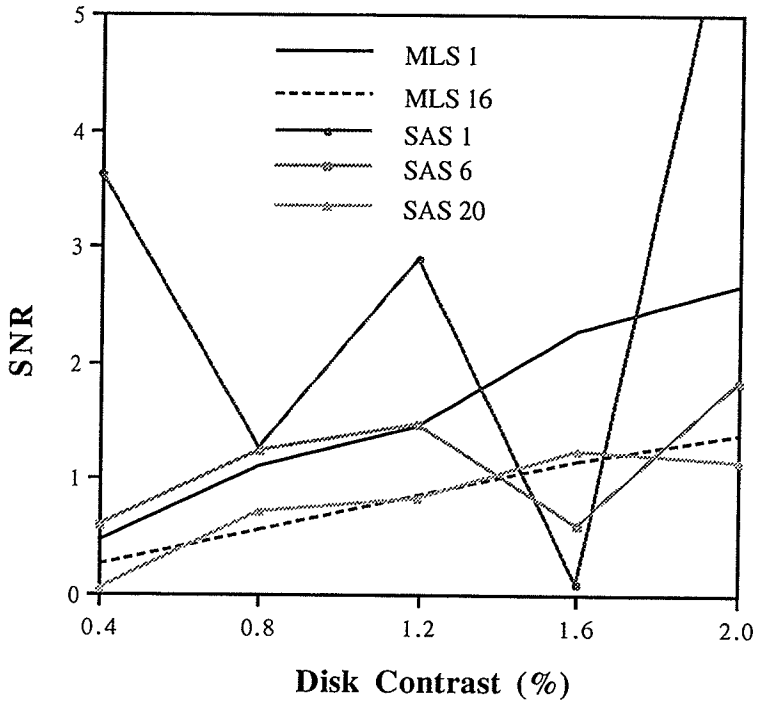

Fig. 7.2.2 Plots of the SNR measured from the 5 disks versus their contrast for 1 and 16-iteration MLS and also for 1, 6 and 20-iteration SAS. The reconstructions are from 100 projections with a photon number per measurement of 1.28×10^7. The MLS's SNR monotonically and almost linearly increases with the disk contrast (the 1st iteration has the largest SNR). But in the SAS reconstructions, larger contrast disks have lower SNR and lower contrast ones have larger SNR, as the 1 and 6-iteration curves exhibited. For example, Disk 4 (having the second largest contrast 1.6%) has almost 0 SNR in the 1st iteration. Although the 20-iteration SAS curve approaches a reasonable trend, its values are much lower than those of 1-iteration MLS's.

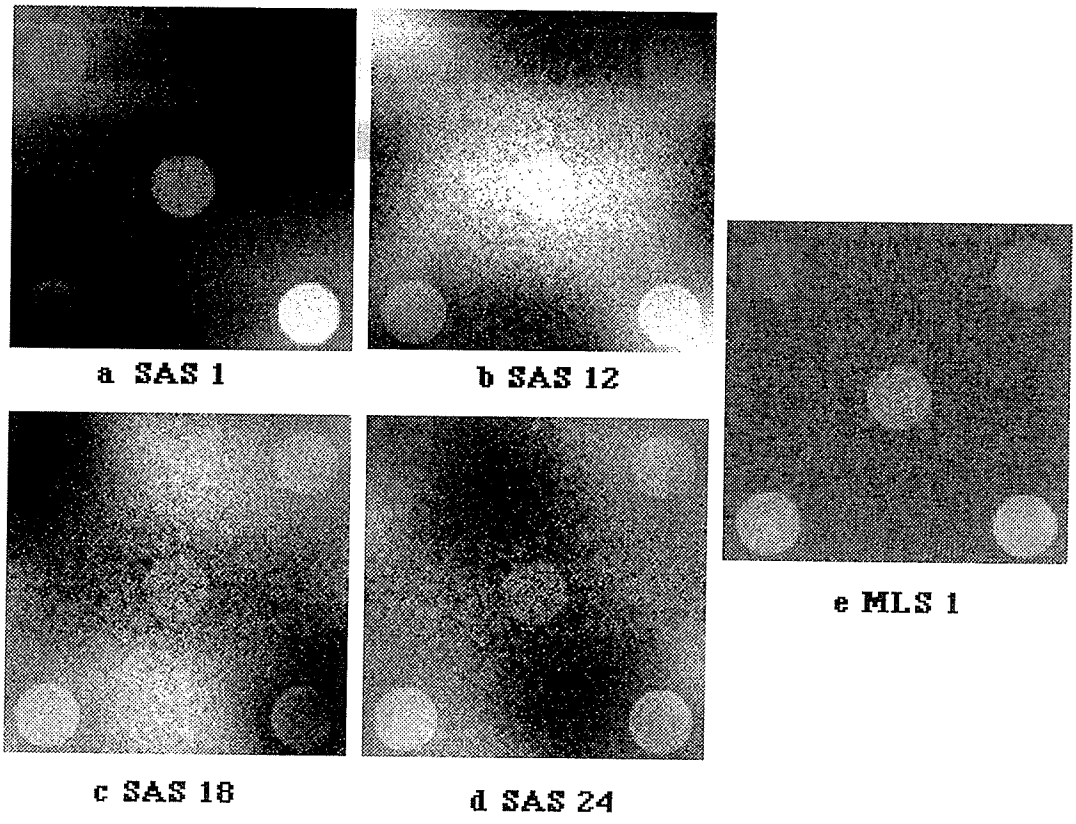

Fig. 7.2.3 The central part of the low contrast phantom (Fig. 5.6.1) in the reconstructions by (a) 1, (b) 12, (c) 18 and (d) 24 iterations of SAS, and (e) 1-iteration MLS, from 800 projections with a photon number per measurement of 1.28×10^7.

ones have larger SNR, as the 1 and 6-iteration curves exhibited. Although the 20-iteration SAS curve approaches a reasonable trend, its values are much lower than those of 1-iteration MLS's.

The performance of SAS becomes even poorer when the number of projections is larger. Fig. 7.2.3 shows another 5 reconstructions from 800 projections. In this case, image features still look poorly reconstructed even after 24-iterations. Fig. 7.2.4 displays two full images by 12-iteration SAS from (a) 100 and (b) 800 projections. We see that (a) converges faster than (b). Fig. 7.2.5 shows further the reconstructions of the contrast detail phantom (see Fig. 5.7.1b) from 400 projections, arranged in the same way as Figs. 7.2.1 and 7.2.3. Fig. 7.2.6 (a) is the 1-iteration MLS from 100 projections, while SAS needs about 20-iterations to get a uniform reconstruction, as (b) exhibited. Even then, the latter still appears with a larger noise level than the former, such that disks of lower contrasts and smaller sizes are relatively difficult to perceive.

We ran further tests to compare MLS to the random permutation scheme (RPS). By doing a sample of 1-iteration RPS reconstructions, we found that the results of RPS just sit in-between those of MLS and SAS. Fig. 7.2.7 and Fig. 7.2.8 each shows 3 reconstructions of the low contrast phantom, from 200 and 800 projections, respectively. In each figure, (a) is from 1-iteration MLS while (b) and (c) are two images randomly picked up from a sample of RPS reconstructions. We found that with a smaller number of projections, like 200, RPS cannot match the performance of MLS (as the two exhibited in Fig. 7.2.7). But with a larger number of projections, like 800, RPS performs relatively better (as Fig. 7.2.8(b) and (c) demonstrate, they look close to (a) although with more noise.) In Fig. 7.2.9, we show the central part of the contrast detail phantom using 1-iteration reconstructions, two by MLS (left)

and the other two by RPS (right). The top two are from 800 projections while the bottom two are from 200 projections. The visual difference between (c) and (d) is clearly larger than that between (a) and (b).

The test was also extended to the high contrast bar pattern phantom (see Fig.5.8.1). Fig. 7.2.10(a) shows its reconstruction from 800 projections by

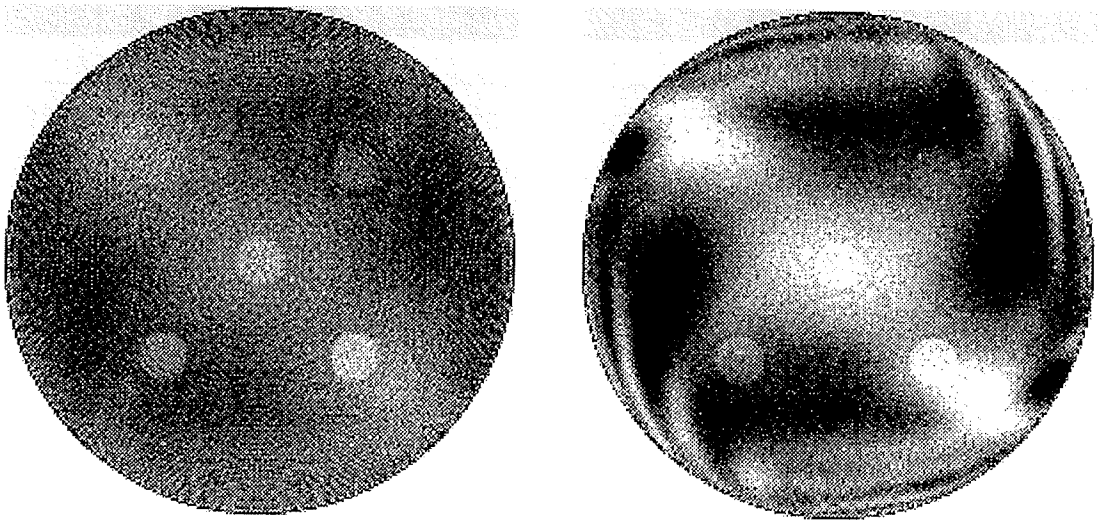

(a) (b)

Fig.7.2.4 Full display (windowed) of the low contrast phantom (Fig. 5.6.1) reconstructed by 12-iteration SAS from (a) 100 and (b) 800 projections. (a) converges faster than (b).

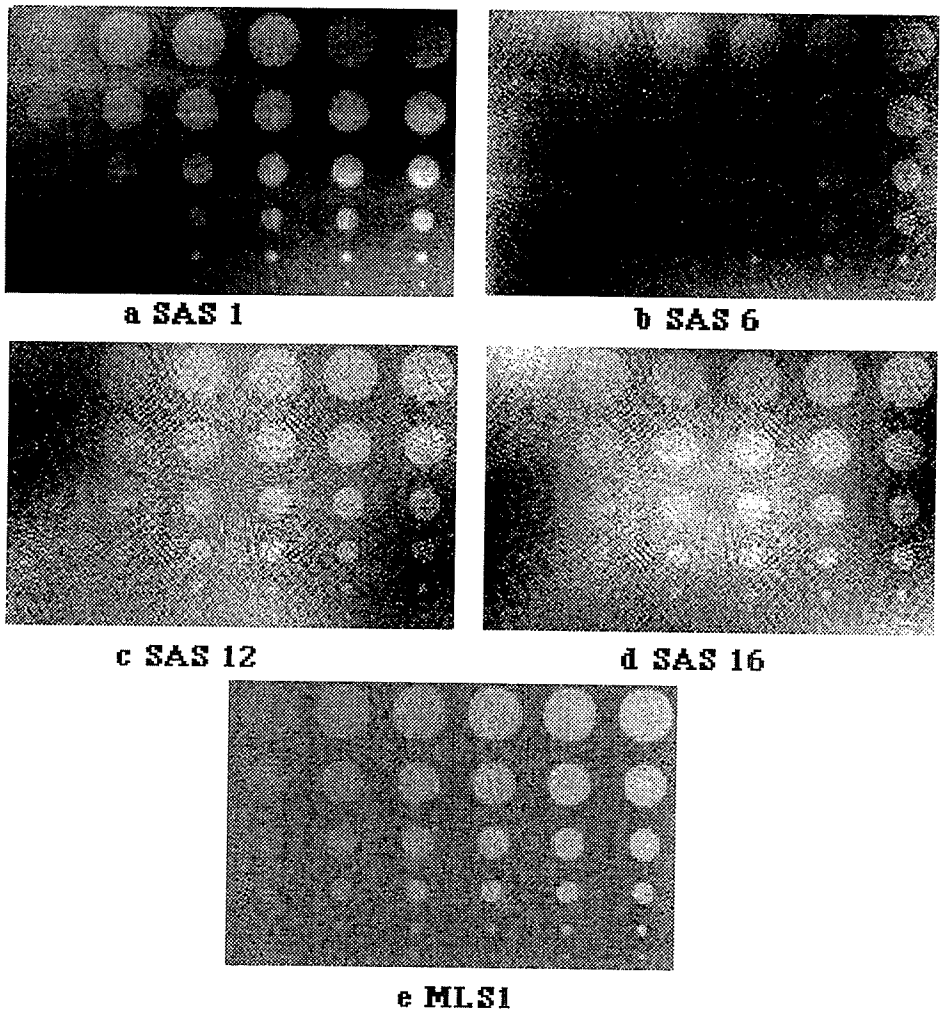

Fig. 7.2.5 The central part of the contrast detail phantom (Fig. 5.7.1) in the reconstructions by (a) 1, (b) 6, (c) 12 and (d) 16-iteration SAS, and (e) 1-iteration MLS, from 400 projections with a photon number per measurement of 1.28×10^7.

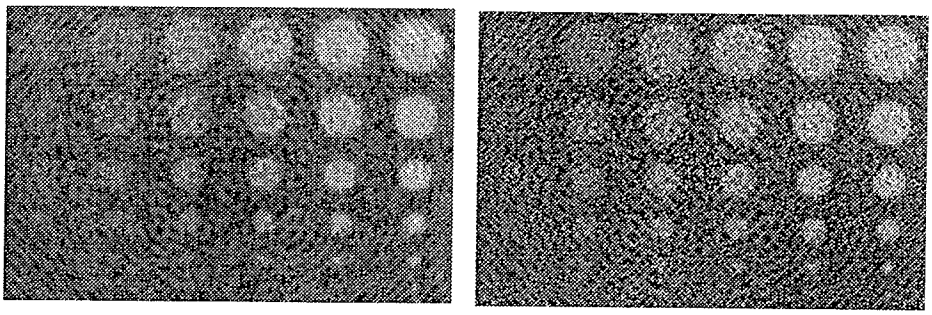

Fig. 7.2.6 The central part of the contrast detail phantom in the reconstructions from 100 projections, by (a) 1-iteration MLS and (b) 20-iteration SAS.

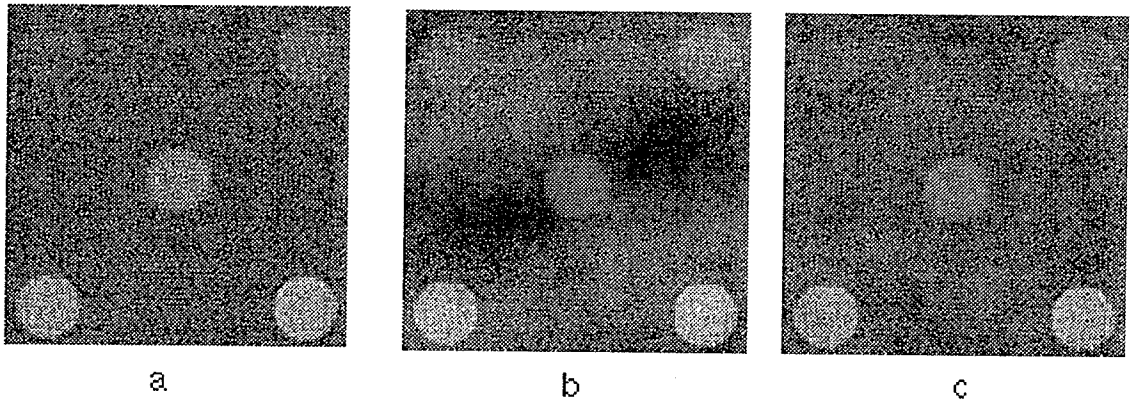

Fig. 7.2.7 The central part of the low contrast phantom in the 1-iteration reconstructions from 200 projections by (a) MLS, (b) and (c) RPS.

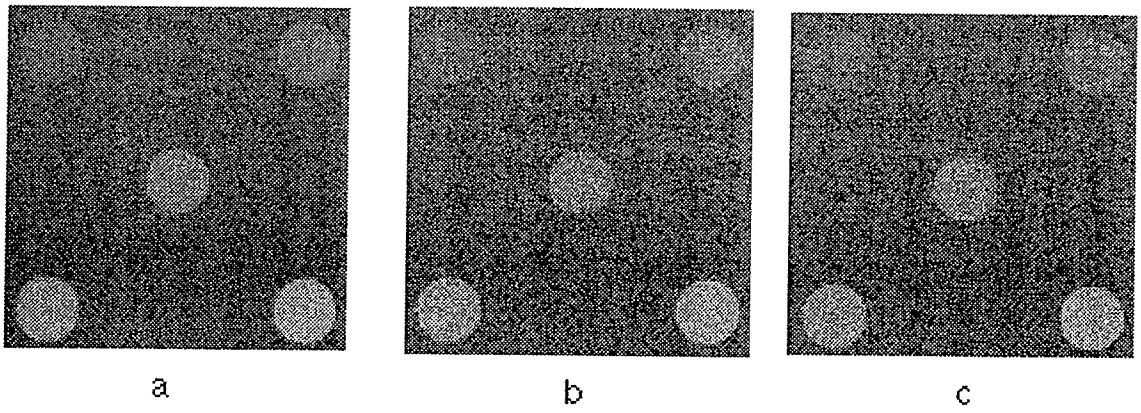

Fig. 7.2.8 The central part of the low contrast phantom in the 1-iteration reconstructions from 800 projections by (a) MLS, (b) and (c) RPS.

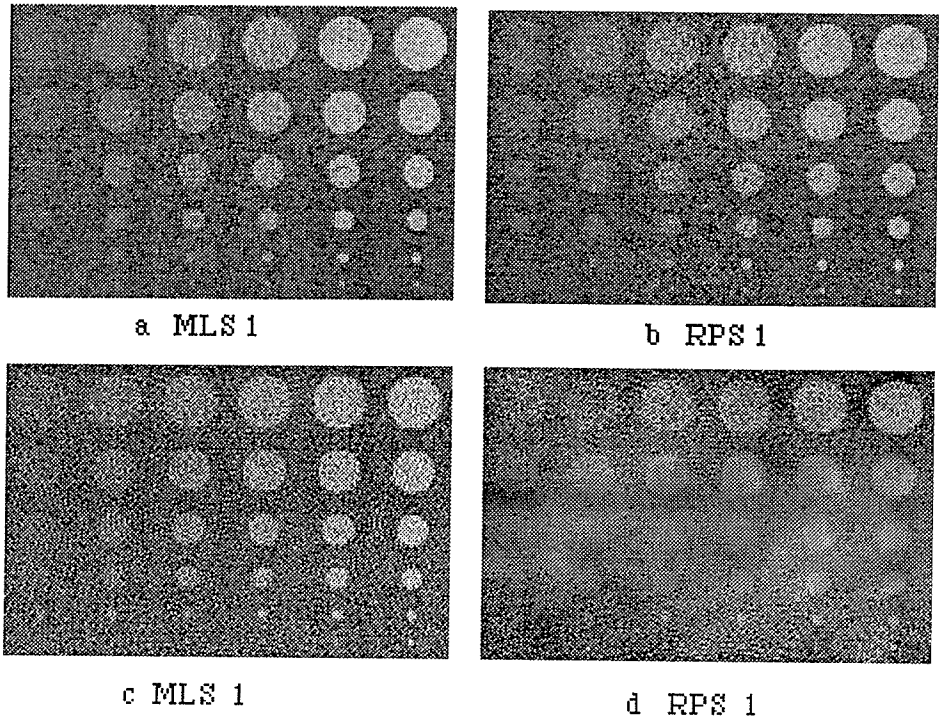

Fig. 7.2.9 The central part of the contrast detail phantom in the 1-iteration reconstructions by MLS and RPS. The top twos are from 800 projections while the bottom twos are from 200 projections.

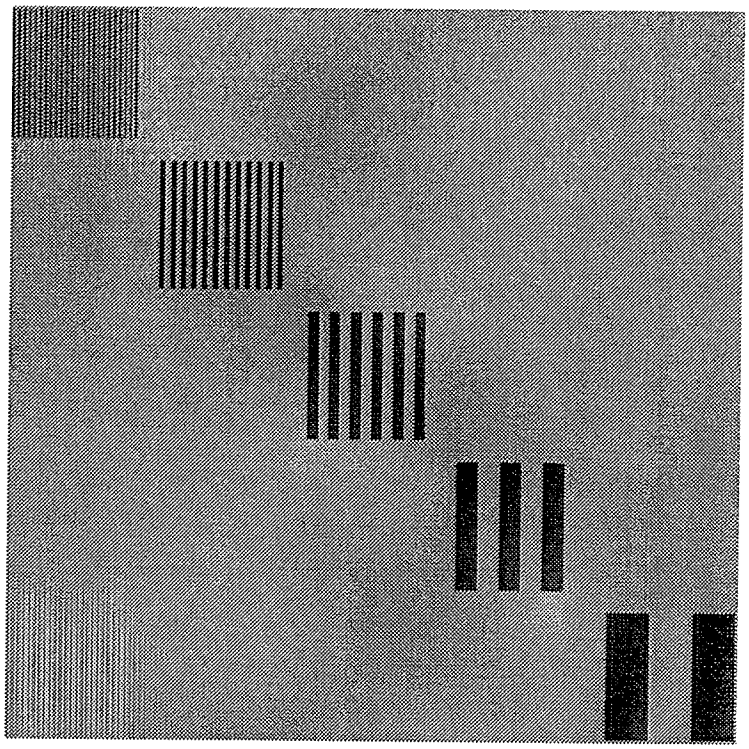

(a)

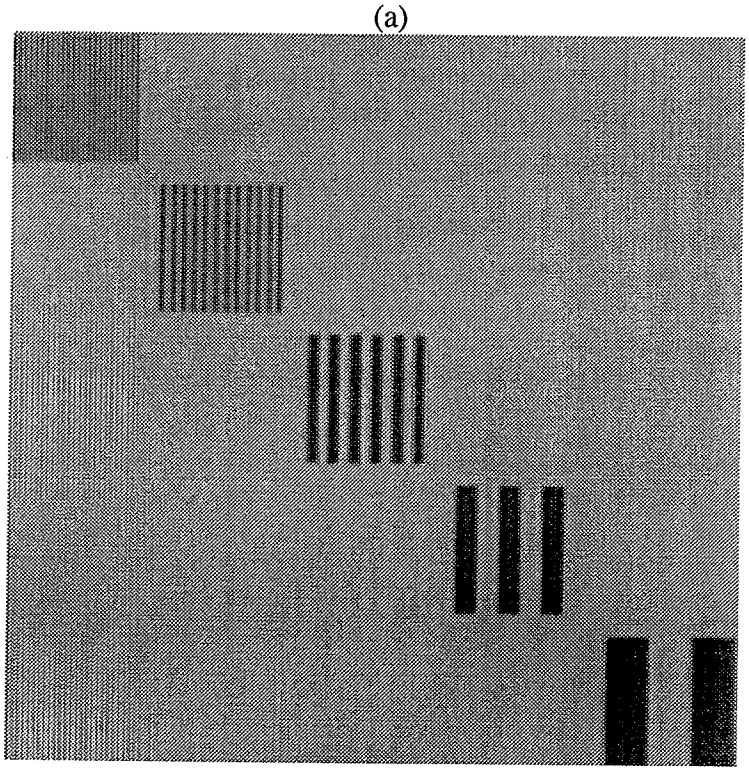

(b)

Fig. 7.2.10 Reconstructions of the bar pattern phantom by SAS from (a) 800 projections by 16-iteration, (b) 200 projections by 8-iteration.

16-iteration SAS and one sees that the bars are still not fully reconstructed and the background appears not uniform in grayness. We also show a reconstruction in 7.2.10(b) from 200 projections by 8-iteration SAS, and in this case, the patterns are relatively quickly reconstructed. In visual appearance, SAS reconstructs a high contrast object much faster than it did a low contrast one. (Compare the number of iterations needed for Fig. 7.2.3d to that needed for Fig. 7.2.9a). The performance of RPS is similar to that noted above.

7.3 Test with the reprojected data from CT Scans

We started this test with the low contrast phantom (Fig. 6.3.1) by reprojecting its CT scan and then doing the reconstruction following the SAS scheme. Fig. 7.3.1 shows four images of its central part from 200 projections, with (a), (b) and (c) from 2, 8 and 16-iteration SAS, respectively, and (d) from 1-iteration MLS. It appears that 16-iteration is still not enough for SAS to produce a uniform reconstruction. Its image (c) is also noisier than the 1-iteration MLS version in (d). Fig. 7.3.2 shows another 2 reconstructions from 800 projections. In this case, 42-iteration SAS (a) is far from generating a satisfactory image comparable to that of 1-iteration MLS (b). Fig. 7.3.3 displays two full images from 200 projections, windowed the same as Fig. 6.3.1c, by (a) 8-iteration SAS and (b) 1-iteration MLS. The image features are twisted severely in (a) while those in (b) are uniformly reconstructed. Fig. 7.3.4 shows the reconstructions of the thin wire (See Fig. 6.2.1) and their corresponding Fourier transforms for the first three iterations of SAS. The point and its Fourier counterpart both are twisted (can be clearly seen in the first two iterations).

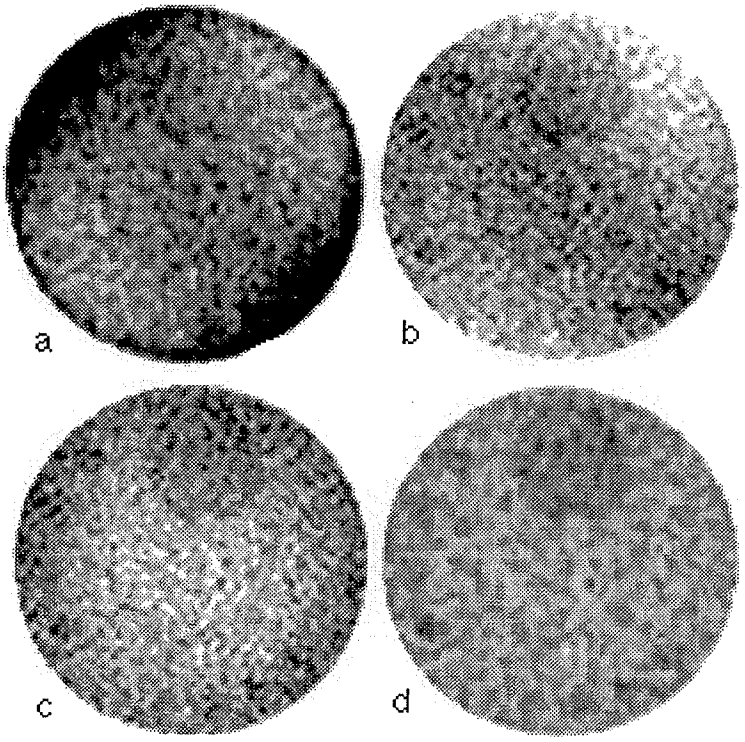

Fig. 7.3.1 Display of the central part of the low contrast phantom (Fig. 6.3.1) reconstructed from 200 projections, by (a) 2, (b) 8 and (c) 16-iteration SAS, and (d) 1-iteration MLS.

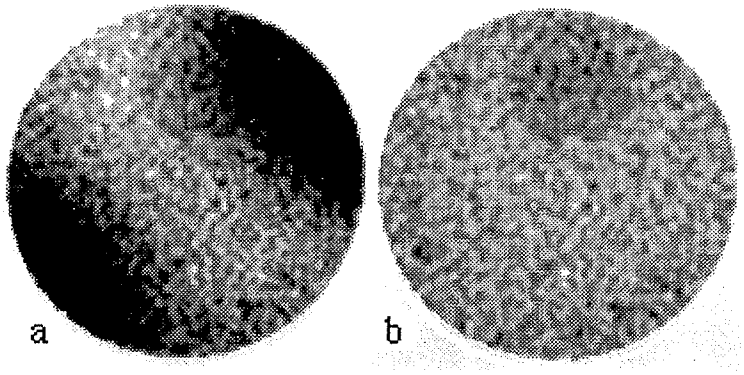

Fig. 7.3.2 Display of the central part of the low contrast phantom (Fig. 6.3.1) reconstructed from 800 projections, by (a) 42-iteration and (b) by 1-iteration MLS.

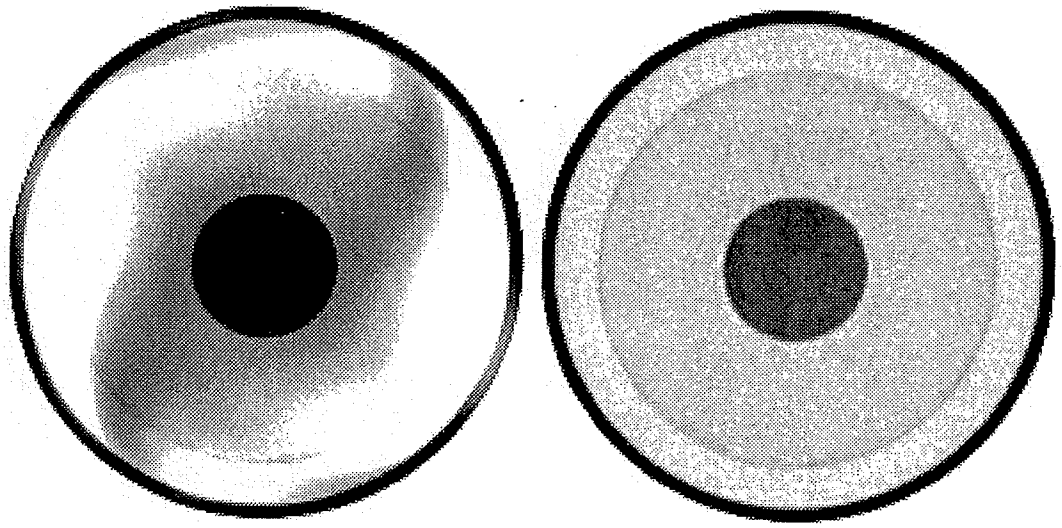

(a) (b)

Fig. 7.3.3 Display of two full images reconstructed from 200 projections (windowed the same as Fig. 6.3.1b), by (a) 8-iteration SAS and (b) 1-iteration MLS. Image features in (a) are twisted while those in (b) are uniformly reconstructed.

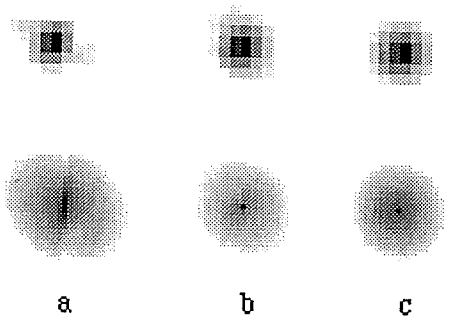

Fig. 7.3.4 The thin wire images (See Fig. 6.2.1) and their corresponding Fourier transform for the first three iterations of SAS.

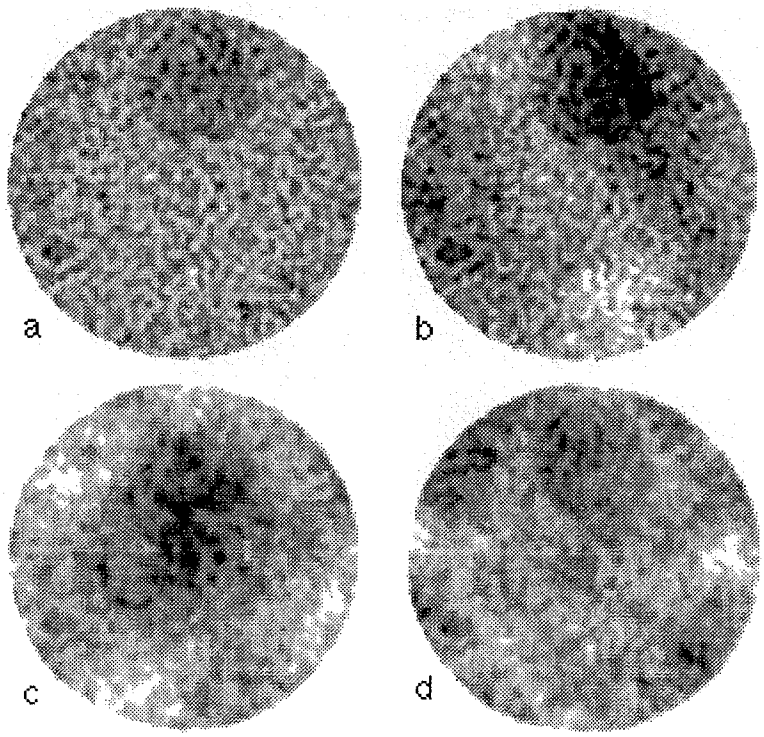

Fig. 7.3.5 The central part of the reconstructions by 1-iteration RPS. The top two are from 800 projections while the bottom two are from 200 projections.

Fig. 7.3.5 shows four sample 1-iteration reconstructions by RPS. The top two are from 800 projections where one ordering may produce a good image (a) while the other may not (b). The bottom two are from 200 projections; both hardly match the visual appearance of the 1-iteration MLS version as shown in Fig. 7.3.1(d).

Tests with the bar pattern phantom (Fig. 6.2.6) also confirm that SAS is relatively faster in reconstructing a high contrast object than a low contrast one. Iterations with a smaller number of projections converge faster than those with larger numbers. For RPS, the performance for a larger number of projections is relatively better.

7.4 Test with real data

These tests employ the data scanned from objects COMPLEX and DEW (see Fig. 4.2.1b and c), by a γ-ray CT [Wowk]. Fig. 7.4.1 and Fig. 7.4.2 each show six reconstructions for COMPLEX and DEW, respectively. In each figure, (a), (b) and (c) are from 1, 2 and 4-iteration MLS, respectively, while (d), (e) and (f) are the corresponding three reconstructions from SAS. 1-iteration MLS produces visually the most promising images for both the objects. (2 and 4-iteration's results appear sharper, but also noisier). The 1 and even 2-iteration SAS cannot fully reconstruct the object's features. The edges are spread and deformed. Hardly had an object gotten adequately reconstructed (as shown in Figs. 7.4.1d and 7.4.2d by 4-iteration), when its image features start appearing much noisier. We found that SAS is also relatively faster for reconstructing high contrast objects in a smaller image matrix than it is in a larger matrix. For example, for COMPLEX and DEW (64x64, 100 projections), 4-iteration SAS is almost adequate and the images look close to those of 4-iteration MLS. But for the bar patterns (see Fig.

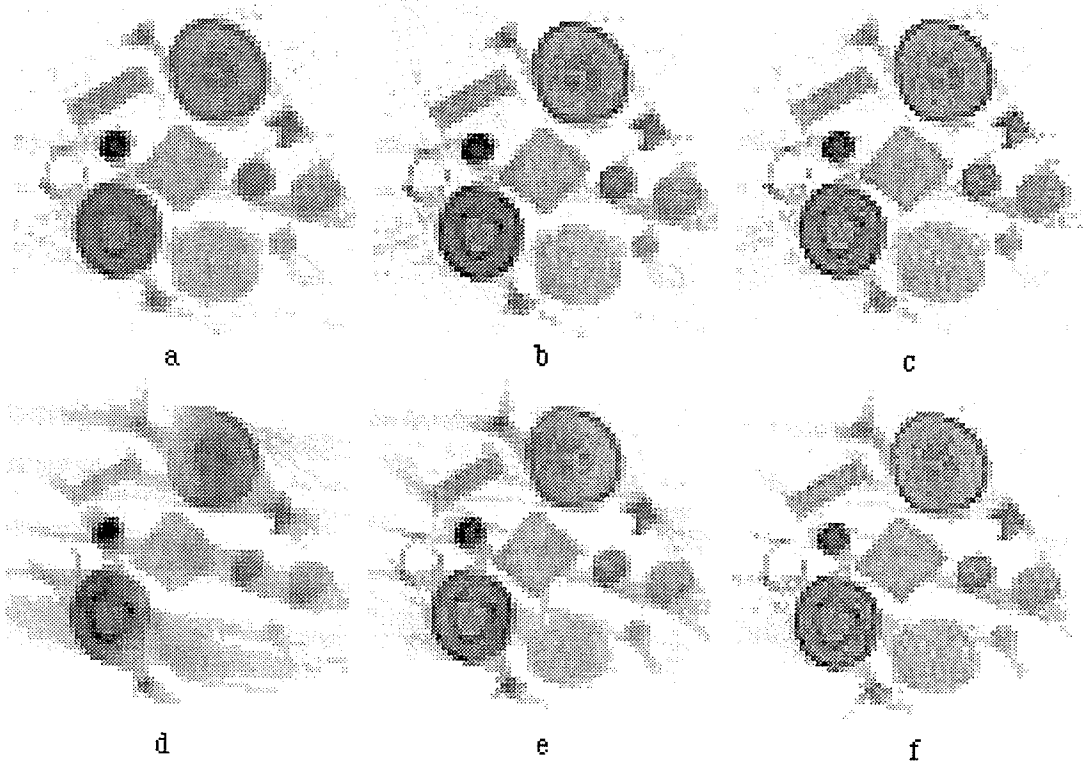

Fig. 7.4.1 Reconstructions of the object COMPLEX from 100 projections. (a), (b) and (c) are by 1, 2 and 4-iteration MLS, respectively. (d), (e) and (f) are the corresponding three reconstructions by SAS, in parallel to (a), (b) and (c) respectively.

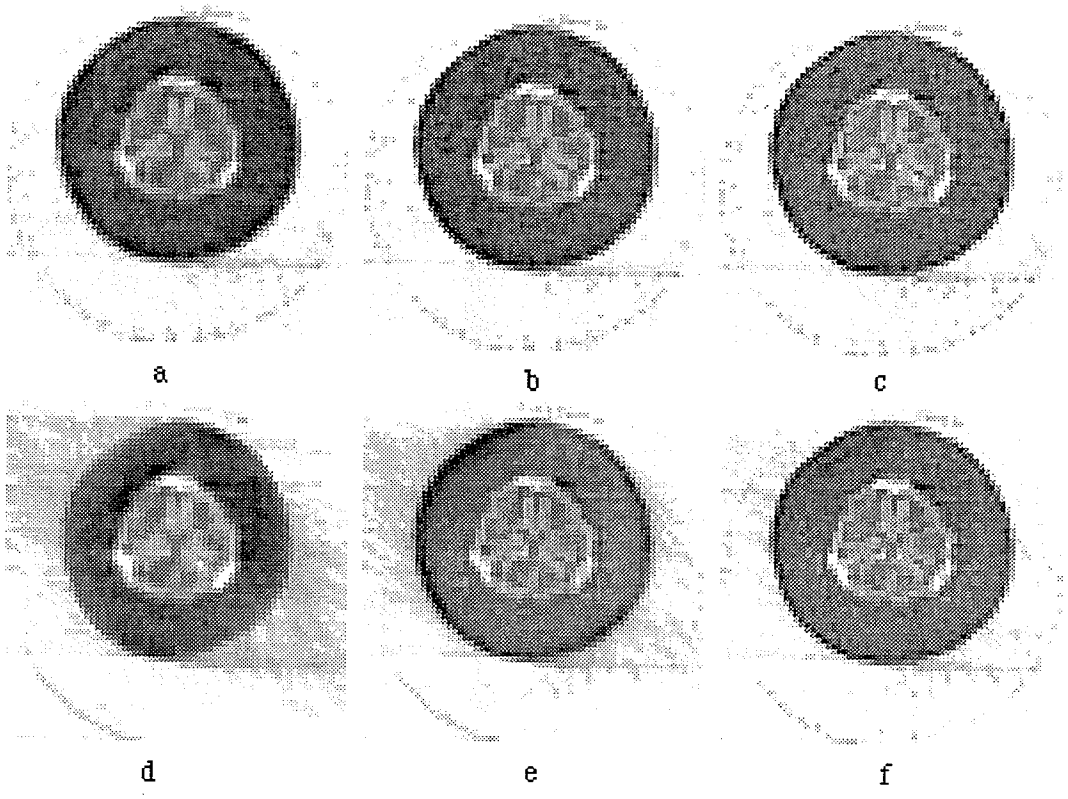

Fig. 7.4.2 Reconstructions of the object DEW from 100 projections. (a), (b) and (c) are by 1, 2 and 4-iteration MLS, respectively. (d), (e) and (f) are the corresponding three reconstructions by SAS, in parallel to (a), (b) and (c) respectively.

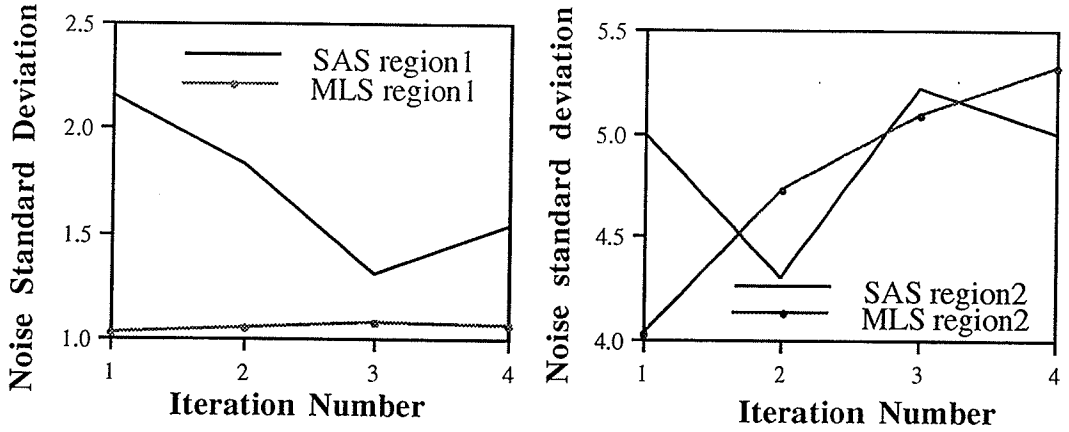

Fig. 7.4.3 The noise standard deviation inside (a) region 1 and (b) region 2 in object COMPLEX (see Fig. 4.2.1b) versus the iteration number of MLS and SAS.

7.2.10a, 512x512, 800 projections), 16-iteration SAS is not enough, although in both situations the sampling criterion Eq. (5.16) was satisfied.

For COMPLEX, we plot in Fig. 7.4.3 the noise standard deviation (SD) measured inside (a) region 1 and (b) region 2 (see Fig. 4.2.1b) versus the iteration number. We found that SAS produces unanimously greater noise than MLS in region 1. In region 2, the SD of SAS, oscillating versus iterations, is always larger than that of 1-iteration MLS.

We also compared MLS to RPS by doing a sample of 1-iteration RPS reconstructions. Fig. 7.4.4 shows 3 images of COMPLEX, (a) is from MLS, (b) and (c) are randomly picked up from the RPS samples. One sees that while (b) is about the same as (a) in visual appearance, (c) is much inferior to (a). Fig. 7.4.5 shows the plots of noise standard deviation measured in the 2 small regions in Fig. 4.2.1b, for a sample of 10 images by RPS. Also plotted, as horizontal lines, are the two values of MLS, each for one region. Clearly, RPS is more noise prone than MLS.

7.5 Discussion and conclusion

The key disadvantage of SAS is that it cannot reconstruct object features uniformly and symmetrically. The features are twisted severely in the early stages of iterations. It is also very hard to reconstruct a low contrast object, especially from a larger number of projections. (For example, for 800 projections, 40 iterations are still far from enough.) Even if a uniform reconstruction is obtained after many iterations, it cannnot show a low contrast detectibility matching that of 1-iteration MLS. Although RPS outperforms SAS dramatically for some orderings, it is not a reliable scheme, let alone being able to produce intermediate multiresolution reconstructions at multilevels as the MLS does (see Figs. 3.8 and 3.11). Also

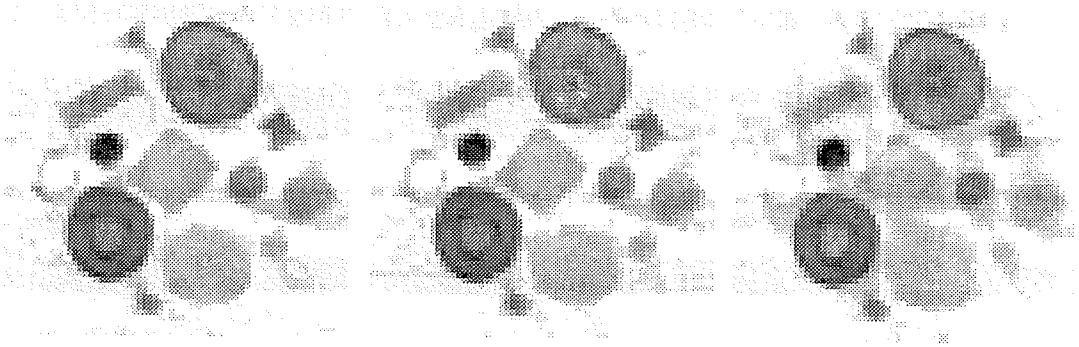

a b c

Fig. 7.4.4 Reconstructions of object COMPLEX from 100 projections. (a) is by 1-iteration MLS. (b) and (c) are picked up from a sample of 1-iteration RPS reconstructions

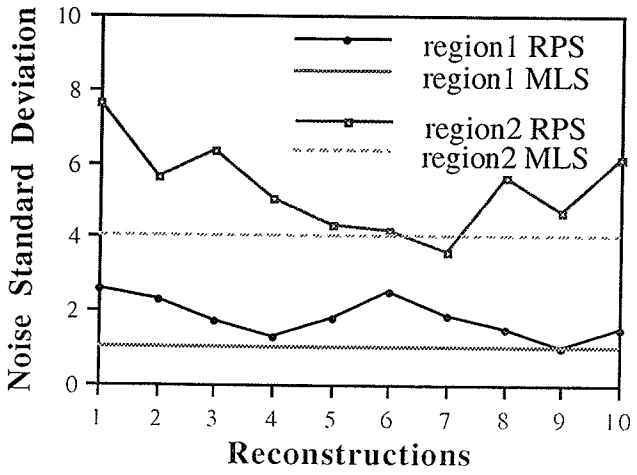

Fig. 7.4.5 Plots of the noise standard deviation inside region 1 and region 2 of object COMPLEX (see Fig.4.2.1b and c) for a sample of 10 1-iteration reconstructions by RPS. Also plotted in horizontal lines are the two values, each for one region, measured from the reconstructions by MLS. Note that since RPS produces less uniform reconstructions than MLS, it is possible that in some small regions, the noise standard deviation of RPS is smaller than that of MLS (see the 7-iteration results in region 2 in this figure).

note that RPS takes time to permute projections, which is not negligible for a large number of projections such as 800.

In conclusion, MLS not only outperforms CBP in many situations as we tested in the last three chapters, but also improves the performance of ART itself as seen in this chapter. At this point, we conclude that MLS is superior to all of the current CT reconstruction techniques, particularly for imaging low contrast objects from smaller numbers of projections.

References

Herman G. T. and L. B. Meyer, Algebraic reconstruction techniques can be made computationally efficient *IEEE Trans. Med. Imaging* 12, 600-609, 1993.

Hounsfield G. N., A method of and apparatus for examination of a body by radiation such as x or gamma radiation. The Patent Office, London, Patent Specification 1283915, 1972.

Kuhl D. E., R. Q. Edwards, A. R. Ricci and M. Reivich, Quantitative section scanning using orthogonal tangent correction, *J. Nucl. Med.* 14, 196-200, 1973.

McClean B. A., T. R. Overton, T. N. Hangartner and S. Rathee, A special purpose x-ray fan-beam CT scanner for trabecular bone density measurement in the appendicular skeleton, *Phys. Med. Biol.* 35, 11-19, 1990.

Rathee S., Z. J. Koles and T. R. Overton, *Image restoration in computed tomography: restoration of experimental CT images, IEEE Trans. Med. Imaging* 11, 546-553, 1992.

Shepp L. A. and B. F. Logan, The Fourier reconstruction of a head section, *IEEE Trans. Nucl. Sci.* 21, 21-43, 1974.

van Dijke M. C. A., *Iterative methods in image reconstruction,* Ph.D. dissertation, Rijksuniversiteit Utrecht, Utrecht, The Netherlands, 1992.

Wowk B., *Computed Gamma Ray Tomography,* Lab report, Department of Physics, University of Manitoba, Winnipeg, Manitoba, Canada, 1992.

Chapter 8
Applications of MLS ART to CT Reconstructions and Recent Progress in CT

In this chapter, we first discuss the applications of MLS ART to diagnostic x-ray CT and other kinds of CT reconstructions in medicine. We then briefly discuss recent progress in CT research and development including CT applications to both basic and applied science research. The MLS scheme can be readily applied to almost all of the recent CT models for improved SNR since in these machines the projection data is limited.

8.1 Dose reduction in x-ray CT

In section 3.6, we suggested that patient dose control in CT is possible if projections are directly taken along the MLS directions and the reconstructions are done at each consecutive MLS level.

The experimental tests made in chapters 4, 5 and 6 further confirm that MLS can reduce patient dosage in two ways, in comparison to CBP: 1. when the number of projections is taken to satisfy the sampling criterion, reducing the number of projections by at least a factor of 2 can preserve the spatial resolution; 2. in situations where a limited amount of projection data can be taken, MLS also needs smaller dosage for low contrast object detections.

For case 1, dose reduction can be made in situations where spatial resolution is of prime concern. For example, in diagnostic CT for imaging small details such as the spine or middle ear and bones such as the temporal bones [Morgan]. If the number of projections reduces from 800 down to 400 projections, then 2 to 3 iteration MLS is required. High spatial resolution CT is also important in the initial assessment and follow-up of patients with

infiltrative lung disease, for which clinical practice has been limited to some extent by concern over the high dose delivered to the thorax [Mayo].

In CT, there is a relationship between patient dosage (D), detector (or beam) width (w), noise standard deviation (σ) and slice thickness (or beam height h) derived by Brooks and Di Chiro [1976]:

$$D \sim \frac{1}{w^3 \sigma^2 h}$$

For a fixed beam height h and beam width w, reducing the standard deviation σ by 2 will quadruple the dosage D. On the other hand, if the standard deviation σ is kept unchanged, reduction of w for a twofold improvement of resolution is at the expense of an eightfold increase in dosage. This means spatial resolution has the strongest effect on the patient dose (if h is chosen to vary in proportion with w, then resolution enters even as a fourth power [Brooks, Barrett]). By using MLS, the improvement in spatial resolution is equivalent to using a smaller size of detector, which technically may be difficult to accomplish.

For case 2, when a limited amount of projection data can be taken, MLS will produce larger SNR than CBP. Further, the smaller the number of projections, the larger the ratio of the MLS dose efficiency over that of CBP.

8.2 More applications of MLS in medicine

MLS can also find applications in medicine in the following areas:

1. Quantitative x-ray CT, particularly bone densitometry [McClean, Goodsitt, Holdsworth, Robertson].
2. CT angiography or DSA using CT [Henri, Stehling, Napel].
3. Emission computed tomography (PET, SPECT) [Herman].

4.Tomographic therapy [Mackie, Brahme, Redpath, Lewis, Swindell, Bortfeld, Webb, Galvin, Iwamoto] and inverse treatment planning [Holmes, Gokhale].

5. CT fluoroscopy [Katada, Hiraoka].

For topic 1, the reconstruction accuracy of the attenuation coefficients is important and information is quantitatively extracted after processing the attenuation map.

For topic 2, imaging blood vessels of small diameter also requires that CT images have higher spatial resolution and accuracy.

For topic 3, emission tomographic reconstruction can obtain the greatest benefits from the new technique for its inherently limited data and for that CBP cannot be employed at all. Recently, Herman [1993] used a projection access order for ART (which is inferior to MLS) applied to PET reconstruction. He found that ART can be made to match the performance of a standard expectation maximization (EM) technique but at an order of magnitude less computations. We expect MLS will provide even better results. Researches to compare MLS with all conventional emission reconstruction techniques such as the EM, the MLE (maximum likelihood estimation) and the MAP (maximum a *posteriori*) can be made based on the physical criteria.

Topic 4 covers new research and development areas in radiotherapy treatment planning by CT. Tomographic therapy, as its name implies, is for radiation treatment made at a number of orientations. The treated volume can be reconstructed by measuring the transmitted rays of treatment beams. An obvious advantage of this technique is to monitor the patient alignment during the treatment. Details of the technique have been discussed by Hendee [1995]. Recently, a therapeutic CT, called CT-PORT, has been developed and

marketed by Toshiba. It was claimed to allow extremely accurate treatment planning and to fully replace the conventional x-ray simulator [Ogino]. Inverse treatment planning, on the other hand, reconstructs the dosage distribution itself instead of the linear attenuation coefficients.

For topic 5, an important potential application of MLS lies in CT fluoroscopy [Katada, Hiraoka], a relatively new concept which has been demonstrated in 1994 and 1995 Radiological Society of North American (RSNA) meeting. A 1-second 3rd-generation scanner has been equipped with a slip ring such that a continuous stream of projections are available. These projections are submitted to a pipeline of 6 independent CBP processors to reconstruct up to 6 images/second (reconstruction time per frame < 0.2s) (The technique, which allows real time viewing, is used in CT guided interventional procedures such as tumor location using needels, etc.) The MLS ART processor may be manufactured to replace the CBP ones to further reduce the reconstruction time by using smaller number of projections without loss of image quality (images of multi-resolution level are available).

8.3 Further advantages of MLS

MLS does not need normalization due to the fact that it modifies the reconstruction to conform to the projection data at each step, while CBP does need normalization to scale the very large pixel values (since the projection data, after being filtered, is further backprojected) down to the CT# range. This suggests that using MLS, the calibration and QA work for CT scanners can be reduced.

Non-linear corrections such as the beam hardening effect can be made during the iterative MLS reconstruction (this can be a future research topic).

Kijewski [1978] once proposed an efficient iterative correction method for multicomponent objects such as the human body. In this method, a preliminary reconstruction is made using the single component (such as water) beam hardening correction algorithm which is detailed in [Barrett]. This eliminates gross shading and cupping artifacts. The resulting image is then subjected to a threshold (any attenuation coefficient larger or smaller than some certain value) or other test which simply determines those parts of the body that contain bone. The algorithm then corrects the projections to account for the different spectral absorption properties in these regions, resulting in an essentially artifact free image. Now we can employ MLS to do this iterative correction more efficiently. (The 1st order correction can be made by 1 iteration. Each higher order can also be made in 1-iteration.) Other artifacts such as those streaks generated from opaque objects (surgical clips, metal implants, dental fillings etc.) can also be minimized by removing rays that pass through or graze them. The corrections on CT using CBP now are made prior to the reconstruction, and hence are less precise.

8.4 Recent progress in CT and its applications

Much research and development in CT now employs synchrotron radiation (SR) for its excellent properties of high monochromaticity (eliminating beam hardening effects), high intensity and tunable energy [Momose, Itai, Nagata, Dilmanian, Zeman, Wu].

The most important progress in SR-CT is the development of phase-contrast x-ray (PCX) CT [Momose] which is an extension of the phase-contrast optical CT [Noda and Cheng] to the x-ray energy range. It provides sectional images of organic materials with high contrast. For organic

materials, the common attenuation x-ray CT produces little contrast. Using PCX-CT, the phase shift (refractive index) integral (in addition to the attenuation integral) is measured across the object with an interferometer. These phase shift integrals taken along different directions were fed into a reconstruction algorithm to produce a phase-contrast tomogram. Highly monochromatic synchrotron radiation x rays with 0.1% FWHM (full width half maximum, ~40% in clinical x-ray CT) make the phase shift measurement feasible.

The chemical shift of an x-ray absorption edge (for example K edge) of an element can also be measured by fluorescence detection with higher sensitivity than that by absorption measurement [Iida]. SR x-rays are used to excite the chemical state of the element. The emitted x-ray fluorescence is detected and then reconstructed (similar to emission computed tomography).

The SR source also allows K-edge subtraction of iodine and other high-Z elements for digital subtraction imaging using CT [Zeman, Wu]. Dual energy scans, one just below and the other just above the K-edge of iodine have been taken and then subtracted. The difference image is basically the iodine attenuation at the K-edge. This is also called single element CT imaging or, dual photon absorptiometry (DPA) [Fryer]. Naturally, with an energy tunable source, multiple elements can be imaged one at a time by SR-CT.

In all of the CT reconstructions using an SR source to date, a limited number of projections have been taken. For example, in [Momose], only 100 phase-shift projections were taken, but the image was reconstructed on a large 512x512 matrix. In [Nagata], the image size is also 512x512 but the number of projections is just 200. In [Iida], the image size is 65x65 and the projection number is 40.

High energy x-rays (bremsstrahlung) of a few MeVs produced from electron linear accelerators have also been used for large and dense object scanning [Kanamori, Isumi], but the projection data are also limited. In [Isumi], a 1024x1024 image is reconstructed from just 900 projections.

CT models using heavy particles have also been developed. Proton CT was shown to have more dose efficiency than x-ray CT to obtain a tomogram of better low contrast resolution. Different properties like energy loss [Hanson], nuclear scattering centers [Duchazeaubeneix] and electron density [Takada] have been measured and reconstructed. Neutron CT [Overlay, McFarland, Pfister] was also built to take advantage of the neutron's unique scattering and absorption properties to study structure and flaw development of materials. Although x-rays are poorly absorbed by light elements, low energy neutrons can interact strongly with light elements. Further, due to the details of nuclear structure, a small difference in atomic number between nuclei can result in interaction properties differing by several orders of magnitude, thus offering the potential of tremendous increases in detection sensitivity. Proton or neutron CT machines are also limited in their ability to take many projections. In [Takada], a 174x174 image is reconstructed from 180 projections. In [McFarland], a number of 512x512 images are reconstructed from only 90 or 45 projections, which is far less than that required by the sampling criterion.

Other types of CT models using different kinds of radiation or interactions, such as infrared [Kassab], ultrasound [Jago], laser [Faris, Kawata], x-ray diffraction [Harding] and biomagnetics [Ramon], etc., are either developed or under investigation. Scattering x-ray CT has been designed to reconstruct the electron density of objects since the Compton cross section is directly proportional to electron density. Dual energy x-rays were also used in CT for

the classification of tissue types by decomposing the attenuation coefficients from Photoelectric and Compton scattering and displaying them in a 2D space [Macovski]. Dual energy CT scans combined with two additional physical quantities of an MRI scan, such as the proton relaxation times (T_1 , T_2) may lead to finer discrimination amongst normal and pathological tissues in a 4D space [Gordon]. CT scanners using different techniques such as film [Segal], nuclear spectroscopy [Martz], and video [Ou] have also been developed.

CT has evolved to a new stage where many applications have been found besides the medical applications. The inner structure of any object can be nondestructively viewed as long as an adequate radiation source and detection system is available. For example, in nuclear physics, CT has been used to determine the relative amount of light collected as the result of the deposition of a known amount of energy at a point within the volume of a scintillating detector [Dowell]. In [Dowell], muons traverse many well defined paths through the scintillator. A CT technique is used to produce 3D images of the nonuniformities in light generation and collection. CT has also been applied to evaluate radioactive objects and materials [Sawicka, Goto, Gould] such as the ceramic reactor-fuel pellets, the nuclear reactor assembly [Kalos]. Applications in geophysics [Kawamura], astronomy [Qiu], plasma physics [Hino], material science and nondestructive testing [Phillips, Bossi, Martz], ionospheric investigation [Raymund], environmental sciences [Brown, Lindgren] and many other areas have been found. There are also experiments applying CT technique for temporal observation of rapidly translating or dynamically deforming objects [Zoltani]. Recently, there is a new and important imaging technique developed in materials science [Wolfe]. It may be adapted to become a phase contrast acoustic CT or phonon CT method.

Conclusion

In conclusion, except for clinical x-ray CT where a large number of projections can be easily taken by its very specific design, almost all other CT applications are limited in the amount of projection data. Usually data acquisition takes too much time or the technique and setup have inherent limitations. In these cases our new MLS reconstruction technique can be readily applied for improved SNR. To date, almost all the non-medical x-ray CT's use CBP for image reconstruction and strong streak artifacts can be seen in the images of many publications, as in phase contrast images [Momose] and in neutron tomograms [McFarland].

References

Barrett H. H. and W. Swindell, *Radiological imaging, the theory of image formation, detection and processing,* Academic Press, 1981.

Bortfeld T., J. Burkelbach, R. Boesecke and W. Schlegel, Methods of image reconstruction from projections applied to conformal radiotherapy, *Phys. Med. Bio.* 35, 1423-1434, 1990.

Bossi R. H. and G. E. Georgeson, The application of x-ray computed tomography to materials development, *JOM- Journal of the minerals, metals & materials society* 43, 8-15, 1991.

Brahme A., B. Lind and P. Nafstadius, Radiotherapeutic computed tomography with scanned photon beams, *International Journal of Radiation Oncology Biology Physics* 13, 95-101, 1987.

Brooks R. A. and G. Di Chiro, Statistical limitations in x-ray reconstructive tomography, *Med. Phys.* 3, 237-240, 1982.

Brown G. O., M. L. Stone and J. E. Gazin, Accuracy of gamma-ray computerized tomography in porous media, *Water Resources Research* 29, 479-486, 1993.

Cheng Y. S., Two-dimensional grating interferometric imaging by computed tomography, *Optics Letters* 4, 230-232, 1987.

Dilmanian F. A., Computed tomography with monochromatic x-rays from the National-Synchrotron-Light-Source, *Nuclear Instruments & Methods in Physics Research B* 56-7, 1208-1213, 1991.

Dowell D. H., Computed tomography of scintillates with muons - understanding the response to high energy gamma-rays, *Nuclear Instruments & Methods in Physics Research A* 286, 183-201, 1990.

Duchazeaubeneix J. C., *J. Comput. Assist. Tomogr* . 4, 803, 1980.

Faris G. W. and R. L. Byer, Quantitative optical tomographic imaging of a supersonic jet, *Optics letters* 11, 413-415, 1986.

Fryar J., K. J. McCarthy and A. Fenelon, Multielement imaging in computerized x-ray tomography, *Nuclear Instruments & Methods in Physics Research A* 271, 671-677, 1988.

Fryar J., K. J. McCarthy and A. Fenelon, Differential x-ray absorptiometry applied to computerized x-ray tomography, *Nuclear Instruments & Methods in Physics Research A* 259, 557-565, 1987.

Galvin J. M., C. Sims, G. Dominiak and J. S. Cooper, The use of digitally reconstructed radiographs for 3D treatment planning and CT simulation, *International Journal of Radiation Oncology Biology Physics* 31, 935-942, 1995.

Goodsitt M. M. and R. H. Johnson, Precision in quantitative CT - impact of x-ray dose and matrix size, *Med. Phys.* 19, 1025-1036, 1992.

Gokhale P. and E. M. A. Mussein, Determination of beam orientation in radiotherapy planning, *Med. Phys.* 21, 393-400, 1994.

Gordon R. and J. Coumans, Combining multiple imaging techniques for *in vivo* pathology: a quantitative method for coupling new imaging modalities, *Med. Phys.* 11, 79-80, 1984.

Goto T. and H. Kato, A radioactivity assay-method using computed tomography, *Nuclear Technology* 100, 322-330, 1992.

Gould R. and Kenney E. S., Image reconstruction for a radiation-field mapping device, *Nuclear Technology* 89, 247-251, 1990.

Hanson K. M., J. N. Bradbury, T.M. Cannon, R. L. Hutson, D. B. Laubacher, R. J. Macek, M. A. Paciotti and C.A. Taylor, Computed tomography using proton energy loss, *Phys. Med. Biol.* 26, 965-983, 1981.

Harding G., J. Kosanetzky and U. Neitzel, X-ray diffraction computed tomography, *Med. Phys.* 14, 515-525, 1987.

Hendee W. R., X rays in medicine, *Physics Today*, Nov. issue, 51-56, 1995.

Herman G. T. and L. B. Meyer, Algebraic reconstruction techniques can be made computationally efficient, *IEEE Trans. Med. Imaging* 12, 600-609, 1993.

Holmes T. W. and T. R. Mackie, A filtered backprojection dose calculation method for inverse treatment planning, *Med. Phys.* 21, 303-314, 1994.

Hino M., T. Aoto, M. Nakajima and S. Yuta, Light-emission computed tomography system for plasma diagnostics, *Applied Optics* 26, 4742-4746, 1987.

Hiraoka H., T. Rifu and B. Westerman, Physical characterization of CT fluoroscopy, *Radiology* 196, Nov. issue (RSNA scientific program), 431-431, 1995.

Holdsworth D. W., M. Drangova and A Fenster, A high-resolution XRII-based quantitative volume CT scanner, *Med. Phys.* 20, 449-462, 1993.

Iida A., M. Takahashi, Y. Gohshi and K. Sakurai, SR x-ray based fluorescence imaging by image reconstruction technique, *Rev. Sci. Instrum.* 60, 2458-2461, 1989.

Itai Y., High contrast computed tomography with synchrotron-radiation, *Review of Scientific Instruments* 66, 1385-1387, 1995.

Iwamoto K. S., A. Norman, A. R. Kagan, M. Wollin, A. Olch, J. Bellotti, M. Ingram and R. G. Skillen, The CT scanner as a therapy machine, *Radiotherapy and Oncology*, 19, 337-343, 1990.

Izumi S., S. Kamata, K. Satoh and H. Miyai, High energy computed tomography for industrial applications, *IEEE Trans. Nucl. Sci.* 40, 158-161, 1993.

Jago J. R. and T. A. Whittingham, Experimental studies in transmission ultrasound computed tomography, *Phys. Med. Biol.* 36, 1515-1527, 1991.

Kalos M. H., S. A. Davis, P. S. Mittelman and P. Mastras, *Conceptual Design of a vapor fraction instrument.*, White Plains, NY: Nuclear Development Corp. of America, pp. 31, 1961.

Kanamori T., S. Kamata and S. Ito, Cross-sectional imaging of large and dense materials by high energy x-ray CT using linear accelerator, *Journal of Nuclear Science and Technology* 26, 826-832, 1989.

Kassab A. J. and C. K. Hsieh, Application of infrared-scanners and inverse heat-conduction methods to infrared computerized axial tomography, *Review of Scientific Instruments* 58, 89-95, 1987.

Katada K., H. Anno, S. Koga, Y. Ida and S. Sata, Initial trial with CT fluoroscopy, *Radiology* 190, 622-622, 1994.

Kawamura T., Nondestructive, 3-Dimensional density measurements of ice core samples by x-ray computed tomography, *Journal of Geophysical Research - Solid Earth and Planets* 95, 2407-2412, 1990.

Kawata S., O. Nakamura, T. Noda, H. Ooki, K. Ogino, Y. Kuroiwa and S. Minami, Laser computed tomography microscope, *Applied Optics* 29, 3805-3809, 1990.

Kijewski P. K. and B. E. Bjarngard, Correction for beam hardening in computed tomography, *Med. Phys.* 5, 209-211, 1978.

Krestel E., *Imaging systems for medical diagnostics*, Siemens Medical Division, 1991.

Lewis D. G., W. Swindell, E. J. Morton, P. M. Evans and Z. R. Xiao, A megavoltage CT scanner for radiotherapy verification, *Phys. Med. Biol.* 37, 1985-1999, 1992.

Lindgren L. D., Medical CAT-scanning - x-ray absorption coefficients, CT-numbers and their relation to wood density, *Wood Science and Technology* 25, 341-349, 1991.

Mackie T. R., Tomotherapy: A new concept for the delivery of dynamic conformal radiotherapy, *Med. Phys.* 20, 1709-1719, 1993.

Macovski A., R. E. Alvarez, J. L.-H. Chan, J. P. Stonestrom and L. M. Zatz, Energy dependent reconstruction in x-ray computerized tomography, *Comput. Biol. Med.* 6, 325-336, 1976.

Martz H. E., G. P. Roberson, D. J. Schneberk and S. G. Azevedo, Nuclear-spectroscopy based, 1st-generation, computerized tomography scanners, *IEEE. Trans. Nucl. Sci.* 38, 623-635, 1991.

Martz H. E., G. P. Roberson, M. F. Skeate, D. J. Schneberk, and S. G. Azevedo, Computerized tomography studies of concrete samples, *Nuclear Instruments & Methods in Physics Research B* 58, 216-226, 1991.

Mayo J. R., S. A. Jackson and N. L. Muller, High resolution CT of the chest - radiation dose, *American Journal of Roentgenology* 160, 479-481, 1993.

McClean B. A., T. R. Overton, T. N. Hangartner and S. Rathee, A special purpose x-ray fan-beam CT scanner for trabecular bone density measurement in the appendicular skeleton, *Phys. Med. Biol.* 35, 11-19, 1990.

McFarland E. W., R. C. Lanza and G. W. Poulos, Multidimensional neutron-computed tomography using cooled charge-coupled-devices, *IEEE Trans. Nucl. Sci.* 38, 612-622, 1991.

Morgan C. L., *Basic principles of computed tomography,* University Park Press, Baltimore, 1983.

Momose A., Demonstration of Phase-contrast x-ray computed tomography using an x-ray interferometer, Nuclear Instruments & Methods in Physics Research A 352, 622-628, 1995.

Momose A., T. Takeda and Y. Itai, Phase-contrast x-ray computed tomography for observing biological specimens and organic materials, *Rev. Sci. Instrum.* 66, 1434-1436, 1995.

Nagata Y., H. Yamaji, K. Hayashi, K. Kawashima, K. Hyodo, H. Kawata and M. Ando, High energy high resolution monochromatic x-ray computed tomography using the photon factory vertical wiggler beamline, *Rev. Sci. Instrum.* 63, 615-618, 1992.

Napel S., CT angiography with spiral CT and maximum intensity projection, *Radiology* 185, 607-610, 1992.

Noda T., S. Kawata and S. Minami, 3-Dimensional phase contrast imaging by a computed tomography microscope, *Applied Optics* 31, 670-674, 1992.

Ogino T., W. Shimizu and N. Moriyama, "CT Port" as a radiation therapy treatment-planning system with helical CT (SE), *Radiology* 197, Nov. issue (RSNA scientific program), p446, 1995.

Overlay J. C., Element-sensitive computed tomography with fast neutrons, *Nuclear Instruments & Methods in Physics Research B*, 24-5, 1058-1062, 1987.

Ou L. Z., M. Colman, O. Nalcioglu, B. Rabbani and W. W. Roeck, Video based x-ray computed tomography, *IEEE Trans. Nucl. Sci.* 33, 527-530, 1986.

Pfister G., A. K. Schatz, C. Siegel, E. Steichele, W. Waschkowski and T. Bucherl, Nondestructive testing of materials and components by computerized tomography with fast and thermal reactor neutrons, *Nuclear Science and Engineering* 110, 303-315, 1992.

Phillips D. H. and J. J. Lannutti, X-ray computed tomography for the testing and evaluation of ceramic processes, *American Ceremic Society Bulletin* 72, 69, 1993.

Qiu P., Y. Qiu, P. Qian and Z. Liu, High resolution image-reconstruction at Yunnan-Observatory, *IAU Symposia* 158, 346-348, 1994.

Ramon. C, M. G. Meyer, A. C. Nelson, F. A. Spelman and J. Lamping, Simulation studies of biomagnetic computed tomography, *IEEE Trans. Bio. engineering* 40, 317-322, 1993.

Raymund T. D., J. R. Austen, S. J. Franke, C. H. Liu, J. A. Klobuchar and J. Stalker, Application of computerized tomography to the investigation of ionospheric structures, *Radio Science* 25, 771-789, 1990.

Redpath A. T., Computerized tomography on a radiotherapy simulator, *Phys. Med. Bio.* 32, 286-286, 1987.

Robertson D. D. and H. K. Huang, Quantitative bone measurements using x-ray computed tomography with 2nd order correction, *Med. Phys.* 13, 474-479, 1986.

Sawicka B. D., Computed tomography of radioactive objects and materials, *Nuclear Instruments & Methods in Physics Research A* 299, 468-479, 1990.

Segal Y. and Cohen B., Film based industrial computerized tomography, *Nuclear Instruments & Methods in Physics Research A* 254, 202-209, 1987.

Stehling M. K., J. A. Lawrence, J. L. Weintraub and V. Raptopoulos, CT angiography -expanded clinical applications, *American Journal of Roentgenology* 163, 947-955, 1994.

Swindell W., E. J. Morton, P. M. Evans and D. G. Lewis, The design of megavoltage projection imaging system: Some theoretical aspects, *Med. Phys.* 18, 855-866, 1991.

Takada Y., K. Kondo, T. Marume, K. Nagayoshi, I. Okada and K. Takikawa, Proton computed tomography with a 250 MeV pulsed-beam, *Nuclear Instruments & Methods in Physics Research A* , 273, 410-422, 1988.

Takada Y. and I. Abe, Multiple pencil beams for proton computed tomography, *Nuclear Instruments & Methods in Physics Research A* 262, 511-521, 1987.

Webb S., Nonstandard CT-scanners - their role in radiotherapy, *International Journal of Radiation Oncology Biology Physics* 19, 1589-1607, 1990.

Wolfe J. P., Acoustic wavefronts in crystalline solids (new imaging techniques have made possible the first observations of vibrational wavefronts from point sources, providing insight into the propagation and interference of acoustic waves in solids), *Physics Today*, Sept. issue, 34-40, 1995.

Wu X. Y., Multiple energy computed tomography (MECT) at the NSLS - status report, *Review of Scientific Instruments* 66, 1346-1347, 1995.

Zeman H. D., An x-ray monochromator for dual-energy computerized tomography using synchrotron radiation, *Nuclear Instruments & Methods in Physics Research B* 56-7, 1218-1222, 1991.

Zoltani C. K., F. A. Dibianca and K. J. White, Flash x-ray computed tomography facility for microsecond events, *Rev. Sci. Instrum.* 57, 602-611, 1986.

Chapter 9 Discussion, Conclusion and Future Work

In this chapter, we first summarize a conclusion of the thesis work. After that, we propose some topics for future studies.

9.1 Discussion and Conclusion

Morgan [1983] (also see [Brooks 1976b]) once pointed out that there are two major limitations of CBP: 1. bandlimiting and 2. interpolation, both affecting the spatial resolution. Although the backprojection can be made without interpolation (at the cost of reducing reconstruction speed), the bandlimiting cannot be improved since CBP itself is an integration method and it suffers from bandlimiting in digital situations. He also indicated that there are two major limitations of ART: 1. slow speed and 2. possible lack of convergence, both affecting the image quality and speed. We see that with the advent of new MLS technique, both the drawbacks of ART are addressed.

The MLS ART may be applied to solve other large non-tomographic linear systems when the unknowns are also similarly intercorrelated. For example, it might be applicable for solving multi-body interaction problems in quantum mechanics. It may also be useful in the design of large electronic circuit networks and control systems, etc. The solution can be initially coarse and then refined gradually.

It is worth noting that although there are some parallel implementations of ART [Fitchett] which can also appreciably increase the computational speed of classical ART, they can not produce image qualities matching those produced from the MLS ART in noisy situations. Unless the parallelism is

also confined to pairs of projections approximately 90° apart, the correlations between neighboring projections will still exist.

In this thesis we proposed a novel algebraic image reconstruction technique for computed tomography in which the projections are arranged and accessed in a multilevel scheme (MLS). Extensive tests using various sources of data confirmed that the scheme outperforms the conventional convolution backprojection (CBP) method, by producing a larger MTF when the number of projections is taken above half of that required by the sampling criterion and a larger SNR when the number is taken below that half. It also improves the performance of ART itself, in both the computational speed (by more than 10 times) and the physical image quality (both the high and low contrast detectibilities).

9.2 Future work

Future work can be classified into three different categories: 1) further comparison study between CBP and MLS by employing more sophisticated image quality criteria and using real data, 2) further CT reconstruction research topics based on the MLS technique itself, and 3) the implementation of MLS on modern fan beam CT scanners.

9.2.1 Sophisticated physical measures and real data determination

The comparison studies made in chapters 4-7 can be further extended by employing more sophisticated physical criteria. These measures are either the spatial frequency dependent ones, or quantities based on the different models of the detection process. From the measured MTF, NPS (as in Chapter 5),

and/or the visual spatial frequency response function (VRF), the more complicated measures listed below can be calculated.

Spatial frequency dependent measures These measures include the signal-to-noise ratio (SNR), the detective quantum efficiency (DQE) and the noise equivalent quanta (NEQ). The $SNR(f)$ is defined as [Munro]

$$SNR^2(f) = \frac{S^2(f) \cdot MTF^2(f)}{NPS(f)} \tag{9.1}$$

where $S(f)$ is the sinusoidally varying unit contrast input signal [Doi, Nishikawa] and $S(f) \cdot MTF(f)$ is the output signal.

The $DQE(f)$ is a measure of the efficiency of a real detector compared to an ideal detector which is capable of detecting all of the quanta and adding no additional noise to the image. It is defined as [Munro, Barrett]

$$DQE(f) = [SNR_{out}(f) / SNR_{in}(f)]^2 \tag{9.2}$$

Considering $SNR_{in}(f) = S(f)\sqrt{N}$ for an x-ray beam of N incident quantas which obeys Poission statistics, Eq. (9.2) becomes

$$DQE(f) = MTF^2(f) / [N \cdot NPS(f)]$$

The noise equivalent quanta (NEQ) is the multiplication of DQE with the number of input x-ray quanta N, or

$$NEQ(f) = N \cdot DQE(f) = MTF^2(f) / NPS(f) \tag{9.3}$$

Measures based on the detection process models The relationship between the physical and visual image quality was investigated by Loo et al. [1984] for the task of detecting nylon beads in radiographs. They calculated the physical image quality according to different models of the detection process. The results of the work indicate that human detection performance

most closely resembles that of a sub-optimal statistical decision process whose SNR is in the form of

$$SNR^2 = \frac{(2\pi\int_0^\infty u \cdot S_s^2(u) \cdot VRF^2(u)du)^2}{2\pi\int_0^\infty u \cdot (S_s^2(u)VRF^2(u)) \cdot (S_w(u)VRF^2(u))du} \qquad (9.4)$$

where $S_s(u)$ and $S_w(u)$are the signal and noise power spectra, respectively and $VRF(u)$ is the visual response function of human eyes [Carlson].

Experimental determination of physical measures Tests can be further made using the real projection data taken from clinical x-ray CT. Picker International [Picker] kindly provided scan data from a series of CT quality assurance phantoms. Therefore all the quantities can be precisely measured or calculated.

9. 2. 2 Further CT reconstruction research topics

Besides those applications MLS can find in CT reconstructions (see sections 8.2 and 8.3) such that corresponding researches can be carried out, some further research topics based on MLS are outlined as follows:

1. Apply MLS for reconstructions using incomplete data (less than 180° view, missed rays or projections, part of an object scanned etc.) which occasionally happens in industrial tomography. In these situations, classical ART produces better results than CBP. We expect MLS-ART can do even better work.

2. Incorporate a *priori* information for the reconstruction. The information can be obtained either from an adjacent slice of the cross section to be reconstructed, or from an estimation of the information content of projection data using some modeling techniques, such as those in [Soderstrom, Gokhale]. MLS can then start with the projection containing the largest high frequency

information. A different way is to take a few projections first and then do the reconstruction. Further projections can then be selectively taken. Henri et al. [1993] performed an analysis of the projection geometry for few projection reconstructions of sparse objects. Their interests lie in reconstructing cerebral vasculature from a limited set of digital subtraction angiography (DSA) data, which remains the preferred method for imaging blood vessels.

3. Apply Wiener deconvolution of the point spread function (PSF) of the "reconstruction operator" [Dhawan] for MLS ART. This will further improve the high and low contrast detectibilities of CT reconstructions, especially from a limited number of projections. Since the PSF of CT is not quite space invariant [Barrett], those methods used by Rathee [1992] for non-linear CT image restoration can be readily employed.

4. Apply MLS ART to the modern spiral/helical CT and cone beam CT. In the past several years, the major thrust in CT has been to improve the reconstruction algorithms for spiral/helical CT [Wang, Vannier, Kalender] and cone beam CT obtained using area detectors [Smith, Wang 1993, Lee, Chen]. The primary advantage of spiral/helical CT is its capability of scanning a complete anatomical volume in a single breath hold, ensuring slice-to-slice contiguity. Spiral/helical CT requires that planar projection sets be produced from raw helical scan data via interpolation. We can apply the MLS version for fan beam geometry as described below to do helical CT reconstructions using the planar data after the interpolation. The MLS ordering can also be directly used for cone beam reconstruction using ART or other techniques.

5. Feasibility investigation of CT mammography. The typical skin dosage for a routine mammography is ~450$mRad$ (2 exposures), and the x-ray beam energy is ~ 20KeV. For this energy, $(\frac{\mu_{ab}}{\rho})_a$ = 0.4942 cm^2/g and $(\frac{\mu_{ab}}{\rho})_f$=0.5026 cm^2/g. Combining Eqs. (5.5), (5.6) and (5.7) will yield

$$\Phi = 6.11 \times 10^9 D_t / cm^2$$

For $D_t = 0.45 Rad$, the incident photon fluence $\Phi = 2.75 \times 10^9 / cm^2$. Suppose the scanning slice has a diameter of L=10mm. ($\mu L = 7.72$) For a reasonable spatial resolution, we assume thickness of h=1.0mm., and the detector width w=1.0mm , then a total of $n_0 = \Phi hw = 2.75 \times 10^7$ photons can be used and the detected photons will be

$$n = n_0 e^{-\mu L} = 2.75 \times 10^7 \times 5 \times 10^{-4} = 1.38 \times 10^3$$

If we expect the uncertainty of detected photons ≤~1% (in the clinical CT level), then marginally only 1 projection can be taken. Therefore it is worth to investigate how the spatial and low contrast detectibilities varies with different number of projections, or different number of x-ray quanta per detector reading, under the constraint of a fixed total dosage. Higher energy x-rays may also be used to improve the noise statistics at the cost of reduced contrast.

9. 2. 3 Implementation of MLS in fan beam CT scanners

The MLS scheme so far is only applied for parallel projections. In modern CT machines including spiral/helical ones, fan beams are commonly used for fast imaging. The scanning generally covers 0°-360°. One way of using MLS is to remap the divergent projections into parallel ones. Since the remapped data also spans 0°-360°, one must first employ the MLS scheme to reorder the projections in between 0°-180° and then to those in between 180°-360°.

We can also consider rearranging the fan beam data itself. The direct employment of MLS won't work efficiently for ordering projections. For example, in the Siemens Somotom-Plus scanner, the fan beam opening angle is 42.5°, the minimum intersection angle of rays in two projections 90° apart can be as low as 47.5° (see Fig. 9.1). To avoid this problem, one idea may be

as follows. For a pair of projections 90° apart, instead of updating all the rays in one projection and then all those in the other, we can update, one ray in one projection and one in the other, with the two perpendicular to each other. For instance, in Fig. 9.1, the update sequence is: ray 1 in 0° view and then ray 1 in 90° view, and ray 2 in 0° view and then ray 2 in 90° view... The update continues for rays in the next pair of projections: 45° and 135°. An even better way is to update all rays having the same index number, each from one projection, in the MLS ordering. Suppose there are a total of R rays in one projection, then the update will take R rounds to update the projections in 0°-180°. In one round, the situation is exactly the same as that for parallel projections. A more efficient way is to update rays in bundles since a bundle of rays covering a small angle is still reasonably close to parallel.

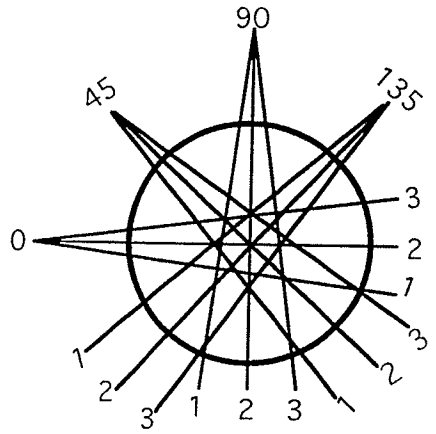

Fig. 9.1 A schematic diagram for fan-beam CT projections.

References

Barrett H. H. and W. Swindell, *Radiological imaging, the theory of image formation, detection and processing* (Academic Press), Vol. 2, 1981.

Brooks R. A. and G. Di Chiro, Principles of computer assisted tomography, *Phys. Med. Biol.* 21, 689-732, 1976b.

Carlson C. R., R. W. Cohen and I. Gorog, Vision Research 17, 351, 1977.

Chakraborty D. P. and G. T. Barnes, Signal-to-noise ratio considerations in radiological imaging, *Med. Phys.* 10, 467-469, 1983.

Chen J., A theoretical framework of regional cone-beam tomography, *IEEE Trans. Med. Imag. 11*, 342-350, 1992.

Cohen G., D. L. McDaniel and L. K. Wagner, Analysis of variations in contrast-detail experiments, *Med. Phys.* 11, 469-473, 1984.

Dhawan A. P., *NEVOSCOPY: Three-dimensional computed tomography of nevi and melanomas in situ by transillumination to detect early cutaneous malignant melanomas,* Ph.D. thesis, University of Manitoba, 1985.

Dhawan A. P., R. M. Rangayyan & R. Gordon, Image restoration by Wiener deconvolution in limited-view computed tomography, *Applied Optics* 24, 4013-4020, 1985.

Doi K., *MTF's and Wiener spectra of radiographic screen-film systems,* HHS Publ. No. 82-8187 (FDA), 1982.

Fitchett J. W., *A locally synchronous globally asynchronous vertex-8 processing element for image reconstruction on a mesh,* M.Sc. thesis, University of Manitoba, Winnipeg, Canada, 1993.

Gokhale P. and E. M. A. Mussein, Determination of beam orientation in radiotherapy planning, *Med. Phys.* 21, 393-400, 1994.

Henri C. J., D. L. Collins and T. M. Peters, Analysis of projection geometry for few-view reconstruction of sparse objects, *Med. Phys.* 20, 1537-1547, 1993.

Kalender W. A., Spiral CT: physical principles, image quality and applications, *Radiology* 196 (Nov.), 52, 1995.

Katada K., H. Anno, S. Koga, Y. Ida and S. Sata, Initial trial with CT fluoroscopy, *Radiology* 190, 622-622, 1994.

Lattard D. and G. Mazare, A VLSI implementation of parallel image reconstruction, *CVGIP: Graphical Models and Image Processig* 53, 581-591, 1991.

Lee S. Z., J. B. Ra, S. K. Hilal and Z. H. Cho, True three-dimensional cone beam reconstruction (TTCR) algorithm, *IEEE Trans. Med. Imag. 8,* 304-312, 1989.

Loo L. D., K. Doi and C. E. Metz, A comparison of physical image quality indices and observer performance in the radiographic detection of nylon beads, *Phys. Med. Biol.* 29, 837-856, 1984.

Munro P. F., J. A. Rawlinson and A. Fenster, Therapy imaging: A signal-to-noise analysis of metal plate/film detectors, *Med. Phys.* 14, 975-984, 1987.

Nishikawa R. M. and M. J. Yaffe, Signal-to-noise properties of mammographic film-screen systems, *Med. Phys.* 12, 32-39, 1985.

Ogino T., W. Shimizu and N. Moriyama, "CT Port" as a radiation therapy treatment-planning system with helical CT (SE), *Radiology* 197 (Nov.), 446, 1995.

Picker International, *Software documentation for CT data acquisition* (proprietary information), 1995.

Rathee S., Z. J. Koles and T. R. Overton, Image restoration in computed tomography: Restoration of experimental CT images, *IEEE Trans. Med. Imag.* 11, 546-553, 1992.

Smith B. D., Cone beam tomography: Recent advances and a tutorial review, *Opt. Eng.* 29, 524-534, 1990.

Soderstrom S. and A. Brahme, Selection of suitable beam orientations in radiation therapy using entropy and Fourier transform measures, *Phys. Med. Biol.* 37, 911-924, 1992.

Vannier M. W and G. Wang, Spiral CT refines temporal bone imaging, Diagnostic Imaging 15, 116-121, 1993.

Vannier M. W and G. Wang, M. W. Skinner and G. H. Esselman, Imaging the temporal bone by spiral CT, MEDIZIN IM BILD 1, 23-29, 1995.

Wang G. and M. W. Vannier, Longitudinal resolution in volumetric x-ray computerized tomography - Analytical comparison between conventional and helical computerized tomography, *Med. Phys.* 21, 429-33, 1994.

Wang G. and M. W. Vannier, Longitudinal resolution in volumetric x-ray computerized tomography - Analytical comparison between conventional and helical computerized tomography, *Med. Phys.* 21, 429-33, 1994.

Wang G., J. A. Brink and M. W. Vannier, Theoretical FWTM values in helical CT, *Med. Phys.* 21, 753-4, 1994.

Wang G. and M. W. Vannier, Spatial variation of section sensitivity profile in spiral computed tomography, *Med. Phys.* 21, 1491-7, 1994.

Wang G. and M. W. Vannier, Preliminary study on helical CT algorithms for patient motion estimation and compensation, *IEEE Trans. Med. Imag. 14*, 205-211, 1995.

Wang G., T. Lin, P. Cheng and D. M. Shinozaki, A general cone beam reconstruction algorithm, *IEEE Trans. Med. Imag. 12* , 486-496, 1993.

Appendix The Computer Source Codes

The source codes listed in this appendix are written in Pascal (for Sun workstations) and used throughout the thesis. They consist of two parts. Part I are the procedures for image reconstruction for both the MLS ART and CBP, which includes projecting an image for a set of projection data, projecting and reconstructing one projection, adding Gaussian noise to a projection etc. Part II are the codes for constructing test phantoms in Chapter 5. In each part, we first gave a short explanation for each procedure (their *objective*, their typical *input* and *output* plus an additional *note*). The computer codes are listed afterwards.

Part I

procedure FullProjection(var vsize, hsize: integer);
Objective: Full projection of an input image to get a set of projection data.
Input: an image *im* of size 512 x512 (*vsize* x *hsize*) read in from an external text file.
Output: a total of *nproj* projections stored in the array *ptheta* , with its weight matrix strored in the array *W*, where *k* is the projection index and *j* is the ray index.
Note: Linear interpolation is used when doing the projection.

procedure OneProjection(projnum: integer);
Objective: Get one projection (i.e. reprojection) from an intermediate ART reconstruction.
Input: the projection index *projnum* and the image *im* reconstructed from the previous projections.
Output: the single projection data stored in the array *pthetaq* with *k* = *projnum* .
Note: Linear interpolation is used when doing the projection. The image *im* will be updated in the procedure *imodification* below, by comparing this projection with the actual projection data stored in the array *ptheta.*

procedure imodification(projnum: integer);
Objective: update the image *im* one projection at a time by ART.
Input: the projection data obtained from the procedure *OneProjection (projnum)* above.
Output: the updated image *im* by ART.
Note: Linear interpolation is used when doing the image modification.

procedure ReconsOneProj (projnum: integer);
Objective: backprojection of one projection indexed *projnum* to the image *im* by CBP.
Input: the projection data after convolution filtration using the procedure *ConvFilteringProjection* below.
Output: the updated image *im* by CBP.
Note: Linear interpolation is used when doing the backprojection.

procedure ProjectionData;
Objective: Full projection of an image *im* to get a set of projection data.
Input: an image *im* of size 512 x512 (*vsize* x *hsize*).
Output: a total of *nproj* projections stored in the array *p* , with its weight matrix strored in the array *w*, where *k* is the projection index and *d* is the ray index.
Note: this is the same procedure as the *FullProjection* above except for that precise projection instead of linear interpolation is used when doing the calculation. It is slower although more accurate.

procedure OneProjectionAndModification(k: integer);
Objective: Get one projection (i.e. reprojection) from an intermediate ART reconstruction *im* and update *im* using this projection.
Input: the projection index *k* and the image *im* reconstructed from the previous projections.
Output: the updated image *im* by ART.
Note: this is the procedure combining both the *OneProjection and imodification* above. Further, precise projection instead of linear interpolation is used when doing the calculation. It is slower although more accurate.

procedure ReconstructionOneProjection(k: integer);
Objective: backprojection of a single projection indexed *k* to the image *im* by CBP.
Input: the projection data after convolution filtration using the procedure *ConvFilteringProjection* below.
Output: the updated image *im* by CBP.
Note: this is the same procedure as the *FullProjection* above except for that precise projection instead of linear interpolation is used when doing the calculation. It is slower although more accurate.

procedure AddPhotonNoise;
Objective: Add Gaussian noise to a set of projection data.
Input: the pseudo projection data calculated either from the procedure*FullProjection* or from the procedure *ProjectionData.*
Output: the noisy projection data to simulate real CT data.
Note: See Section 5.2 for more detail.

procedure MLSProjectionOrders;
Objective: calculate the MLS orders for a total of *nproj* projections.
Input: the number of projections *nproj* .
Output: the MLS order of the *nproj* projections stored in the 1D array *projord.*
Note: the algorithm is detailed in
H. Guan and R. Gordon, A projection access order for speedy convergence of algebraic reconstructions techniques (ART): A multilevelscheme (MLS) for computed tomography, Phys. in Med. and Biol. 39, 2005-2022, 1994.

procedure ConvFilteringProjection (fBAND: integer);
Objective: Convolution filtration (fBAND=1) of a set of *nproj* projection data by CBP.
Input: a set of *nproj* projections data stored in the array *p*
Output: the set of *nproj* projections data after convolution filtration. They are stored in the same array *p* (replace the input).
Note: See Section 2.3.1 for more detail.

Computer codes:

```
{Full Projection of an input image to get a set of projection data. Linear interpolation is used}
    procedure FullProjection(var vsize, hsize: integer);
            var
            theta, costh, sinth, tr, pthmax, pthmin, total: real;
            i, j, k, t: integer;
            dFile: text;
    begin
            reset(dFile, 'input.dat'); {read input image}
            vsize:=512;
            hsize:=512;
            for i := -vsize div 2 to vsize div 2 - 1 do
                    for j := -hsize div 2 to hsize div 2 - 1 do
                            read(dFile, im^[i, j]);
            close(dFile);
            pthmax := -maxint;
            pthmin := maxint;

            {initialize the projection and the weight array}
```

```
{ptheta is the actual projection array,
{pthetaq is the array store temporary projection
 for updating}
for i := 0 to nproj - 1 do
        for j := -hsize to hsize - 1 do
                begin
                        ptheta^[i, j] := 0;
                        pthetaq^[i, j] := 0;
                        W^[i, j] := 0;
                end;

for k := 0 to nproj - 1 do
  begin
        {projection angle}
        if nproj mod 4 = 0 then
          theta := (k + 0.5) * 180.0 / nproj
        else
          theta := k * 180.0 / nproj;
    costh := cos(theta * pi / 180);
    sinth := sin(theta * pi / 180);

    for i := -vsize div 2 to vsize div 2 - 1 do
    for j := -hsize div 2 to hsize div 2 - 1 do
        if (theta = 0) then
          begin
                ptheta^[k, i] := ptheta^[k, i] + im^[i, j];
                W^[k, i] := W^[k, i] + 1;
          end
        else if (theta = 90) then
          begin
                ptheta^[k, j] := ptheta^[k, j] + im^[i, j];
                W^[k, j] := W^[k, j] + 1;
          end
        else
        begin
          tr := i * costh + j * sinth;
          if (tr >= 0) then
                t := trunc(tr)
          else
                t := trunc(tr - 1);
          ptheta^[k, t] := ptheta^[k, t] + im^[i, j] *
                        (1 - abs(tr - t));
          ptheta^[k, t + 1] := ptheta^[k, t + 1] +
                        im^[i, j] * abs(tr - t);
          W^[k, t] := W^[k, t] + (1 - abs(tr - t));
          W^[k, t + 1] := W^[k, t + 1] + abs(tr - t);
        end;
  end;


{Get one projection (reprojection), indexed as projnum., from an intermediate ART
reconstruction. Linear Interpolation is used.}
procedure OneProjection(projnum: integer);
        var
```

```
                theta, costh, sinth, tr: real;
                i, j, k, t: integer;
    begin
            k := projnum;
            if nproj mod 4 = 0 then
                    theta := (k + 0.5) * 180.0 / nproj
            else
                    theta := k * 180.0 / nproj;
            costh := cos(theta * pi / 180);
            sinth := sin(theta * pi / 180);

            for t := -hsize to hsize - 1 do
                    pthetaq^[k, t] := 0;

            for i := -vsize div 2 to vsize div 2 - 1 do
             for j := -hsize div 2 to hsize div 2 - 1 do
              if (theta = 0) then
                    pthetaq^[k, i] := pthetaq^[k, i] + im^[i, j]
              else if (theta = 90) then
                    pthetaq^[k, j] := pthetaq^[k, j] + im^[i, j]
              else
               begin
                    tr := i * costh + j * sinth;
                    if (tr >= 0) then
                            t := trunc(tr)
                    else
                            t := trunc(tr - 1);
                    pthetaq^[k, t] := pthetaq^[k, t] +
                         im^[i, j] * (1 - abs(tr - t));
                    pthetaq^[k, t + 1] := pthetaq^[k, t + 1]
                            + im^[i, j] * abs(tr - t);
               end;
    end;


{Update the projection indexed as projnum by ART. Linear interpolation is used}
  procedure imodification(projnum: integer);
            var
                    theta, costh, sinth, tr: real;
                    i, j, k, t: integer;
   begin
      k := projnum;
      if nproj mod 4 = 0 then
              theta := (k + 0.5) * 180.0 / nproj
      else
              theta := k * 180.0 / nproj;
      costh := cos(theta * pi / 180);
      sinth := sin(theta * pi / 180);

      for i := -vsize div 2 to vsize div 2 - 1 do
        for j := -hsize div 2 to hsize div 2 - 1 do
          begin
            if (theta = 0) then
                    begin
```

```
                    t := i;
                    tr := i;
                end
            else if (theta = 90) then
                begin
                    t := j;
                    tr := j;
                end
            else
                begin
                    tr := i * costh + j * sinth;
                    if (tr >= 0) then
                        t := trunc(tr)
                    else
                        t := trunc(tr - 1);
                end;
            if W^[k, t] <> 0 then
               im^[i, j] := im^[i, j] + (ptheta^[k, t] -
            pthetaq^[k, t])/ W^[k, t] * (1 - abs(tr - t));
            if W^[k, t + 1] <> 0 then
               im^[i, j] := im^[i, j] + (ptheta^[k, t + 1] -
                 pthetaq^[k, t + 1])/ W^[k, t + 1] * abs(tr - t);
            if im^[i, j] < 0 then
                im^[i, j] := 0;
    end;
end;


{Backprojection of one projection indexed asprojnum to the image im by CBP.
Linear interpolation is used}
procedure ReconsOneProj (projnum: integer);
        var
            theta, costh, sinth: real;
            i, j, k, t: integer;
            tr: real;
begin
        k := projnum;
        if nproj mod 4 = 0 then
            theta := (k + 0.5) * 180.0 / nproj
        else
            theta := k * 180.0 / nproj;
        costh := cos(theta * pi / 180);
        sinth := sin(theta * pi / 180);

        for i := -vsize div 2 to vsize div 2 - 1 do
          for j := -hsize div 2 to hsize div 2 - 1 do
            begin
              if (theta = 0) then
                  begin
                      t := i;
                      tr := i;
                  end
              else if (theta = 90) then
                  begin
```

```
                        t := j;
                        tr := j;
                    end
                else
                    begin
                        tr := i * costh + j * sinth;
                        if (tr >= 0) then
                            t := trunc(tr)
                        else
                            t := trunc(tr - 1);
                    end;
                im^[i, j] := im^[i, j] + ptheta^[k, t] *
                  (1 - abs(tr - t)) + ptheta^[k, t + 1] *
                  abs(tr - t);
            end;
    end;


{Precise projection of an input image im to get a total of nproj projection data. It is much
 slower than the interpolation method although more accurate.}
{im: input image. -Global}
{p: projection data. -Global}
procedure ProjectionData;
    var
    theta,sinth,costh,abssinth,abscosth,oc,luc,btc,op12,op23,halffre,fr: real;
    op: array [1..4] of real;
    dw: array [1..3] of real;
    i,j,k,d,dstart,dmiddle,n:integer;
 begin
    for k := 0 to nproj - 1 do
        for d := -hsize to hsize - 1 do
            p^[k, d] := 0;
    for d := -hsize to hsize - 1 do
        vn[d] := 0;

    for k := 0 to nproj - 1 do
      begin
        theta := k*pi/nproj;
        costh := cos(theta);
        sinth := sin(theta);
        abscosth := abs(costh);
        abssinth := abs(sinth);
        luc := abs(abscosth-abssinth)/2;
        btc :=   (abscosth+abssinth)/2;

        if (theta<=pi/4) or (theta >3*pi/4) then
            halffre:= 1/(2*abscosth)
        else if (theta<=3*pi/4) or (theta>pi/4) then
            halffre:= 1/(2*abssinth);

        for i := -vsize div 2 to vsize div 2 - 1 do
          for j := -hsize div 2 to hsize div 2 - 1 do
            begin
              oc := i*costh +j *sinth;
```

```
                op[1]:=oc-btc;
                op[2]:=oc-luc;
                op[3]:=oc+luc;
                op[4]:=oc+btc;
                op12:=abs(op[1]-op[2]);
                op23:=abs(op[2]-op[3]);

                for n:=1 to 4 do
                begin
                        d:=trunc(op[n]);
                        fr:=op[n]-d;
                        if (op[n]>=0) and (fr>=0.5) then
                                d:=d+1
                        else if (op[n]<0) and (fr<-0.5) then
                                d:=d-1;
                        vn[d]:=vn[d]+1;
                        if n=1 then
                                dstart:=d
                end;
                dmiddle:=dstart+1;

                case vn[dstart] of
        1:      begin
                  dw[1]:= (dstart+0.5-op[1])*halffre;
                  case vn[dmiddle] of
                  2: dw[2]:= 1- dw[1]-(op[4]-dmiddle-0.5)*halffre;
                  3: dw[2]:=1-dw[1];
                end;
                end;
        2:      begin
                  dw[1]:= (op12+(dstart+0.5-op[2])*2)*halffre;
                  dw[2]:= 1- dw[1];
                end;
        3:      begin
                  dw[1]:= (op12+op23*2+(dstart+0.5-op[3]))*halffre;
                  dw[2]:= 1- dw[1];
                end;
          end;
                  dw[3]:=1- dw[1]-dw[2];

                for d:=dstart to dstart+2 do
                        begin
                          p^[k,d]:=p^[k,d]+dw[d-dstart+1]*im^[i,j];
                          w^[k,d]:=w^[k,d]+dw[d-dstart+1];
                          vn[d]:=0;
                        end;
        end;
    end;
end;


{Make one projection of the reconstructing image by ART and compare it to the
 actual projection data and then update the reconstruction. Precise projection is used.}
{im: input image. -Global}
```

```
{p: projection data. -Global}
{pq: one projection data for updating. -Global}
procedure OneProjectionAndModification(k: integer);
    var
    theta,sinth,costh,abssinth,abscosth,oc,luc,btc,op12,op23,
   halffre,fr: real;
    op: array [1..4] of real;
    dw: array [1..3] of real;
    i,j,d,dstart,dmiddle,n:integer;
begin
    theta := k * pi/ nproj;
    costh := cos(theta);
    sinth := sin(theta);
    abscosth := abs(costh);
    abssinth := abs(sinth);
    btc := abs(abscosth+abssinth)/2;
    luc := abs(abscosth-abssinth)/2;
    if (theta<=pi/4) or (theta >3*pi/4) then
        halffre:= 1/(2*abscosth)
    else if (theta<=3*pi/4) or (theta>pi/4) then
        halffre:= 1/(2*abssinth);
    for i := -vsize div 2 to vsize div 2 - 1 do
      for j := -hsize div 2 to hsize div 2 - 1 do
       begin
        oc := i*costh +j *sinth;
        op[1]:=oc-btc;
        op[2]:=oc-luc;
        op[3]:=oc+luc;
        op[4]:=oc+btc;
        op12:=abs(op[1]-op[2]);
        op23:=abs(op[2]-op[3]);

        for n:=1 to 4 do
        begin
            d:=trunc(op[n]);
            fr:=op[n]-d;
            if (op[n]>=0) and (fr>=0.5) then
                d:=d+1
            else if (op[n]<0) and (fr<-0.5) then
                d:=d-1;
            vn[d]:=vn[d]+1;
            if n=1 then
                dstart:=d
        end;
        dmiddle:=dstart+1;

        case vn[dstart] of
        1:      begin
                 dw[1]:= (dstart+0.5-op[1])*halffre;
                 case vn[dmiddle] of
                 2: dw[2]:= 1- dw[1]-(op[4]-dmiddle-0.5)*halffre;
                 3: dw[2]:=1-dw[1];
                end;
                end;
```

```
        2:      begin
                  dw[1]:= (op12+(dstart+0.5-op[2])*2)*halffre;
                  dw[2]:= 1- dw[1];
                end;
        3:      begin
                  dw[1]:= (op12+op23*2+(dstart+0.5-op[3]))*halffre;
                  dw[2]:= 1- dw[1];
                end;
        end;
                  dw[3]:=1- dw[1]-dw[2];

        for d:=dstart to dstart+2 do
                begin
                        pq^[k,d]:=pq^[k,d]+dw[d-dstart+1]*im^[i,j];
                        vn[d]:=0;
                end;
    end;

for i := -vsize div 2 to vsize div 2 - 1 do
    for j := -hsize div 2 to hsize div 2 - 1 do
     begin
        oc := i*costh +j *sinth;
        op[1]:=oc-btc;
        op[2]:=oc-luc;
        op[3]:=oc+luc;
        op[4]:=oc+btc;
        op12:=abs(op[1]-op[2]);
        op23:=abs(op[2]-op[3]);

        for n:=1 to 4 do
        begin
                d:=trunc(op[n]);
                fr:=op[n]-d;
                if (op[n]>=0) and (fr>=0.5) then
                        d:=d+1
                else if (op[n]<0) and (fr<-0.5) then
                        d:=d-1;
                vn[d]:=vn[d]+1;
                if n=1 then
                        dstart:=d
        end;
        dmiddle:=dstart+1;

        case vn[dstart] of
        1:      begin
                  dw[1]:= (dstart+0.5-op[1])*halffre;
                  case vn[dmiddle] of
                  2: dw[2]:= 1- dw[1]-(op[4]-dmiddle-0.5)*halffre;
                  3: dw[2]:=1-dw[1];
                end;
                end;
        2:      begin
                  dw[1]:= (op12+(dstart+0.5-op[2])*2)*halffre;
                  dw[2]:= 1- dw[1];
```

```
                end;
            3:  begin
                  dw[1]:= (op12+op23*2+(dstart+0.5-op[3]))*halffre;
                  dw[2]:= 1- dw[1];
                end;
            end;
                  dw[3]:=1- dw[1]-dw[2];

            for d:=dstart to dstart+2 do
             begin
               if w^[k,d]>0 then
               im^[i,j]:=im^[i,j]+(p^[k,d]-pq^[k,d])/w^[k,d]*dw[d-dstart+1];
               vn[d]:=0;
             end;
            if im^[i, j] < 0 then
                  im^[i, j] := 0;
        end;
end;


{Reconstruction one projection for CBP after the convolution filtration. Precise
backprojection is used}
{im: input image. -Global}
{p: projection data. -Global}
procedure ReconstructionOneProjection(k: integer);
    var
    theta,sinth,costh,abssinth,abscosth,oc,luc,btc,op12,op23,
     halffre,fr: real;
    op: array [1..4] of real;
    dw: array [1..3] of real;
    i,j,d,dstart,dmiddle,n:integer;
begin
    theta := k * pi/ nproj;
    costh := cos(theta);
    sinth := sin(theta);
    abscosth := abs(costh);
    abssinth := abs(sinth);
    btc := abs(abscosth+abssinth)/2;
    luc := abs(abscosth-abssinth)/2;
    if (theta<=pi/4) or (theta >3*pi/4) then
          halffre:= 1/(2*abscosth)
    else if (theta<=3*pi/4) or (theta>pi/4) then
          halffre:= 1/(2*abssinth);
    for i := -vsize div 2 to vsize div 2 - 1 do
      for j := -hsize div 2 to hsize div 2 - 1 do
       begin
          oc := i*costh +j *sinth;
          op[1]:=oc-btc;
          op[2]:=oc-luc;
          op[3]:=oc+luc;
          op[4]:=oc+btc;
          op12:=abs(op[1]-op[2]);
          op23:=abs(op[2]-op[3]);
```

```
                for n:=1 to 4 do
                begin
                        d:=trunc(op[n]);
                        fr:=op[n]-d;
                        if (op[n]>=0) and (fr>=0.5) then
                                d:=d+1
                        else if (op[n]<0) and (fr<-0.5) then
                                d:=d-1;
                        vn[d]:=vn[d]+1;
                        if n=1 then
                                dstart:=d
                end;
                dmiddle:=dstart+1;

                case vn[dstart] of
                1:      begin
                         dw[1]:= (dstart+0.5-op[1])*halffre;
                         case vn[dmiddle] of
                         2: dw[2]:= 1- dw[1]-(op[4]-dmiddle-0.5)*halffre;
                         3: dw[2]:=1-dw[1];
                        end;
                        end;
                2:      begin
                         dw[1]:= (op12+(dstart+0.5-op[2])*2)*halffre;
                         dw[2]:= 1- dw[1];
                        end;
                3:      begin
                         dw[1]:= (op12+op23*2+(dstart+0.5-op[3]))*halffre;
                         dw[2]:= 1- dw[1];
                        end;
                end;
                         dw[3]:=1- dw[1]-dw[2];

                for d:=dstart to dstart+2 do
                        begin
                         im^[i, j] := im^[i, j]+dw[d-dstart+1]*p^[k,d];
                         vn[d]:=0;
                        end;
        end;
end;


{Add Gaussian noise to projection data}
{nproj: the number of CT projections. - Global }
{photon: the number of photons used in a single measurement. -Global}
{phonum: the number of photons detected in a single measurement }
{p: the projection data. -Global}
{hsize, vsize: an image's vertical and horizontal size}
{SD: the standard deviation of photons}
{NOISE: the noise deviation obtained after the Gaussian sampling}
procedure AddPhotonNoise;
        var
                k, d: integer;
                ran1, ran2, ran3, ran4, SD, NOISE, phonum: real;
```

```
begin
 for k := 0 to nproj - 1 do
 for d := -hsize to hsize - 1 do
   begin
        {scale the projection data down to tissue attenuation range}
        p^[k, d] := p^[k, d] / (3200 * vsize / 128);
        {after attenuation}
        phonum := photon * exp(-p^[k, d]);
        SD := sqrt(phonum);

        if (SD = 0) then {Gaussian sampling}
                NOISE := 0
        else
                begin
                  repeat
                        ran1:=random(seed)*2-1;
                        ran2 := 3 * sqrt(2) * ran1 * SD;
                        ran3:=random(seed);
                        ran4 := exp(-(ran2 * ran2) / (2 * SD * SD));
                  until (ran3 <= ran4);
                        NOISE := ran2;
                end;
        phonum := phonum + NOISE; {the actually detected photons}
        {output noisy projection data}
        p^[k, d] := ln(photon / phonum) * (3200 * vsize / 128);
   end;
end;


{MLSProjectionOrders: Calculate the MLS orders for a total of nproj  projections, the
details of it is published in:
H. Guan and R. Gordon, A projection access order for speedy  convergence of algebraic
reconstructions techniques (ART): A multilevel  scheme (MLS) for computed tomography,
Phys. in Med. and Biol. 39,  2005-2022, 1994.}
{nproj: the number of CT projections. - Global}
{projord: the array to hold the MLS ordering. - Global}
{pflag: the flag array to signal if a projection index in a sequential
 order is used or not: 1 used, 0 not used. - Global}
{L: the index of a multilevel}
{N: the number of projections in a level}
{kl, kr: search the left and right side of an index which is already  used, in the last level}
procedure MLSProjectionOrders;
label
        10, 20;
var
        i,j,k,N,kl,kr:integer;
begin

        projord[1] := 0; {ordering the first level}
        projord[2] := nproj / 2;
        N := 1;    {ordering the second to the second last levels}
        for i := 1 to L - 1 do
          begin
                N := N * 2;
```

```
            for j := 1 to N do
                projord[N + j] := projord[j] + nproj / (2 * N);
        end;
    for j := 0 to nprojminus1 do
            pflag[j] := 0;
    for j := 1 to N do
        begin
            k := round(projord[j]);
            projord[j] := k;
            pflag[k] := 1;
        end;

    for j := N + 1 to nproj do  {ordering the last level}
        begin
            k := round(projord[j]);
            if pflag[k] = 1 then
                begin
                    for i := k to nprojminus1 do
                        if (pflag[i] = 0) then
                            begin
                                kr := i - k;
                                goto 10;
                            end;
                    kr := 0;
    10:
                    for i := k downto 0 do
                        if (pflag[i] = 0) then
                            begin
                                kl := i - k;
                                goto 20;
                            end;
                    kl := 0;
    20:
                    if (kl = 0) or (kr = 0) then
                        k := k + kl + kr
                    else if kr + kl <= 0 then
                        k := k + kr
                    else
                        k := k + kl
                end;
            projord[j] := k;
            pflag[k] := 1;
        end;
end;


{Convolution filtration of the projection data by the ramp filter }
{h: the kernal for the ramp filter}
{p: the projection data}
{hsize, vsize: an image's vertical and horizontal size}
procedure ConvFilteringProjection (fBAND: integer);
    var         {Frequency BAND 1:full Band, -1:half Band}
        k, m, n: integer;
        h1nMINUSm, phi, temp, sign: real;
```

```
                data: array[1..ndat2] of double;
begin
 for k := 0 to nproj - 1 do      {theta ,    tao=1}
    begin
        for n := -hsize to hsize - 1 do                  {t}
          begin
                temp := 0;
                for m := -hsize to hsize - 1 do                  {t'}
                if p^[k, m] <> 0 then
                  begin
                   if (fBAND = 1) then      {full Band}
                        if ((n - m) mod 2 = 0) and (n <> m) then
                         h1nMINUSm := 0
                        else if n = m then
                         h1nMINUSm := 1 / 4
                        else
                         h1nMINUSm := -1 / (sqr((n - m) * pi))
                    else
                         begin       {half band}
                          if n = m then
                           h1nMINUSm := 1 / 16
                          else if (n - m) mod 4 = 0 then
                            h1nMINUSm := 0
                          else
                           begin
                               phi := (n - m) * pi / 4;
                               if (n - m) mod 2 = 0 then
                                  h1nMINUSm := -1 / (16 * phi * phi)
                               else
                                  begin
                                       phi := (n - m) * pi / 4;
                                       if (n - m) mod 2 = 0 then
                                          h1nMINUSm := -1 / (16 * phi * phi)
                                       else
                                          begin
                                            sign := abs(n - m) / (n - m);
                                            if abs(n - m) mod 4 = 3 then
                                                  sign := -sign;
                                            h1nMINUSm := -(1 / (32 * phi * phi) -
                                                  sign / (16 * phi));
                                          end;
                                  end;
                           end;
                                       temp := temp + p^[k, m] * h1nMINUSm;
                        end;
                        data[n + hsize + 1] := temp;
                end;

                for n := -hsize to hsize - 1 do
                  p^[k, n] := data[n + hsize + 1];
    end;
end;
```

Part II

procedure CD_DiskCenterPositions;
Objective: set the disk center coordinates and the radius in the *contrast detail phantom* (see Fig. 5.7.1).
Input: none
Output: the disk center coordinates (x, y) for a total of 6 sets of disks (each set consists of 6 disks of the same size) stored in the array *centers* and the 6 radius stored in the array *r* .
Note: The disks are laid on an 512x512 image (-256 to 255, -256 to 255)

procedure CD_CreatePhantom;
Objective: create the *contrast detail phantom* (see Fig. 5.7.1).
Input: the disk center coordinates (x, y) and the radius r created using the procedure *CD_DiskCenterPositions* above.
Output: the *contrast detail phantom.*
Note: a large background disk with a dark edge is first created before creating the contrast detail disks.

procedure BarCenterPositions;
Objective: set the bar center coordinates in the *bar pattern phantom* (see Fig. 5.8.1).
Input: none
Output: the bar center coordinates (x, y) stored in the array *centers* for the total 5 sets of bars.
Note: The bars are laid on an 512x512 image (-256 to 255, -256 to 255)

procedure Bar__CreatePhantom;
Objective: create the *bar pattern phantom* (see Fig. 5.8.1).
Input: the bar center coordinates (x, y) created using the procedure *BarCenterPositions* above.
Output: the *bar pattern phantom*
Note: a large background disk with a dark edge is first created before creating the bars.

procedure MeanStdMTF(pp:integer);
Objective: calculate the MTF from the reconstructions of the bar pattern phantom.
Input: the reconstructed bar pattern phantom image *im.*
Output: the MTF stored in the array *msm.*
Note: see section 2.4.4 for more detail .

procedure LC_DiskCenterPositions;
Objective: set the disk center coordinates and the radius in the *low contrast phantom* (see Fig. 5.6.1).
Input: none
Output: the disk center coordinates (x, y) for a total of 5 disks.
Note: The disks are laid on an 512x512 image (-256 to 255, -256 to 255)

procedure LC_CreatePhantom;
Objective: create the *low contrast phantom* (see Fig. 5.6.1).
Input: the disk center coordinates (x, y) created using the procedure *LC_DiskCenterPositions* above.
Output: the *low contrast phantom.*

Note: a large background disk with a dark edge is first created before creating the contrast detail disks.

procedure MeanStdSNR(pp:integer);
Objective: calculate the SNR from the reconstructions of the low contrast phantom.
Input: the reconstructed low contrast phantom image *im*.
Output: the SNR stored in the array *msc*.
Note: see section 2.4.2 for more detail .

procedure FFTran;
Objective: Fourier transform of the central part of an image *im* .
Input: an image *im* of sizes 512x512. Only the central 256x256 is calculated.
Output: the Fourier amplitude of the central part of *im* .
Note: There are two major applications of this procedure as described on the top of the code.

Computer codes:

```
{Disk center coordinates and radius in the contrast detail phantom.
Image size 512x512 (-256 to 255, -256 to 255)
Both r and centers are global arrays}
 procedure CD_DiskCenterPositions;
     var
      i, j, x, y: integer;
     begin
          for i := 1 to 6 do
            begin
                {radius for each set of 6 disks having same size}
                r[i] := 20-(i-1)*4;
                if (i=6) then
                        r[i] := 2;
                x := -100 + (56 - 4*(i-2))*(i-1);
                for j := 1 to 6 do
                        begin
                                y := -160 + 64 * (j-1);
                                centers[i, j, 1] := x;
                                centers[i, j, 2] := y;
                        end;
            end;
     end;


 {Create the contrast detail phantom image im . hfhvsize is half of the image size or 256}
 procedure CD_CreatePhantom;
     var
       i, j, i0, j0, p, q: integer;
      graystep: real;
     begin
       { create a large background disk with edges}
       for i := -hfhvsize to hfhvsizeminus1 do
              for j := -hfhvsize to hfhvsizeminus1 do
          if (i*i+j*j< sqr(hfhvsizeminus1)) and
            (i*i+j*j>= sqr(hfhvsizeminus1-2)) then
                im^[i, j]:=255
          else if i*i+j*j< sqr(hfhvsizeminus1-2) then
```

```
                    im^[i, j]:=127
            else
                    im^[i, j]:=0;

    {create the 6 group of disks, total 36 ones }
    graystep := 1;
    for p := 1 to 6 do
      for q := 1 to 6 do
          begin
            i0 := centers[p, q, 1];
            j0 := centers[p, q, 2];
            for i := i0 - r[p]-1 to i0 +r[p]+1 do
               for j := j0 - r[p]-1 to j0+r[p]+1 do
                  if sqr(i-i0)+sqr(j-j0)<= r[p]*r[p] then
                    im^[i, j]:=im^[i,j] - q*graystep;
          end;
end;


{Bar center coordinates in the Bar pattern phantom - Global, Image size 512x512.  a=16.
The standard deviation will be measured inside a central square of 32x32 pixels=npxls
in each set of bar patterns}
 procedure BarCenterPositions;
  var
   i, j: integer;
  begin
        centers[1, 1] := -112;
        centers[1, 2] := -112;
        centers[2, 1] := -56;
        centers[2, 2] := -56;
        centers[3, 1] := 0;
        centers[3, 2] := 0;
        centers[4, 1] := 56;
        centers[4, 2] := 56;
        centers[5, 1] := 112;
        centers[5, 2] := 112;

        {No. 6 is not for a bar pattern, but for
              a uniform square later for the noise
              correction}
        centers[6, 1] := -vsize div 4;
        centers[6, 2] := 0;
        npxls:=0;
              for i:=-a to a-1 do
                      for j:=-a to a-1 do
                              npxls:=npxls+1;
  end;


{ Create the bar pattern phantom,  hfhvsize is half of the image size or 256 }
  procedure Bar__CreatePhantom;
    var
        i, j, i0, j0, k, n, barwidth: integer;
      begin
```

```
    {create a large background disk with edges}
    for i := -hfhvsize to hfhvsizeminus1 do
            for j := -hfhvsize to hfhvsizeminus1 do
        if (i*i+j*j< sqr(hfhvsizeminus1)) and
          (i*i+j*j>= sqr(hfhvsizeminus1-2)) then
                    im^[i, j]:=143
                else if i*i+j*j< sqr(hfhvsizeminus1-2) then
                    im^[i, j]:=127
                else
                    im^[i, j]:=0;

    {create the 5 sets of bar patterns, A = 24. Each set occupies 48x48 pixels}
        barwidth:=1;
        for k := 1 to 5 do
     begin
        i0 := centers[k, 1];
        j0 := centers[k, 2];
        for i := i0 - A to i0 + A - 1 do
          for j := j0 - A to j0 + A - 1 do
            begin
            n:=(j-j0+A) div barwidth;
            if n mod 2 = 0 then
              im^[i, j]:=im^[i,j]+128;
            end;
        barwidth:=barwidth*2;
     end;
   end;


{The MTF calculation from the Bar pattern reconstructions.
 msm is a 3D global array:
    1st index: pp - iteration number.
    2nd index: 1 - mean, 2 - the standard deviation, 3 - MTF value.
    3rd index: k - bar pattern index}
procedure MeanStdMTF(pp:integer);
  var
        i,j,k,i0,j0: integer;
        sum, M0 : real;
  begin
    {the mean}
    for k := 1 to 6 do
      begin
        sum:=0;
        i0 := centers[k, 1];
        j0 := centers[k, 2];
        for i := i0 - a to i0 + a -1 do
          for j := j0 - a to j0 + a -1 do
              sum:= sum +im^[i,j];
        msm[pp, 1, k]:=sum/npxls;
      end;

      {the standard deviation}
      for k := 1 to 6 do
      begin
```

```
            sum:=0;
            i0 := centers[k, 1];
            j0 := centers[k, 2];
            for i := i0 - a to i0 + a -1 do
              for j := j0 - a to j0 + a -1 do
                sum:= sum + sqr(im^[i,j]-msm[pp, 1, k]);
            msm[pp, 2, k]:=sum/(npxls-1);
        end;

      {MTF calculation}
        M0:=64;
        for k := 1 to 5 do
            begin
              {noise correction by the No. 6 square}
                  msm[pp, 3, k]:= sqrt(msm[pp, 2, k] - msm[pp, 2, 6]);
                  msm[pp, 3, k]:= pi*sqrt(2)*msm[pp, 3, k]/(4*M0);
            end;
            msm[pp, 3, 6]:=0;
      end;


{Disk center coordinates in the low contrast phantom. Image size 512x512, vsize=512,
hsize=512, r=20. The noise standard deviation will be measured inside a circle of r,
centered at each disk whose radius r0 = 24}
procedure LC_DiskCenterPositions;
  var
   i, j: integer;
  begin
      centers[1, 1] := -(vsize div 16)*3;
      centers[1, 2] := -(hsize div 16)*3;
      centers[2, 1] := -(vsize div 16)*3;
      centers[2, 2] :=  (hsize div 16)*3;
      centers[3, 1] :=  0;
      centers[3, 2] :=  0;
      centers[4, 1] :=  (vsize div 16)*3;
      centers[4, 2] := -(hsize div 16)*3;
      centers[5, 1] :=  (vsize div 16)*3;
      centers[5, 2] :=  (hsize div 16)*3;

      {No. 6 is not for a disk center, but for
            a uniform circle in the background}
      centers[6, 1] :=  -vsize div 4;
      centers[6, 2] :=  0;
      npxls:=0;
      for i:=-r-1 to r+1 do
            for j:=-r-1 to r+1 do
                  if i*i+j*j <=r*r then
                        npxls:=npxls+1;
  end;


{Create the low contrast phantom:  hfhvsize is half of the image size or 256}
  procedure LC_CreatePhantom;
      var
```

```
        i, j, i0, j0, k: integer;
        graystep: real;
  begin
    {create a large background disk with edges}
     for i := -hfhvsize to hfhvsizeminus1 do
       for j := -hfhvsize to hfhvsizeminus1 do
           if (i*i+j*j< sqr(hfhvsizeminus1)) and
             (i*i+j*j>= sqr(hfhvsizeminus1-2)) then
               im^[i, j]:=255
           else if i*i+j*j< sqr(hfhvsizeminus1-2) then
               im^[i, j]:=127
           else
               im^[i, j]:=0;

    {create the 5 low contrast disks, r0 = 24 }
       graystep := 1;
       for k := 1 to 5 do
          begin
               i0 := centers[k, 1];
               j0 := centers[k, 2];
               for i := i0 - r0-1 to i0 +r0+1 do
                  for j := j0 - r0-1 to j0+r0+1 do
                     if sqr(i-i0)+sqr(j-j0)<= r0*r0 then
                       im^[i, j]:=im^[i,j] - k*graystep;
          end;
  end;


{Calculate the signal to noise ratio SNR of the low contrast disks, r=20}
 {msm is a 3D global array:
  1st index: pp - iteration number.
  2nd index: 1 - mean, 2 - the standard deviation, 3 - SNR value.
  3rd index: k - disk index}
  procedure MeanStdSNR(pp:integer);
       var
               i,j,k,i0,j0: integer;
               sum :   real;
     begin
       {the mean}
       for k := 1 to 6 do
          begin
               sum:=0;
               i0 := centers[k, 1];
               j0 := centers[k, 2];
               for i := i0 - r-1 to i0 + r+1 do
                  for j := j0 - r-1 to j0 + r+1 do
                     if sqr(i-i0)+sqr(j-j0)<= r*r then
                       sum:= sum +im^[i,j];
              msc[pp, 1, k]:=sum/npxls;
          end;

         {the noise standard deviation}
          for k := 1 to 6 do
          begin
```

```
            sum:=0;
            i0 := centers[k, 1];
            j0 := centers[k, 2];
            for i := i0 - r-1 to i0 + r+1 do
               for j := j0 - r-1 to j0 + r+1 do
                  if sqr(i-i0)+sqr(j-j0)<= r*r then
                    sum:= sum + sqr(im^[i,j]-msc[pp, 1, k]);
            msc[pp, 2, k]:=sum/(npxls-1);
        end;

       {the SNR}
       for k := 1 to 5 do
         msc[pp, 3, k]:= abs(msc[pp, 1, k]-msc[pp, 1, 6]) /sqrt(msc[pp, 2, k]+ msc[pp, 2, 6]);
       msc[pp, 3, 6]:=0;
  end;


{Fourier transform of the difference image of a reconstruction to its original water only
 phantom for calculating the noise power spectrum, only the central part 256x256 is
 calculated}
{This procedure is also used for calculating the MTF using the thin wire method if desired,
 just put a small square of image like 32x32 centered at the wire (i0, j0) into the data
 array by replacing hfhvsize with 32 and im^[i - hfhvsize div 2, j - hfhvsize div 2]
 with im^[i+i0-16, j+j0-16]}
  procedure FFTran;
       var
            i, j, ii, ndim: integer;
   begin
            {put the 256x256 image im into a 1D array data -Global}
       for i := 0 to hfhvsize - 1 do
            for j := 0 to hfhvsize - 1 do
                 begin
                      ii := 1 + 2 * j + 2 * i * hfhvsize;
                      data^[ii] := im^[i - hfhvsize div 2,
                              j - hfhvsize div 2];
                      if (i + j) mod 2 = 1 then {FFT always centered }
                              data^[ii] := -data^[ii];
                      data^[ii + 1] := 0;
                 end;
       nn[1] := hfhvsize;
       nn[2] := hfhvsize;
       ndim := 2;

     {Fourier transform of the data, see Numerical Recipe the fourn function}
       fourn(data, nn, ndim, -1);

     {Get the Fourier amplitude}
       for i := 0 to hfhvsize - 1 do
            for j := 0 to hfhvsize - 1 do
                 begin
                    ii := 1 + 2 * j + 2 * i * hfhvsize;
                    c[i, j]:= c[i,j] + sqrt(sqr(data^[ii])+ sqr(data^[ii+1]));
                 end;
  end;
```